Mass Loss from Hot, Luminous Stars

Adam Warwick Burnley

Thesis submitted for the degree of Doctor of Philosophy
of the University of London

Department of Physics & Astronomy
University College London

July 2003

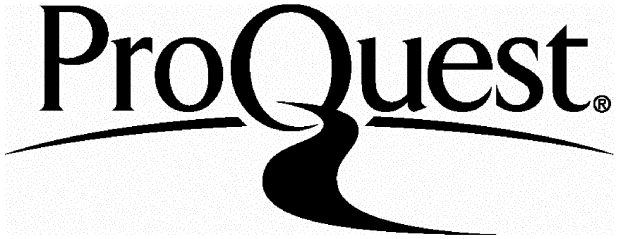

For Mum and Dad

"If you just set out to be liked, you would be prepared to compromise on anything at any time, and you would achieve nothing."

Margaret Thatcher

"Remember that not getting what you want is sometimes a wonderful stroke of luck."

The Dalai Lama

Dramatic observational evidence for mass loss: the star HD 148937 (O6.5f?p) and associated nebulosity, NGC 6164-5. This extremely hot, luminous star is losing mass continually from its outer layers, but more violent outbursts have produced the symmetrical shells of material seen here. Image obtained by David Malin using the Anglo-Australian Telescope (AAT).

ABSTRACT

A general enquiry into the physics of mass loss from hot, luminous stars is presented.

Hα spectroscopy of 64 Galactic early-type stars has been obtained using the telescopes of the Isaac Newton Group (ING) and the Anglo-Australian Observatory (AAO). The sample was selected to include objects with published radio and/or mm fluxes. The Hα observations are quantitatively modelled using a modified version of the FORSOL code developed by Puls *et al.* (1996). FORSOL has been coupled with the PIKAIA subroutine (Charbonneau and Knapp, 1996) to create PHALTEE (Program for Hα Line Transfer with Eugenic Estimation), in order to search a specified parameter space for the 'best' (quasi-least-squares) model fit to the data, using a genetic algorithm. This renders Hα modelling both more objective and automated. Where possible, both mass-loss rates and velocity field β-exponents are determined for the sample.

New mm-wave observations of nineteen Galactic early-type stars, including a subset of the Hα sample, have been obtained using the Sub-millimetre Common User Bolometer Array (SCUBA). Where possible, mean fluxes are calculated, and these data used with the results of a literature survey of mm and cm fluxes to determine mass-loss rates for a larger sample, of 53 Galactic early-type stars. The incidence of nonthermal emission is examined, with 23% of the sample exhibiting strong evidence for nonthermal flux. The occurrence of binarity and excess X-ray emission amongst the nonthermal emitters is also investigated.

For the subset of 36 stars common to both the Hα *and* mm/radio samples, the results permit a comparison of mass-loss rates derived using diagnostics that probe the wind conditions at different radial depths. A mean value of $\log(\dot{M}_{\rm radio}/\dot{M}_{\rm H\alpha}) = 0.02 \pm 0.05$ is obtained for the thermal radio emitters. The wind-momentum–luminosity relationship (WLR) for the sample is also investigated.

ACKNOWLEDGEMENTS

First, and most importantly, I would like to thank my supervisor, Ian Howarth, for his guidance and advice throughout the course of my PhD. The completion of this thesis would not have been possible without his invaluable contributions.

I would also like to thank my parents for their love and encouragement over the years, and for giving me the opportunity to pursue my dreams. Without their unwavering support, the journey to where I am now would have been much more difficult. Thanks, Mum and Dad.

I am greatly indebted to Rich Townsend for his expert help with all things computer-related (come to think of it, with absolutely anything...), and for the use of his new spectral grids. Special thanks go to Richard Price and Rich Townsend (again!) for their thesis style files, and to Raman for his extremely helpful comments regarding this work. I am especially grateful to Allan Willis for his sterling work in keeping the wolves from my door.

Thanks to the members of A25, past and present: Chris, Rich T, Thomas, Ki-Won, and Fab. Our many discussions (of things astronomical and otherwise), whilst indulging in something alcoholic have been a vital part of the 'educational' experience. Thanks to Jay, Barbara, Sophie, Roger, Rich Norris, Dugan, Matt, Sams Searle and Thompson, Jo, and Paul. A big hello to all those who have known me during my time at UCL: to those who have moved on to pastures new and to those who are still hanging in there. Huge thanks to Ben for being there right the way to the end.

And to Grandma Brown, who didn't quite see me finish the whole thing off, but who gave the very good advice to 'take just one day at a time' (although lately several days would appear to have attacked me at once...).

Contents

List of Figures

List of Tables

CHAPTER 1

Introduction

This thesis is concerned with the physics of mass loss from hot, luminous stars. The term 'hot star' is used here to refer primarily to stars of spectral types O and B (effective temperature, $T_{\rm eff} \gtrsim 10\,000$ K), whilst the description 'luminous' should be read as excluding subdwarfs. Such objects occupy the upper left-hand corner of the Hertzsprung-Russell (H-R) diagram, and are synonymously known as massive, early-type or OB stars. All these terms will be used throughout this work.

1.1 Spectral classification

In order to organise the diversity of stellar spectra both in a tractable manner and in a way which encourages an astrophysical interpretation, stars are classified according to the appearance of their spectra. This classification is essentially a concise description of the key morphological features in the optical spectrum. Spectral classification greatly simplifies the treatment and comparison of results, and is one of the standard tools employed in the explanation of stellar evolution.

1.1.1 The Harvard classification scheme

The core of modern spectral classification is the Harvard scheme, developed at the Harvard Observatory by Cannon and Pickering (1918) for the Henry Draper (HD) catalogue. Initially, the Harvard scheme alphabetically classified stars according to the strengths of the hydrogen Balmer lines in their spectra, with the A stars having the strongest Balmer

lines. After some rearrangement and the omission of certain letters, the final ordering corresponded to a sequence of decreasing temperature:-

$$\text{O}-\text{B}-\text{A}-\text{F}-\text{G}-\text{K}-\text{M}$$

$$\longrightarrow$$

Decreasing temperature

The stars near the beginning of the sequence are known as 'early-type' stars, and those towards the end 'late type' (the Harvard workers erroneously thought that their original arrangement was an evolutionary sequence). Within each spectral class there are subdivisions (subtypes), denoted by a number ≥ 0 to < 10, where the '0' subtype is the hottest (the exception being the O stars, where the '2' subtype is the hottest; Walborn *et al.*, 2002).

1.1.2 MK luminosity classification

Two stars with the same temperature may have very different luminosities, and the effects of this difference can be observed in their spectra. To take account of this, a two-dimensional classification scheme was introduced by Morgan *et al.* (1943), which incorporates luminosity as well as temperature. Known as the MK system after its principal authors (the original 1943 work is commonly referred to as the MKK Atlas), it defines six major luminosity classes, denoted by the Roman numerals I–VI (see Table 1.1). Stars belonging to class I (the supergiants) are the most luminous, whilst stars of luminosity class V (the dwarfs) comprise the main sequence in the H-R diagram. The term 'main sequence', however, refers to stars burning hydrogen at their cores, and is often used interchangeably with 'dwarf' (i.e., luminosity class V). This can introduce ambiguity, as 'giants' and 'supergiants' of spectral types O and B probably also burn hydrogen at their cores. In this sense they are actually main-sequence objects. Care must therefore be taken when using luminosity-type nomenclature: throughout this work, the term 'main sequence' will be employed to refer to stars of luminosity class V. Within the supergiant and giant classifications there are further subclasses, e.g. Ia, Iab and Ib, where the 'a' subclass is the most luminous.

Table 1.1: The MK luminosity classification scheme

Class	Name
I	Supergiant
II	Bright giant
III	Giant
IV	Subgiant
V	Dwarf
VI	Subdwarf

NOTE: The subdwarf 'VI' classification is rarely used.

1.2 The initial mass function (IMF)

The most important factor when considering the evolution of a star is its initial mass. A star's mass determines both its main-sequence lifetime and its contribution to the enrichment of the interstellar medium (ISM) with heavy elements. High-mass stars dominate the luminosity of young galaxies and clusters, and are the primary source of the alpha elements, such as oxygen and magnesium. Intermediate-mass stars dominate the luminosity in older stellar systems, and, via Type Ia supernovae (SNe), are the origin of the iron-peak elements. Low-mass stars contain most of the baryonic mass which is involved in star formation. When the initial stellar mass is considered in conjunction with evolutionary models (e.g. Schaller *et al.*, 1992; Meynet *et al.*, 1994), it is possible to project other stellar parameters (e.g. $T_{\rm eff}$ and luminosity) at any point during the star's lifetime.

The initial mass function (IMF) describes the relative numbers of stars which form as a function of their main-sequence mass from a unit mass of ISM. Essentially, it describes the probability of a star forming with a given mass, and thus specifies the distribution in mass of a newly-formed stellar population. It is fundamentally important for a description of the luminosity and chemical evolution of the Universe.

Salpeter (1955), in his seminal investigation of the solar neighbourhood IMF, used the observed *luminosity* function for main-sequence stars (i.e., the number of stars observed at absolute visual magnitude M_V, per unit magnitude, per unit volume) to calculate the rate of star formation as a function of stellar mass. The mass function, $\phi(m)$, is just the

probability of a star forming with mass m, and is defined such that:-

$$\mathrm{d}N = \phi(m)\mathrm{d}m \tag{1.1}$$

where $\mathrm{d}N$ is the number of stars, per unit volume, of absolute visual magnitude in the interval, M_V to $(M_V + \mathrm{d}M_V)$, and $\phi(m)\mathrm{d}m$ is the number of stars formed at the same time, per unit volume, with initial masses in the interval, m to $(m + \mathrm{d}m)$. The mass function is, empirically, well described by a power law:-

$$\phi(m) = am^{\gamma} \tag{1.2}$$

Salpeter (1955) found an IMF slope, $\gamma = -2.35$. This power law appears to adequately apply for stellar masses in the range 1–100 $M_{\odot}$. Scalo (1986), however, demonstrated that a single power law cannot reproduce the shape of the IMF over the full stellar mass range. Scalo's (1986) treatment gives a decrease in slope at low masses (observations have since confirmed this), and a steeper function relative to the Salpeter IMF at high masses (the observational case for this remains uncertain). It has been suggested (Massey, 1998) that there is no 'upper mass cutoff' to the IMF, with statistics, rather than physics, limiting the highest-mass stars that we observe. The recent overview provided by contributions in the proceedings of the 38th Herstmonceux Conference on 'The Stellar IMF' (Gilmore and Howell, 1998) indicates that the stellar IMF is nearly a universal function. To a good first approximation, it would appear to apply at all metallicities, at all star formation rates, in all environments, and at all times.

1.3 Early-type stars

Early-type stars, the subject of this thesis, are amongst the hottest, most massive and most luminous stars known (see Table 1.2 for typical parameters). Whilst on the main sequence, they 'burn' hydrogen into helium at their cores via the CNO cycle. The rate of this conversion is extremely high, such that early-type stars have much shorter (but more violent) lives than lower-mass stars (notwithstanding the larger reserves of hydrogen fuel in massive-star cores). An O star will typically have a main-sequence (i.e., core H-burning) lifetime of only a few million years, making such objects useful tracers of star-forming regions. Early-type stars also possess powerful stellar winds, through which they continually lose mass (e.g. Morton, 1967*a*; Abbott *et al.*, 1981; Leitherer, 1988*a*;

Lamers and Leitherer, 1993; Puls *et al.*, 1996; Herrero *et al.*, 2000, 2002). During the final stages of their evolution, as Luminous Blue Variables (LBVs), Wolf-Rayet (WR) stars and, ultimately, supernovae, they may inject vast amounts of enriched material into the ISM (see the Frontispiece for an image of the star HD 148937, which is surrounded by symmetrical shells of material, believed to have been ejected during violent mass-loss outbursts). Thus, although massive stars form only a small fraction of the stellar population within the Galaxy (because of the nature of the IMF), they play an important rôle in its evolution, both chemically and kinematically (Abbott, 1982). The properties of such objects are therefore of great interest.

Table 1.2: Representative parameters for early-type stars

Spectral	$T_{\rm eff}$ (kK)			log $(L/L_\odot)$			$R/R_\odot$			$M/M_\odot$		
type	Ia	III	V	Ia	III	V	Ia	III	V	Ia	III	V
O3	50.7	51.0	51.2	6.27	6.15	6.04	17.8	15.3	13.2	115.9	101.4	87.6
O4	47.7	48.2	48.7	6.21	6.05	5.88	18.6	15.1	12.3	104.7	82.8	68.9
O4.5	46.2	46.8	47.4	6.18	5.99	5.81	19.1	15.0	11.8	95.7	75.8	62.3
O5	44.7	45.4	46.1	6.14	5.93	5.73	19.6	15.0	11.4	86.5	68.4	56.6
O5.5	43.2	44.0	44.8	6.10	5.88	5.65	20.1	14.9	11.0	79.5	62.0	50.4
O6	41.7	42.6	43.6	6.07	5.82	5.57	20.6	14.8	10.7	74.7	56.6	45.2
O6.5	40.2	41.3	42.3	6.03	5.76	5.49	21.2	14.8	10.3	69.6	52.0	41.0
O7	38.7	39.9	41.0	5.98	5.70	5.40	21.8	14.7	10.0	64.3	47.4	37.7
O7.5	37.2	38.5	39.7	5.94	5.63	5.32	22.4	14.7	9.6	59.2	43.0	34.1
O8	35.7	37.1	38.5	5.90	5.57	5.24	23.1	14.7	9.3	54.8	39.0	30.8
O8.5	34.2	35.7	37.2	5.85	5.50	5.15	23.8	14.7	9.0	50.6	35.6	28.0
O9	32.7	34.3	35.9	5.80	5.43	5.06	24.6	14.7	8.8	46.7	32.6	25.4
O9.5	31.2	32.9	34.6	5.74	5.36	4.97	25.4	14.7	8.5	43.1	29.9	23.3
B0	···	31.5	33.3	···	5.29	4.88	···	14.7	8.3	···	27.4	21.2
B0.5	···	30.2	32.1	···	5.21	4.79	···	14.8	8.0	···	25.1	19.3

NOTES: Data are taken from Vacca *et al.* (1996). The masses quoted are evolutionary masses (i.e., those derived by placing the star in the H-R diagram and obtaining the mass from evolutionary tracks). Additional O2 and O3.5 spectral subtypes were introduced by Walborn *et al.* (2002). See §1.3.1 for comments regarding newer temperature calibrations.

1.3.1 O-type stars

O stars are the hottest and most massive of the 'normal', core H-burning stars, with effective temperatures in the range $\sim$30 000–50 000 K (the upper limit is somewhat open to question at the current time) and masses in the range $\sim$20–120 $M_{\odot}$ (again, the upper limit is not well determined). They comprise the majority of stars studied in this thesis. The O-star parameters listed in Table 1.2 are taken from the empirical calibrations of Vacca *et al.* (1996), which were based on plane-parallel, hydrostatic, pure H/He model atmosphere analyses. These parameters are intended merely to serve as representative quantities. Newer calibrations, based on spherically expanding, line-blanketed (see §3.1.5) model atmospheres, which include the effects of mass loss, have recently been published for O-type supergiants (Crowther *et al.*, 2002*b*; Herrero *et al.*, 2002; Bianchi and Garcia, 2002) and O-type dwarfs (Martins *et al.*, 2002). These analyses yield lower effective temperatures than unblanketed studies, especially for early O-type stars ($\sim$4000 K lower for luminosity class V and $\sim$8000 K lower for luminosity class I).

O stars are characterised by the lines of hydrogen (H), neutral helium (He I) and singly ionised helium (He II) in their optical spectra; the presence of He II in traditional classification spectra is the defining characteristic of O-type stars. The strengths of the He I and He II lines are closely correlated with photospheric temperature; He II increases in strength towards earlier (hotter) types and He I decreases in strength. Indeed, within the O-star domain, the primary classification criteria are the relative line ratios of He I to He II (which are not *directly* influenced by metallicity effects). The He II λ4686 Å line can be used as a luminosity indicator, being in absorption in dwarfs and emission in giants and supergiants.

Many O-type stars exhibit further optical emission lines; those with N III (λ4634–41 Å) and He II (λ4686 Å) in emission are designated Of stars. The Of stars are a group of particular interest, possibly representing an evolutionary stage intermediate to that of 'normal' O stars and WR stars (Langer *et al.*, 1994). In order to describe the observed spectral morphology of O stars in greater detail, Walborn (1971, and subsequent papers) defined additional spectral designations (see Table 1.3), thus refining the MK classification scheme, which in its original form did not include luminosity-class criteria for O-type stars. Luminosity classes were assigned using Si and N lines, and the O-star regime extended beyond the earliest (O4) MK standards to the O3 subtype (defined by the absence of

He I λ4471 Å in classification-quality photographic spectra). More recently, Walborn *et al.* (2002) introduced the new O2 and O3.5 spectral subtypes in order to accommodate the range in classification criteria afforded by high-quality digital spectra.

Table 1.3: Walborn's O-type star spectral designations

Designation	Criteria
f	strong N III 4634–41 emission, He II 4686 emission
(f)	medium N III 4634–41 emission, no He II 4686 emission or absorption
((f))	weak N III 4634–41 emission, strong He II 4686 absorption
f*	N IV 4058 emission > N III 4640 emission (O3)
(f*)	f* plus weak He II 4686 absorption
((f*))	f* plus strong He II 4686 absorption
f^+	f characteristics plus Si IV 4089, 4116 emission (O4–6)
f?p	C III 4647–51 emission like N III 4634–41; H P-Cyg profiles
e	Balmer cores in emission
(e)	probable emission at Hβ
e^+	α-Cyg shell lines in emission
n	broad nebulous or diffuse lines
(n)	in between n and ((n))
((n))	Si IV 4116 and He I 4121 just merged
[n]	broadening H lines $\gg$ He lines
nfp	He II centrally reversed emission
N	N III, N II absorption lines enhanced
C	C III, C II absorption lines enhanced, N lines deficient

REFERENCE: Divan and Prévot-Burnichon (1988).

1.3.2 B-type stars

B stars are rather cooler and typically less massive than O stars, with effective temperatures in the range $\sim$10 000–30 000 K and masses in the range $\sim$2–20 $M_\odot$. They are characterised by the presence of H and He I in their optical spectra. H-line strength increases towards the later (cooler) B-star subclasses, whilst He I (after peaking in strength

around B2–B3) decreases. He II is absent in traditional classification spectra (but can be detected in early-B stars by using high-quality digital spectra).

Two important subgroups of B stars are the Be and B[e] stars. These are emission-line objects that exhibit evidence for equatorially-enhanced winds (often referred to as 'disks'). Be stars are non-supergiant B stars whose spectra show (or have shown) Balmer lines in emission (Slettebak, 1988); they are also observed often to have much stronger infrared excesses than 'normal' early-type stars (Allen and Swings, 1976). Possible scenarios invoked to explain the Be-star phenomenon include: a) a rotationally-enhanced stellar wind (Bjorkman and Cassinelli, 1993); b) nonradial pulsation (e.g. Baade and Balona, 1994); and c) an interacting binary (e.g. Harmanec, 1987). Typically much more luminous than the Be stars, B[e] stars are a very heterogeneous group of B-type stars (Lamers *et al.*, 1998) that show forbidden emission lines in their optical spectra (Allen and Swings, 1976).

1.3.3 A-type supergiants

A-type supergiants are massive ($\sim$5–25 $M_{\odot}$) stars that have most probably evolved from main-sequence $\sim$B0–B5 stars, and have effective temperatures ranging from $\sim$7500–10 000 K. Their extreme luminosity, coupled with the fact that the peak of their spectral energy distribution is at visual wavelengths, means they are usually the brightest (up to $M_V \simeq -9$) single, 'normal' stars observed in optical surveys of other galaxies. Their potential as independent distance indicators through use of the wind-momentum–luminosity relationship (WLR; see §7.2) means they are of increasing interest in extragalactic astronomy (Kudritzki *et al.*, 1995, 1999; McCarthy *et al.*, 1997, 2001; Kudritzki, 1998). The dominant feature of an A-type spectrum is the presence of strong hydrogen Balmer lines (peaking at subtype A2); the He I lines present in earlier spectral types are absent in classification-quality spectra.

1.3.4 Luminous Blue Variables (LBVs)

Luminous Blue Variables (LBVs) are extremely massive, extremely luminous, evolved stars, which exhibit different degrees of light and colour variability (Conti, 1984; Humphreys, 1989). The variability ranges from small-scale photometric microvariations on a timescale of days (e.g. van Genderen, 1989) to large-amplitude changes lasting many years (the latter being associated with episodes of dramatic mass loss; e.g. Langer *et al.*, 1999). The luminosities of LBVs ($\sim 10^6$ $L_{\odot}$) are similar to those of WR stars, and are remarkably

constant for a given object, considering the stars' intrinsic variability. When at photometric visual minimum, LBVs have effective temperatures in excess of $\sim$ 15 000–20 000 K (similar to B-type supergiants); during visual maximum this can drop to around 8000 K (similar to A-type supergiants). LBVs are believed to be in a very short-lived ($\lesssim 10^5$ yrs) evolutionary stage, intermediate to that of O stars and WR stars. A vast amount of mass is lost during the LBV phase: mass-loss rates during an outburst can be as high as $\sim 10^{-5}$–10^{-4} $M_\odot$ yr^{-1}, effectively removing the outer layers of the star. Indeed, LBVs are often observed to possess circumstellar material in the form of shells or ejecta nebulae. The well known LBV, η Carinae, underwent a particularly violent outburst in 1846, temporarily becoming visually the second brightest star in the sky. LBVs lie very close to the Humphreys-Davidson limit (Humphreys and Davidson, 1979), an observed upper luminosity limit in the H-R diagram, above which no stars are normally seen. The outbursts may be directly related to whatever mechanism brings about the Humphreys-Davidson limit, preventing the most luminous stars from becoming red supergiants (RSGs) by allowing them to shed sufficient mass.

1.3.5 Wolf-Rayet (WR) stars

Wolf-Rayet (WR) stars are believed to be the highly evolved descendants of massive, O-type stars (> 25 $M_\odot$; see Crowther *et al.*, 1995*b*), and may be the progenitors of certain types of supernovae (types Ib/Ic; see, e.g. Chu, 2002). The idea that WR stars are young, Population I objects is supported by the fact that they are often seen associated with OB stars in open clusters, or as binary companions to OB stars (the incidence of binarity amongst WR stars is high; e.g. van der Hucht, 2001). Their original outer layers have previously been lost through strong stellar winds (either continuously or in outbursts associated with the LBV phase), revealing the products of interior nuclear processing at their surfaces. WR stars are observed to be hydrogen deficient, and are characterised by strong, broad emission lines of ionised He, N, C and O in their spectra. These lines originate in their powerful, optically thick stellar winds, which typically have velocities in the range $\sim$ 1000–4000 km s^{-1}. The winds drive mass-loss rates of order $\sim 10^{-5}$ $M_\odot$ yr^{-1}. WR stars have extremely high effective temperatures, typically in the range $\sim$ 30 000–90 000 K (to the extent that $T_{\rm eff}$ can be defined for such objects).

WR stars are subdivided into three main groups based upon their spectra: the WN stars (nitrogen spectra dominant, some carbon); the WC stars (carbon spectra dominant,

no nitrogen); and the rare WO stars (oxygen spectra dominant, the ratio C/O < 1). The WN stars appear to exhibit the products of CNO-cycle buring, whereas the more evolved WC and WO stars show the products of helium burning and α-capture. The spectral classification of OB stars is closely coupled to stellar effective temperature and luminosity; however, in the case of WR stars, the classification is based mainly upon the emission-line ratios of ions of He, N, C and O, formed in an optically thick stellar wind. WR spectral types, therefore, give only an approximate indication of the temperature and ionisation in WR winds. The WR classification scheme allows for the following spectral subtypes: WN2–WN11, WC4–WC9 and WO1–WO4 (see van der Hucht, 2001, for a review of the classification criteria for WR stars). Crowther *et al.* (1995*b*) proposed the following evolutionary scenarios for massive stars, dependent upon initial stellar mass, M_i:-

(i) O $\rightarrow$ Of $\rightarrow$ WNL $\rightarrow$ WN7 ($\rightarrow$ WNE) $\rightarrow$ WC $\rightarrow$ SN for $M_i > 60M_\odot$

(ii) O $\rightarrow$ Of $\rightarrow$ LBV $\leftrightarrow$ WN9–11 $\rightarrow$ WN8 $\rightarrow$ WNE $\rightarrow$ WC $\rightarrow$ SN for $40M_\odot \lesssim M_i < 60M_\odot$

(iii) O $\rightarrow$ Of $\rightarrow$ RSG $\rightarrow$ WN8 $\rightarrow$ WNE $\rightarrow$ WC $\rightarrow$ SN for $25M_\odot < M_i \lesssim 40M_\odot$

where WNE and WNL refer to 'early-' (WN2–5) and 'late-type' (WN6–11) WN stars, respectively. Thus, WR stars are crucially important to our understanding of the final stages of massive-star evolution.

1.4 Mass loss

As stated previously, throughout most of their lives, early-type stars continually lose mass by way of strong stellar winds (e.g. Abbott *et al.*, 1981). A stellar wind is a (more or less) continuous outflow of material from the outer layers of a star into the ISM. All stars lose mass, but the mass-loss rates depend greatly upon the type of object concerned. The sun (spectral type G2V) sheds mass at a rate of $\sim 10^{-14}$ $M_\odot$ yr^{-1}, thus losing a negligible amount of material over a Hubble time. A typical O star, however, with a mass-loss rate in the region of $\sim 10^{-7}$–10^{-6} $M_\odot$ yr^{-1}, will lose a few solar masses during its main-sequence lifetime. Being a significant fraction of the initial stellar mass, this 'evaporation' has a number of important consequences.

First, mass loss profoundly alters evolutionary tracks in the H-R diagram (e.g. Chiosi and Maeder, 1986), thus helping to clarify the relationships between different types of

massive star (e.g. OB stars, LBVs, WR stars; see Langer *et al.*, 1994). Secondly, as a result of the outer envelopes being stripped away, CNO-processed material may be exposed at the stellar surface; these products are observable spectroscopically and can be used as a test of stellar evolution. Also, because of its effect on the stellar interior, mass loss influences the nature of supernovae precursors. Thirdly, through the deposition of nucleosynthetically enriched material, momentum and energy, the wind ejecta have an impact on the nature of the ISM (e.g. Abbott, 1982). In addition to these important consequences, the presence of a wind may also affect the emergent stellar spectrum, which in turn can influence a star's spectral classification. For these reasons, the study of mass loss from hot, luminous stars is of considerable interest and warrants quantitative analysis.

1.4.1 Fundamental concepts

Massive-star winds are driven by radiation: ions in the wind are 'pushed out' from the star by the scattering of photons in spectral lines. The opacity of one strong line can be as much as $\sim 10^6$ larger than the electron-scattering opacity. However, the large radiation force on the ions would not be efficient were it not for the Doppler effect. In a static atmosphere with strong line absorption, radiation would be absorbed and scattered in the lower layers, meaning that the outer layers would not receive photons at the line frequency. In a radially-expanding atmosphere (e.g. a stellar wind), the presence of a velocity gradient allows the ions to 'see' photospheric radiation as red-shifted. Thus, ions in the outer atmosphere are able to absorb unattenuated radiation from the photosphere. It is for this reason that radiative acceleration is a very efficient mechanism for driving stellar winds. Material escaping from the outer layers of a star is monotonically accelerated outwards (in the case of a smooth wind) from a small velocity (typically $v \leq 1$ km s^{-1}) at the stellar photosphere, to some high velocity at a large distance from the star. The modern version of *radiation-driven wind theory* was developed by Lucy and Solomon (1970) and Castor *et al.* (1975).

Motivated by rocket-based observations of the UV spectra of OB supergiants (Morton, 1967*b*, and subsequent papers), UV spectroscopy from the *Copernicus* and *International Ultraviolet Explorer (IUE)* satellites has shown mass loss to be a ubiquitous characteristic of massive-star evolution. Evidence for stellar winds has now been acquired at all wavelengths from X-ray to radio; the scale of the phenomenon, however, is dependent upon both the type of star and its luminosity. The two crucial parameters characterising

stellar mass loss that can be derived from observations, are the mass-loss rate, $\dot{M}$, and the terminal velocity of the wind, v_∞. $\dot{M}$ and v_∞ are important because:-

(i) The value of $\dot{M}$ greatly affects stellar evolution (e.g. Chiosi and Maeder, 1986; Meynet *et al.*, 1994).

(ii) Different theories of stellar winds predict different values of $\dot{M}$ and v_∞. By comparing observations with model predictions, it is possible to learn which mechanism is responsible for driving mass loss and the wind acceleration.

(iii) Material escaping from a star carries with it chemical enrichment, kinetic energy and momentum into the ISM. A knowledge of the value of $\frac{1}{2}\dot{M}v_\infty^2$ permits an investigation of the effects of stellar winds on the ISM (Abbott, 1982).

Mass-loss rates of order $\sim 10^{-6}\ M_\odot\ \mathrm{yr}^{-1}$ are not unusual for early-type stars (e.g. Puls *et al.*, 1996; Herrero *et al.*, 2000, 2002), and the most massive O stars can have terminal velocities in excess of 3000 km s^{-1} (e.g. Howarth *et al.*, 1997*b*).

For a star with a spherically symmetric, steady and homogeneous wind, $\dot{M}$ is related to the density, ρ, and velocity, v, at any point in the wind via:-

$$\dot{M} = 4\pi r^2 \rho(r) v(r) \tag{1.3}$$

where r is the radial distance measured from the centre of the star. This equation states that material is neither destroyed nor created in the wind (i.e., it is the equation of mass continuity). The distribution of the velocity of the wind with radial distance from the star is known as the velocity law, $v(r)$. The numerical realisation of the original version of radiation-driven wind theory (Castor *et al.*, 1975) assumed the star to be a point source of radiation, and predicted a velocity law of:-

$$v(r) = v_\infty \left(1 - \frac{R_*}{r}\right)^\beta \tag{1.4}$$

where R_* is the radius of the star and $\beta = 0.5$ describes the steepness of the velocity law (the smaller the value of β, the faster the wind acceleration). Radiation-driven wind theory has, however, since been refined. Friend and Castor (1983) found $\beta \approx 1$ by considering multiple scattering, in which the presence of overlapping lines allows a photon to be scattered many times in different lines. Friend and Abbott (1986) corrected for the finite size of the stellar disk and found $\beta \approx 0.8$. The same result was obtained by Pauldrach

et al. (1986). Relative to the winds of cool stars, $\beta = 0.8$ corresponds to a fast acceleration, with the wind reaching 80% of its terminal velocity at $r = 4.1\ R_*$ (i.e., 3.1 R_* above the stellar photosphere). In general, the parameterisation given in Equation 1.4 (with varying values of β) provides a useful characterisation of accelerating outflows, and in particular is a fair description of most subsequent models and observations.

1.5 Mass-loss diagnostics

There are a number of spectroscopic and continuum diagnostics available that can be used to estimate $\dot{M}$, v_∞, or both, including: a) P-Cygni profiles of UV resonance lines; b) radio and IR continuum emission; and c) emission lines, especially Hα. These reflect, respectively, bound–bound, free–free and free–bound processes.

1.5.1 UV P-Cygni profiles

The most sensitive indicators of mass loss are the spectral lines due to atomic transitions from the ground state (known as resonance transitions) of abundant ions in the stellar wind. The resonance lines of many atoms and ions abundant in O-star winds are located in the UV region of the spectrum ($\lambda < 2000$ Å). Commonly used examples in the spectra of early-type stars include the resonance-line doublets of C IV ($\lambda\lambda$1550 Å), N V ($\lambda\lambda$1240 Å) and Si IV ($\lambda\lambda$1400 Å). Because of the outflowing nature of the wind, the relatively high abundance of these ions (together with the large oscillator strengths of their resonant transitions) produces a blue-shifted absorption component and a red-shifted emission component. The Doppler shifts give the lines a characteristic shape, known as a P-Cygni profile (named after the first star in which this type of profile was observed). The formation of a P-Cygni profile can be explained qualitatively by considering the contributions from different regions of the stellar envelope.

Figures 1.1 and 1.2 are schematic illustrations of the photon-scattering process and the formation of a P-Cygni profile, respectively. Figure 1.1 shows a plane through a smooth, spherically symmetric stellar wind. The x- and y-axes are in units of R_* and the observer is located in the z-direction. Four scatterers, labelled a–d, are shown. These ions are all located at the same radial distance from the star and therefore have the same radial expansion velocity. The line-of-sight velocity ($v_{\rm LOS}$) of a scattered photon depends upon the cosine of the angle, θ, between the radial velocity vector and the line of sight of the

observer. When an incoming photon interacts with one of the ions, it is scattered into some different direction:-

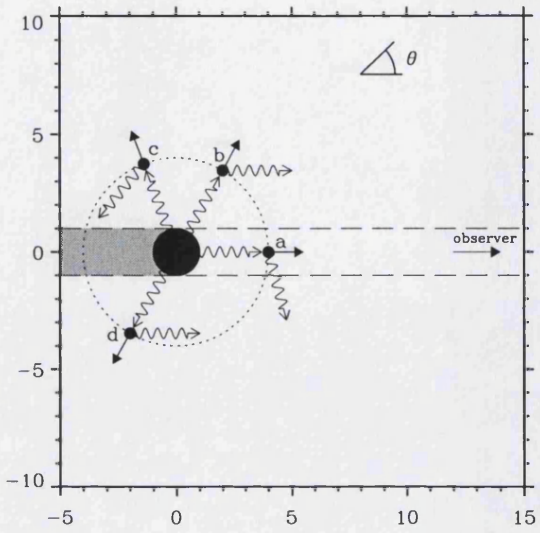

Figure 1.1: Schematic diagram of the photon-scattering process. See text for explanation. (Figure taken from Fullerton, 1997).

(a) **Ion 'a': blue-shifted absorption.** Photons are scattered out of the line of sight by material moving towards the observer in the 'tube' in front of the stellar disk. This material has a velocity of between zero and the maximum expansion velocity at which the ion still exists (frequently v_∞), producing a blue-shifted absorption trough between $v_{\rm LOS} = 0$ and (typically) $v_{\rm LOS} = -v_\infty$.

(b) **Ion 'b': blue-shifted emission.** Photons are scattered into the line of sight by material moving towards the observer in the 'halo' surrounding the stellar disk. This produces blue-shifted emission.

(c) **Ion 'c'.** Photons originally unobservable are scattered into a new direction that is also unobservable. No absorption or emission is produced in the observed line profile.

(d) **Ion 'd': red-shifted emission.** Photons are scattered into the line of sight by material moving away from the observer in the 'halo' surrounding the stellar disk. This produces red-shifted emission.

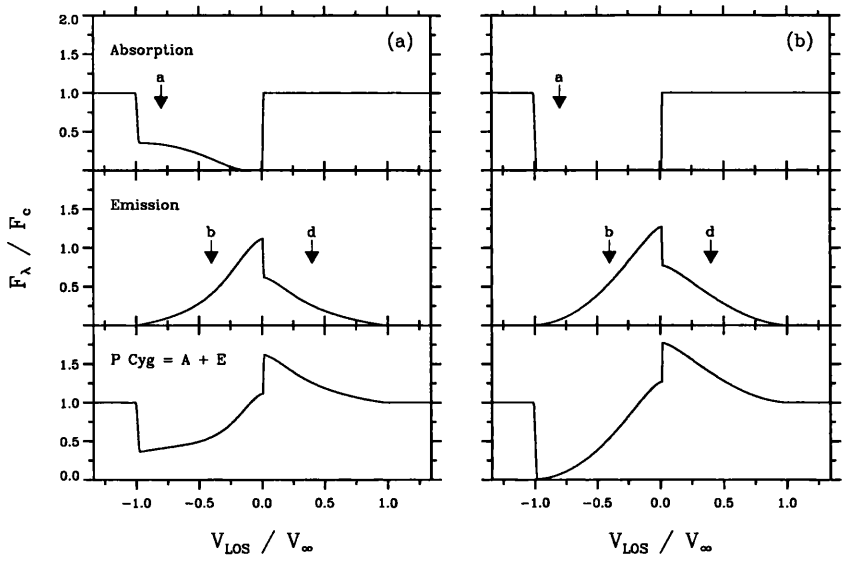

Figure 1.2: Schematic diagram showing the formation of a P-Cygni profile of a UV resonance line, for the case of: (a) a moderately strong line; and (b) a strong line. (Figure taken from Fullerton, 1997).

There is also continuum emitted from the stellar photosphere (possibly with a photospheric absorption component at the rest wavelength of the line concerned). When added together, these different contributions result in a P-Cygni profile, with its characteristic blue-shifted absorption trough and red-shifted emission lobe. This is illustrated in Figure 1.2, where the photons scattered by ions 'a', 'b' and 'd' are mapped to positions in the observed line profile. The ratio of the emission strength to the absorption strength depends upon the size of the region in which the scattering occurs, relative to the size of the star. If the stellar disk is small (i.e., pointlike) compared to the size of the scattering region and emits only continuum, no radiation is lost by back-scattering into the star. In this case, and if the line is formed purely by scattering, the emission is equal to the absorption (since photon numbers are conserved).

Theoretical P-Cygni profiles can be computed and compared to observations to yield information on the velocity law of the wind (e.g. Hamann, 1981*a*,*b*; Lamers *et al.*, 1987; Groenewegen and Lamers, 1989; Haser, 1995). For strongly saturated lines, the black (zero intensity) absorption trough extends to a Doppler velocity of about $-v_\infty$ (if the ion exists throughout the entire wind), and the profile shape depends primarily on the velocity law. It is therefore possible to measure v_∞ and (in principle) derive the velocity law from a saturated P-Cygni profile. The maximum observable velocity, $v_{\rm obs}$, is easily

measured to an accuracy of order 100 km s^{-1}. Care must be taken, however, as v_{obs} does not (in general) equal the terminal velocity, v_∞. If the winds are at all turbulent, or have non-monotonic velocity laws, then the maximum flow velocity, v_{max}, will normally exceed v_∞. In sufficiently saturated lines, it is expected that $v_{obs} \approx v_{max} \gtrsim v_\infty$.

A widely observed phenomenon in the *unsaturated* P-Cygni profiles of OB stars are narrow absorption features (Snow, 1977; Prinja and Howarth, 1986). These take the form of distinct dips in the P-Cygni profile, typically seen as broad, low-velocity optical depth enhancements, which migrate (within the profile) to become high-velocity, narrow absorption features (Prinja *et al.*, 1987; Prinja and Howarth, 1988). Howarth and Prinja (1989) suggested that the central velocity of narrow absorption features might provide a better indicator of v_∞ than does v_{obs}, and noted that the maximum velocity of fully saturated absorption gives a similar value.

Determining the mass-loss rate from UV P-Cygni profiles requires a knowledge of the fractional abundances of the ions concerned (Howarth and Prinja, 1989; Kudritzki *et al.*, 1999; Herrero *et al.*, 2001). Because resonance lines are produced by minority ions in the wind, these fractions are small and poorly known (e.g. Groenewegen and Lamers, 1991). Another problem is that there is a limited dynamical range; lines are often very optically thick or thin, whereas only intermediate optical depths are useful. These facts, along with the need for satellite observations, limit the use of UV P-Cygni profiles in stellar-wind studies. Nevertheless, useful work can still be done: UV spectra obtained with the *Hubble Space Telescope (HST)* and *Far Ultraviolet Spectroscopic Explorer (FUSE)* have been used to determine the parameters of massive stars in the Magellanic Clouds (Crowther *et al.*, 2002*a*,*b*), M31 (Bresolin *et al.*, 2002) and M33 (Urbaneja *et al.*, 2002).

1.5.2 Radio and IR continuum emission

As a result of free–free processes, an ionised stellar wind emits continuum emission, which, because of the diminishing relative importance of the photospheric emission, is most easily observed from IR to radio wavelengths. Assuming that the wind is steady, and given that the emission is thermal in origin, observations of the radio continuum flux should provide the most accurate and reliable method for determining the mass-loss rate from an early-type star (e.g. Abbott *et al.*, 1980, 1981; Leitherer and Robert, 1991; Leitherer *et al.*, 1995; Scuderi *et al.*, 1998).

The observed radio emission is produced in the outer part of the wind, at $\gtrsim 10^2\ R_*$,

where the outflow has reached its terminal velocity. Thus, acceleration effects do not have to be taken into consideration when interpreting the data, and a simple r^{-2} density distribution can be used to describe the outflow. Provided that the radio emission is thermal in origin (i.e., produced by free–free radiation in the outer part of the wind), then the mass-loss rate is simply related to the measured flux, the star's distance, and the terminal velocity of the wind (see §5.5, Equation 5.2; Wright and Barlow, 1975; Panagia and Felli, 1975). This method of determining mass-loss rates is virtually independent of abundances, and of details of ionisation fractions of metals. In §5 and §6, mm and cm continuum emission will be used to derive mass-loss rates for a sample of Galactic early-type stars.

There are, however, a number of drawbacks to using radio continuum emission:-

(i) The number of early-type stars with accurate measurements in the radio is small. This is because the large distances of these objects and the intrinsic weakness of the emission conspire to make flux densities at radio wavelengths rather low (typically less than a few mJy). Generally, only higher-luminosity objects have stellar winds strong enough to be detected.

(ii) Distances to sources need to be known.

(iii) UV or other observations are required to give v_∞ (this is true for all diagnostics of $\dot{M}$). Measurements of v_∞ in UV resonance lines, which represent the outflow at $\sim 10\ R_*$, are usually extrapolated to the radio-emitting region of the wind, assuming a constant outflow velocity.

(iv) Free–free emission is a density-squared (ρ^2) process, and is therefore sensitive to clumping in the wind (Abbott *et al.*, 1981). The presence of structure within a density distribution that is assumed to be smooth will cause $\dot{M}$ to be overestimated when using Equation 5.2 (see §7.1).

(v) Many OB stars are observed to be sources of *nonthermal* radio emission (Bieging *et al.*, 1989; Altenhoff *et al.*, 1994). This contaminates (and can indeed dominate) the free–free emission, invalidating the use of Equation 5.2 to calculate mass-loss rates.

The use of IR continuum emission as a mass-loss diagnostic (e.g. Barlow and Cohen, 1977; Runacres and Blomme, 1996) is complicated by the fact that it is sensitive to the

density structure in the inner part of the wind. Nevertheless, IR emission is a useful probe of conditions nearer the star, in the region where the outflow is still undergoing acceleration.

1.5.3 Emission lines

Early-type stars with mass-loss rates in excess of $\sim 10^{-6}$ $M_{\odot}$ yr^{-1} show broad, wind-formed emission lines in their spectra, particularly those of H, He I and He II. The best known, and typically the strongest of these, is Hα (λ6563 Å). The strength and shape of the Hα profile can provide information about both $\dot{M}$ *and* the velocity law of the wind (e.g. Puls *et al.*, 1996). If the wind is optically thin for a line transition (and this is often approximately valid for Hα), the mass-loss rate can be derived directly (and accurately) from the total luminosity of the line, given that v_{∞} is known. The height and width of the central part of the line profile can be used to constrain the β-exponent of the velocity law. Hα has been used to determine mass-loss rates for a variety of hot stars (e.g. Leitherer, 1988*a*; Scuderi *et al.*, 1992; Lamers and Leitherer, 1993; McCarthy *et al.*, 1997; Kudritzki *et al.*, 1999); the techniques employed will be discussed further in §3.3 and §3.4, and, in §4, the Hα line will be used to derive mass-loss rates for a sample of 64 Galactic early-type stars.

A major advantage of using Hα is that (unlike UV P-Cygni profiles) the line is readily observable from the ground, but, as with other mass-loss diagnostics, there are complicating factors. Hα is formed primarily by recombination (as are most of the atomic emission lines observed in O-type stars) and thus has an emissivity proportional to ρ^2. This means that, like radio continuum emission, the Hα line is sensitive to clumping in the wind: estimates of mass loss made assuming a smooth flow will cause $\dot{M}$ to be systematically overestimated. The ρ^2-dependence of recombination lines also implies that most of the observed emission originates from a region of high density: the lower layers of the wind. As this is the region in which most of the wind acceleration occurs, the widths of emission lines like Hα are less than v_{∞}, typically $\sim$few hundred km s^{-1}. Thus, the terminal velocity of the wind must be obtained from UV or other observations.

1.6 Overview of thesis

This thesis aims to provide a general enquiry into the physics of mass loss from hot, luminous stars.

In §2, the observational considerations and data reduction of the Hα spectroscopy of 64 Galactic early-type stars are presented. The observations described were acquired using the telescopes of the Isaac Newton Group (ING) and the Anglo-Australian Observatory (AAO). In §3, the FORSOL code developed by Puls *et al.* (1996) is introduced. FORSOL is a very fast, approximate method of modelling the Hα profiles of O stars, in order to determine their mass-loss rates (and, in certain instances, velocity field β-exponents). Sensitivity tests are performed to investigate how a FORSOL-calculated Hα profile is affected by different stellar and wind parameters. In §4, a new program, PHALTEE, is introduced, which searches within a specified parameter space for the 'best' (quasi-least-squares) FORSOL fit to an observed Hα profile. This renders Hα modelling both more objective and automated, while minimising the necessity for manual intervention. PHALTEE is used to model quantitatively the Hα profiles of, and thereby derive $\dot{M}$ and β for, the datasets presented in §2.

New mm-wave observations of nineteen early-type stars (including a subset of the Hα sample) are presented in §5. These data were obtained using the Sub-millimetre Common User Bolometer Array (SCUBA). Where possible, mean fluxes are calculated and used to determine mass-loss rates. Presented in §6 are the results of a literature survey of mm and cm fluxes, which, when combined with the mm fluxes from §5, comprise observations of 53 Galactic early-type stars. Again, where possible, mean fluxes are calculated and used to determine mass-loss rates. The incidence of nonthermal emission is also examined, and the occurrence of binarity and excess X-ray flux amongst the nonthermal emitters investigated, looking for evidence that might indicate a causal relationship between these phenomena. Finally, Chapter 7 contains a review of the work contained within this thesis. For the subset of stars common to both the Hα *and* mm/radio samples, the mass-loss rates derived using the different diagnostics are compared. The wind-momentum–luminosity relationship (WLR) is also investigated. A discussion of the possible directions of future work is included.

CHAPTER 2

Hα: Observations and Data Reduction

Hα observations of 64 Galactic early-type stars were obtained over the years 1992–2000, using the telescopes of the Isaac Newton Group (ING) on the island of La Palma, and the Anglo-Australian Observatory (AAO) at Siding Spring, Australia.

2.1 INT observations

Hα spectroscopy of 30 Galactic early-type stars was obtained using the Intermediate Dispersion Spectrograph (IDS) on the 2.5-m Isaac Newton Telescope (INT), a part of the ING. The observations were made by I. D. Howarth and the author on the nights of July 17th and 18th, 2000.

2.1.1 The sample

The target stars listed in Table 2.1 were selected to include objects with published radio fluxes, with a view to comparing mass-loss diagnostics (see §7.1). The sample comprises nineteen O stars, ten B stars and one A supergiant (HD 197345/α Cyg). α Cyg (commonly known as Deneb) is exceptional for its spectral type in having measurable flux at radio and mm wavelengths, and detectable Hα emission. There is a bias in the sample towards supergiants (a consequence of the requirement that the targets have measurable radio emission), with 21 stars of luminosity class I, three of luminosity class III, one of luminosity class IV and five of luminosity class V. The V magnitudes of the sample range from 1.24 (α Cyg) to 13.96 (the 'A' component of MWC 349). Figure 2.6 shows the location of the sample in the H-R diagram.

Table 2.1: INT target stars

HD	Name	Spectral type	Reference	V	Exp (s)	S/N
2905	κ Cas	BC0.7Ia	W72	4.16	20	180
5394	γ Cas	B0.5IVe	R68	2.39[a]	2	60
14947	···	O5If+	W73	8.00	600	190
15558	···	O5III(f)	W71	7.81	600	180
15570	···	O4If+	W71	8.10	600	170
149757	ζ Oph	O9.5V	M55	2.56	5	130
164794	9 Sgr	O4:V((f))	W72	5.97	60	130
166734	···	O7Ib(f) + O8–9I	W73	8.42	300	90
167971	MY Ser	O8Ib(f)p	W72	7.50	240	170
168112	···	O5III(f)	W73	8.52	300	140
168607	···	B9Ia+	H78	8.29	60	70
169454	···	B1Ia+	W76	6.61	150	80
169515	RY Sct	B0V + O5.5V	K79	9.14[e]	500	70
169582	···	O6If	W73	8.70	300	140
190429A	···	O4If+	W72	7.12	180	210
190603	···	B1.5Ia+	W71	5.66[e]	50	40
192281	···	O5Vn((f))p	W72	7.55	240	220
193237	P Cyg	B1Ia+	H78	4.80[e]	1	20
194279	···	B1.5Ia	H78	7.09[e]	180	30
195592	···	O9.7Ia	W71	7.08	90	110
197345	α Cyg/Deneb	A2Ia	M73	1.24	1	30
206267A	···	O6.5V((f))	W73	5.67	50	240
210839	λ Cep	O6I(n)fp	W73	5.05	30	240
···	Cyg OB2 No.5	2× O7Ianfp	W73	9.16[c]	800	110
···	Cyg OB2 No.7	O3If	M91	10.55[d]	900	110
···	Cyg OB2 No.8A	O5.5I(f)	M91	9.06[d]	900	120
···	Cyg OB2 No.9	O5If	M91	10.96[d]	1200	100
···	Cyg OB2 No.12	B5Ie	M91	11.46[d]	900	80
···	V433 Sct	B1.5Ia	H78	8.24	300	40
···	MWC 349	O9:III: + BOIII	L98, C85	13.96[b]	300	5

NOTES: References for spectral types and other data are provided on page 39.

NOTES TO TABLE 2.1: The Cyg OB2 stars are referred to by their designation number from Schulte's (1958) list, given that these names are in common use in the literature.

Spectral types are from: M55 — Morgan *et al.* (1955); R68 — Racine (1968); W71 — Walborn (1971); W72 — Walborn (1972); M73 — Morgan and Keenan (1973); W73 — Walborn (1973); W76 — Walborn (1976); H78 — Humphreys (1978); K79 — King and Jameson (1979); C85 — Cohen *et al.* (1985); M91 — Massey and Thompson (1991); L98 — Lamers *et al.* (1998).

O-star V magnitudes are from Garmany's unpublished catalogue of O stars. B-star V magnitudes (along with that for α Cyg) are from Humphreys (1978), except for: a) Humphreys' field star catalogue; b) Cohen *et al.* (1985) — the value listed is the mean continuum V magnitude of the 'A' component; c) Torres-Dodgen *et al.* (1991); d) Massey and Thompson (1991); e) the on-line SIMBAD astronomical database.

The sixth column gives the exposure time in seconds. Signal to noise is calculated for a small spectral region between 6440 and 6490 Å.

2.1.2 The Intermediate Dispersion Spectrograph (IDS)

The IDS is a long-slit spectrograph mounted at the Cassegrain focal station of the INT. It is equipped with two cameras, of focal lengths 235 and 500 mm; the observations presented in this thesis were made with the 500-mm camera. This was used in conjunction with an R1200R grating (i.e., a ruling of 1200 lines mm^{-1}) to give a dispersion of 15.5 Å mm^{-1} at the detector. The detector used was a Tektronix 5 (TEK 5) CCD. This chip has a pixel size of 24 μm, giving a maximum possible spectral resolution of 0.74 Å FWHM (corresponding to two pixels on the detector); all spectra were obtained using a slit width of 1.0″, giving a resolution element of around 48 μm at the detector (2.0 × 24 μm pixels). This corresponds to a resolving power, $R = \lambda/\Delta\lambda \simeq 9000$ (a resolution of $\sim$34 km s^{-1}). The spectra were centred at the wavelength of the Hα feature (6563 Å), with complete spectral coverage from roughly 6327–6727 Å. One exposure was normally obtained for each target, with exposure times ranging from 1–1200 s. The signal to noise achieved ranged from 5 to 240, with an average of $\sim$ 120 (calculated for a small spectral region between 6440 and 6490 Å).

2.1.3 Data reduction

Data reduction was performed with the Starlink packages FIGARO (Shortridge *et al.*, 1997) and DIPSO (Howarth *et al.*, 1997*a*). The initial steps were undertaken by I. D. Howarth

and involved using the IRAF routine IMCOPY to transform the data into the standard FITS format required by the Starlink package CONVERT; CONVERT could then be used to change these images into the NDF format required by other Starlink packages. Bias subtraction was subsequently performed to give 'raw' data files, and these files flat-fielded and any cosmic rays removed with the FIGARO routine BCLEAN, to produce 'cleaned', flat-fielded data frames. The remaining steps in the data reduction process were undertaken by the author. Using DIPSO, the spectra were rectified to unit flux by division with a polynomial fit to the observed continuum. Figures 2.1, 2.2 and 2.3 show, as an example, the spectrum of HD 149757 at three stages in the reduction procedure.

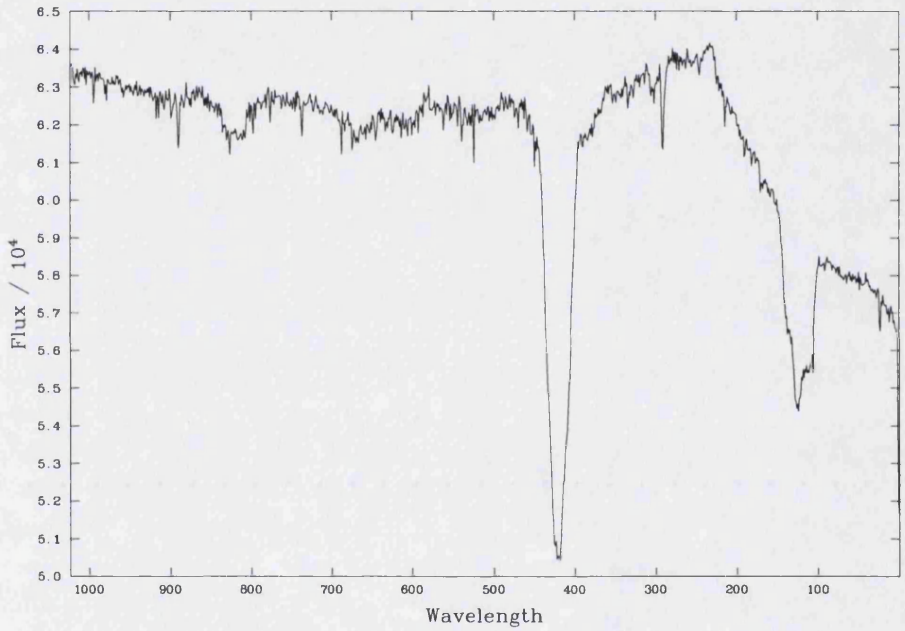

Figure 2.1: Spectrum of HD 149757 after bias subtraction only. The wavelength units are arbitrary.

Hα observations are affected by water vapour absorption in the Earth's atmosphere, which causes the telluric lines seen in stellar spectra. Telluric lines are intrinsically very narrow (approximately equal to the thermal width of the atmosphere), meaning that they saturate very easily. Hence they tend to appear fully saturated or else not at all. In a dry atmosphere, telluric lines are undetectable; if there is any water vapour present, then intrinsically saturated telluric lines are seen. The INT spectra were corrected for telluric absorption by division with a telluric standard, constructed from an AAT echelle spectrum of a broad-lined star which showed strong telluric features. Small inter-order gaps at the

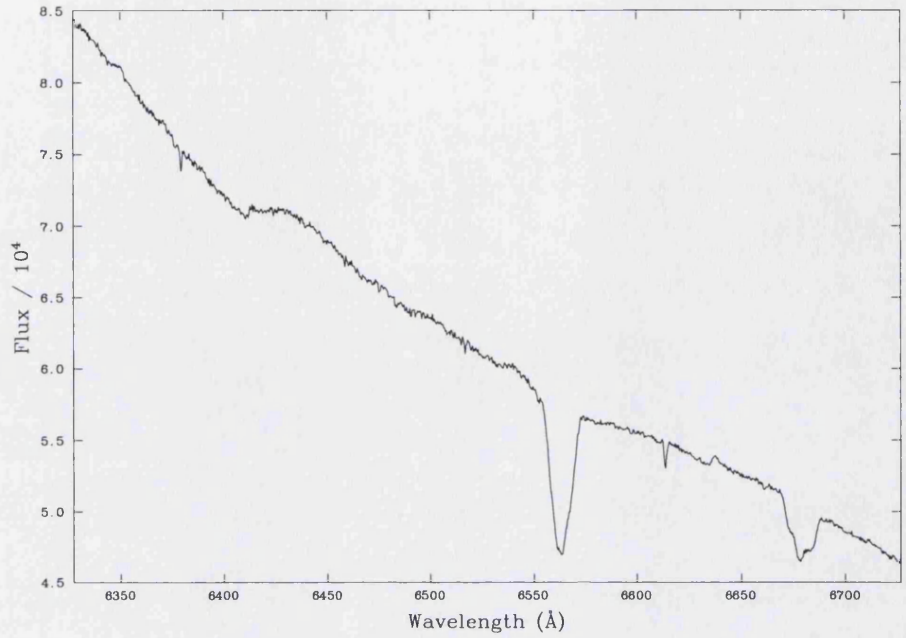

Figure 2.2: Spectrum of HD 149757 after flat-fielding and cosmic-ray subtraction.

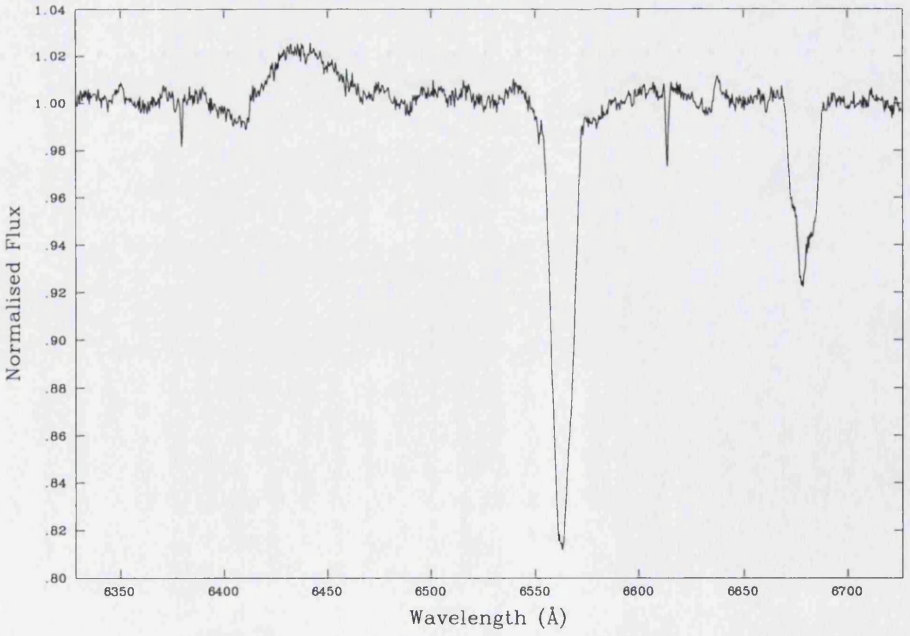

Figure 2.3: Spectrum of HD 149757 after rectification and telluric correction.

longest wavelengths were bridged using a WHT echellogram, scaled to match the AAT line strengths. The telluric correction involved: a) smoothing the telluric standard to the resolution of the stellar spectra, using a Gaussian filter; b) correcting for the difference in strength between the lines in the telluric standard and those in the stellar spectra; and finally c) division of the stellar spectra by the thus modified telluric standard. After removing the telluric lines from the stellar spectra, corrections for the radial velocities of the individual stars were applied. Figure 2.4 shows, as an example, the spectrum of HD 189957 before and after telluric correction.

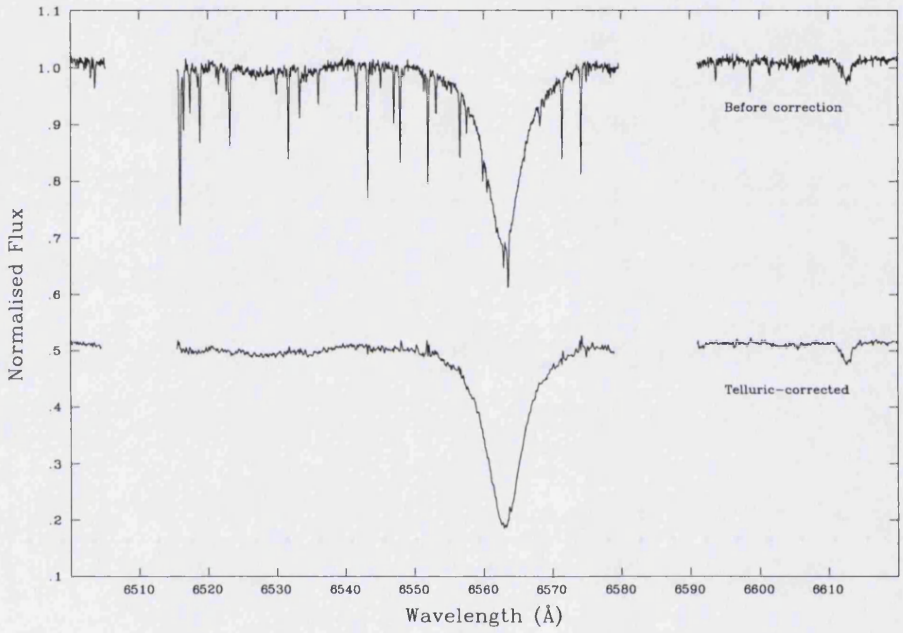

Figure 2.4: Spectrum of HD 189957 before and after telluric correction. The lower spectrum has been vertically offset by -0.5 continuum units.

2.2 WHT observations

High-resolution, high signal-to-noise spectroscopy of 22 Galactic O stars was acquired using the Utrecht Echelle Spectrograph (UES) on the 4.2-m William Herschel Telescope (WHT), a part of the ING. The observations were made by I. D. Howarth and K. W. Siebert over the nights of August 12th–15th, 1995, as part of a campaign of detailed spectroscopic analysis of selected early-type stars. Full details can be found in Siebert (1999).

2.2.1 The sample

These data were acquired originally with a view to performing a *differential* fine spectroscopic analysis (in particular looking for object-to-object variations in the helium abundance of O stars). Hence a large sample of objects populating a small part of the H-R diagram was desirable (see Figure 2.6). In order to obtain the required number of high-quality spectra, one of the main criteria for target-star selection was brightness: the V magnitudes of the sample range from 1.75 for HD 37742 (ζ Ori) to 9.54 for HD 191781. Additionally, a number of stars classified as OC and ON by Walborn (1976) were included, with a view to investigating possible evolutionary sequences. Table 2.2 lists the target stars. The sample comprises solely late-type O stars (spectral types O8–O9.7). There are twelve stars of luminosity class I, four of luminosity class II, two of luminosity class III, and four of luminosity class V.

2.2.2 The Utrecht Echelle Spectrograph (UES)

UES is a cross-dispersed echelle spectrograph, which was permanently mounted on one of the Nasmyth platforms at the $f/11$ focus of the WHT. It offers high resolution combined with good wavelength coverage. Echelle gratings have much larger blaze angles (typically 63° from the normal) than conventional gratings, giving much higher dispersion. They can operate at orders beyond 100, but, because of order overlap, some kind of filtering is required. In the case of UES, this is achieved using cross-dispersion by prisms, which leads to a display format suitable for two-dimensional detectors. The observations presented here were made using a 31.6 grooves mm^{-1} echelle grating in conjunction with the 700-mm camera and a TEK 5 CCD. All spectra were obtained using a slit width of 1.5″, giving a resolution element of around 64 μm at the detector (2.7 × 24 μm pixels), which corresponds to a resolving power of about 40 000 (a resolution of $\sim$8 km s^{-1}). Two grating settings were used, centred at 4190 Å in order 136, and 5426 Å in order 105, giving complete spectral coverage from roughly 3780–5670 Å, and further coverage with inter-order gaps up to 6980 Å (see Figure 2.5). The data presented here are those acquired with a central wavelength of 5426 Å. Two or three exposures were obtained for each target, giving total exposure times ranging from 10–3000 s. The signal to noise achieved ranged from 70 to 220, with an average of $\sim$ 140 (calculated for a small spectral region between 6450 and 6490 Å).

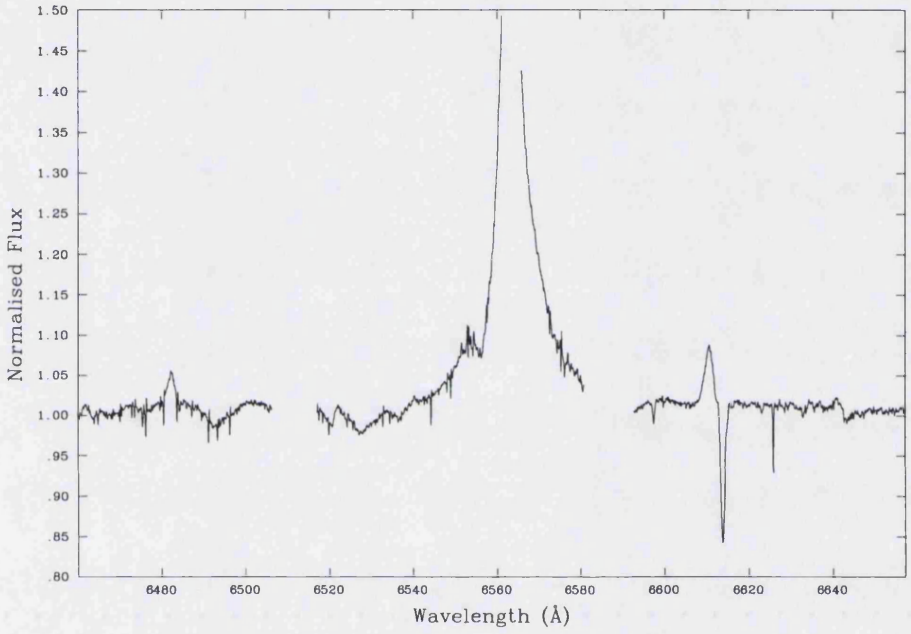

Figure 2.5: Spectrum of HD 195592, centred on the Hα feature at 6563 Å. Note the large inter-order gaps. Hα is saturated in this case, as the data were acquired originally with a view to performing an absorption-line analysis, making it necessary to obtain good signal to noise in the continuum. Scattered light from the strong emission may have caused the small features at $\sim$6480 and 6640 Å in the adjacent orders. HD 195592 is the only star in the WHT sample to be affected by such saturation.

Table 2.2: WHT target stars

HD	Name	Spectral type	V	No. exp	Total exp (s)	S/N
10125	···	O9.7II[a]	8.22	2	2700	150
12323	···	ON9V[c]	8.90	2	2400	200
13745	V354 Per	O9.7II((n))[a]	7.88	2	1500	90
16429	···	O9.5II((n))[c]	7.67	2	1500	110
30614	α Cam	O9.5Ia[a]	4.26	2	100	220
34078	AE Aur	O9.5V[a]	5.81	2	350	210
36486	δ Ori A	O9.5II[b]	2.20	2	10	110
37742	ζ Ori	O9.7Ib[a]	1.75	3	19	200
188209	···	O9.5Iab[b]	5.64	3	400	180
189957	···	O9.5III[a]	7.22	2	1000	200
191781	···	ON9.7Iab[b]	9.54	2	2500	110
194280	···	OC9.7Iab[b]	8.39	2	3000	120
195592	···	O9.7Ia[a]	7.08	2	500	80
201345	···	ON9V[b]	7.66	3	3000	160
202124	···	O9.5Iab[a]	7.80	2	1000	90
207198	···	O9Ib–II[b]	5.96	3	600	100
209975	19 Cep	O9.5Ib[a]	5.11	3	300	140
210809	···	O9Iab[c]	7.55	2	1000	170
214680	10 Lac	O9V[a]	4.87	3	150	70
218195	···	O9III[a]	8.34	2	1400	120
218915	···	O9.5Iab[b]	7.18	3	3000	150
225160	···	O8Ib(f)[a]	8.19	2	2000	150

NOTES: Table adapted from Siebert (1999). Spectral types are from: a) Walborn (1971); b) Walborn (1972); c) Walborn (1973). V magnitudes are from Garmany's unpublished catalogue of O stars. The fifth and sixth columns give the number of exposures and the total exposure time in seconds, respectively. Signal to noise is calculated for a small spectral region between 6450 and 6490 Å.

2.2.3 Data reduction

Echelle data reduction was performed by K. W. Siebert, using the Starlink packages ECHOMOP (Mills *et al.*, 1997), FIGARO and DIPSO (full details of the procedure can be found in Siebert, 1999). The raw, two-dimensional images were first bias subtracted and cleaned of any cosmic rays with FIGARO. The multi-step ECHOMOP package was then used to further reduce and optimally extract the data from the echelle format. The basic steps are as follows:-

(i) Order identification and tracing

(ii) Flat-fielding

(iii) Sky subtraction

(iv) Spectrum extraction

(v) De-blazing

The final step, the removal of the echelle blaze function, is an important consideration when reducing echelle data. The blaze intensity profile is such that the central-wavelength intensity of each order is strongest, falling off at longer and shorter wavelengths. These data were de-blazed using a routine developed by Ian Howarth called SPLIF (see Siebert, 1999). SPLIF fits a surface to the extracted spectra in the spectral versus spatial (order number) plane, after which the data are divided by this surface (further details are given in Siebert, 1999).

Using DIPSO, the extracted orders were then rectified to unit continuum and merged to form a single spectrum for each star. The author corrected for telluric absorption by division with a scaled, shifted, and smoothed telluric standard, as described in §2.1.3.

2.3 AAT observations

High-resolution, high signal-to-noise spectroscopy of twelve Galactic O stars was acquired using the University College London Echelle Spectrograph (UCLES) on the 3.9-m Anglo-Australian Telescope (AAT), a part of the AAO. The observations were made by I. D. Howarth and K. C. Smith over the nights of June 19th–22nd, 1992, as part of an investigation of the helium chemistry of late-ONC supergiants. Full details can be found in Smith and Howarth (1994).

2.3.1 The sample

The sample was selected from late-O supergiants with Walborn classifications, originally with a view to investigating morphologically distinct objects in a small part of the H-R diagram (see Figure 2.6). The target list comprises solely objects of spectral type O9–O9.7, with V magnitudes ranging from 4.89 (HD 149038/μ Nor) to 8.83 (HD 123008).

Table 2.3: AAT target stars

HD	Name	Spectral type	V	No. exp	Total exp (s)	S/N
105056	GS Mus	ON9.7Iae[a]	7.55	10	7400	170
123008	···	ON9.7Iab[c]	8.83	18	16000	170
149038	μ Nor	O9.7Iab[a]	4.89	6	1200	220
149404	V918 Sco	O9Ia[a]	5.50	4	800	230
152003	···	O9.7Iab[a]	7.03	6	5400	250
152147	···	O9.7Ib[a]	7.31	6	5400	220
152249	···	OC9.5Iab[a]	6.48	7	4000	190
152405	···	O9.7Ib–II[a]	7.20	6	5400	120
152424	···	OC9.7Ia[a]	6.35	7	4200	230
154368	···	O9.5Iab[b]	6.18	6	3600	250
154811	···	OC9.7Iab[b]	6.91	8	7200	160
156212	···	O9.7Iab[b]	7.91	8	7200	630

NOTES: Spectral types are from: a) Walborn (1972); b) Walborn (1973); c) Walborn (1976). V magnitudes are from Garmany's unpublished catalogue of O stars. The fifth and sixth columns give the number of exposures and the total exposure time in seconds, respectively. Signal to noise is calculated for a small spectral region between 6620 and 6660 Å.

2.3.2 The UCL Echelle Spectrograph (UCLES)

UCLES is mounted at the $f/36$ Coudé focus of the AAT, and is, in most important respects, UES' 'twin' instrument. The observations presented here were made using a 31.6 grooves mm^{-1} grating in conjunction with the 700-mm camera and a 1024 × 1024 Thomson CCD. All spectra were obtained using a slit width of 2.0″, giving a resolution element of approximately 110 μm at the detector (5.7 × 19 μm pixels). This corresponds to a resolving power of about 23 000 (a resolution of $\sim$ 13 km s^{-1}). At least two exposures (at five spectrograph settings) were taken for each target, giving complete spectral coverage

from 3630–7020 Å. The signal to noise achieved ranged from 120 to 630, with an average of $\sim$ 200 (calculated for a small spectral region between 6620 and 6660 Å, and excluding the very high SNR of 630 achieved for HD 156212).

2.3.3 Data reduction

Echelle data reduction was performed by I. D. Howarth, using the Starlink reduction packages FIGARO and ECHOMOP. Bias subtraction and cosmic-ray removal was done with FIGARO. ECHOMOP was then used to flat-field and extract the data. Using DIPSO, the extracted orders were rectified to unit continuum and merged to form a single, continuous spectrum for each star. The author corrected for telluric absorption by division with a scaled, shifted, and smoothed telluric standard, as described in §2.1.3.

2.3.4 HD 66811 (ζ Pup)

Hα spectroscopy of HD 66811 (ζ Pup), spectral type O4I(n)f (Walborn, 1972), was also obtained using UCLES, during a separate observing run. The observations were made by J.-F. Donati, I. D. Howarth, P. Petit, M. Semel and the author over the nights of December 5th–12th, 2000, as part of a search for surface magnetic fields in early-type stars, using extremely sensitive spectropolarimetry. The Semel polarimeter was mounted at the Cassegrain focus of the AAT, and linked to UCLES through a double optical fibre and an image slicer (for further details, see Donati *et al.*, 2002). A 31.6 grooves mm^{-1} grating was used in conjunction with an MITLL2 CCD to obtain polarimetric exposures consisting of a sequence of four individual subexposures. The resolving power achieved was about 60 000 (a resolution of $\sim$ 5 km s^{-1}). One hundred and thirty-three subexposures were taken, with complete spectral coverage from 4300–7150 Å. The echelle spectra were extracted by J.-F. Donati, using software described in Donati *et al.* (1997). The spectrum presented here is the mean of all the observations obtained throughout the run (the author corrected for telluric absorption by division with a scaled, shifted, and smoothed telluric standard, as described in §2.1.3). Time-series analysis performed by Howarth (personal communication) shows evidence for low-amplitude variability, but *not* of a periodic nature; there is no evidence for the $\sim$ 8.5-hr period variation in photospheric lines seen previously (Baade, 1991; Reid and Howarth, 1996).

Table 2.4: ζ Pup

HD	Name	Spectral type	V	No. exp	Total exp (s)	S/N
66811	ζ Pup	O4I(n)f	2.26	133	39 900	190

NOTES: Spectral type is from Walborn (1972). V magnitude is from Garmany's unpublished catalogue of O stars. The fifth and sixth columns give the number of exposures and the total exposure time in seconds, respectively. Signal to noise is calculated for a small spectral region between and 6620 and 6660 Å.

2.4 Summary of observations

Table 2.5 summarises the Hα observations presented in this chapter, giving the number of target stars, spectral coverage, resolution and signal to noise (or range thereof) for each of the four observing runs. The INT00 targets were selected primarily on the basis of available radio or mm data, moderated by accessibility from La Palma at the time of the observations. This sample was supplemented by a more or less heterogeneous collection of targets chosen for known Hα emission, or other characteristics considered 'interesting' at the time. The data from the WHT95, AAT92 and AAT00 observing runs comprise solely O stars (mainly late-type supergiant).

Figure 2.6 shows the location of the entire Hα sample in the H-R diagram. The zero-age main-sequence (ZAMS) line for solar metallicity is included for reference (taken from Meynet *et al.*, 1994). The $\log L$ and $T_{\rm eff}$ values were largely taken from the literature; these are provided, along with references, in Table 4.3. Figure 2.7 is a histogram showing the distribution over spectral type of all 64 target stars (HD 195592 appears in both the INT00 and WHT95 datasets). The sample comprises 53 O stars, ten B stars and one A star; there are 49 stars of luminosity class I–II, five of luminosity class III, and ten of luminosity class IV–V. Late O-type supergiants are particularly well represented.

Table 2.5: Summary of observations

Observing run	No. stars	Spectral coverage (Å)	Resolution (km s^{-1})	S/N
INT00	30	6327–6727	34	5–240
WHT95	22	3780–6980†	8	70–220
AAT92	12	3630–7020	13	120–630
AAT00	1	4300–7150	5	190

NOTES: The four observing runs are denoted by the following acronyms: INT00 ≡ INT run in July 2000; WHT95 ≡ WHT run in August 1995; AAT92 ≡ AAT run in June 1992; AAT00 ≡ AAT run in December 2000. † — Complete spectral coverage from roughly 3780–5670 Å, and further coverage with inter-order gaps up to 6980 Å (see Figure 2.5).

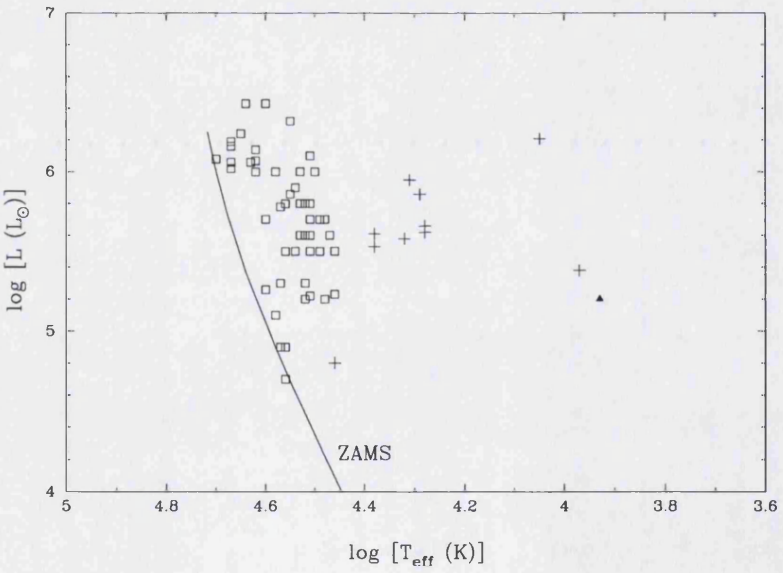

Figure 2.6: Temperature-luminosity H-R diagram showing the location of all 64 stars in the Hα sample. '□' represent O stars, '+' represent B stars and '▲' represents the A2Ia star, α Cyg. The ZAMS line for solar metallicity is also given (Meynet *et al.*, 1994).

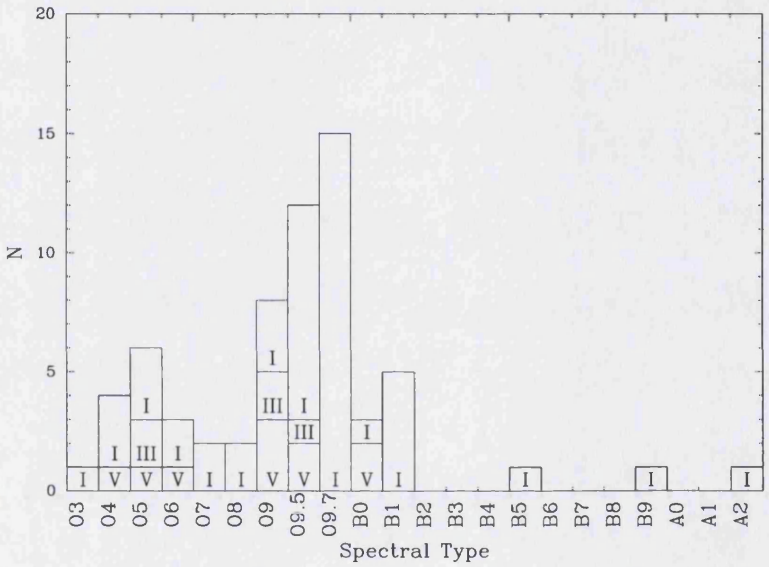

Figure 2.7: Histogram showing the distribution over spectral type of the Hα sample. 'I' denotes luminosity class I–II, 'III' denotes luminosity class III, and 'V' denotes luminosity class IV–V.

CHAPTER 3

Hα: Models

In anticipation of using the FORSOL code of Puls *et al.* (1996) to model Hα line profiles and thereby determine mass-loss rates, this chapter contains a discussion of the physics of stellar atmospheres, and in particular the formation of the Hα line in the winds of early-type stars. A new program, PHALTEE, will be introduced in §4, which searches within a specified parameter space for the 'best' FORSOL fit to an observed Hα profile.

Throughout this work, the 'core-halo' approximation for a star and its wind is adopted. This model assumes that there exists an artificial division between the stellar photosphere and interior (the 'core'), and the stellar wind (the 'halo'); in reality there is a smooth transition between the photosphere and the wind. The approximation is, however, tolerable for O stars, and has the advantage of being computationally much less intensive than 'unified atmosphere' approaches (see §3.3.2). In addition to these practical considerations, it is partially justified by the very sharp decrease in density at the core/halo boundary (e.g. Castor *et al.*, 1975).

§3.1 and §3.2 describe the principles underlying the model photospheric, or core, spectra used in this work. §3.3 and §3.4 then elaborate on the 'wind' aspects of the models and introduce the FORSOL code. Finally, §3.5 presents the results of sensitivity tests performed to investigate the effects of different stellar and wind parameters on a model Hα profile.

3.1 Theoretical model atmospheres

A stellar spectrum generally takes the form of a continuous flux distribution, upon which numerous absorption and/or emission lines are superimposed. Theoretical model atmo-

spheres involve calculating the structure of the stellar atmosphere and generating (normally subsequently) a synthetic emergent spectrum. The computation of the models can be simplified by a number of assumptions common in hot-star analyses:-

- **Plane-parallel geometry.** The assumption is that the stellar atmosphere consists of plane-parallel layers. This implies that the geometrical height of the atmosphere - in particular, the line-forming layer - is small when compared to the radius of the star. However, for objects with extended atmospheres (and in particular significant stellar winds), this may not be valid and a treatment that uses spherical geometry is preferable. The major advantage of the assumption of plane-parallel geometry is that it reduces a two- or three-dimensional problem to a computationally more tractable one-dimensional problem.

- **Hydrostatic equilibrium.** The assumption is that the inward gravitational forces are exactly balanced by the outward gas and radiation pressure forces at every point within the star. Hence there is no net mass flow and no time-dependent effects, such as shocks (i.e., the star is in steady state).

- **Radiative equilibrium.** It is assumed that radiation is the only process through which energy is transported from the interior of the star through the photosphere. Other effects, such as convection (an important energy-transporting mechanism in late-type stars) are considered to be negligible.

- **Chemical homogeneity.** The stellar atmosphere is assumed to be chemically homogeneous and thus can be represented by a unique chemical composition.

3.1.1 Radiative transfer

The propagation of radiation through a stellar atmosphere is described by the equation of radiative transfer. Radiative transfer is a consideration of the processes through which photons are created (emission), destroyed (absorption), or redirected (scattering), and the resultant change in measurable intensity, I_ν:-

$$\frac{\mathrm{d}I_\nu}{\mathrm{d}\tau_\nu} = -I_\nu + S_\nu \tag{3.1}$$

where S_ν is the source function, the ratio of total emissivity to total opacity, given by:-

$$S_\nu(\tau_\nu) = \frac{j_\nu}{\kappa_\nu} \tag{3.2}$$

and τ_ν is the optical depth, a dimensionless quantity, defined as the number of mean free paths along the line of sight, L:-

$$\tau_\nu = \int_0^L \kappa_\nu \rho \mathrm{d}l \tag{3.3}$$

j_ν and κ_ν are the mass coefficients of emissivity and absorption, respectively. The solution of the equation of radiative transfer (Equation 3.1) yields the total emergent flux at the stellar surface. In particular, the formal solution of the transfer equation (given the assumptions in §3.1) is:-

$$F_\nu = 2\pi \int_0^\infty S_\nu(\tau_\nu) E_2(\tau_\nu) \mathrm{d}\tau_\nu \tag{3.4}$$

where F_ν is the total emergent flux at frequency ν, and $E_2(x)$ is the second exponential integral given by (Mihalas, 1978):-

$$E_2(x) = \int_1^\infty \frac{e^{-xt}}{t^2} \mathrm{d}t \tag{3.5}$$

Thus it is possible to calculate the flux at a given frequency, ν, if κ_ν and j_ν are known.

3.1.2 Local Thermodynamic Equilibrium (LTE)

In the treatment of stellar atmospheres, the assumption of Local Thermodynamic Equilibrium (LTE) means that thermodynamic equilibrium can be considered to hold at the local values of the temperature, T, and the particle number density, n. The gas is thereby characterised by the local values, at radius r, of $T(r)$ and $n(r)$. In particular, the following statements apply:-

- The source function, S_ν, is given by the Planck function, B_ν:-

$$B_\nu(T) = \frac{2h\nu^3/c^2}{\exp\left[\frac{h\nu}{kT}\right] - 1} \tag{3.6}$$

  where h is the Planck constant, c is the speed of light and k is the Boltzmann constant.

- The excitation equilibrium of the gas is given by the Boltzmann equation:-

$$\frac{n_j}{n_i} = \frac{g_j}{g_i} \exp\left[\frac{-(E_j - E_i)}{kT}\right] \tag{3.7}$$

  where g_i is the degeneracy of level i and E_i is the energy of that level measured from the ground state.

- The ionisation equilibrium of the gas is given by the Saha equation:-

$$\frac{N_j}{N_{j+1}} = n_e \frac{U_j}{U_{j+1}} \left(\frac{h^2}{2\pi m_e kT} \right)^{3/2} \exp\left[\frac{\chi_j}{kT} \right] \tag{3.8}$$

where m_e is the electron mass, n_e is the number density of electrons, N_j is the total number density of ionisation stage j, and χ_j is its ionisation potential. U is the partition function, given by:-

$$U_j = \sum_{j=1}^{\infty} g_j \exp\left[\frac{-E_j}{kT} \right] \tag{3.9}$$

- The velocity distribution of the particles is Maxwellian:-

$$f(v)\mathrm{d}v = \left(\frac{m}{2\pi kT} \right)^{3/2} \exp\left[\frac{-mv^2}{2kT} \right] \mathrm{d}v \tag{3.10}$$

where m and v are the particle mass and velocity, respectively.

3.1.3 Non-LTE situations

The assumptions of LTE greatly simplify the calculation of model atmospheres. It is an adequate approximation in the interiors of stars, where particle densities are high and collisions dominate excitation and ionisation processes. However, the observed stellar spectral lines are formed much higher, in the atmosphere, where the densities are lower and there can be significant departures from LTE. In stars hotter than $\sim$ 10 000 K (i.e., OB stars), radiation tends to dominate over collisional processes and drives the excitation and ionisation strucutures away from LTE. To allow for these departures from LTE, 'non-LTE' methods are employed. Non-LTE methods permit the level populations of certain atoms and ions to depart from their Saha-Boltzmann values, giving a much more realistic description of the stellar atmosphere (and hence a better fit to the observed line profiles). Departure coefficients are used to describe the ratios of the *actual* level populations to the LTE level populations. Non-LTE methods are particularly important in hot, low-gravity stars (i.e., early-type supergiants: a substantial fraction of the stars investigated in this thesis). They are, however, computationally intensive, and as a consequence, only selected levels of certain atoms/ions are usually considered.

3.1.4 Line broadening

Spectral line profiles are always of finite width; they are never perfectly sharp. A line exhibits a profile, the intensity of which varies with wavelength. A number of processes

contribute to the broadening of spectral lines, and by interpreting their observable effects it is possible to make certain deductions about the physical conditions in the line-forming region(s).

- **Natural broadening.** This is intrinsic to an atom and arises as a direct result of the Heisenberg Uncertainty Principle. The upper and lower energy levels of a transition are of finite width, producing a Natural (Lorentz) profile, which has its maximum absorption/emission at, and is symmetric about, the rest frequency of the transition, ν_0.

- **Pressure (Stark) broadening.** This is caused by the energy levels of an atom being perturbed by neighbouring particles (the Stark effect). The nearer the perturbating particle, the larger the perturbation. Thus, pressure broadening is directly dependent upon the particle density: the greater the density, the greater the width of the spectral line. Pressure broadening also produces the Lorentz wings.

- **Thermal Doppler broadening.** This is due to the microscopic velocities of the atoms in the stellar atmosphere (at a certain temperature, T, the gas particles have a Maxwellian distribution of velocities; see Equation 3.10). It depends upon the temperature and composition of the gas, with the spectral lines of heavy elements being narrower than those of light elements, since, on average, heavy atoms move more slowly than light ones. Thermal Doppler broadening produces a Gaussian profile.

- **Microturbulent broadening.** This is an *ad hoc* parameter often invoked to explain the increased widths of lines observed in early-type spectra. It can be considered as arising as a result of motions in the stellar atmosphere, although the exact physical origins of the velocity fields is not well understood (Smith and Howarth, 1998). Siebert (1999), in a study of 23 Galactic O-type stars of spectral type O8–O9.7, found that for all but two objects, a microturbulent velocity of 15 km s^{-1} was optimal. Tests conducted by Smith *et al.* (1998) and McErlean *et al.* (1998) demonstrated that hydrogen Balmer lines are for the most part unaffected by microturbulent line broadening, as they tend to be dominated by both a large Stark effect and by significant Doppler broadening. Hα, the line diagnostic used in this study, is a Balmer line; hence, in this work, the effects of microturbulence are largely unimportant.

The convolution of the Lorentz and Gaussian profiles produces the observed Voigt profile.

3.1.5 Line blanketing

A major obstacle when comparing models to observations is 'line blanketing' caused by the presence of spectral lines. In particular, the presence of a multitude of weak metal absorption lines in the UV has a major impact on the opacity of the atmospheres of early-type stars. The increased opacity due to these lines causes the flux to be redistributed. This 'line blanketing' changes the temperature structure of the atmosphere, leading to higher temperatures in the inner regions ('back-warming') and cooling of the outer layers. The treatment of line blanketing whilst simultaneously allowing for non-LTE effects is an extremely complex problem, with an almost limitless number of levels and rates to be calculated. The model grids used in this thesis do not take into account the effects of line blanketing. Comparisons with more complete models show that neglecting the effects leads to overestimates of the stellar effective temperature (e.g. Hubeny *et al.*, 1998); the corollary is that when line blanketing *is* incorporated into stellar atmosphere models, it is possible to fit a given star with a lower $T_{\rm eff}$ (Crowther *et al.*, 2002*b*; Herrero *et al.*, 2002; Bianchi and Garcia, 2002; Martins *et al.*, 2002).

3.2 Model photospheric spectra

The grids of model photospheric ('core') spectra used in this thesis were calculated by Keith Smith at UCL, using TLUSTY (Hubeny, 1988; Hubeny and Lanz, 1995), and are described in Smith and Howarth (1998). They are plane-parallel, hydrostatic, non-LTE, pure H/He atmospheres (Hubeny and Lanz, 1995, have, however, modified TLUSTY to incorporate the effects of line blanketing). Hydrogen and helium are included in the atmospheric structure calculations, with the model atoms comprising 9, 14 and 14 levels for H I, He I and He II, respectively. CNO ions are included implicitly in the calculations (assuming LTE ionisation fractions), but they do not contribute to the opacity; they are included solely for the purpose of number conservation. TLUSTY was used to perform the subsequent statistical equilibrium calculations, assuming fixed temperature and pressure distributions. Finally, the line transfer calculations were carried out using the code SURFACE (Giddings, 1981; Butler, 1984; Butler and Giddings, 1985). Model spectra are interpolated over $T_{\rm eff}$

and $\log g$ within the grids using the software TGKIEL, written by Keith Smith. The helium abundance, Y(He), can take the values 0.05, 0.09 (solar), 0.20 and 0.30, and is interpolated as necessary. TLUSTY atmospheres have been used (as opposed to newer, line-blanketed models), because the stellar parameters used throughout this thesis have largely been taken from the literature, and have (in general) been derived using unblanketed models. Also, FORSOL (see §3.4) was developed for use with 'simple' models. Table 3.1 gives the parameter ranges covered by the model grids and, as an example, Figure 3.1 shows the observed Hα spectrum of HD 210839, together with the model photospheric profile for the adopted parameter values of $T_{\rm eff} = 37\,000$ K, $\log g = 3.55$ and Y(He) = 0.25 (values taken from Table 4.3).

Table 3.1: Parameter ranges for the O-star model atmosphere grids

Parameter	Minimum	Maximum	Increment
$T_{\rm eff}$ (K)	25 000	44 000	1000
$\log g$	2.6	4.5	0.1
Y(He)	0.05	0.30	···

The effective temperatures and gravities of some of the B-type stars in the thesis sample (and those of α Cyg) fall outside the range of the model atmosphere grids (where the minimum available $T_{\rm eff} = 25\,000$ K and minimum available $\log g = 2.6$). For use with these objects, new spectral grids have been calculated by Richard Townsend at UCL, again using TLUSTY. They are plane-parallel, hydrostatic, non-LTE, pure H/He atmospheres. These grids offer an expansion in the range of available effective temperatures and gravities (see Table 3.2), although (at the time of writing) the helium abundance must take the value Y(He) = 0.09.

Table 3.2: Parameter ranges for the B-star model atmosphere grids

Parameter	Minimum	Maximum	Increment
$T_{\rm eff}$ (K)	10 000	50 000	1000
$\log g$	1.4	5.0	0.1

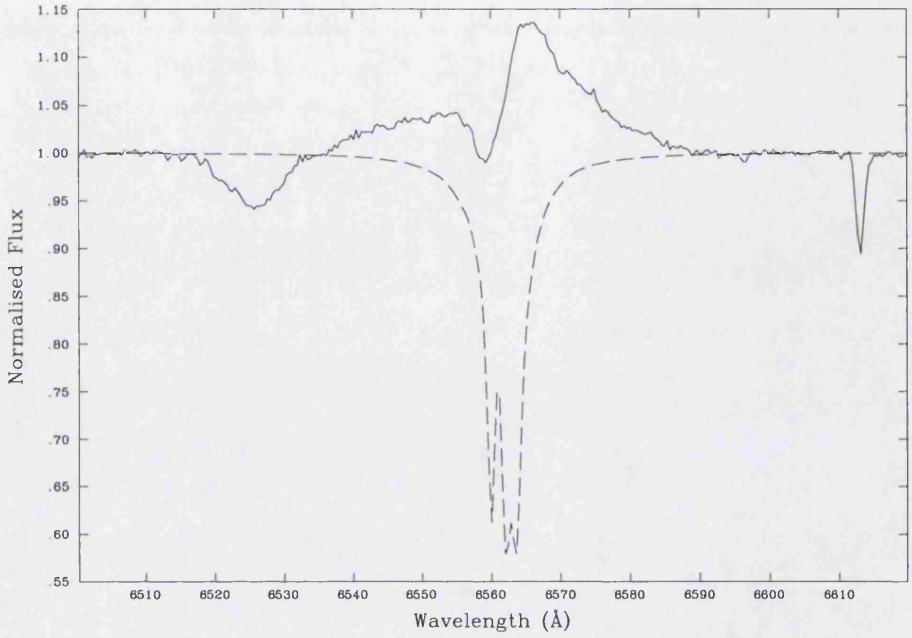

Figure 3.1: The observed Hα spectrum of HD 210839 (solid line), together with the model photospheric profile for the adopted stellar parameters (dashed line).

3.3 Hα line formation

The absorption and/or emission lines seen superimposed on the continua of hot-star spectra arise from transitions involving the bound states of atoms and ions in the stellar atmosphere. The strength of the lines depends upon the product of oscillator strength, excitation and ionisation fraction, and elemental abundance. The Hα line, along with many other emission lines observed in early-type spectra, is primarily formed by the free–bound process of radiative recombination and subsequent cascades. In particular, the Hα line arises as a result of the $n = 3 \rightarrow 2$ transition (the lowest-energy transition in the Balmer series of hydrogen). In O-type and early-B stars, the Hα feature actually consists of two components: Hα itself (λ6562.84 Å) and the blueward He II$_{4\leftrightarrow6}$ blend (λ6560.25 Å). The difference in wavelength corresponds to a velocity shift of only $\Delta v = 120$ km s^{-1}, which means that the He II blend must be taken into account when considering the observed profile. The two transitions have similar energies and gf-values, such that the ratio of the He II to H line opacities is of order 0.1 in the sonic region (for solar composition), but can reach unity in the outer wind, where the b_4 departure coefficient of He II (which describes the ratio of the *actual* population of the $n = 4$ level of He II to the LTE population) may

be of order 10 (Puls *et al.*, 1996). The He II blend can therefore significantly affect the equivalent width and shape of the combined profile.

3.3.1 Core-halo model

For O stars, it is possible to determine mass-loss rates reasonably accurately simply by using the strength of the Hα emission from the stellar wind (e.g. Klein and Castor, 1978; Leitherer, 1988*a*,*b*). The equivalent width of a synthetic Hα line formed in a hydrostatic model atmosphere is subtracted from the observed equivalent width of Hα to give the total equivalent width of the stellar-wind Hα emission. This may then be converted into a mass-loss rate via the equation of mass continuity (Equation 1.3), typically, though not necessarily, by assuming:-

- A β-type velocity law.
- Optically-thin line emission (i.e., all photons produced by the $n = 3 \rightarrow 2$ transition reach the observer).
- A constant value of the departure coefficient, b_3, of the $n = 3$ level of hydrogen.
- A constant ratio of wind temperature, T_e, to effective temperature, $T_{\rm eff}$.

This technique has been used by Lamers and Leitherer (1993) to determine the mass-loss rates of Galactic O stars. It is a much more accurate method than the use of UV resonance lines (where the uncertainties in the ionisation fractions constitute a major obstacle; see §1.5.1), because (i) hydrogen is the dominant element by mass, and (ii) it is virtually fully ionised in O-star winds. By considering only the observed line flux, the method does, however, waste valuable information contained in the line profile. The shape of the profile can give an indication as to the nature of the velocity field (i.e., the velocity law β-exponent). Furthermore, the assumption of optically-thin line emission is incorrect (Hα is never entirely optically thin throughout the wind), and Puls *et al.* (1996) showed that line *absorption* also needs to be considered.

3.3.2 Unified model atmospheres

A more exact approach that avoids the artificial divide between the hydrostatic photosphere and the supersonic stellar wind was introduced by Gabler *et al.* (1989, 1990). These

'unified model atmosphere' treatments use non-LTE radiative transfer with a *continuous* transition between the sub- and supersonic atmosphere to calculate line profiles. Recent refinements, such as the CMFGEN code of Hillier and Miller (1998), have incorporated line blanketing due to thousands of overlapping spectral lines. This has made the determination of stellar parameters much more accurate. However, because of the large parameter space that needs to be investigated, unified model atmosphere techniques are computationally both intensive and expensive, making the investigation of a large sample of stars (such as in this thesis) difficult.

3.4 [TG]FORSOL

Puls *et al.* (1996) addressed the different problems presented by the core-halo and unified model atmosphere approaches, and, using the advantages of each method, developed a very fast, approximate, but accurate method of determining mass-loss rates from the Hα profiles of O stars. The code, known as FORSOL, uses H and He II departure coefficients obtained from a grid of unified model atmospheres, together with photospheric non-LTE line profiles as the inner boundary for radiative transfer solution in the core-halo approximation, to derive a wind-contaminated Hα profile. FORSOL will be used in §4 to model the Hα observations presented in §2, and thus derive mass-loss rates for the stellar sample. A major advantage of using FORSOL to determine mass-loss rates is that the profile-generating procedure itself is extremely fast. Each Hα profile can be generated interactively with minimal delay (a few seconds) between input and output, making this approach particularly suitable for analysing a large sample of objects.

3.4.1 Assumptions and approximations

FORSOL employs a number of basic assumptions and approximations which are discussed below.

3.4.1.1 Hydrodynamical structure

- **Stationarity.** It is assumed that there are no time-dependent effects in the wind. FORSOL is intended to provide time-averaged mass-loss rates, based on mean atmospheric parameters.

- **Smooth flow.** The wind is assumed to be smooth, with no clumps or shocks. This might prove to be surprising, given that there is overwhelming evidence to the contrary. On a theoretical level, radiation-driven stellar winds have been shown to be intrinsically unstable on small scales (Owocki, 1992). This leads to a highly structured and variable flow, which might manifest itself in the form of shocks and other inhomogeneities. The time evolution of a 'clumpy' wind can, in principle, explain observed variable P-Cygni profiles (Puls *et al.*, 1993). The formation of broad, black absorption troughs in the saturated P-Cygni profiles of UV resonance lines has been attributed to a shocked stellar wind (Lucy, 1982; Puls *et al.*, 1994). 'Discrete absorption components' (DACs) have been observed in the P-Cygni profiles of many OB stars. These absorption enhancements are seen to migrate from low velocities to high velocities on a timescale of days, narrowing as they do so (Prinja *et al.*, 1987; Prinja and Howarth, 1988). Soft X-ray emission, thought to originate in the outer wind regions, is observed in early-type stars (e.g. Chlebowski *et al.*, 1989), and has been attributed to the existence (and interaction) of shocks in the wind (e.g. Feldmeier, 1995).

  It might appear, therefore, that the assumption of smooth flow is somewhat inappropriate. It must be borne in mind though that stellar-wind Hα emission originates from layers between 1.0 and 1.5 R_*, thought to be below the level at which *intrinsic* wind instabilities set in (Owocki, 1994). The fact that the observed X-ray emission and the black absorption troughs seen in saturated UV P-Cygni profiles (both thought to be due to wind structure) are believed to originate in the outer wind is consistent with this argument (see, respectively, Hillier *et al.*, 1993; Owocki, 1994). For these reasons, as well as pragmatism, the assumption of smooth flow is considered to be appropriate for the analysis presented in §4. If the winds *are* clumped, however, this means that the mass-loss rates are actually *lower* than those derived assuming a smooth wind (Abbott *et al.*, 1981, and see §7.1).

- **Spherical symmetry.** A spherically symmetric density stratification and velocity field is assumed. This is justified for objects with low rotational velocities, as the equator-to-pole variation in the effective surface gravity is small. For objects with high rotational velocities, the results should be treated with more caution (see §3.4.1.4).

3.4.1.2 Core-halo approximation

Unlike unified model atmospheres, the FORSOL treatment comprises only line formation in the wind. However, the underlying photospheric profile is taken into account consistently as the inner boundary for the radiative transfer solution. It is *not* simply incorporated as an additional constant to correct the equivalent width of the wind profile. The results thus obtained are more or less indistinguishable from unified model atmosphere calculations (see Puls *et al.*, 1996).

FORSOL was modified by Richard Townsend at UCL to allow Keith Smith's photospheric profiles (see §3.2) to be used automatically as the inner boundary for the radiative transfer solution. The resulting code, known as 'TGFORSOL', uses FORSOL to model the wind, with the core photospheric Hα profile being interpolated from Keith Smith's model grids. Tests established that the Munich (Puls *et al.*, 1996) and UCL photospheric spectra, generated with independent codes, yield essentially the same results.

3.4.1.3 Broadening

For the photospheric profiles, Doppler broadening only is assumed in the atmospheric structure and statistical equilibrium calculations, with Stark broadening being included in the final line-formation calculations. Rauch and Werner (1988) demonstrated the validity of this approximation for O-type subdwarfs, and it should be even more appropriate for the objects investigated in this thesis, whose atmospheric pressures are lower. The line profile in the wind ($n_e \sim$ few $\times\ 10^{12}$ cm^{-3}) is assumed to be Doppler broadened only, as Stark broadening only becomes effective for electron densities $n_e \gtrsim 10^{13}$ cm^{-3}. The models used do not include any instrumental broadening convolution, as these are slow to perform, and unnecessary in this case because of the high resolution of the data.

3.4.1.4 Rotation

The influence of the rotation of the star on the line-formation process is neglected. Following the recommendation of Puls *et al.* (1996), a *final* convolution of the emergent profile with the rotational profile for the *photospheric* value of the projected rotational velocity, $v \sin i$, is used to account for the stellar rotation (the calculated Hα profiles therefore do not show any structure on a scale of less than $v \sin i$). This should give satisfactory results both for thin winds (where the line is formed very close to the photosphere) and for thick

winds (where the wings become almost independent of any normalised convolution).

For stars with large rotational velocities ($v_{\rm rot} \gtrsim 250$ km s^{-1}), however, the influence of stellar rotation on the Hα line-formation process becomes important. Puls *et al.* (1996) modified $v \sin i$ to smaller values for such objects, to account for the fact that the wind emission is formed in a differentially rotating medium with an 'effective' rotational speed lower than the 'photospheric' speed. Petrenz and Puls (1996, 2000), using *2-D* wind models, *did* consider the effect of stellar rotation. They demonstrated that the influence of gravity darkening (the surface-temperature gradient from hot poles to cooler equatorial regions) on the line-formation process is negligible. They also discovered that differential rotation reduces emission in the line core, whilst enhancing emission in the wings (equivalent width is conserved), and that the density contrast caused by deflection of material from the poles to the equator (a result first found by Bjorkman and Cassinelli, 1993) leads to an increase in overall emission. Petrenz and Puls (1996) estimated that the maximum error in the derivation of $\dot{M}$ introduced by neglecting these factors is $\sim$70%, with typical errors in the region $\sim$20–30%. Petrenz and Puls (2000) concluded that the influence of stellar rotation in the derivation of Hα mass-loss rates is, in most cases, a second order effect.

3.4.2 Parameterisation of departure coefficients

Unified model atmospheres are used to parameterise the departure coefficients, b_i, of hydrogen ($i = 2, 3, 4, 5$) and ionised helium ($i = 4, 6, 8, 10$), as a function of wind velocity, v (i.e., depth in the wind). Boundary values for the departure coefficients are specified and the b_i linearly interpolated as a function of v (see Puls *et al.*, 1996, for fuller details). Tables 3.3 and 3.4 give illustrative values for the departure coefficients at the inner boundary ($b_i^{\rm in}$, at $v = 0.01$ for H and $v = 0.1$ for He II) and at the outer boundary (b_i^{∞}, at v_∞). The He II boundary values are dependent upon the density-sensitive quantity, $D = \dot{M}/(R_* v_\infty)^{1.5}$; see Table 3.4. An additional boundary value ($b_i^{\rm min}$) is tabulated for H at $v = 0.1$, as the b_2 departure coefficient has a minimum around this velocity.

It should be borne in mind that the departure coefficients are calculated by recalibrating the original departure coefficients (valid for the specific temperature stratification of the unified atmospheres) to a constant electron temperature of $T_{\rm e} = 0.75\ T_{\rm eff}$, which is an average value for the line-forming region of the models. The approximate departure coefficients are accurate to within typically 20% when compared to a run of 'exact' depar-

ture coefficients obtained from unified model atmospheres. The b_i used in this work are from detailed models of O stars and are considered to be the same for all O-star subtypes. They may not be exactly applicable to the B stars in the sample; however, it is worthwhile noting that the departure coefficients affect the determination of the mass-loss rate by a power of only 0.5.

Table 3.3: Boundary values of the H departure coefficients, b_i ($i = 2, 3, 4, 5$). v is expressed as a fraction of the terminal velocity, v_∞. Table taken from Puls *et al.* (1996).

i	$b_i^{\rm in}$ $(v = 0.01)$	$b_i^{\rm min}$ $(v = 0.1)$	b_i^{∞} $(v = 1.0)$
2	1.5	1.2	1.3
3	1.2	1.1	1.1
4	1.1	1.0	1.0
5	1.0	0.9	0.9

3.4.3 FORSOL input parameters

The emergent Hα profile is calculated by solving the formal integral for the overlapping Hα and He II components. In order to do this, FORSOL requires a number of input parameters. Some of these are physical stellar and wind parameters, and some control the way in which the profile of the Hα complex is calculated. These parameters are now summarised.

3.4.3.1 Wind parameters

- $\dot{M}$ ($M_\odot$ yr^{-1}). Mass-loss rate.
- $v_{\rm min}$ (km s^{-1}). Minimum velocity at the base of the wind (i.e., at $r = R_*$), set to 1 km s^{-1}. This value gives the best agreement with unified model atmospheres, both in terms of profile shape and equivalent width (Puls *et al.*, 1996).
- v_∞ (km s^{-1}). Terminal velocity of the wind.
- β. Velocity law β-exponent.

3.4.3.2 Stellar parameters

- $T_{\rm eff}$ (K). Effective stellar temperature.

Table 3.4: Boundary values of the He II departure coefficients, b_i ($i = 4, 6, 8, 10$). v is expressed as a fraction of the terminal velocity, v_∞. The parameter D is given by $D = \dot{M}/(R_* v_\infty)^{1.5}$ ($\dot{M}$ in $10^{-6}\ M_\odot\ \mathrm{yr}^{-1}$, R_* in $R_\odot$ and v_∞ in km s^{-1}). Table taken from Puls *et al.* (1996).

		b_i^{in} ($v = 0.1$)	
i	$\log D \leq -7.3$	$-7.3 < \log D \leq -6.3$	$\log D > -6.3$
4	3.0	$-9.05 - 1.65 \log D$	1.35
6	3.5	$-12.56 - 2.2 \log D$	1.3
8	3.5	$-12.56 - 2.2 \log D$	1.3
10	2.2	$-6.56 - 1.2 \log D$	1.0
		b_i^{∞} ($v = 1.0$)	
i	$\log D \leq -6.9$	$-6.9 < \log D \leq -5.8$	$\log D > -5.8$
4	20.6	$-76.0 - 14 \log D$	5.2
6	25.4	$-71.2 - 14 \log D$	10
8	25.4	$-71.2 - 14 \log D$	10
10	20.2	$-62.6 - 12 \log D$	7.0

- **$\log g$**. Gravity.
- **R_* ($R_\odot$)**. Stellar radius.
- **v_{rot} (km s^{-1})**. Stellar rotational velocity. The projected rotational velocity, $v \sin i$, is a satisfactory estimate for this, as far as the observed Hα profile is concerned (see §3.4.1.4).
- **Y(He)**. Helium abundance by number.
- **T_{rad} / T_{eff}**. Ratio of the radiation temperature of the neighbouring continuum to effective temperature, set to 0.77. This is an average value resulting from a grid of unified model atmospheres.

3.4.3.3 Departure coefficients

- **optauto (yes/no)**. Specifies whether or not to use the default boundary values of the departure coefficients for the $i = 2, 3$ (H) and $i = 4, 6$ (He II) levels (calibrated to an electron temperature of $T_{\mathrm{e}} = 0.75\ T_{\mathrm{eff}}$; see §3.4.2). If the precomputed default

values are *not* used, values for the departure coefficients must be explicitly specified in the parameter input file.

- T_e / T_{eff}. Ratio of the electron temperature to effective temperature, set to 0.75. Results are insensitive to this.

3.4.3.4 FORSOL parameters

- **x(inf)max**. Maximum normalised velocity over which the calculation is performed, set to 1.0.
- **nf**. The number of frequency points calculated, set to 100.
- R_{max} (R_*). Maximum radius to which iterations are performed, set to 100 R_*.
- **'HH' or 'H'**. Specifies whether or not to include the He II blend ('HH' and 'H', respectively). It is always included here.
- **λ(air) (Å)**. Wavelengths of the H and He lines, set to $H\alpha_{3\leftrightarrow 2}$ = λ6562.84 Å and $He\,II_{4\leftrightarrow 6}$ = λ6560.25 Å.
- g_ν. Gaunt factors of the two transitions, set to $gf_H = 5.1256$ and $gf_{He} = 5.7376$.
- **T or F**. Specifies whether or not to incorporate the photospheric profile. It is always included here.

3.5 Sensitivity tests

A number of sensitivity tests have been performed to investigate how the calculated Hα profile is affected by different stellar and wind parameters. In particular, a detailed study was undertaken to examine the effect of the hydrogen and helium departure coefficients on the shape of the emergent profile. The results of the sensitivity tests enable more insightful adjustments to be made to the parameters when fitting an observed profile with a theoretical model.

The ranges of the input parameters considered in the sensitivity tests are given in Table 3.5; the remaining input parameters (mainly controlling the mechanics of calculating the Hα profile) were held constant. Unless being varied, the adopted values of the adjustable parameters were as listed in the fifth column.

Table 3.5: Parameter ranges for the sensitivity tests

Parameter	Minimum	Maximum	Increment	Default
β	0.5	3	0.5	1.0
$\log g$	2.6	4.4	0.6	3.5
$\dot{M}$ ($M_\odot$ yr^{-1})	1×10^{-7}	1×10^{-5}	$5 \times 10^{-7,-6\dagger}$	1×10^{-6}
R_* ($R_\odot$)	5	50	5‡	20
$T_{\rm eff}$ (K)	25 000	43 000	3000	35 000
v_∞ (km s^{-1})	500	3000	500	1750
$v \sin i$ (km s^{-1})	90	330	60	100
Y(He)	0.10	0.25	0.05	0.10
$b_3^{\rm in}$ (H)	0.5	1.3	0.2	Puls value[a]
$b_4^{\rm in}$ (He)	1.0	5.5	1.5	Puls value[b]
b_6^{∞} (He)	5.0	25.0	5.0	Puls value[b]

NOTES: † — The region $\dot{M} = 1$–5×10^{-6} $M_\odot$ yr^{-1} is explored in greater detail, using smaller increments of 1×10^{-6} $M_\odot$ yr^{-1}; ‡ — Excluding 35 and 45 $R_\odot$; (*a*) — See Table 3.3; (*b*) — See Table 3.4.

In Figures 3.2–3.15, each parameter is investigated in turn. The calculated emergent Hα profiles are represented by solid lines (to aid clarity, for $\log g$ and Y(He), these are vertically offset by an arbitrary number of continuum units). Additionally, for reference, on each plot, the corresponding core photospheric spectrum is included (dashed lines). This gives an indication as to the contribution of the underlying photospheric profile to the overall equivalent width. The photospheric profile itself is only affected by varying $T_{\rm eff}$, $\log g$ and Y(He).

3.5.1 Velocity law β-exponent

Varying β has no effect on the core photospheric profile; any changes in the emergent Hα profile are due to changes in the wind emission. The high-velocity wings are almost independent of the velocity law: it is the central emission peak that is controlled by β. High, narrow wind emission is seen for large β (corresponding to a slowly accelerating flow, with a 'flat' velocity law in the inner regions; see Equation 1.4), and lower, broader wind emission for small β (a quickly accelerating flow). This is because, for a slowly accelerating wind, there is more emitting material at low velocity close to the star. For the typical O star presented here, the effect of increasing β from 0.5 to 3.0 (with other parameters held constant) is extremely pronounced: the profile changes from pure absorption to emission as the photospheric absorption profile becomes less significant. For objects with dense winds that contribute greatly to the Hα profile, the profile shape is so sensitive to the influence of the velocity law that the value of β can be determined in parallel with $\dot{M}$. For stars with only a small contribution from the wind (i.e., the Hα profile is primarily photospheric in nature), the profile is largely insensitive to changes in β (this is clearly demonstrated by model fits to observed Hα data; see §4.5.1). In these latter cases, it is perhaps wiser to rely more on theoretical predictions.

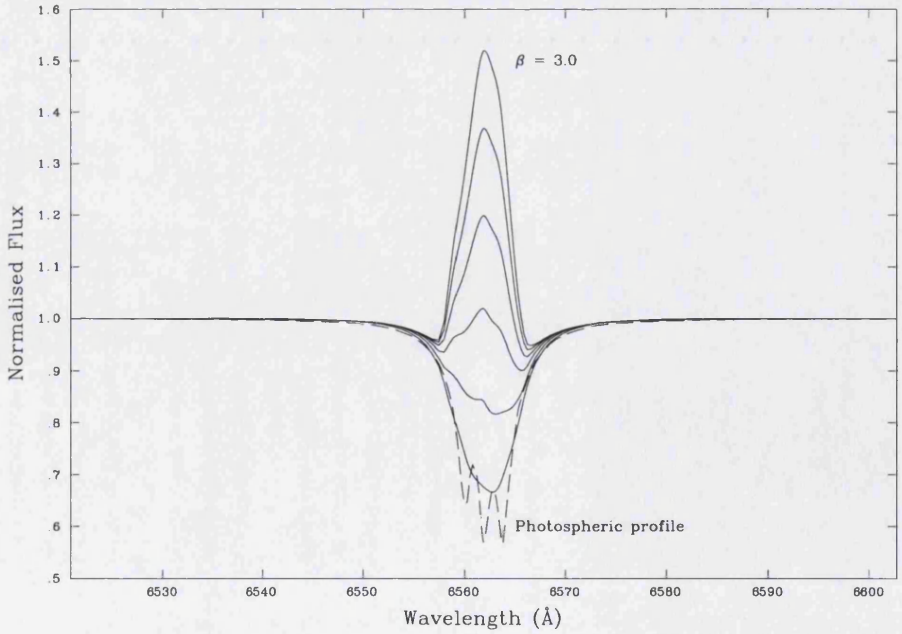

Figure 3.2: Hα profiles adopting velocity law β-exponents of 3.0, 2.5, 2.0, 1.5, 1.0 and 0.5.

3.5.2 Gravity, $\log g$

The rôle of $\log g$ is only to affect the core photospheric spectrum (the only difference between the solid and dashed lines in Figure 3.3 is that the solid profiles have been convolved with the rotational profile for the photospheric value of $v \sin i$). As expected, higher gravities give more extended absorption wings, as a result of increased pressure broadening.

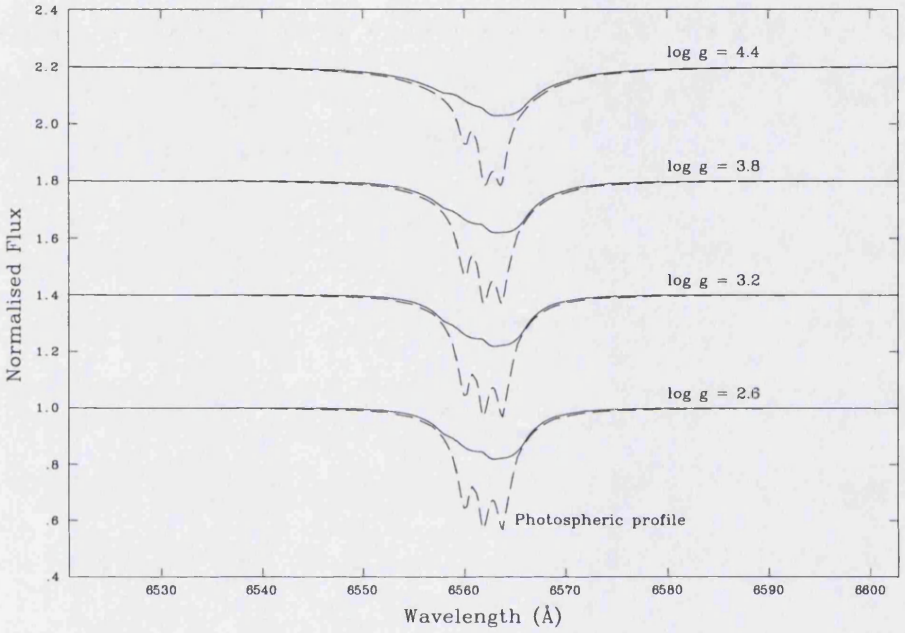

Figure 3.3: Hα profiles adopting logarithmic gravities of 4.4, 3.8, 3.2 and 2.6.

3.5.3 Mass-loss rate, $\dot{M}$

Varying the mass-loss rate has no effect on the core photospheric spectrum, but the emergent Hα profile is dramatically affected because of the influence of $\dot{M}$ on the wind emission. As $\dot{M}$ is increased, the Hα profile changes from pure absorption to extremely strong, broad emission. Increasing the mass-loss rate increases the emission over the *whole* of the emergent profile (including the high-velocity wings), because the wind density is higher at *all* velocities.

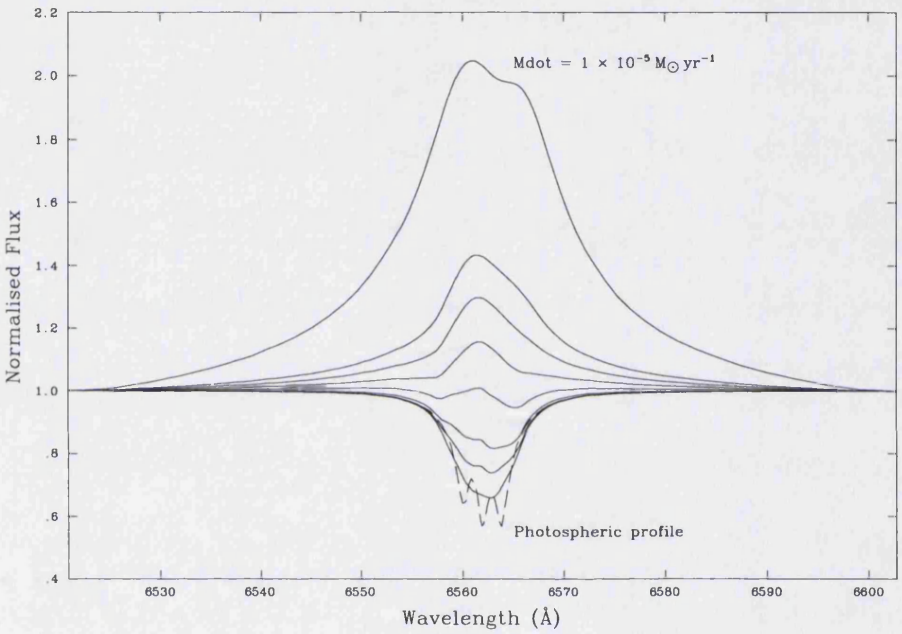

Figure 3.4: Hα profiles adopting mass-loss rates of 10, 5, 4, 3, 2, 1, 0.5 and 0.1 $\times$ 10^{-6} $M_{\odot}$ yr^{-1}.

3.5.4 Stellar radius, R_*

The core photospheric profile is unaffected by varying R_*. Decreasing R_*, whilst keeping $\dot{M}$ (and v_∞) fixed, increases the wind density (since $\rho[r] = \dot{M}/4\pi R_*^2 v_\infty$), and hence the wind emission.

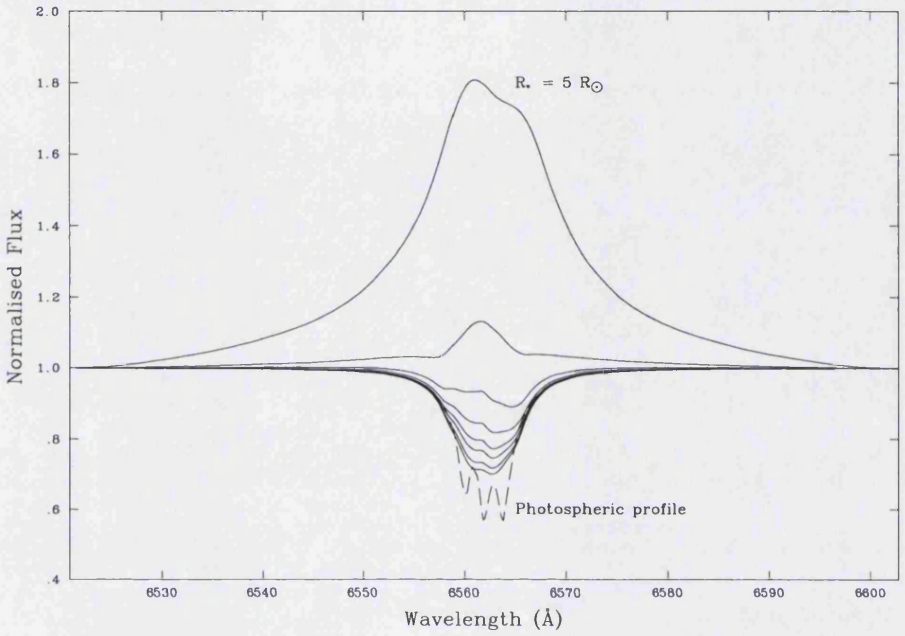

Figure 3.5: Hα profiles adopting stellar radii of 5, 10, 15, 20, 25, 30, 40 and 50 $R_\odot$.

3.5.5 Effective temperature, $T_{\rm eff}$

Varying $T_{\rm eff}$ affects both the core spectrum and the wind emission; this can be seen in the photospheric and emergent profiles in Figure 3.6 (for clarity, the photospheric profiles have been vertically offset by -0.2 continuum units). The main influence of $T_{\rm eff}$, however, is on the departure coefficients, through which lower effective temperatures result in more wind emission. An additional effect is the dilution of the Hα line by the continuum at higher effective temperatures.

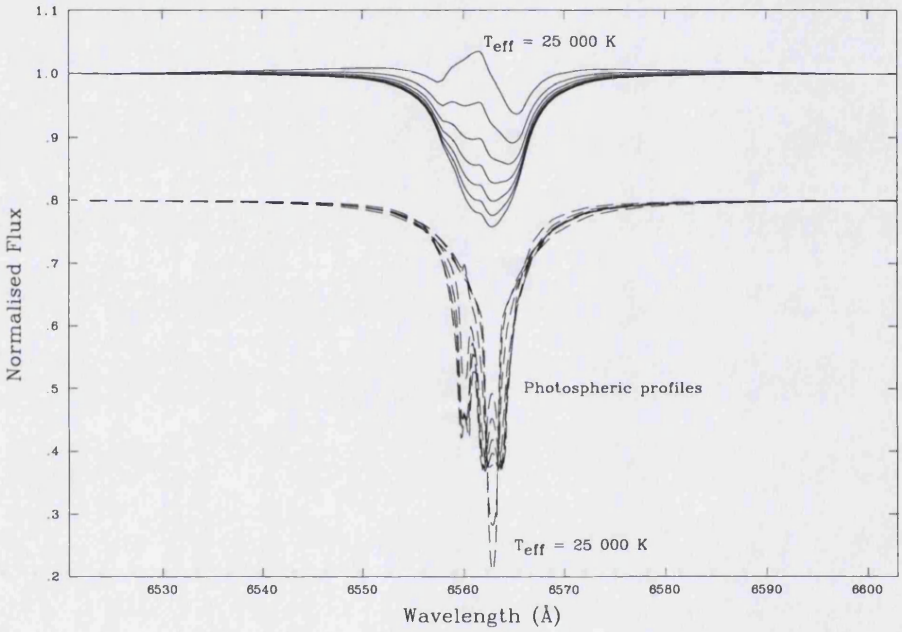

Figure 3.6: Hα profiles adopting effective temperatures of 25, 28, 31, 34, 37, 40 and 43 kK.

3.5.6 Terminal velocity, v_∞

The core photospheric profile is unaffected by varying v_∞. Increasing the terminal velocity has two effects: first, it 'spreads' the emission over a larger wavelength range, reducing the strength of the central emission peak; secondly, it decreases the density throughout the entire wind (via the equation of mass continuity), resulting in decreased emission overall.

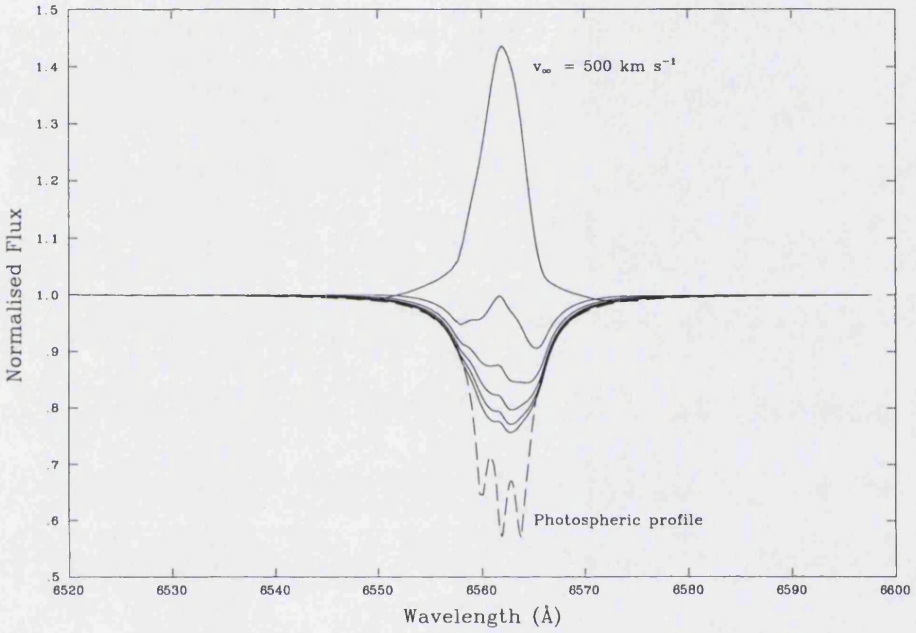

Figure 3.7: Hα profiles adopting terminal velocities of 500, 1000, 1500, 2000, 2500 and 3000 km s^{-1}.

3.5.7 Rotation velocity, $v \sin i$

As expected, the core (unconvolved) photospheric profile is unaffected by varying $v \sin i$. The simple treatment of rotation (see §3.4.1.4) means that the emergent profiles are merely 'smoothed' with increasing $v \sin i$; equivalent width is conserved.

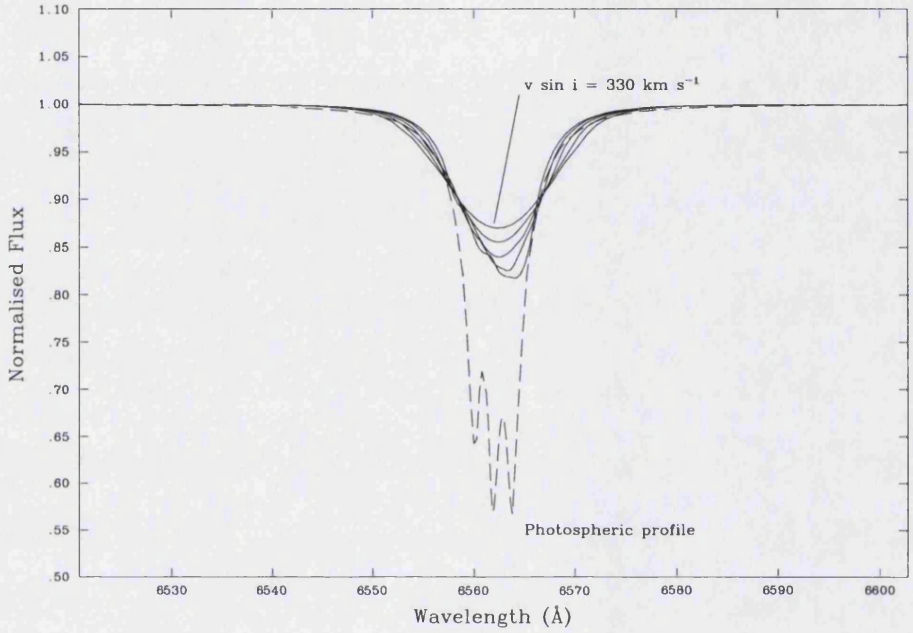

Figure 3.8: Hα profiles adopting rotation velocities of 330, 270, 210, 150 and 90 km s^{-1}.

3.5.8 Helium abundance, Y(He)

The helium abundance has very little influence on either the photospheric profile or the emergent profile.

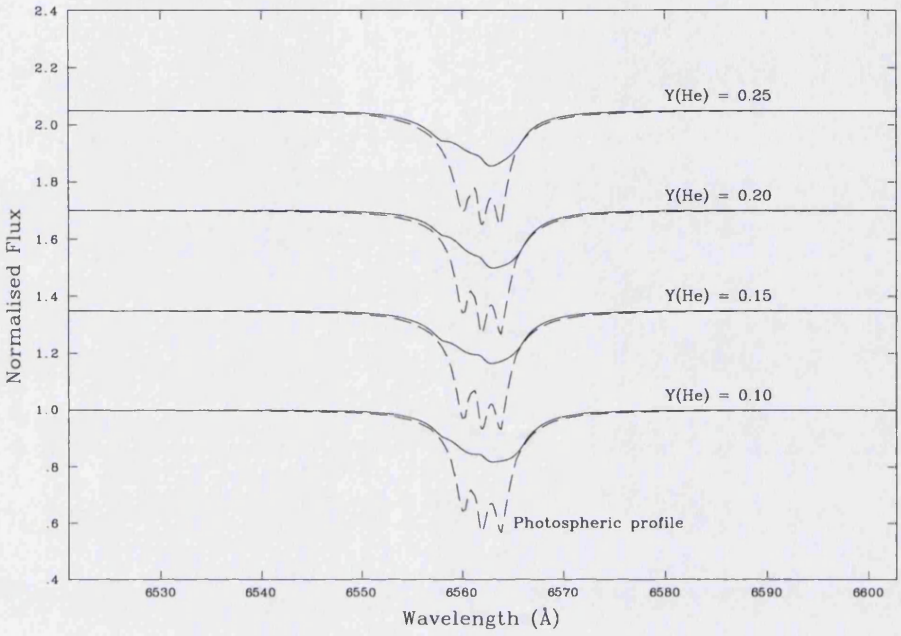

Figure 3.9: Hα profiles adopting helium abundances of 0.25, 0.20, 0.15 and 0.10.

3.5.9 Equation of mass continuity

The equation of mass continuity, Equation 1.3, states that at any point in the wind:-

$$\rho(r) = \frac{\dot{M}}{4\pi r^2 v(r)} \tag{3.11}$$

For simplicity, here it will be assumed that $v(r)$ is equal to v_∞. The emissivity, ϵ, of the Hα line is proportional to the density squared:-

$$\epsilon \propto \rho^2(r) \tag{3.12}$$

Thus, the total emission, E, in the line is:-

$$E \propto \int_{\text{Vol}} \rho^2(r) \mathrm{d}V \tag{3.13}$$

$$E \propto \int_{R_*}^{\infty} \left(\frac{\dot{M}}{4\pi r^2 v_\infty} \right)^2 4\pi r^2 \mathrm{d}r \tag{3.14}$$

$$E \propto \int_{R_*}^{\infty} \frac{\dot{M}^2}{r^2} \mathrm{d}r \tag{3.15}$$

$$E \propto -\left[\frac{\dot{M}^2}{r} \right]_{R_*}^{\infty} \tag{3.16}$$

$$E \propto \frac{\dot{M}^2}{R_*} \tag{3.17}$$

To obtain the continuum-normalised line strength, I, it is necessary to divide through by the continuum luminosity, L, which is proportional to R_*^2 (Equation 4.1):-

$$I \propto \frac{\dot{M}^2}{R_*^3} \tag{3.18}$$

The strength of the stellar wind contribution is a function of $\dot{M}^2/R_*^3$; this quantity might therefore be expected to give constant Hα-line strength for constant v_∞ (fixing v_∞, however, is not necessarily physical, but changing its value will alter the profile shape). Figure 3.10 shows the effect on the generated Hα profile, of varying $\dot{M}$ and R_*, whilst holding $\dot{M}^2/R_*^3$ constant at 2.5×10^{-15} $M_\odot^2$ yr^{-2} $R_\odot{}^{-3}$ (the pairs of $\dot{M}$, R_* values adopted to generate the individual profiles are listed in Table 3.6). It can be clearly seen that there is indeed a degeneracy in the line profiles when $\dot{M}^2/R_*^3$ is held constant.

Table 3.6: Values of $\dot{M}$ and R_* adopted to generate the profiles shown in Figure 3.10

$\dot{M}$ ($M_\odot$ yr^{-1})	R_* ($R_\odot$)
5×10^{-5}	100.0
1×10^{-5}	34.2
5×10^{-6}	21.5
1×10^{-6}	7.4
5×10^{-7}	4.6
1×10^{-7}	1.6
5×10^{-8}	1.0

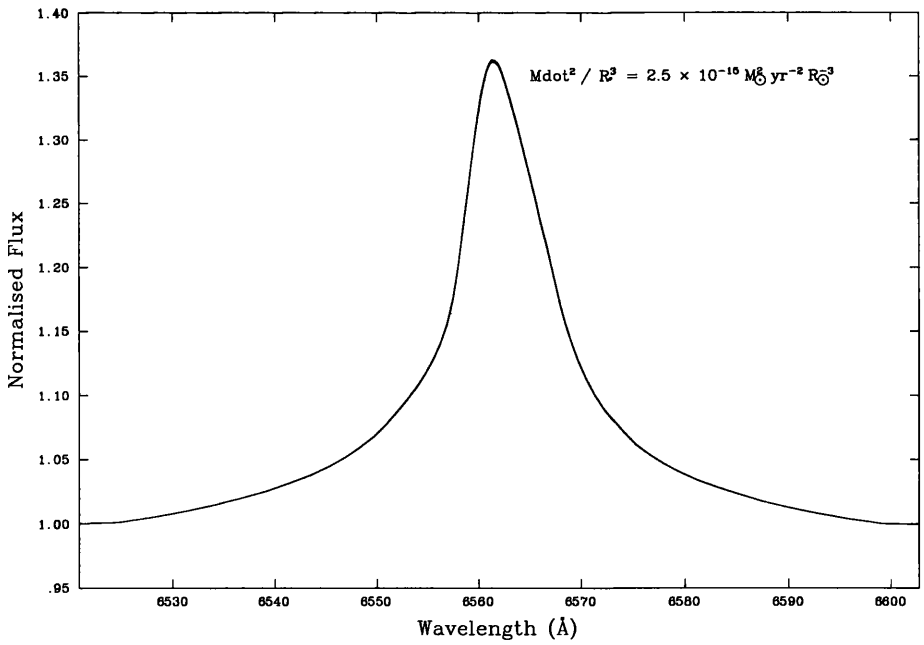

Figure 3.10: Hα profiles adopting $\dot{M}^2/R_*^3$ constant at 2.5×10^{-15} $M_\odot^2$ yr$^{-2}{R_\odot}^{-3}$, whilst varying $\dot{M}$ and R_*.

3.5.10 Hydrogen and helium departure coefficients

FORSOL offers the choice of either using the precomputed, density- and temperature-dependent default values of the $b_3^{\rm in}$ (H), $b_4^{\rm in}$ (He) and b_6^{∞} (He) departure coefficients, or else specifying their values explicitly in the parameter input file. Sensitivity tests were performed using the parameters of the star α Cam (see Table 4.3) to investigate quantitatively the effects on the Hα profile of varying these departure coefficients. This star was chosen because its model Hα profile (when using the default values of the departure coefficients) exhibits a very strong P-Cygni shape. The changes in the P-Cygni profile are more instructive than would be the case if (for example) a simple absorption profile were selected. Physically, with regard to the H$\alpha_{3\rightarrow 2}$ and He II$_{4\leftrightarrow 6}$ transitions, the departure coefficients have the following effects:-

(i) $b_3^{\rm in}$ (H) changes the H emission in the inner part of the wind (an increase in value results in an increase in population of the $n = 3$ level, and hence an increase in emissivity).

(ii) $b_4^{\rm in}$ (He) changes the He opacity in the inner part of the wind (an increase in value results in an increase in population of the $n = 4$ level, and hence an increase in opacity).

(iii) b_6^{∞} (He) changes the He emission in the outer part of the wind (an increase in value results in an increase in population of the $n = 6$ level, and hence an increase in emissivity).

which correspond to the following observable effects on the Hα profile (Figures 3.11–3.15):-

(i) $b_3^{\rm in}$ (H) greatly influences the shape of the central part of the profile by controlling the height of the Hα emission maximum around 6563 Å (the extended high-velocity wings are largely unaffected). Decreasing the value of $b_3^{\rm in}$ (H) from 1.3 to 0.5 (whilst holding all other parameters constant) reduces the height of the emission maximum, and can change a straightforward emission line (or P-Cygni profile) into a double-peaked profile of very different appearance. A 'double' P-Cygni profile may be observed: the blueward profile attributable to the He II blend at 6560 Å, and the redward profile attributable to Hα at 6563 Å (the He II P-Cygni profile is not observable until the Hα emission has been sufficiently reduced).

(ii) $b_4^{\rm in}$ (He) also greatly influences the shape of the central part of the profile (as well as the blue high-velocity wing) by controlling the depth of the absorption due to the He II blend. By increasing the He absorption, increasing $b_4^{\rm in}$ (He) from 1.5 to 5.5 (whilst holding all other parameters constant) increases the strength of the P-Cygni profile, producing a strong decline from the emission maximum towards the absorption minimum.

(iii) b_6^{∞} (He) affects the level of emission throughout the entire profile: increasing b_6^{∞} (He) increases the emission at every point, from the central peak (or P-Cygni profile), to the high-velocity wings; the detailed shape of the profile, however, remains largely unaffected. The influence of b_6^{∞} (He) is much less pronounced than that of either $b_3^{\rm in}$ (H) or $b_4^{\rm in}$ (He) though. In the case of α Cam, increasing b_6^{∞} (He) from 5.0 to 25.0 (whilst holding all other parameters constant) results in a change in the level of emission of only $\sim 9\%$ on average (measured at the same wavelength point).

It is notable that the profiles react asymmetrically to changes in $b_4^{\rm in}$ (He) and b_6^{∞} (He). This enables both quantities to be adjusted in tandem to model the blue wing of the Hα profile. Puls *et al.* (1996) found that in order to fit an observed Hα profile, it was necessary in some cases to increase the He opacity in the inner wind by reducing $b_4^{\rm in}$ (He) from its standard value, but *also* to decrease the He emission in the outer wind by decreasing the value of b_6^{∞} (He). They suggested that the need to vary the helium departure coefficients from those values obtained using the results from unified model atmospheres might be a result of neglecting the effects of EUV line blocking (cf. Pauldrach *et al.*, 1994; Schaerer and Schmutz, 1994).

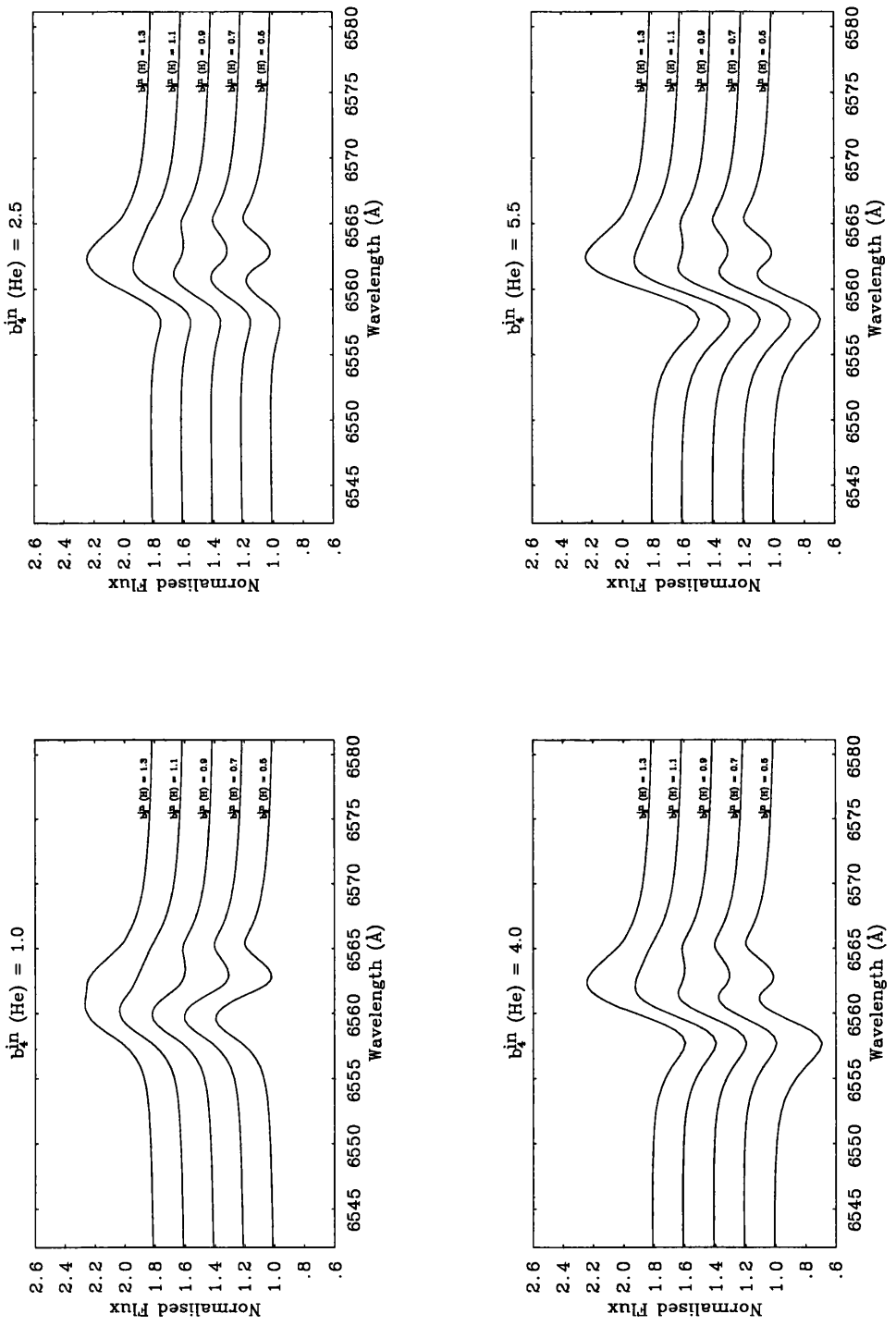

Figure 3.11: Hα profiles adopting b_6^{∞} (He) = 5.0, while varying $b_3^{\rm in}$ (H) and $b_4^{\rm in}$ (He).

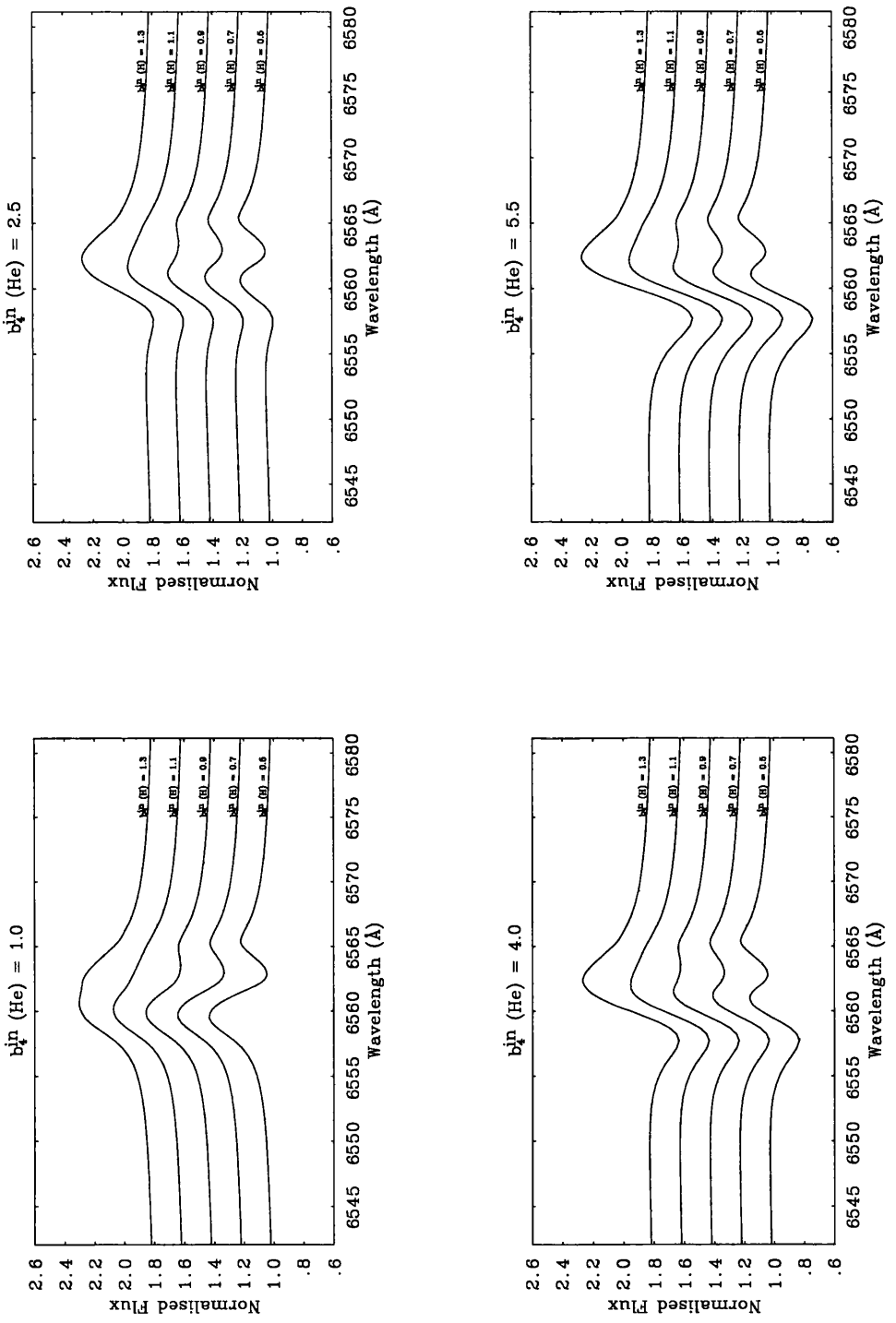

Figure 3.12: Hα profiles adopting b_6^{∞} (He) = 10.0, while varying $b_3^{\rm in}$ (H) and $b_4^{\rm in}$ (He).

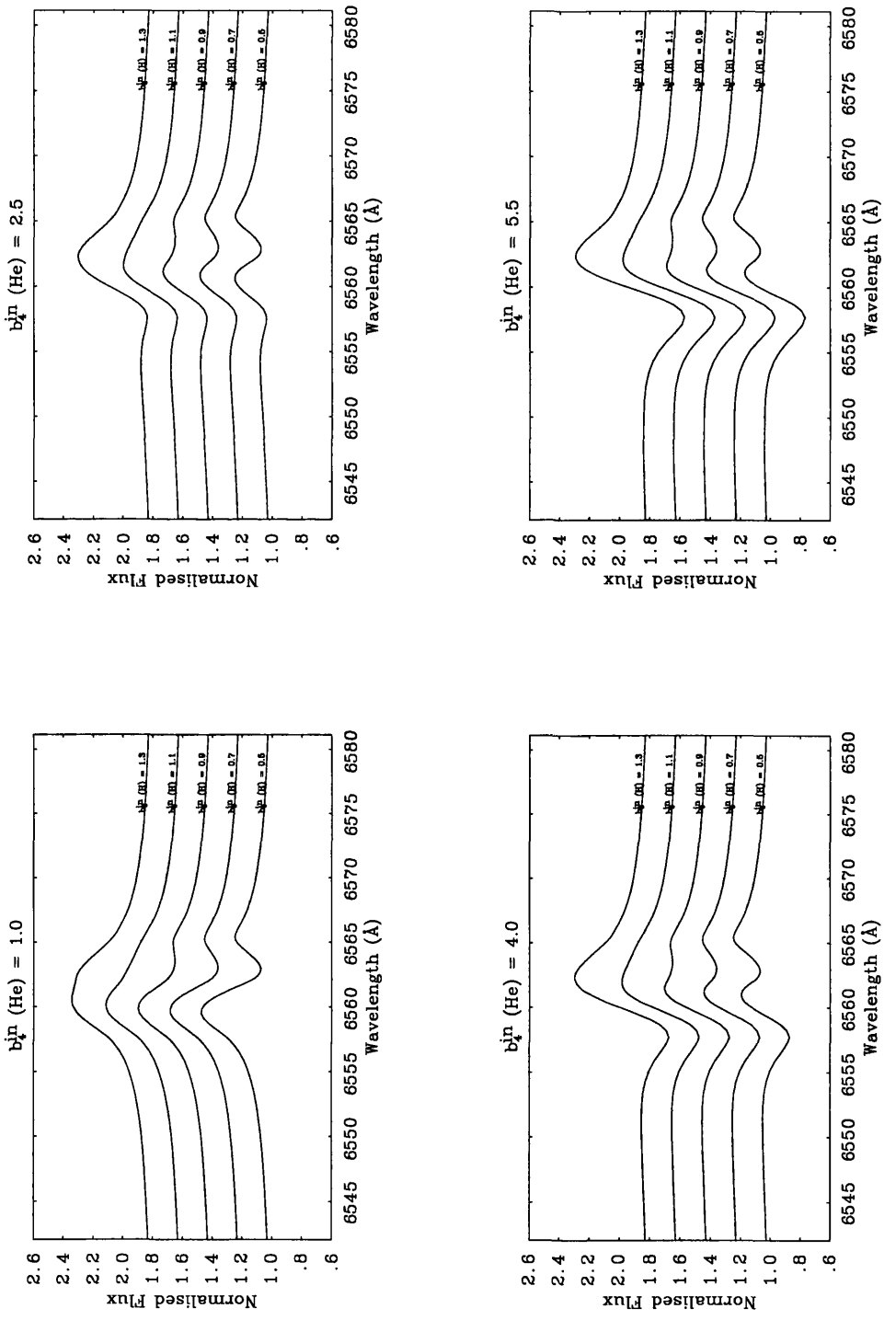

Figure 3.13: Hα profiles adopting b_6^{∞} (He) = 15.0, while varying $b_3^{\rm in}$ (H) and $b_4^{\rm in}$ (He).

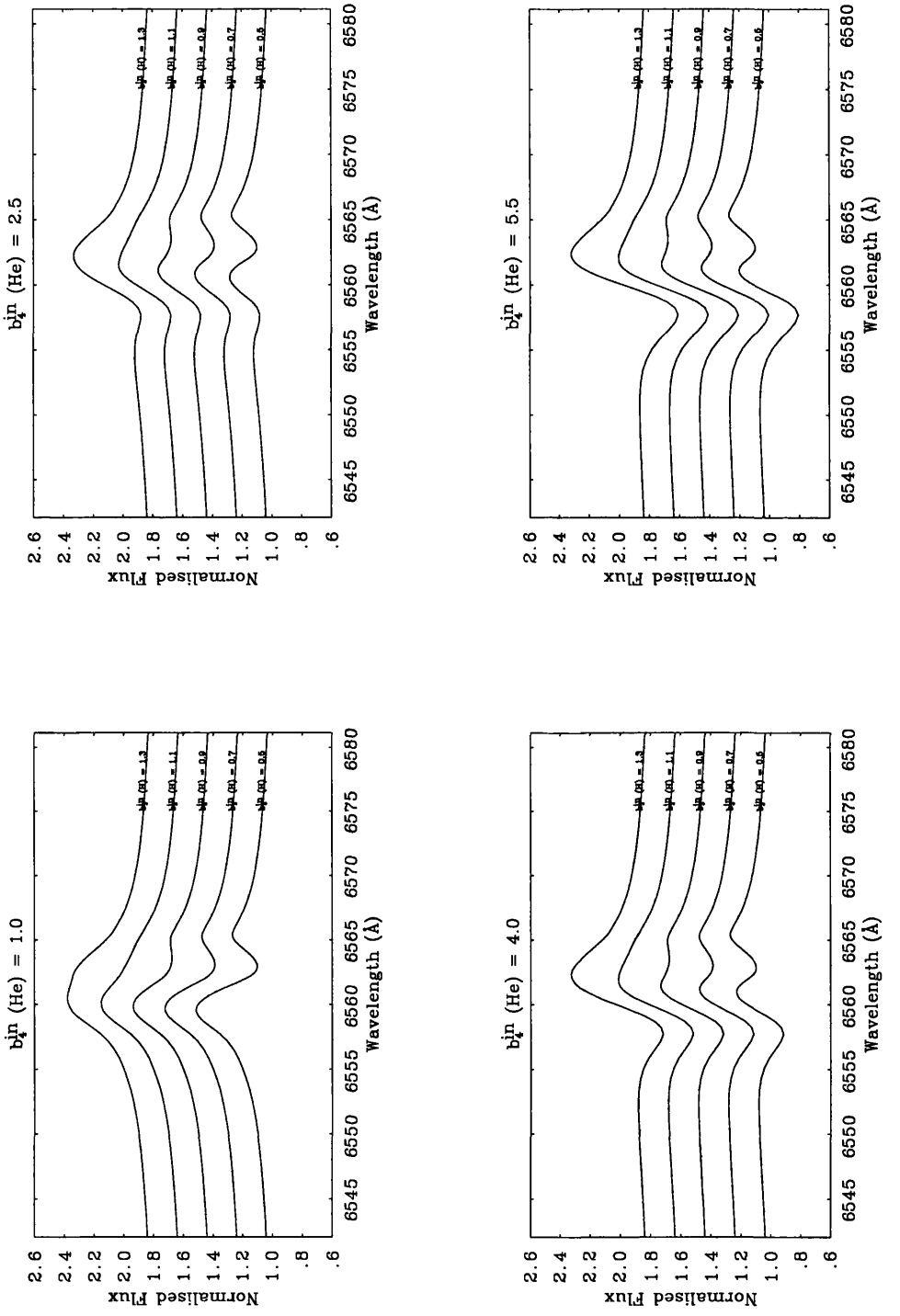

Figure 3.14: Hα profiles adopting b_6^{∞} (He) = 20.0, while varying $b_3^{\rm in}$ (H) and $b_4^{\rm in}$ (He).

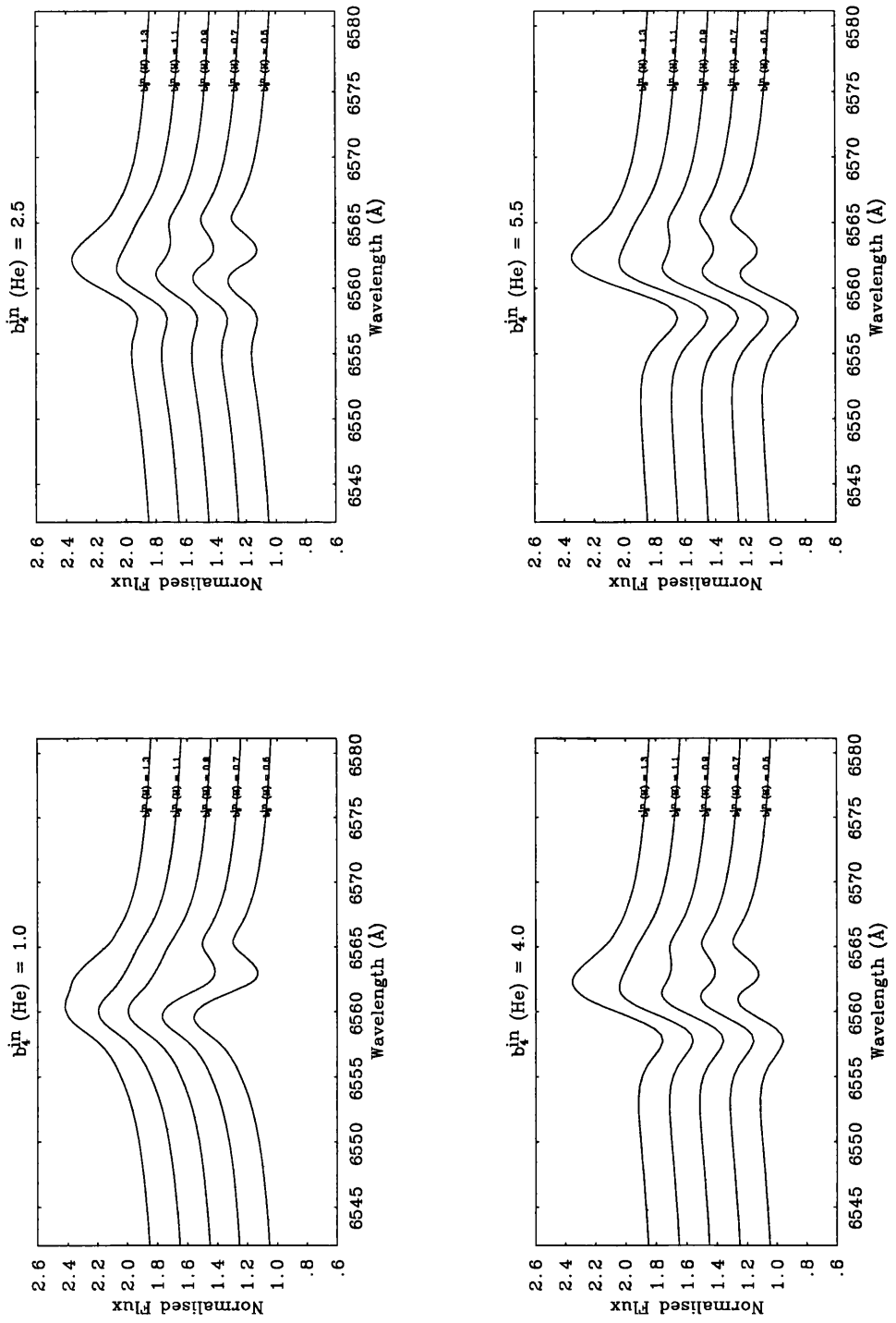

Figure 3.15: Hα profiles adopting b_6^{∞} (He) = 25.0, while varying b_3^{in} (H) and b_4^{in} (He).

CHAPTER 4

Hα: Analyses

4.1 PHALTEE

In order to derive insight from the Hα observations presented in §2, it is necessary to compare them to the theoretical models discussed in §3. The aim is to compare the observed flux with the model flux, adopting the model parameters that optimally fit the observations. To this end, a new program, PHALTEE (Program for Hα Line Transfer with Eugenic Estimation), has been developed by Ian Howarth, which couples TGFORSOL with the PIKAIA subroutine (Charbonneau and Knapp, 1996) to search within a specified parameter space for the 'best' (quasi-least-squares) TGFORSOL fit to the Hα data, using a genetic algorithm. This renders Hα modelling both more objective and automated, while minimising the necessity for manual intervention. Thus, the previously described sensitivity tests provide a useful guide to the interpretation of the results, and to the parameter spaces to be searched.

4.1.1 The PIKAIA subroutine

PIKAIA is a subroutine package that optimises (maximises) a user-supplied 'fitness' function over an n-dimensional parameter space, using a basic genetic algorithm. In the case of PHALTEE, the fitness function to be maximised is an *inverse* chi-squared function (PHALTEE does not *minimise* residuals; it *maximises* fitness). This is used to find the 'evolved' parameter set that minimises the difference in the sum of the squares of the residuals between the predictions of TGFORSOL and the observations.

Genetic algorithms are a class of search techniques that employ the biological principle of natural selection in a computational setting. The approach that genetic algorithms employ to perform numerical optimisation may appear superficially similar to Monte Carlo methods, but the use of basic evolutionary operations constitutes an important difference. A PIKAIA evolutionary run (a 'search') proceeds as follows:-

(i) An initial 'population' of solutions is generated, randomly distributed in parameter space.

(ii) The fitness of each member of the current population is evaluated.

(iii) Pairs of 'parent' solutions are selected to take part in the 'breeding' process, described below. The probability of a given solution participating in the breeding process is proportional to that solution's fitness (i.e., better solutions breed more often: natural selection).

(iv) Each pair of parent solutions is bred to produce two new 'offspring' solutions. The breeding process involves encoding the parameters defining each parent solution as a 'chromosome'. After this, there is the possibility of performing 'crossover' and 'mutation' operations (see §4.1.1.3 and §4.1.1.4, respectively) on the chromosomes, thus yielding two *new* chromosomes. Decoding the new chromosomes produces a pair of offspring parameter sets, which are then put into 'temporary storage'.

(v) Selection and breeding is repeated until the number of offspring produced equals the number of members of the current population (this is an arbitrary but convenient choice).

(vi) The offspring population is used to replace the parent population (although the fittest member of the parent population always 'survives', to ensure maximum fitness never decreases; this strategy is known as 'elitism').

(vii) The whole process is repeated from step (ii) until some termination criterion is achieved.

A number of biological terms are used to describe the search technique employed by PIKAIA and these warrant further discussion.

4.1.1.1 Selection

PIKAIA uses a stochastic (as opposed to deterministic) sampling technique to select parent solutions, in which the probability of a solution being selected is proportional to its fitness. The sampling mechanism used is known as the 'Roulette Wheel Algorithm', whereby each solution is ascribed a 'sector' of a 'roulette wheel' whose angular dimension depends upon the fitness of the solution. A random number is used to select a solution for breeding: the equivalent of spinning the roulette wheel. The probability of the wheel stopping in any given sector (i.e., a solution being selected) is proportional to the angular extent of that sector and hence the fitness of the corresponding solution.

4.1.1.2 Chromosomes

So that various genetic operators can be used in the breeding process, the information contained in each parent solution is encoded in a chromosome-like structure. PIKAIA encodes each parameter describing the parent solution using 1-digit, base 10 integers. The parameters then become a sequence of 1-digit numbers: a 'chromosome'. For example, a solution described by two parameters, (x, y), once encoded, would become:-

$$(x, y) = (0.12345, 0.67890) \rightarrow 1234567890$$

The chromosome 1234567890 can be considered to be made up of ten 'genes', each having ten possible 'alleles' (i.e., the 1-digit base 10 integers). After the breeding process, the chromosome is decoded, yielding the two new parameter values.

4.1.1.3 Crossover

PIKAIA uses a single crossover operator which acts on a pair of parent chromosomes to produce a pair of offspring chromosomes. The crossover operator randomly selects a cutting point along the chromosomes and cuts both parents at that point. The fragments to the right of the cut are then interchanged and appended to the remaining fragments. For example:-

0123456789 → 0123 | 456789	Parent chromosome 'A' being cut
9876543210 → 9876 | 543210	Parent chromosome 'B' being cut
0123 + 543210 → 0123543210	Formation of offspring chromosome 'C'
9876 + 456789 → 9876456789	Formation of offspring chromosome 'D'

Offspring thus produced incorporate 'chunks' of information from their parents. The crossover operation is not applied in every case; it is only applied if a randomly generated number exceeds some pre-specified crossover rate. This crossover rate remains constant throughout the search; the calculations described here use a crossover probability of 0.85. If the crossover operator is not applied, the two offspring are exact copies of their parents.

4.1.1.4 Mutation

PIKAIA uses a single mutation operator which can vary throughout the course of a run. The mutation operator generates a random number for each gene of an offspring chromosome and applies a mutation to a gene if this number exceeds some pre-specified mutation rate. The mutation takes the form of a random integer replacing the gene. PIKAIA permits either a uniform mutation rate, or one that can be dynamically adjusted. In the latter mode (which is the mode employed by PHALTEE), PIKAIA monitors the degree of convergence in the population and adjusts the mutation rate as necessary. An initial mutation rate is specified, as are upper and lower bounds to the allowed range of mutation rates. The calculations described here use an initial mutation rate of 0.005; the minimum mutation rate is 0.0005 and the maximum is 0.25. Mutation is important, as it reduces the probability of convergence on a *local* fitness maximum in the specified parameter space.

4.1.2 Modelling

As input, PHALTEE requires an observed Hα spectrum and a parameter file (the observed spectrum must be stored as an NDF, with wavelength in Å and flux normalised to unity). The spectrum must be cleaned of telluric lines (see §2.1.3 for a description of telluric removal). The parameter file contains essentially the same information as a TGFORSOL input file, with some additions that control the way in which PIKAIA conducts a search. Parameters may be defined as fixed, or a range of values may be specified, in which case the

optimum value in that range is sought. The output is a set of 'best' parameter estimates, the corresponding model spectrum and, for reference, the associated input (photospheric) spectrum.

PHALTEE imposes no limit on the number of generations that can evolve, but has a default of 500. There is, however, a population-size limit of 128 members, with a default of 100. The number of members of a population must also be even. This is because each breeding process produces two offspring (one offspring could be discarded, but that would be computationally inefficient). Since each generation produces an even number of offspring (replacing the parent population), the first parent population needs an even number of members. For single-parameter searches, 20 generations, each containing 20 members, was found to be sufficient; in the case of there being two or more free parameters, 100 generations, each containing 100 members, were used. Increasing these numbers does not change the results materially. The termination criterion for a PHALTEE search is defined by the number of generations. Because the process generates a finite number of discrete points in parameter space (as opposed to conducting a continuous search), it will not, in general, find 'the' best fit. In practice, however, the best fit found will be very close to the formal least-squares solution (to actually arrive at 'the' least-squares solution would require an arbitrarily large number of generations). It is in this sense that 'best' fits are obtained.

A major advantage of using PHALTEE over (for example) a simple least-squares fit, is that PHALTEE does not require the calculation of the derivatives of the goodness of fit function with respect to the model parameters. As the derivatives concerned are non-analytical, this is extremely beneficial (and in any case, PHALTEE does, in effect, return a least-squares fit). PHALTEE is also, through use of the mutation operator (§4.1.1.4), very robust against *local* minima.

The results of modelling the Hα observations using PHALTEE are now presented.

4.2 Modelling the observations

PHALTEE was used to fit the observed Hα profiles, and hence derive 'best' values for:-

(a) The mass-loss rate, $\dot{M}$.

(b) The velocity law β-exponent.

(c) The $b_3^{\rm in}$ departure coefficient of hydrogen, $b_3^{\rm in}$ (H).

(d) The $b_4^{\rm in}$ departure coefficient of helium, $b_4^{\rm in}$ (He).

(e) The b_6^{∞} departure coefficient of helium, b_6^{∞} (He).

Allowing the departure coefficients to float leads to cosmetic improvements in the modelling; i.e., it leads to 'visually' better fits to the observed Hα profiles. To a much lesser extent, the crucial parameters, $\dot{M}$ and β, are also affected, and the uncertainty thus introduced into their values is investigated in §4.5. Before presenting the PHALTEE results, however, it is worthwhile considering how Puls *et al.* (1996) used FORSOL to model Hα profiles.

4.2.1 Puls fitting procedure

The interactive fitting procedure employed by Puls *et al.* (1996) used, as an initial estimate, a value of β determined by the equivalent width, W_λ, of the Hα profile (note that throughout this work, W_λ is defined to be positive for net emission). The β-values (shown in Table 4.1) were based upon the results of an investigation of the influence of the steepness of the velocity law on the curve of growth. The mass-loss rate was then adjusted to optimally fit the data. This gave extremely good fits in many cases and a good determination of $\dot{M}$. The mass-loss rate and b_6^{∞} (He) were then modified to fit the almost β-independent high-velocity wings of the profile. For those objects with Hα in emission, it was possible to adjust β to fit the central emission peak, and thus derive the value of β in parallel with $\dot{M}$. There were instances, however, when even further modifications were required. This was most often the case with the P-Cygni profiles of supergiants whose equivalent widths are larger than zero. In these cases, it was necessary to modify one or more of: a) $b_3^{\rm in}$ (H); b) $b_4^{\rm in}$ (He); and c) b_6^{∞} (He).

Table 4.1: 'Standard' values of β used in initial model fits

W_λ (Å)	β
$W_\lambda < 0.5$	1.0
$0.5 \leq W_\lambda < 1.3$	0.8
$W_\lambda \geq 1.3$	0.75

4.2.2 Equivalent widths

The equivalent width of the Hα line was measured for each star in the sample, using the 'EW' command in DIPSO. This command uses a cursor to define two pairs of (x, y) points on a spectrum, between which the equivalent width is measured with respect to a linear 'continuum'. The equivalent widths listed (Table 4.2) are intended merely to serve as a means of obtaining the initial Puls *et al.* (1996) estimates for β (Table 4.1). These (unmodified) β-values can then be compared with those returned from the PHALTEE searches. For this reason, any (small) error on the measured value of W_λ is largely unimportant (errors may arise in instances of large, broad Hα emission, where it can be difficult to ascertain the boundaries of the profile).

4.2.3 Adopted parameters

Table 4.3 lists the adopted stellar and wind parameters used to model the Hα profiles. For multiple objects, the parameters refer to the primary (see Table 6.5 for the binary status of the stars). Where possible, data were taken from the literature, but in certain instances reasonable assumptions were made on the basis of spectral type and luminosity class. Additionally, in some cases, atmospheric parameters were calculated using the following equations:-

- The stellar luminosity, L, radius, R_*, and effective temperature, $T_{\rm eff}$, are related through:-

$$L = 4\pi R_*^2 \sigma T_{\rm eff}^4 \tag{4.1}$$

  where σ is the Stefan-Boltzmann constant.

- The stellar gravity, $\log g$, is given by:-

$$\log g = \log \left[\frac{GM}{R_*^2} \right] \tag{4.2}$$

  where G is the Gravitational constant and M is the stellar mass.

Table 4.2: Hα equivalent widths for the stellar sample

HD	Name	Observing run	W_λ (Å)	β (Puls)	HD	Name	Observing run	W_λ (Å)	β (Puls)
2905	κ Cas	INT00	2.3	0.75	169454	···	INT00	9.0	0.75
5394	γ Cas	INT00	27	0.75	169515	RY Sct	INT00	31	0.75
10125	···	WHT95	−1.0	1.0	169582	···	INT00	1.0	0.8
12323	···	WHT95	−2.7	1.0	188209	···	WHT95	−0.3	1.0
13745	V354 Per	WHT95	−0.7	1.0	189957	···	WHT95	−2.2	1.0
14947	···	INT00	5.4	0.75	190429A	···	INT00	2.7	0.75
15558	···	INT00	−0.2	1.0	190603	···	INT00	5.8	0.75
15570	···	INT00	7.6	0.75	191781	···	WHT95	0.6	0.8
16429	···	WHT95	−0.9	1.0	192281	···	INT00	−1.7	1.0
30614	α Cam	WHT95	2.8	0.75	193237	P Cyg	INT00	90	0.75
34078	AE Aur	WHT95	−2.9	1.0	194279	···	INT00	1.9	0.75
36486	δ Ori	WHT95	−1.5	1.0	194280	···	WHT95	−0.7	1.0
37742	ζ Ori	WHT95	0.9	0.8	195592	···	INT00	7.6	0.75
66811	ζ Pup	AAT00	2.5	0.75	197345	α Cyg	INT00	−1.2	1.0
105056	GS Mus	AAT92	5.2	0.75	201345	···	WHT95	−2.6	1.0
123008	···	AAT92	1.6	0.75	202124	···	WHT95	2.4	0.75
149038	μ Nor	AAT92	−0.8	1.0	206267A	···	INT00	−2.2	1.0
149404	V918 Sco	AAT92	6.0	0.75	207198	···	WHT95	−1.6	1.0
149757	ζ Oph	INT00	−2.2	1.0	209975	19 Cep	WHT95	−1.0	1.0
152003	···	AAT92	0.7	0.8	210809	···	WHT95	0.9	0.8
152147	···	AAT92	−1.1	1.0	210839	λ Cep	INT00	2.3	0.75
152249	···	AAT92	0.6	0.8	214680	10 Lac	WHT95	−3.0	1.0
152405	···	AAT92	−1.8	1.0	218195	···	WHT95	−2.3	1.0
152424	···	AAT92	2.9	0.75	218915	···	WHT95	−0.4	1.0
154368	···	AAT92	0.5	0.8	225160	···	WHT95	2.2	0.75
154811	···	AAT92	−0.7	1.0	···	Cyg OB2 No.5	INT00	13	0.75
156212	···	AAT92	−1.3	1.0	···	Cyg OB2 No.7	INT00	1.7	0.75
164794	9 Sgr	INT00	−1.9	1.0	···	Cyg OB2 No.8A	INT00	1.2	0.8
166734	···	INT00	8.0	0.75	···	Cyg OB2 No.9	INT00	4.8	0.75
167971	MY Ser	INT00	4.2	0.75	···	Cyg OB2 No.12	INT00	6.5	0.75
168112	···	INT00	−0.8	1.0	···	V433 Sct	INT00	5.7	0.75
168607	···	INT00	26	0.75	···	MWC 349	INT00	2200	0.75

NOTES: The equivalent width, W_λ, is defined to be positive for net emission and negative for net absorption (note that this is the opposite of normal practice). For reference, the third column gives the observing run during which the observation was obtained (an explanation of the acronyms used is provided with Table 2.5). The observation of HD 195592 from the WHT95 run has been omitted, as the Hα line is saturated (see Figure 2.5), thus making it impossible to obtain a value for the equivalent width.

Table 4.3: Adopted parameters for the Hα sample

HD	Name	Spectral type	$T_{\rm eff}$ (K)	$\log g$	R_* ($R_\odot$)	v_∞ (km s^{-1})	$v \sin i$ (km s^{-1})	Y(He)	$\log L$ ($L_\odot$)	Notes
2905	κ Cas	BC0.7Ia	24 000$^{\rm M99}$	2.70$^{\rm M99}$	37†	1105	91$^{\rm H97}$	0.09†	5.61$^{\rm M99}$	‡
5394	γ Cas	B0.5IVe	28 800$^{\rm B89}$	3.69†	10$^{\rm B89}$	1600$^{\rm B89}$	260$^{\rm B89}$	0.09†	4.80$^{\rm B89}$	‡
10125	···	O9.7II	32 500	3.3	17	1735$^{\rm P90}$	132	0.15	5.5	‡
12323	···	ON9V	36 000	4.1	5	1175	131	0.17	4.7	
13745	V354 Per	O9.7II((n))	33 000	3.3	13	1905	176	0.20	5.3	
14947	···	O5If+	40 000$^{\rm H00}$	3.67$^{\rm H00}$	15$^{\rm H00}$	2400$^{\rm H00}$	140$^{\rm H00}$	0.20$^{\rm H00}$	5.70$^{\rm H00}$	
15558	···	O5III(f)	46 500$^{\rm H00}$	3.86$^{\rm H00}$	19$^{\rm H00}$	2800$^{\rm H00}$	120$^{\rm H00}$	0.07$^{\rm H00}$	6.16$^{\rm H00}$	
15570	···	O4If+	42 000$^{\rm H00}$	3.80$^{\rm H00}$	22$^{\rm H00}$	2600$^{\rm H00}$	105$^{\rm H00}$	0.15$^{\rm H00}$	6.14$^{\rm H00}$	
16429	···	O9.5II((n))	35 000	3.4	25	1765$^{\rm P90}$	216	0.12	5.9	‡
30614	α Cam	O9.5Ia	33 000	3.1	20	1590	90	0.13	5.6	
34078	AE Aur	O9.5V	37 000	4.2	7	1505$^{\rm P90}$	30	0.09	4.9	‡
36486	δ Ori A	O9.5II	34 000	3.4	24	2060	126	0.10	5.8	
37742	ζ Ori	O9.7Ib	34 000	3.3	30	1860	109	0.10	6.0	
66811	ζ Pup	O4I(n)f	42 000$^{\rm P96}$	3.60$^{\rm P96}$	19$^{\rm P96}$	2485	219$^{\rm H97}$	0.12$^{\rm P96}$	6.0$^{\rm P96}$	
105056	GS Mus	ON9.7Iae	28 900$^{\rm H89}$	3.25†	23$^{\rm H89}$	680	68$^{\rm H97}$	0.09†	5.5†	‡
123008	···	ON9.7Iab	33 000$^{\rm S98}$	3.05$^{\rm S98}$	24$^{\rm S94}$	1250	98$^{\rm H97}$	0.15$^{\rm S98}$	5.8†	
149038	μ Nor	O9.7Iab	30 000$^{\rm S98}$	3.05$^{\rm S98}$	27$^{\rm L93}$	1830	86$^{\rm H97}$	0.09$^{\rm S98}$	5.7†	
149404	V918 Sco	O9Ia	32 500$^{\rm S98}$	2.95$^{\rm S98}$	34$^{\rm L93}$	2450	100$^{\rm H97}$	0.12$^{\rm S98}$	6.1†	
149757	ζ Oph	O9.5V	32 500$^{\rm P96}$	3.85$^{\rm P96}$	13$^{\rm P96}$	1505	372$^{\rm H97}$	0.19$^{\rm P96}$	5.22$^{\rm P96}$	
152003	···	O9.7Iab	30 500$^{\rm S98}$	3.00$^{\rm S98}$	25$^{\rm V96}$	2010	110$^{\rm H97}$	0.09$^{\rm S98}$	5.7†	
152147	···	O9.7Ib	30 000$^{\rm S98}$	3.15$^{\rm S98}$	25$^{\rm V96}$	1735$^{\rm P90}$	88$^{\rm H97}$	0.09$^{\rm S98}$	5.7†	‡
152249	···	OC9.5Iab	32 500$^{\rm S98}$	3.15$^{\rm S98}$	24$^{\rm H89}$	2010	99$^{\rm H97}$	0.08$^{\rm S98}$	5.8†	
152405	···	O9.7Ib–II	30 500$^{\rm S98}$	3.20$^{\rm S98}$	15$^{\rm H89}$	1860	77$^{\rm H97}$	0.09$^{\rm S98}$	5.2†	

Continued overleaf

HD	Name	Spectral type	$T_{\rm eff}$ (K)	$\log g$	R_* ($R_\odot$)	v_∞ (km s^{-1})	$v \sin i$ (km s^{-1})	Y(He)	$\log L$ ($L_\odot$)	Notes
152424	···	OC9.7Ia	31 500^{S98}	2.95^{S98}	33^{L93}	1760	86^{H97}	0.09^{S98}	6.0†	
154368	···	O9.5Iab	32 000^{S98}	3.00^{S98}	24^{S94}	1850	102^{H97}	0.13^{S98}	5.7†	
154811	···	OC9.7Iab	31 000^{S98}	3.10^{S98}	24^{S94}	1735^{P90}	125^{S94}	0.09^{S98}	5.7†	‡
156212	···	O9.7Iab	29 500^{S98}	3.15^{S98}	25^{V96}	1735^{P90}	88^{H97}	0.08^{S98}	5.6†	‡
164794	9 Sgr	O4:V((f))	46 400^{L93}	3.68^{L93}	16^{L93}	2750	70^{H97}	0.10^{L93}	6.02^{L93}	
166734	···	O7Ib(f) + O8–9I	35 500^{B89}	3.20†	38^{B89}	2600^{B89}	150^{B89}	0.09†	6.32^{B89}	‡
167971	MY Ser	O8Ib(f)p	35 500^{B89}	3.45†	22^{B89}	2185	97^{H97}	0.09†	5.86^{B89}	‡
168112	···	O5III(f)	46 800^{B89}	3.92†	16^{B89}	2700^{B89}	90^{B89}	0.09†	6.06^{B89}	‡
168607	···	B9Ia+	9 300^{V92}	1.0^{V92}	190†	140^{C80}	25†	0.18^{L95}	5.38^{V92}	‡
169454	···	B1Ia+	20 400^{B89}	2.35†	74^{B89}	850^{B89}	60^{B89}	0.18†	5.95^{B89}	‡
169515	RY Sct	B0V + O5.5V	24 000^{D01}	2.78^{D01}	34^{D01}	1500^{P90}	89^{H97}	0.09†	5.53†	‡
169582	···	O6If	41 700^{V96}	3.44^{V96}	21^{V96}	2300^{P90}	127^{H97}	0.09†	6.07^{V96}	‡
188209	···	O9.5Iab	33 000	3.1	19	1650	65	0.14	5.6	
189957	···	O9.5III	33 000	3.5	12	1505^{P90}	85	0.11	5.2	‡
190429A	···	O4If+	42 400^{L93}	3.48^{L93}	20^{L93}	1880	105^{H97}	0.15^{L93}	6.06^{L93}	
190603	···	B1.5Ia+	21 000^{M99}	2.35^{M99}	47†	485	79^{H97}	0.18†	5.58^{M99}	‡
191781	···	ON9.7Iab	31 000	3.1	20	1735^{P90}	89	0.16	5.5	‡
192281	···	O5Vn((f))p	46 800^{B89}	3.85†	19^{B89}	2700^{B89}	270^{B89}	0.09†	6.19^{B89}	‡
193237	P Cyg	B1Ia+	19 300^{PP90}	2.04^{PP90}	76^{PP90}	200^{PP90}	65^{B89}	0.18†	5.86^{PP90}	‡
194279	···	B1.5Ia	19 000^{M99}	2.15^{M99}	63†	750^{P90}	70^{M99}	0.18†	5.66^{M99}	‡
194280	···	OC9.7Iab	32 000	3.2	21	1735^{P90}	101	0.09	5.6	‡
195592	···	O9.7Ia	31 000	3.0	20	1735^{P90}	54	0.12	5.5	‡
197345	α Cyg	A2Ia	8 600^{A02}	1.3^{A02}	180^{A02}	225^{A02}	25^{A00}	0.07^{A00}	5.20^{A02}	
201345	···	ON9V	36 000	3.9	8	1425	109	0.14	4.9	
202124	···	O9.5Iab	34 000	3.2	19	1820	93	0.13	5.6	

Continued overleaf

HD	Name	Spectral type	$T_{\rm eff}$ (K)	$\log g$	R_* ($R_\odot$)	v_∞ (km s^{-1})	$v \sin i$ (km s^{-1})	Y(He)	$\log L$ ($L_\odot$)	Notes
206267A	···	O6.5V((f))	39 800$^{\rm B89}$	4.03†	9$^{\rm B89}$	2745	108$^{\rm H97}$	0.09†	5.26$^{\rm B89}$	‡
207198	···	O9Ib–II	36 000	3.4	14	2090	67	0.12	5.5	
209975	19 Cep	O9.5Ib	35 000	3.4	16	2010	69	0.09	5.5	
210809	···	O9Iab	36 000	3.3	20	2135	89	0.13	5.8	
210839	λ Cep	O6I(n)fp	37 000$^{\rm H00}$	3.55$^{\rm H00}$	19$^{\rm H00}$	2250$^{\rm H00}$	250$^{\rm H00}$	0.25$^{\rm H00}$	5.78$^{\rm H00}$	
214680	10 Lac	O9V	38 000	4.2	8	1140	30	0.09	5.1	
218195	···	O9III	37 000	3.6	11	2025	59	0.12	5.3	
218915	···	O9.5Iab	34 000	3.2	19	1830	68	0.10	5.6	
225160	···	O8Ib(f)	38 000	3.4	23	1530$^{\rm P90}$	109	0.15	6.0	‡
···	Cyg OB2 No.5	2× O7Ianfp	39 800$^{\rm B89}$	3.45†	34$^{\rm B89}$	2200$^{\rm B89}$	180$^{\rm B89}$	0.09†	6.43$^{\rm B89}$	‡
···	Cyg OB2 No.7	O3If	50 000$^{\rm H01}$	3.72$^{\rm H01}$	15$^{\rm H01}$	3080$^{\rm H01}$	105$^{\rm H01}$	0.18$^{\rm H01}$	6.08†	
···	Cyg OB2 No.8A	O5.5I(f)	44 000$^{\rm H01}$	3.51$^{\rm H01}$	28$^{\rm H01}$	2650$^{\rm H01}$	95$^{\rm H01}$	0.09$^{\rm H01}$	6.43†	
···	Cyg OB2 No.9	O5If	44 500$^{\rm H99}$	3.52$^{\rm H99}$	22$^{\rm H99}$	2200$^{\rm B89}$	135$^{\rm H99}$	0.09$^{\rm H99}$	6.24$^{\rm H99}$	
···	Cyg OB2 No.12	B5Ie	11 200$^{\rm B89}$	1.23†	338$^{\rm B89}$	1400$^{\rm S80}$	75$^{\rm B89}$	0.09†	6.21$^{\rm B89}$	‡
···	V433 Sct	B1.5Ia	19 200†	2.37†	59$^{\rm L88}$	1100$^{\rm L88}$	75$^{\rm H97}$	0.18†	5.62$^{\rm L88}$	‡
···	MWC 349	O9:III: + B0III	28 800$^{\rm L98}$	3.52†	17†	50$^{\rm A81}$	97$^{\rm H97}$	0.09†	5.23$^{\rm L98}$	‡

NOTES: References for spectral types are provided with Tables 2.1, 2.2, 2.3 and 2.4; sources for other data are provided on page 97. ‡ — Notes pertaining to individual stars start on page 97, after the sources.

SOURCES FOR TABLE 4.3:-

- $T_{\rm eff}$. Otherwise unreferenced values are from Siebert (1999). † — Calculated using Equation 4.1 and the listed values of R_* and $\log L$.
- $\log g$. Otherwise unreferenced values are from Siebert (1999). † — Calculated using Equation 4.2 and the listed value of R_*, together with a value for the stellar mass, M, obtained from the literature (see notes to individual stars).
- R_*. Otherwise unreferenced values are from Siebert (1999). † — Calculated using Equation 4.1 and the listed values of $T_{\rm eff}$ and $\log L$.
- v_∞. Otherwise unreferenced values are from Howarth *et al.* (1997*b*).
- $v \sin i$. Otherwise unreferenced values are from Siebert (1999). † — Assumed value.
- Y(He). Otherwise unreferenced values are from Siebert (1999). † — Assumed value.
- $\log L$. Otherwise unreferenced values are from Siebert (1999). † — Calculated using Equation 4.1 and the listed values of $T_{\rm eff}$ and R_*.

The parameters were obtained as detailed above unless indicated otherwise in Table 4.3. In these instances the sources are:-

C80 — Chentsov (1980); S80 — Souza and Lutz (1980); A81 — Altenhoff *et al.* (1981); L88 — Leitherer (1988*a*); B89 — Bieging *et al.* (1989); H89 — Howarth and Prinja (1989); P90 — Prinja *et al.* (1990); PP90 — Pauldrach and Puls (1990); V92 — van Genderen *et al.* (1992); L93 — Lamers and Leitherer (1993); S94 — Smith and Howarth (1994); L95 — Leitherer *et al.* (1995); P96 — Puls *et al.* (1996); V96 — Vacca *et al.* (1996); H97 — Howarth *et al.* (1997*b*); L98 — Lamers *et al.* (1998); S98 — Smith *et al.* (1998); H99 — Herrero *et al.* (1999); M99 — McErlean *et al.* (1999); A00 — Albayrak (2000); H00 — Herrero *et al.* (2000); D01 — Djurašević *et al.* (2001); H01 — Herrero *et al.* (2001); A02 — Aufdenberg *et al.* (2002).

‡ — Notes to individual stars:-

HD 2905 (κ Cas). A value of Y(He) = 0.09 is assumed on the basis that McErlean *et al.* (1999) noted the star's CN status was normal-to-moderate.

HD 5394 (γ Cas). A value of $M = 18\ M_\odot$ taken from Bieging *et al.* (1989) was used to calculate $\log g$. Y(He) is assumed to be solar.

HD 10125. v_∞ is the mean value for the star's spectral type and luminosity class, as given in Prinja *et al.* (1990).

HD 16429. v_∞ is the mean value for the star's spectral type and luminosity class, as given in Prinja *et al.* (1990).

HD 34078 (AE Aur). v_∞ is the mean value for the star's spectral type and luminosity class, as given in Prinja *et al.* (1990).

HD 105056 (GS Mus). A value of $M = 34\ M_\odot$ taken from Howarth and Prinja (1989) was used to calculate $\log g$. Y(He) is assumed to be solar.

HD 152147. v_∞ is the mean value for the star's spectral type and luminosity class, as given in Prinja *et al.* (1990). $v \sin i$ is the median value for the star's spectral type, as given in Howarth *et al.* (1997*b*).

HD 154811. v_∞ is the mean value for the star's spectral type and luminosity class, as given in Prinja *et al.* (1990).

HD 156212. v_∞ is the mean value for the star's spectral type and luminosity class, as given in Prinja *et al.* (1990). $v \sin i$ is the median value for the star's spectral type, as given in Howarth *et al.* (1997*b*).

HD 166734. A value of $M = 83\ M_\odot$ taken from Bieging *et al.* (1989) was used to calculate $\log g$. Y(He) is assumed to be solar.

HD 167971 (MY Ser). A value of $M = 50\ M_\odot$ taken from Bieging *et al.* (1989) was used to calculate $\log g$. Y(He) is assumed to be solar.

HD 168112. A value of $M = 78\ M_\odot$ taken from Bieging *et al.* (1989) was used to calculate $\log g$. Y(He) is assumed to be solar.

HD 168607. The value Y(He) = 0.18 reflects an adopted helium overabundance relative to solar of a factor of two. $v \sin i$ is assumed to be the same as for α Cyg ($v \sin i = 25$ km s^{-1} is a typical value for supergiants of this spectral type).

HD 169454. A value of $M = 45\ M_\odot$ taken from Bieging *et al.* (1989) was used to calculate $\log g$. Y(He) is assumed to be the same as for HD 168607 (reflecting the evolved nature of these objects).

HD 169515 (RY Sct). v_∞ is the mean value for the star's approximate spectral type and luminosity class, as given in Prinja *et al.* (1990); however, because no value was available for spectral type B0V, the value used is that for an O9V star. $v \sin i$ is the median value for the star's spectral type, as given in Howarth *et al.* (1997*b*), although the value used pertains to luminosity class I. Y(He) is assumed to be solar, in accordance with Djurašević *et al.* (2001).

HD 169582. v_∞ is the mean value for the star's spectral type and luminosity class, as given in Prinja *et al.* (1990). $v \sin i$ is the median value for the star's spectral type, as given in Howarth *et al.* (1997*b*). Y(He) is assumed to be solar.

HD 189957. v_∞ is the mean value for the star's spectral type and luminosity class, as given in Prinja *et al.* (1990).

HD 190603. A value of Y(He) = 0.18 is assumed on the basis that McErlean *et al.* (1999) noted the star's CN status was highly processed.

HD 191781. v_∞ is the mean value for the star's spectral type and luminosity class, as given in Prinja *et al.* (1990).

HD 192281. A value of $M = 93\ M_\odot$ taken from Bieging *et al.* (1989) was used to calculate $\log g$. Y(He) is assumed to be solar.

HD 193237 (P Cyg). Y(He) is assumed to be the same as for HD 168607 (reflecting the evolved nature of these objects).

HD 194279. v_∞ is the mean value for the star's spectral type and luminosity class, as given in Prinja *et al.* (1990). A value of Y(He) = 0.18 is assumed on the basis that McErlean *et al.* (1999) noted the star's CN status was highly processed.

HD 194280. v_∞ is the mean value for the star's spectral type and luminosity class, as given in Prinja *et al.* (1990).

HD 195592. v_∞ is the mean value for the star's spectral type and luminosity class, as given in Prinja *et al.* (1990).

HD 206267A. A value of $M = 32\ M_{\odot}$ taken from Bieging *et al.* (1989) was used to calculate $\log g$. Y(He) is assumed to be solar.

HD 225160. v_{∞} is the mean value for the star's spectral type and luminosity class, as given in Prinja *et al.* (1990).

Cyg OB2 No.5. A value of $M = 118\ M_{\odot}$ taken from Bieging *et al.* (1989) was used to calculate $\log g$. Y(He) is assumed to be solar.

Cyg OB2 No.12. A value of $M = 71\ M_{\odot}$ taken from Bieging *et al.* (1989) was used to calculate $\log g$. Y(He) is assumed to be solar.

V433 Sct. A value of $M = 30\ M_{\odot}$ taken from Leitherer (1988*a*) was used to calculate $\log g$. $v \sin i$ is the median value for the star's spectral type, as given in Howarth *et al.* (1997*b*). Y(He) is assumed to be the same as for HD 168607 (reflecting the evolved nature of these objects).

MWC 349. A value of $M = 34\ M_{\odot}$ taken from Thum *et al.* (1992) was used to calculate $\log g$. $v \sin i$ is the median value for the star's spectral type, as given in Howarth *et al.* (1997*b*), although the value used pertains to luminosity class I. Y(He) is assumed to be solar.

4.2.4 Profile fitting

Having collated the stellar and wind parameters required as input, PHALTEE was used to fit the observed Hα profiles optimally by searching a specified parameter space for the 'best' set of $\dot{M}$, β and b-values (the free, or 'floating', parameters). The subjective, interactive fitting procedure employed by Puls *et al.* (1996), and described in §4.2.1, was used to fit the profiles initially, to give an indication as to whether or not the results returned by PHALTEE (an objective, automated fitting procedure) were sensible. Where good interactive fits could be obtained, they were reproduced extremely well by PHALTEE, and in many instances PHALTEE improved upon the fits obtained from the interactive procedure. As an example, Figure 4.1 shows, for the star Cyg OB2 No.8A, the observed Hα profile (solid line), together with the 'best' interactive TGFORSOL fit (dotted line), and the results of the automated PHALTEE fit (dashed line). The profiles that proved most difficult to fit using the *interactive* method were supergiant profiles, which: i) exhibit a strong decline from emission maximum to absorption minimum (e.g. HD 14947); or ii) exhibit Hα in absorption, but with a central emission peak (e.g. HD 218915). For such objects, PHALTEE returned markedly improved profile fits. Appendix A contains the PHALTEE fits for the entire stellar sample.

The default search ranges for the free PHALTEE parameters are given in Table 4.4. The results of the sensitivity tests presented in §3.5, as well as the interactive fits, were

Figure 4.1: Comparison of the results of the interactive (Puls) and automated (PHALTEE) fitting procedures for Cyg OB2 No.8A. The observed Hα profile is represented by the solid line, the interactive fit by the dotted line, and the PHALTEE fit by the dashed line.

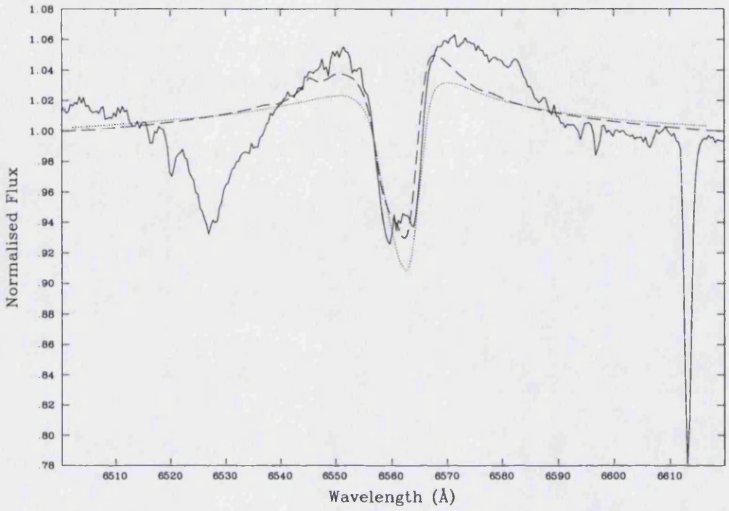

used to select the search ranges. Numerical problems meant that it was not possible to fit the Hα profile of MWC 349 ($W_\lambda \approx 2200$ Å) using PHALTEE, most probably due to the extreme nature of this object. MWC 349 is associated with a surrounding dense cloud of gas and dust (Baldwin *et al.*, 1973), but conflicting evidence regarding its age means that its evolutionary state is still unknown (e.g. Hamann and Simon, 1986, 1988; Cohen *et al.*, 1985). Lamers *et al.* (1998), in their refinement of the B[e]-type star classification system, designated MWC 349 as an unclassified star that exhibits the 'B[e] phenomenon'. In this analysis, the results of the interactive profile fit were used for MWC 349. This would seem justifiable, as the interactive fits for the other objects compare well with the PHALTEE results.

4.3 Results

The numerical results (i.e., the sets of 'best' parameters) from the PHALTEE searches conducted with *all* parameters ($\dot{M}$, β *and* the departure coefficients) floating are presented in Table 4.6 (the uncertainty introduced into the values of $\dot{M}$ and β by allowing the departure coefficients to float is investigated in §4.5). As an illustrative example, Figure 4.2 shows, for the star HD 14947, the observed Hα profile (solid line) and the optimum

Table 4.4: Search ranges for the free PHALTEE parameters

Parameter	Minimum	Maximum
$\dot{M}$ ($M_\odot$ yr^{-1})	1×10^{-8}	1×10^{-4}
β	0.3	2.0
$b_3^{\rm in}$ (H)	0.2	1.2
$b_4^{\rm in}$ (He)	1.35	6.0
b_6^{∞} (He)	2	35

TGFORSOL fit to the profile (dashed line). The absorption feature at 6527 Å is a He II line; the feature at 6612 Å is a diffuse interstellar band (DIB). The set of 'best' parameters is also given. This figure is reproduced in Appendix A, along with equivalent figures for each star in the sample. The combined results for each of the floated parameters are discussed individually in §4.3.1–§4.3.3. Intended to serve as an aid to interpretation, Table 4.5 gives the sample size of the Hα data by spectral type and luminosity class.

Table 4.5: Sample size of the Hα data by spectral type and luminosity class

		Luminosity class			
		All	I–II	III	IV–V
Spectral type	All	64	49	5	10
	Early O	11	7	2	2
	Late O	42	33	3	6
	B	11	9	···	2

NOTES: 'Early' O-type objects are defined to be those of spectral type O5.5 and earlier. The A2Ia star, α Cyg, has been binned with spectral type 'B'.

Figure 4.2: PHALTEE results for HD 14947, obtained with $\dot{M}$, β and the departure coefficients floating. The parenthesised values for the departure coefficients are the precomputed Puls values, calculated using the adopted and derived stellar parameters. The observed Hα profile is represented by the solid line and the optimum TGFORSOL fit to the profile by the dashed line.

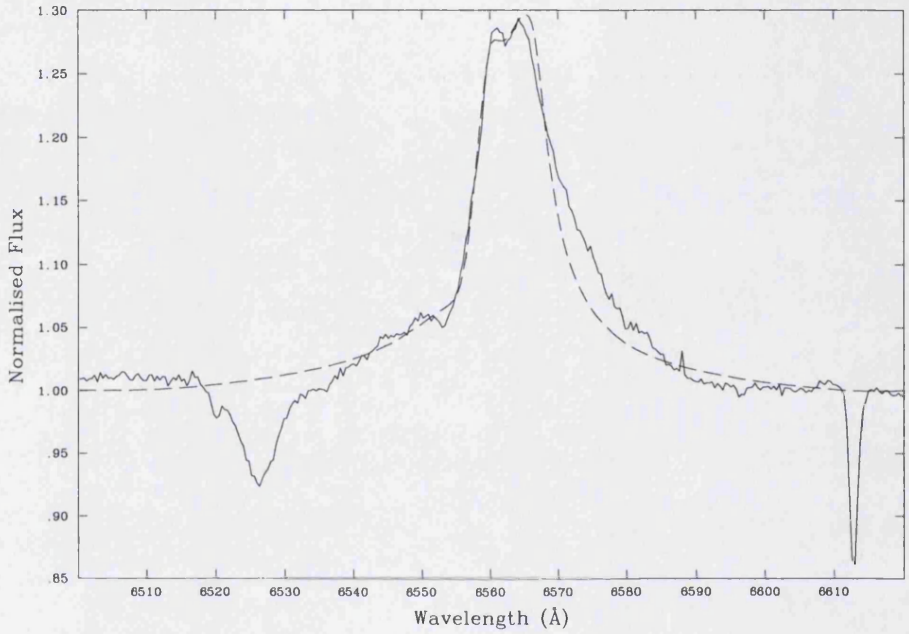

Spectral type:	O5If+	Y(He):	0.20
$T_{\rm eff}$:	40 000 K	$b_3^{\rm in}$ (H):	0.94 (1.20)
$\log g$:	3.67	$b_4^{\rm in}$ (He):	1.87 (1.35)
R_*:	15 $R_\odot$	b_6^{∞} (He):	10.2 (14.6)
v_∞:	2400 km s^{-1}	β:	1.32
$v \sin i$:	140 km s^{-1}	$\dot{M}$:	5.01×10^{-6} $M_\odot$ yr^{-1}

Table 4.6: Numerical results of the PHALTEE searches conducted with the departure coefficients floating

HD	Name	Spectral type	$\dot{M}$	β	$b_3^{\rm in}$ (H)	$b_4^{\rm in}$ (He)	b_6^{∞} (He)
			($10^{-6} M_\odot$ yr^{-1})				
2905†	κ Cas	BC0.7Ia	2.88	0.96	1.07	4.28	9.57
5394	γ Cas	B0.5IVe	2.10	2.00	1.20	1.36	2.01
10125	···	O9.7II	1.27	1.28	0.40	2.76	32.8
12323	···	ON9V	0.086	0.32	0.25	1.37	34.8
13745	V354 Per	O9.7II((n))	1.55	0.92	0.30	2.05	15.4
14947	···	O5If+	5.01	1.32	0.94	1.87	10.2
15558†	···	O5III(f)	7.21	0.89	1.08	2.81	7.17
15570	···	O4If+	12.7	1.02	1.08	1.83	17.3
16429	···	O9.5II((n))	3.89	0.79	0.88	2.80	17.9
30614	α Cam	O9.5Ia	3.04	1.04	0.93	2.81	24.7
34078	AE Aur	O9.5V	0.18	0.30	0.27	1.51	34.4
36486	δ Ori	O9.5II	2.64	1.07	0.88	3.20	35.0
37742	ζ Ori	O9.7Ib	5.81	0.98	0.80	2.30	28.3
66811	ζ Pup	O4I(n)f	5.00	1.55	0.43	2.39	34.3
105056	GS Mus	ON9.7Iae	2.12	0.83	1.19	3.72	2.64
123008	···	ON9.7Iab	2.34	1.43	0.68	3.81	27.9
149038	μ Nor	O9.7Iab	1.12	1.55	1.00	5.02	35.0
149404	V918 Sco	O9Ia	9.07	1.70	0.94	1.38	2.17
149757	ζ Oph	O9.5V	0.58	0.78	0.20	2.33	35.0
152003	···	O9.7Iab	2.51	1.45	0.82	3.59	16.9
152147	···	O9.7Ib	2.18	0.84	0.99	3.75	4.80
152249	···	OC9.5Iab	2.54	1.25	1.10	3.21	28.3
152405	···	O9.7Ib-II	0.62	0.79	1.10	6.00	6.70
152424	···	OC9.7Ia	5.08	1.39	0.63	3.99	34.8
154368	···	O9.5Iab	2.18	1.33	0.99	4.14	34.8
154811	···	OC9.7Iab	3.27	0.73	0.82	3.25	2.00
156212	···	O9.7Iab	1.52	1.03	0.90	4.80	2.42
164794†	9 Sgr	O4:V((f))	1.76	0.77	1.19	1.60	32.7
166734	···	O7Ib(f) + O8-9I	18.5	0.94	1.19	1.41	34.0
167971	MY Ser	O8Ib(f)p	6.13	0.98	0.94	2.85	23.0
168112†	···	O5III(f)	3.24	0.97	1.10	1.71	34.4
168607†	···	B9Ia+	2.24	0.54	1.14	5.98	2.01
169454†	···	B1Ia+	9.37	1.02	1.20	6.00	2.84
169515†	RY Sct	B0V + O5.5V	6.54	1.98	1.20	5.97	12.7
169582	···	O6If	5.27	1.02	1.03	2.16	25.1
188209	···	O9.5Iab	1.70	0.97	1.18	3.22	34.9
189957	···	O9.5III	0.38	0.53	1.19	2.85	34.7
190429A	···	O4If+	5.79	1.03	0.68	2.36	20.3
190603†	···	B1.5Ia+	2.51	0.66	1.20	5.90	6.14

Continued overleaf

HD	Name	Spectral type	$\dot{M}$	β	$b_3^{\rm in}$ (H)	$b_4^{\rm in}$ (He)	b_6^{∞} (He)
			($10^{-6} M_\odot$ yr^{-1})				
191781	···	ON9.7Iab	2.79	0.91	0.87	2.25	10.3
192281	···	O5Vn((f))p	4.36	1.58	0.40	2.14	2.17
193237†	P Cyg	B1Ia+	10.3	2.00	1.08	5.95	2.00
194279†	···	B1.5Ia	1.82	1.05	1.20	5.37	21.6
194280	···	OC9.7Iab	2.37	0.93	0.71	3.18	24.5
195592	···	O9.7Ia	3.00	1.56	1.20	2.56	24.8
197345†	α Cyg	A2Ia	0.38	0.50	0.98	5.53	3.76
201345	···	ON9V	0.32	0.30	1.01	5.12	34.7
202124	···	O9.5Iab	2.87	1.36	0.70	2.95	25.1
206267A	···	O6.5V((f))	0.19	1.57	1.12	1.37	27.9
207198	···	O9Ib-II	1.52	0.68	1.20	2.71	32.4
209975	19 Cep	O9.5Ib	1.81	0.80	1.17	2.70	34.9
210809	···	O9Iab	2.89	1.70	0.69	4.77	34.8
210839	λ Cep	O6I(n)fp	3.96	1.70	0.50	3.19	27.3
214680	10 Lac	O9V	0.16	0.31	0.91	1.84	35.0
218195	···	O9III	0.77	0.59	1.13	3.16	34.8
218915	···	O9.5Iab	1.73	1.02	1.17	2.88	34.9
225160	···	O8Ib(f)	4.46	1.11	1.03	3.28	20.8
···	Cyg OB2 No.5	2× O7Ianfp	25.1	1.22	0.27	2.74	8.57
···	Cyg OB2 No.7†	O3If	6.28	1.19	1.04	1.68	14.5
···	Cyg OB2 No.8A	O5.5I(f)	9.96	0.95	1.11	1.78	30.5
···	Cyg OB2 No.9†	O5If	8.51	1.22	0.67	2.54	29.2
···	Cyg OB2 No.12†	B5Ie	13.9	1.19	1.20	5.99	34.9
···	V433 Sct†	B1.5Ia	5.23	1.00	1.20	5.90	9.47
···	MWC 349‡	O9:III: + BOIII	7.2	0.75	1.20	1.35	10.0

NOTES: The observation of HD 195592 from the WHT95 run has been omitted from the analysis, as the Hα line is saturated (see Figure 2.5), and the results of the PHALTEE search are very sensitive to the peak emission in the line. † — The new photospheric grids calculated by Richard Townsend at UCL were used for these objects (see §3.2). ‡ — It was not possible to fit the Hα profile of MWC 349 using PHALTEE. For this object, the results of the interactive profile fit were used.

4.3.1 Mass-loss rates

The mass-loss rates returned by PHALTEE range from 8.6×10^{-8} $M_\odot$ yr^{-1} for HD 12323 (spectral type ON9V) to 2.51×10^{-5} $M_\odot$ yr^{-1} for Cyg OB2 No.5 (2× O7Ianfp). The mean mass-loss rate for the entire stellar sample is 2.55×10^{-6} $M_\odot$ yr^{-1}. Table 4.7 lists the mean values of derived $\dot{M}$ for different spectral types and luminosity classes. The mean mass-loss rate clearly decreases along the luminosity-class sequence, I–II → III → IV–V,

Table 4.7: Mean values of derived $\dot{M}$ (in 10^{-6} $M_{\odot}$ yr^{-1}) for different spectral types and luminosity classes

$\dot{M}$ (10^{-6} $M_{\odot}$ yr^{-1})		Luminosity class			
		All	I–II	III	IV–V
Spectral type	All	2.55	3.45	2.18	0.63
	Early O	5.62	7.61	5.23	3.06
	Late O	1.90	4.15	2.78	0.25
	B	3.54	5.40	···	4.32

NOTES: 'Early' O-type objects are defined to be those of spectral type O5.5 and earlier. The result for α Cyg (spectral type A2Ia) has been binned with those for spectral type 'B'.

for all spectral types. Indeed, stellar luminosity is known to be the dominant factor in determining $\dot{M}$ for radiatively-driven winds (Castor *et al.*, 1975; Kudritzki, 1998). For this reason, correlating mass-loss rate with luminosity is a standard way of displaying these data (e.g. Howarth and Prinja, 1989).

For hot, luminous stars, with radiatively-driven winds, mass-loss rate has been shown to increase as a function of luminosity such that:-

$$\dot{M} \propto L^{\alpha} \tag{4.3}$$

where $\alpha \approx 1.5$ (see, for example, Garmany and Conti, 1984; Howarth and Prinja, 1989). This correlation shows a large scatter, suggesting dependence upon additional parameters, such as the stellar radius and mass (see §7.2.1 for a discussion of the wind-momentum–luminosity relationship). Figure 4.3 shows the mass-loss rates returned by PHALTEE as a function of stellar luminosity. The solid line represents a least-squares fit to the data, with:-

$$\log \dot{M} = (1.07 \pm 0.09) \log L - (11.7 \pm 0.5) \tag{4.4}$$

where $\dot{M}$ is in $M_{\odot}$ yr^{-1} and L is in $L_{\odot}$. For comparison, and represented by the dashed line, also included is the empirical $\dot{M}$–L relationship of Howarth and Prinja (1989), who, using UV and radio data, found:-

$$\log \dot{M} = 1.69 \log L - 15.4 \tag{4.5}$$

for O-type stars, irrespective of luminosity class. The dependence of mass-loss rate on luminosity derived here is much shallower than that found by Howarth and Prinja (1989). When compared to their results, virtually every star in the sample with $\log L\ (L_{\odot}) \lesssim 6.0$ has a mass-loss rate that is high for its luminosity. Also, the mass-loss rates returned for the eleven B stars are (with two exceptions) all high, lying above the line of the $\dot{M}$–L relationship derived here.

Figure 4.4 again plots $\dot{M}$ as a function of stellar luminosity, but this time the B stars in the sample have been excluded (as before, the solid line represents a least-squares fit to all the data points). The relationship between mass-loss rate and luminosity thus obtained, for the O stars *only* is:-

$$\log \dot{M} = (1.15 \pm 0.09) \log L - (12.2 \pm 0.5) \tag{4.6}$$

With respect to this relationship, the mass-loss rates of the thirteen objects of luminosity class III–V are (with two exceptions) all low. To highlight this, the dashed line in Figure 4.4 is a least-squares fit to objects of luminosity class I–II *only*. The relationship for these objects is:-

$$\log \dot{M} = (1.04 \pm 0.09) \log L - (11.5 \pm 0.5) \tag{4.7}$$

Although they were derived by considering different subsets of the stellar sample, Correlations 4.4, 4.6 and 4.7 are approximately the same (to within roughly $\sim 1\sigma$ in both the slope and intercept). Thus, it might be reasonable to suggest that the presence of B stars in the sample is *not* responsible for the $\dot{M}$–L relationship derived here being very different to that of Howarth and Prinja (1989), who considered only O stars. One possibility is that PHALTEE systematically overestimates $\dot{M}$ for lower luminosity stars (which tend to have Hα in absorption), or else underestimates $\dot{M}$ for higher luminosity stars (which tend to have Hα in emission). The former of these two scenarios is explored further in §4.5.1.

Figure 4.5 shows how the derived value of $\dot{M}$ correlates with the equivalent width, W_{λ}, of the Hα profile. The general trend appears to be for $\dot{M}$ to increase with increasing W_{λ} (Hα). This correlation, however, is most marked for objects with W_{λ} (Hα) $\lesssim 0$ (i.e., objects with Hα in net absorption); mass-loss rates derived for these objects are sensitive to the choice of core photospheric spectrum.

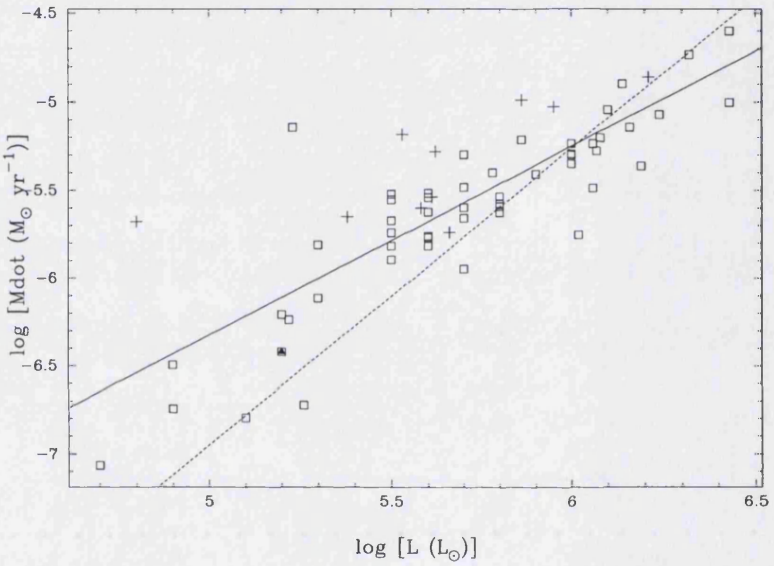

Figure 4.3: Mass-loss rate as a function of stellar luminosity for the entire Hα sample. '□' represent O stars, '+' represent B stars, and '▲' represents the A2Ia star, α Cyg. The solid line represents a least-squares fit to the data; for comparison, the dashed line corresponds to the empirical $\dot{M}$–L relationship found for O stars by Howarth and Prinja (1989).

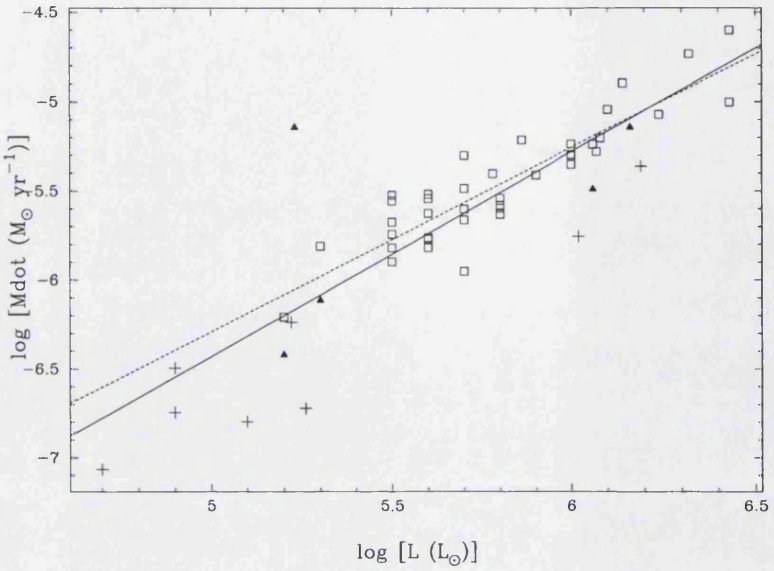

Figure 4.4: Mass-loss rate as a function of stellar luminosity for the 53 O stars in the sample. '□' represent luminosity class I–II, '▲' represent luminosity class III, and '+' represent luminosity class IV–V. The solid line represents a least-squares fit to all the data points. The dashed line represents a least-squares fit to objects of luminosity class I–II *only*.

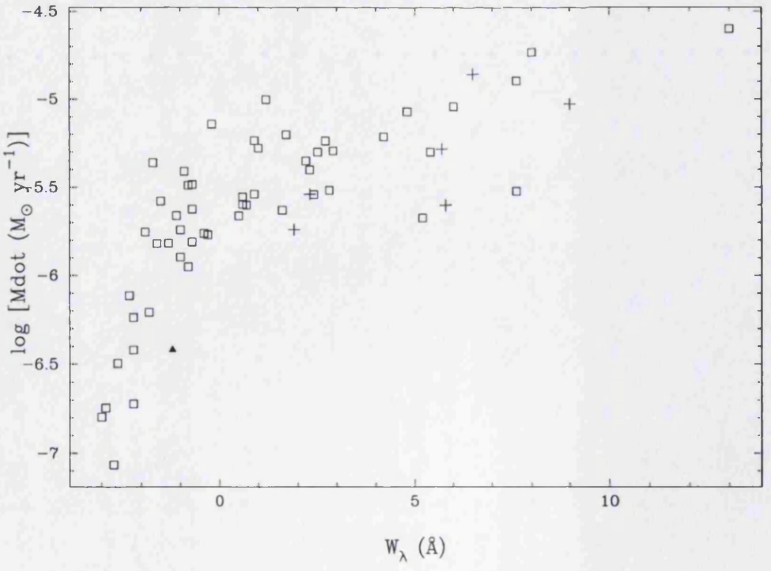

Figure 4.5: Mass-loss rate as a function of W_λ (Hα) for the stellar sample. '□' represent O stars, '+' represent B stars, and '▲' represents the A2Ia star, α Cyg. The five objects with W_λ (Hα) > 25 Å (see Table 4.2) lie outside the range of the plot.

4.3.2 Velocity law β-exponents

The β-values returned by PHALTEE range from 0.30 for HD 34078 and HD 201345 (spectral types O9.5V and ON9V, respectively), to 2.00 for γ Cas and P Cyg (B0IVe and B1Ia+, respectively). The mean β-value for the entire stellar sample is 1.06 (typical values for OB stars are observed to lie in the range $\beta = 0.7$–1.5; Kudritzki, 1998). Table 4.8 lists the mean values of derived β for different spectral types and luminosity classes. There is no obvious dependence on luminosity class, as is the case for $\dot{M}$; β may show a tendency towards higher values for supergiants, but, because of the small number of non-supergiants in the stellar sample (fifteen out of 64), it is difficult to be dogmatic.

Table 4.8: Mean values of derived β for different spectral types and luminosity classes

β		Luminosity class			
		All	I–II	III	IV–V
Spectral type	All	1.06	1.11	0.75	0.99
	Early O	1.14	1.18	0.93	1.18
	Late O	1.02	1.13	0.62	0.60
	B	1.17	0.99	···	1.99

NOTES: 'Early' O-type objects are defined to be those of spectral type O5.5 and earlier. The result for α Cyg (spectral type A2Ia) has been binned with those for spectral type 'B'.

The mean values of $\beta = 1.18$ and 1.13 returned by PHALTEE for early- and late-O supergiants, respectively, are somewhat higher than the results of Puls *et al.* (1996). Using FORSOL to estimate β-values in parallel with $\dot{M}$ for Galactic O-type supergiants with Hα in emission, they found an average value of $\beta \simeq 1.0$. This was rather higher than their result for lower luminosity objects. Herrero *et al.* (2001), using model fits to UV P-Cygni profiles, found (albeit from a small sample of seven Cyg OB2 stars) no such trend towards higher values for supergiants. Their values of $\beta = 0.7$–0.8 agree well with comparable studies by Groenewegen and Lamers (1989) and Haser (1995). The lower β-values are more in accord with radiation-driven wind theory, which predicts $\beta \approx 0.8$ for O-type stars (Friend and Abbott, 1986; Pauldrach *et al.*, 1986). There would appear to be a trend for higher β to be derived from Hα analyses than from UV. Kudritzki *et al.* (1999), using Hα to derive the slope of the velocity law, found β as high as 3.0 for a sample of Galactic B

and A supergiants.

Figure 4.6 shows how the derived value of β correlates with the equivalent width, W_λ, of the Hα profile. The general trend appears to be for β to increase with increasing W_λ (Hα), although there is more scatter (particularly for $W_\lambda \gtrsim 0$) than in the correlation between $\dot{M}$ and W_λ (Hα), shown in Figure 4.5. Because of the sensitivity of the central emission peak (if present) to the slope of the velocity law (see §3.5.1), those values of β derived from objects with Hα in emission (i.e., $W_\lambda \gtrsim 0$) can be considered to be the more accurate. In cases where the observed wind emission is negligible (i.e., the profile is essentially a photospheric absorption profile), the effect of β on the observed profile shape is much more difficult to gauge. This might help to explain the number of instances where the derived β is significantly lower than the canonical value of ~ 0.8 predicted by radiation-driven wind theory. Four extreme cases have derived values of $\beta \simeq 0.3$ (the lower boundary of the PHALTEE searches):-

- HD 12323 (ON9V): $\beta = 0.32$
- HD 34078 (O9.5V): $\beta = 0.30$
- HD 201345 (ON9V): $\beta = 0.30$
- HD 214680 (O9V): $\beta = 0.31$

Each one of these objects is a late-O type dwarf, showing Hα strongly in absorption. Because their Hα profiles are not very sensitive to changes in the slope of the velocity law, varying the velocity-law exponent has little impact on the profile shape. This allows β to take values appreciably different from 0.8–1.0, whilst still achieving 'good' model fits to the observed profiles.

4.3.3 Departure coefficients

Tables 4.9, 4.10 and 4.11 list, for different spectral types and luminosity classes, the mean values of the derived $b_3^{\rm in}$ (H), $b_4^{\rm in}$ (He) and b_6^{∞} (He) departure coefficients, obtained when their values are allowed to float.

The results obtained for $b_3^{\rm in}$ (H) and $b_4^{\rm in}$ (He) are rather higher for the B stars than for the O stars; those obtained for b_6^{∞} (He) are significantly lower. The precomputed default values of these departure coefficients, as used by Puls *et al.* (1996), are parameterised as a

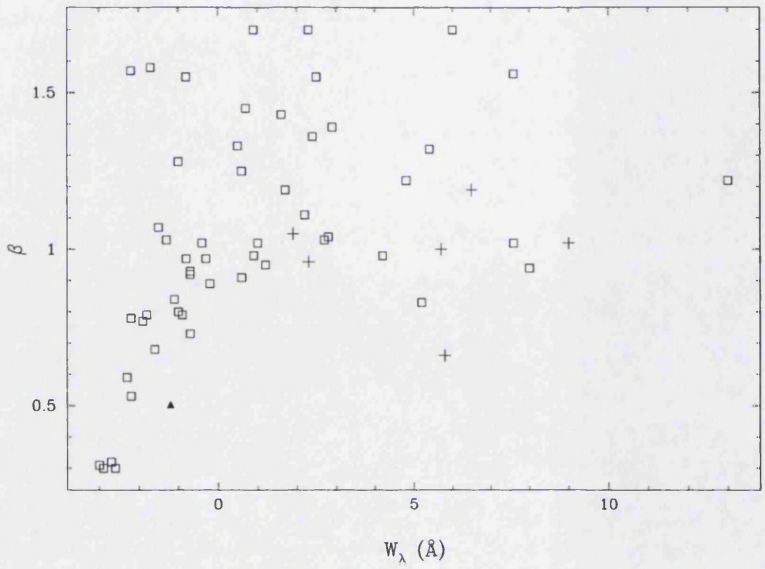

Figure 4.6: β as a function of W_λ (Hα) for the stellar sample. '□' represent O stars, '+' represent B stars, and '▲' represents the A2Ia star, α Cyg. The five objects with W_λ (Hα) > 25 Å (see Table 4.2) lie outside the range of the plot.

Table 4.9: Mean values of derived $b_3^{\rm in}$ (H) for different spectral types and luminosity classes

$b_3^{\rm in}$ (H)		Luminosity class			
		All	I–II	III	IV–V
Spectral type	All	0.92	0.93	1.14	0.78
	Early O	0.88	0.85	1.09	0.80
	Late O	0.87	0.88	1.17	0.64
	B	1.15	1.14	···	1.20

NOTES: 'Early' O-type objects are defined to be those of spectral type O5.5 and earlier. The result for α Cyg (spectral type A2Ia) has been binned with those for spectral type 'B'.

Table 4.10: Mean values of derived $b_4^{\rm in}$ (He) for different spectral types and luminosity classes

$b_4^{\rm in}$ (He)		Luminosity class			
		All	I–II	III	IV–V
Spectral type	All	3.24	3.49	2.38	2.46
	Early O	2.06	2.06	2.26	1.87
	Late O	3.01	3.19	2.45	2.26
	B	5.29	5.66	···	3.67

NOTES: 'Early' O-type objects are defined to be those of spectral type O5.5 and earlier. The result for α Cyg (spectral type A2Ia) has been binned with those for spectral type 'B'.

Table 4.11: Mean values of derived b_6^{∞} (He) for different spectral types and luminosity classes

b_6^{∞} (He)		Luminosity class			
		All	I–II	III	IV–V
Spectral type	All	21.4	20.3	24.2	25.1
	Early O	21.2	22.3	20.8	17.4
	Late O	24.5	22.7	26.5	33.6
	B	9.72	10.3	···	7.36

NOTES: 'Early' O-type objects are defined to be those of spectral type O5.5 and earlier. The result for α Cyg (spectral type A2Ia) has been binned with those for spectral type 'B'.

function of depth in the wind, using the results from a grid of unified model atmospheres for O-type stars. Thus, they may not be exactly applicable to the B stars in the sample. This may go some way towards explaining why the B-star departure coefficients differ significantly from their O-star counterparts when allowed to float.

A number of objects have optimised parameter values at, or very close to, the search boundaries, suggesting that they are not very well fit by PHALTEE, or that the profiles are insensitive to the parameter(s) concerned. Over the search ranges considered, the results of the sensitivity tests in §3.5 do indicate that the Hα profile is far less sensitive to changes in the departure coefficients than to changes in either $\dot{M}$ or β. Thus, comparatively larger changes in $b_3^{\rm in}$ (H), $b_4^{\rm in}$ (He) and b_6^{∞} (He), than in $\dot{M}$ or β, are required in order to obtain 'good' model fits (conversely, the departure coefficients are poorly constrained by the observations).

Specifically, many of the results for b_6^{∞} (He) are extremely close to the upper boundary of the PHALTEE searches; there are also significant differences between the values of b_6^{∞} (He) derived here and those obtained when the departure coefficients are held fixed at their precomputed default values (see Table 4.14). The results of sensitivity tests involving the departure coefficients (§3.5.10) indicate that the influence of b_6^{∞} (He) on the Hα profile is much less pronounced that that of either $b_3^{\rm in}$ (H) or $b_4^{\rm in}$ (He). The *shape* of the Hα profile is largely insensitive to changes in b_6^{∞} (He); i.e., increasing b_6^{∞} (He) increases the level of emission at *every* point. Increasing b_6^{∞} (He) from 5.0 to 25.0 (whilst holding all other parameters constant) results in a change in the level of emission of only $\sim$9% on average (measured at the same wavelength point). Thus, very large changes in b_6^{∞} (He) are required in order to achieve small improvements in the model fits.

It is worthwhile noting that whereas the line opacity scales with $\dot{M}^2$, it scales only linearly with the departure coefficients. Thus, the departure coefficients affect the determination of the mass-loss rate by a power of only 0.5.

4.4 Comparison with other studies

A small subset of nine stars is common to both the thesis sample and the sample of Puls *et al.* (1996). For these objects, Table 4.12 compares the results of this analysis with theirs. With the exception of ζ Oph (where the results differ by more than an order of magnitude), the agreement between the mass-loss rates is reasonable. With the

exception of ζ Oph and HD 209975, the mass-loss rates derived by Puls *et al.* (1996) are systematically higher than those derived in this work. Puls *et al.* (1996), however, adopted slightly different stellar and wind parameters to those used here. Therefore, also given, are the results obtained from PHALTEE when using the *same* (fixed) input parameters as adopted by them (i.e., $\dot{M}$, β and the departure coefficients were still allowed to float). There would appear to be no systematic improvement (or worsening) in agreement between the results by doing so. Differences in the derived $\dot{M}$ and β are probably more likely to be a consequence of differences in the observed Hα profiles than the small differences in adopted input parameters. Early-type supergiants (seven out of the nine objects in Table 4.12) are observed to be variable in their Hα emission on a dynamical timescale of days (e.g. Ebbets, 1982), with the most luminous objects exhibiting changes in Hα luminosity of as much as a factor of three on timescales of years. ζ Oph, a main-sequence object which generally shows Hα in absorption (e.g. see Appendix A), has, in the past, been observed to undergo episodes of double-peaked emission (e.g. Ebbets, 1981). This is associated with the Oe-star phenomenon (Conti and Leep, 1974), analogous to the Be-star phenomenon (see §1.3.2). The star was not, however, in emission at the time of the observations of Puls *et al.* (1996).

Table 4.12: A comparison (for the nine stars common to both studies) of the results from this work with those from Puls *et al.* (1996)

HD	Name	Spectral type	$\dot{M}$ (10^{-6} $M_\odot$ yr^{-1})			β		
			This work	Puls *et al.* (1996)	Using Puls param.	This work	Puls *et al.* (1996)	Using Puls param.
14947	···	O5If+	5.01	7.5	6.30	1.32	1.00	1.33
15558	···	O5III(f)	7.21	7.3	6.31	0.89	0.75	1.25
30614	α Cam	O9.5Ia	3.04	5.2	4.81	1.04	1.10	0.96
66811	ζ Pup	O4I(n)f	5.00	5.9	5.00	1.55	1.15	1.39
149757	ζ Oph	O9.5V	0.58	$\leq$ 0.03	0.59	0.78	1.00	0.79
207198	···	O9Ib-II	1.52	1.6	1.48	0.68	0.75	0.69
209975	19 Cep	O9.5Ib	1.81	0.9	1.77	0.80	0.80	0.75
210809	···	O9Iab	2.89	4.0	3.01	1.70	0.93	1.38
210839	λ Cep	O6I(n)fp	3.96	5.3	4.43	1.70	0.90	1.18

NOTE: The third column of values for $\dot{M}$ and β gives the results obtained from PHALTEE when using the *same* input parameters as those adopted by Puls *et al.* (1996).

Aufdenberg *et al.* (2002), using least-squares comparisons of synthetic spectral energy distributions with observations from UV to radio wavelengths, estimated the mass-loss rate of α Cyg to be $(8 \pm 3) \times 10^{-7}\ M_{\odot}\ \mathrm{yr}^{-1}$. This is a factor of two higher than the value of $3.8 \times 10^{-7}\ M_{\odot}\ \mathrm{yr}^{-1}$ derived here (although their Hα data suggested a mass-loss rate in the range $5 \times 10^{-7}\ M_{\odot}\ \mathrm{yr}^{-1} > \dot{M} > 10^{-7}\ M_{\odot}\ \mathrm{yr}^{-1}$). The fit to the H$\alpha$ profile of α Cyg achieved in this work, however, is rather poor (see Appendix A; Aufdenberg *et al.*, 2002, were also unable to satisfactorily fit the Hα profile of the star).

4.5 Errors

To investigate the effects on the derived values of $\dot{M}$ and β of floating the departure coefficients, Table 4.13 shows the results obtained when b_3^{in} (H), b_4^{in}(He) and b_6^{∞}(He) are *fixed* at their precomputed Puls values (see §3.4.2, in particular Tables 3.3 and 3.4), and only $\dot{M}$ and β are allowed to float. Table 4.14 gives the resultant change in $\dot{M}$ and β introduced by floating the departure coefficients.

Table 4.13: Numerical results of the PHALTEE searches conducted with the departure coefficients fixed

HD	Name	Spectral type	$\dot{M}$	β	$b_3^{\rm in}$ (H)	$b_4^{\rm in}$ (He)	b_6^{∞} (He)
			($10^{-6} M_\odot$ yr^{-1})				
2905†	κ Cas	BC0.7Ia	2.22	0.94	1.20	1.79	20.8
5394	γ Cas	B0.5IVe	1.94	2.00	1.20	1.35	13.1
10125	···	O9.7II	1.87	0.50	1.20	1.57	18.9
12323	···	ON9V	0.099	0.30	1.20	1.93	22.0
13745	V354 Per	O9.7II((n))	1.66	0.44	1.20	1.46	18.0
14947	···	O5If+	4.78	1.13	1.20	1.35	14.9
15558†	···	O5III(f)	5.91	0.84	1.20	1.35	17.0
15570	···	O4If+	13.4	0.93	1.20	1.35	12.9
16429	···	O9.5II((n))	3.92	0.56	1.20	1.47	18.0
30614	α Cam	O9.5Ia	3.26	0.83	1.20	1.35	16.2
34078	AE Aur	O9.5V	0.21	0.30	1.20	2.02	22.7
36486	δ Ori	O9.5II	3.39	0.65	1.20	1.69	20.0
37742	ζ Ori	O9.7Ib	7.30	0.65	1.20	1.35	16.4
66811	ζ Pup	O4I(n)f	7.50	0.72	1.20	1.35	14.7
105056	GS Mus	ON9.7Iae	1.37	1.07	1.20	1.35	15.0
123008	···	ON9.7Iab	2.51	0.93	1.20	1.37	17.2
149038	μ Nor	O9.7Iab	1.26	1.07	1.20	2.40	25.4
149404	V918 Sco	O9Ia	8.84	1.48	1.20	1.57	18.9
149757	ζ Oph	O9.5V	0.59	0.30	1.20	1.95	22.1
152003	···	O9.7Iab	2.62	1.01	1.20	1.90	21.7
152147	···	O9.7Ib	1.40	0.77	1.20	2.18	24.1
152249	···	OC9.5Iab	2.69	1.07	1.20	1.83	21.1
152405	···	O9.7Ib-II	0.055	1.46	1.20	3.00	25.4
152424	···	OC9.7Ia	5.63	0.95	1.20	1.50	18.3
154368	···	O9.5Iab	2.51	0.93	1.20	1.79	20.8
154811	···	OC9.7Iab	2.11	0.60	1.20	1.85	21.3
156212	···	O9.7Iab	0.84	0.84	1.20	2.55	25.4
164794†	9 Sgr	O4:V((f))	3.20	0.63	1.20	1.61	19.3
166734	···	O7Ib(f) + O8-9I	23.1	0.84	1.20	1.35	14.6
167971	MY Ser	O8Ib(f)p	6.31	0.83	1.20	1.35	15.9
168112†	···	O5III(f)	4.82	0.68	1.20	1.35	16.6
168607†	···	B9Ia+	0.52	2.00	1.20	2.38	25.4
169454†	···	B1Ia+	6.46	0.90	1.20	1.49	18.2
169515†	RY Sct	B0V + O5.5V	6.00	2.00	1.20	1.35	16.8
169582	···	O6If	5.47	0.85	1.20	1.35	16.8
188209	···	O9.5Iab	2.01	0.80	1.20	1.58	19.0
189957	···	O9.5III	0.41	0.51	1.20	2.13	23.6
190429A	···	O4If+	6.31	0.73	1.20	1.35	13.7
190603†	···	B1.5Ia+	1.73	0.59	1.20	1.35	17.0

Continued overleaf

HD	Name	Spectral type	$\dot{M}$	β	$b_3^{\rm in}$ (H)	$b_4^{\rm in}$ (He)	b_6^{∞} (He)
			($10^{-6} M_\odot$ yr^{-1})				
191781	···	ON9.7Iab	2.38	0.76	1.20	1.56	18.9
192281	···	O5Vn((f))p	4.38	0.70	1.20	1.55	18.7
193237†	P Cyg	B1Ia+	6.19	2.00	1.20	1.35	10.0
194279†	···	B1.5Ia	1.51	0.93	1.20	2.22	24.5
194280	···	OC9.7Iab	2.76	0.55	1.20	1.51	18.4
195592	···	O9.7Ia	3.11	1.45	1.20	1.37	17.3
197345†	α Cyg	A2Ia	0.22	0.62	1.20	3.00	25.4
201345	···	ON9V	0.38	0.30	1.20	1.68	19.9
202124	···	O9.5Iab	3.25	0.91	1.20	1.35	17.0
206267A	···	O6.5V((f))	0.36	1.14	1.20	2.56	25.4
207198	···	O9Ib-II	1.78	0.60	1.20	1.59	19.1
209975	19 Cep	O9.5Ib	2.26	0.65	1.20	1.52	18.5
210809	···	O9Iab	3.94	0.87	1.20	1.43	17.7
210839	λ Cep	O6I(n)fp	4.40	0.96	1.20	1.35	17.0
214680	10 Lac	O9V	0.18	0.30	1.20	1.99	22.5
218195	···	O9III	0.87	0.53	1.20	1.81	20.9
218915	···	O9.5Iab	2.03	0.88	1.20	1.68	19.9
225160	···	O8Ib(f)	3.99	1.02	1.20	1.35	15.9
···	Cyg OB2 No.5	2× O7Ianfp	25.6	0.91	1.20	1.35	11.4
···	Cyg OB2 No.7†	O3If	6.73	0.97	1.20	1.35	15.1
···	Cyg OB2 No.8A	O5.5I(f)	12.3	0.77	1.20	1.35	15.9
···	Cyg OB2 No.9†	O5If	11.3	0.78	1.20	1.35	12.5
···	Cyg OB2 No.12†	B5Ie	13.7	1.12	1.20	3.00	25.4
···	V433 Sct†	B1.5Ia	4.12	0.82	1.20	1.85	21.3
···	MWC 349‡	O9:III: + B0III	7.2	0.75	1.20	1.35	10.0

NOTES: The observation of HD 195592 from the WHT95 run has been omitted from the analysis, as the Hα line is saturated (see Figure 2.5), and the results of the PHALTEE search are very sensitive to the peak emission in the line. † — The new photospheric grids calculated by Richard Townsend at UCL were used for these objects (see §3.2). ‡ — It was not possible to fit the Hα profile of MWC 349 using PHALTEE. For this object, the results of the interactive profile fit were used.

Table 4.14: Change in the numerical results of the PHALTEE searches introduced by floating the departure coefficients

HD	Name	Spectral type	$\Delta \log \dot{M}$	$\Delta\beta$	$\Delta b_3^{\rm in}$ (H)	$\Delta b_4^{\rm in}$ (He)	Δb_6^{∞} (He)
2905†	κ Cas	BC0.7Ia	0.113	0.02	−0.13	2.49	−11.2
5394	γ Cas	B0.5IVe	0.034	0.00	0.00	0.01	−11.1
10125	···	O9.7II	−0.168	0.78	−0.80	1.19	13.9
12323	···	ON9V	−0.061	0.02	−0.95	−0.56	12.8
13745	V354 Per	O9.7II((n))	−0.030	0.48	−0.90	0.59	−2.60
14947	···	O5If+	0.020	0.19	−0.26	0.52	−4.70
15558†	···	O5III(f)	0.086	0.05	−0.12	1.46	−9.83
15570	···	O4If+	−0.023	0.09	−0.12	0.48	4.40
16429	···	O9.5II((n))	−0.003	0.23	−0.32	1.33	−0.10
30614	α Cam	O9.5Ia	−0.030	0.21	−0.27	1.46	8.50
34078	AE Aur	O9.5V	−0.067	0.00	−0.93	−0.51	11.7
36486	δ Ori	O9.5II	−0.109	0.42	−0.32	1.51	15.0
37742	ζ Ori	O9.7Ib	−0.099	0.33	−0.40	0.95	11.9
66811	ζ Pup	O4I(n)f	−0.176	0.83	−0.77	1.04	19.6
105056	GS Mus	ON9.7Iae	0.190	−0.24	−0.01	2.37	−12.36
123008	···	ON9.7Iab	−0.030	0.50	−0.52	2.44	10.7
149038	μ Nor	O9.7Iab	−0.051	0.48	−0.20	2.62	9.60
149404	V918 Sco	O9Ia	0.011	0.22	−0.26	−0.19	−16.73
149757	ζ Oph	O9.5V	−0.007	0.48	−1.00	0.38	12.9
152003	···	O9.7Iab	−0.019	0.44	−0.38	1.69	−4.80
152147	···	O9.7Ib	0.192	0.07	−0.21	1.57	−19.3
152249	···	OC9.5Iab	−0.025	0.18	−0.10	1.38	7.20
152405	···	O9.7Ib-II	1.052	−0.67	−0.10	3.00	−18.7
152424	···	OC9.7Ia	−0.045	0.44	−0.57	2.49	16.5
154368	···	O9.5Iab	−0.061	0.40	−0.21	2.35	14.0
154811	···	OC9.7Iab	0.190	0.13	−0.38	1.40	−19.3
156212	···	O9.7Iab	0.258	0.19	−0.30	2.25	−23.0
164794†	9 Sgr	O4:V((f))	−0.260	0.14	−0.01	−0.01	13.4
166734	···	O7Ib(f) + O8-9I	−0.096	0.10	−0.01	0.06	19.4
167971	MY Ser	O8Ib(f)p	−0.013	0.15	−0.26	1.50	7.10
168112†	···	O5III(f)	−0.173	0.29	−0.10	0.36	17.8
168607†	···	B9Ia+	0.634	−1.46	−0.06	3.60	−23.4
169454†	···	B1Ia+	0.162	0.12	0.00	4.51	−15.36
169515†	RY Sct	B0V + O5.5V	0.037	−0.02	0.00	4.62	−4.10
169582	···	O6If	−0.016	0.17	−0.17	0.81	8.30
188209	···	O9.5Iab	−0.073	0.17	−0.02	1.64	15.9
189957	···	O9.5III	−0.033	0.02	−0.01	0.72	11.1
190429A	···	O4If+	−0.037	0.30	−0.52	1.01	6.60
190603†	···	B1.5Ia+	0.162	0.07	0.00	4.55	−10.86

Continued overleaf

HD	Name	Spectral type	$\Delta \log \dot{M}$	$\Delta\beta$	$\Delta b_3^{\rm in}$ (H)	$\Delta b_4^{\rm in}$ (He)	Δb_6^{∞} (He)
191781	···	ON9.7Iab	0.069	0.15	−0.33	0.69	−8.60
192281	···	O5Vn((f))p	−0.002	0.88	−0.80	0.59	−16.53
193237†	P Cyg	B1Ia+	0.221	0.00	−0.12	4.60	−8.00
194279†	···	B1.5Ia	0.081	0.12	0.00	3.15	−2.90
194280	···	OC9.7Iab	−0.066	0.38	−0.49	1.67	6.10
195592	···	O9.7Ia	−0.016	0.11	0.00	1.19	7.50
197345†	α Cyg	A2Ia	0.237	−0.12	−0.22	2.53	−21.64
201345	···	ON9V	−0.075	0.00	−0.19	3.44	14.80
202124	···	O9.5Iab	−0.054	0.45	−0.50	1.60	8.10
206267A	···	O6.5V((f))	−0.278	0.43	−0.08	−1.19	2.50
207198	···	O9Ib-II	−0.069	0.08	0.00	1.12	13.3
209975	19 Cep	O9.5Ib	−0.096	0.15	−0.03	1.18	16.4
210809	···	O9Iab	−0.135	0.83	−0.51	3.34	17.1
210839	λ Cep	O6I(n)fp	−0.046	0.74	−0.70	1.84	10.3
214680	10 Lac	O9V	−0.051	0.01	−0.29	−0.15	12.5
218195	···	O9III	−0.053	0.06	−0.07	1.35	13.9
218915	···	O9.5Iab	−0.069	0.14	−0.03	1.20	15.0
225160	···	O8Ib(f)	0.048	0.09	−0.17	1.93	4.90
···	Cyg OB2 No.5	2× O7Ianfp	−0.009	0.31	−0.93	1.39	−2.83
···	Cyg OB2 No.7†	O3If	−0.030	0.22	−0.16	0.33	−0.60
···	Cyg OB2 No.8A	O5.5I(f)	−0.092	0.18	−0.09	0.43	14.6
···	Cyg OB2 No.9†	O5If	−0.123	0.44	−0.53	1.19	16.7
···	Cyg OB2 No.12†	B5Ie	0.006	0.07	0.00	2.99	9.50
···	V433 Sct†	B1.5Ia	0.104	0.18	0.00	4.05	−11.83
···	MWC 349‡	O9:III: + B0III	···	···	···	···	···

NOTES: In column 4, a *negative* value of $\Delta \log \dot{M}$ implies that a *smaller* value of $\dot{M}$ was obtained when the departure coefficients were floated. † — The new photospheric grids calculated by Richard Townsend at UCL were used for these objects (see §3.2). ‡ — It was not possible to fit the Hα profile of MWC 349 using PHALTEE. For this object, the results of the interactive profile fit were used. Hence the absence of error information.

Figures 4.7–4.11 plot, for all 64 stars in the sample, the change introduced into the derived values of $\dot{M}$, β, $b_3^{\rm in}$ (H), $b_4^{\rm in}$ (He) and b_6^{∞} (He) by allowing the departure coefficients to float. The solid lines on the plots indicate the mean change introduced, and the dashed lines indicate the $\pm$ 1σ levels. The spectral types of the stars are indicated, with the results for α Cyg being binned with those for spectral type 'B'. The 'Sample' number on the abscissae of the plots is simply a label corresponding to the position of the star in Table 4.14.

(a) $\dot{M}$. The mean value of $\Delta \log \dot{M} = 0.015 \pm 0.189$. The majority of objects have neg-

ative $\Delta \log \dot{M}$, but the very large *positive* changes obtained for the stars HD 152405 (O9.7Ib–II) and HD 168607 (B9Ia+) have raised the mean. These stars have values of $\Delta \log \dot{M} = 1.052$ and 0.634, respectively: more than 5σ and 3σ away from mean, respectively. The B stars all exhibit positive, and on average, larger, $\Delta \log \dot{M}$ than the O stars. All except one B star (Cyg OB2 No.12) have $\Delta \log \dot{M}$ greater (i.e., more positive) than the mean.

(b) **Velocity law β-exponent.** The mean value of $\Delta\beta = 0.19 \pm 0.33$. In direct contrast to the results obtained for $\Delta \log \dot{M}$, every B star has a value of $\Delta\beta$ less (i.e., less positive) than the mean. The stars HD 152405 and HD 168607 have very large *negative* changes of $\Delta\beta = -0.67$ and -1.46, respectively: more than 2.5σ and 5σ away from mean, respectively. This might suggest that large positive changes in $\dot{M}$ are being compensated for by large negative changes in β. Figure 4.12 plots $\Delta\beta$ as a function of $\Delta\dot{M}$: the correlation coefficient is -0.47 (with a probability of arising by chance of less than 0.1%, for a sample of this size). Is there a correlation between $\dot{M}$ and β? This idea will be commented on in §4.5.1.

(c) **Departure coefficients.** The mean value of $\Delta b_3^{\rm in} = -0.28 \pm 0.29$. The PHALTEE search ranges were such that $b_3^{\rm in}$ (H) was only allowed to vary to values *lower* than the default (Puls *et al.*, 1996) value of 1.20. The B stars in particular exhibit quite small changes in $b_3^{\rm in}$ (H): several B stars (along with several of the O stars) have optimised parameter values of, or very near to, 1.20 (i.e., $\Delta b_3^{\rm in} \simeq 0$), even when *all* parameters are allowed to float.

The mean value of $\Delta b_4^{\rm in} = 1.56 \pm 1.33$. There is, in general, a larger (positive) change in $b_4^{\rm in}$ (He) for the B stars than for the O stars.

The mean value of $\Delta b_6^{\infty} = 2.67 \pm 12.60$. The large error on this value suggests that b_6^{∞} (He) is not very well constrained by the observations. The B stars all (with one exception) show negative changes in b_6^{∞} (He). This coincides with the general increase in $\dot{M}$ seen for these stars, when all parameters are allowed to float. Interestingly, the only B star which exhibits a positive change in b_6^{∞} (He), Cyg OB2 No.12 ($\Delta b_6^{\infty} = 9.50$), also exhibits the smallest positive change in $\dot{M}$ ($\Delta \log \dot{M} = 0.006$). Perhaps allowing the departure coefficients to float enables $\dot{M}$ to increase by permitting a compensatory decrease in b_6^{∞} (He). Indeed, sensitivity tests show that an increase in either $\dot{M}$ or b_6^{∞} (He) results in an increase in emission over the whole of

the Hα profile (see §3.5.3 and §3.5.9, respectively). Incidences of positive Δb_6^∞ (He) seem to coincide with incidences of negative $\Delta \log \dot{M}$, and vice versa. Figure 4.13 plots b_6^∞ (He) as a function of $\Delta \log \dot{M}$: the correlation coefficient is -0.81 (with a probability of arising by chance of less than 0.1%, for a sample of this size).

When all parameters are allowed to float, the changes in the departure coefficients are much larger than the changes in either $\dot{M}$ or β. The departure coefficients can vary by a comparatively large amount in order to achieve an 'optically' (i.e., by eye) good fit to an Hα profile, suggesting that they are rather poorly constrained by the observations. It is worthwhile noting that the values of $b_4^{\rm in}$ (He) and b_6^∞ (He) depend upon $\dot{M}$ (which might in turn be affected by β; see above and §4.5.1) through the density-sensitive quantity, $D = \dot{M}/(R_* v_\infty)^{1.5}$ (see Table 3.4). The advantage of using an efficient search algorithm, like PIKAIA (see §4.1.1), is that it takes care of all the dependencies and correlations between parameters in n-dimensional search space.

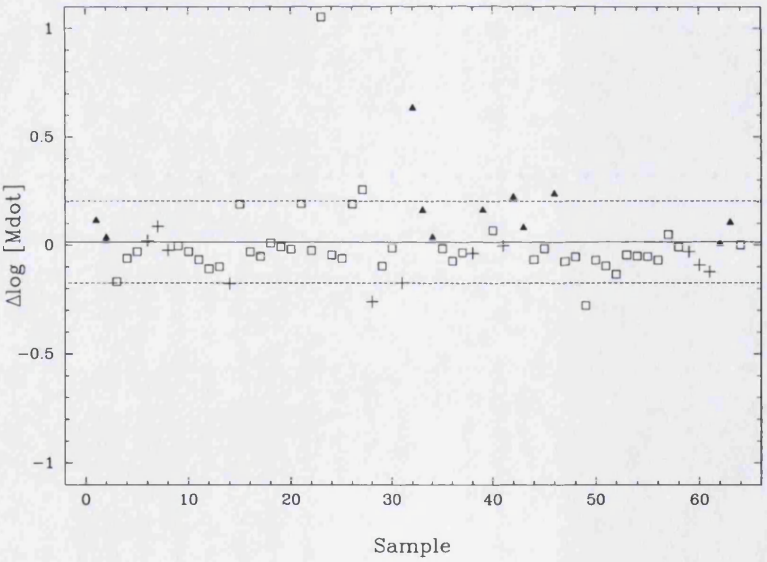

Figure 4.7: The change introduced into $\log \dot{M}$ when the b_i are allowed to float. '+' represent early O-type stars, '□' represent late O-type stars, and '▲' represent B-type stars. The solid line indicates the mean value of $\Delta \log \dot{M}$, and the dashed lines indicate the $\pm$ 1σ levels.

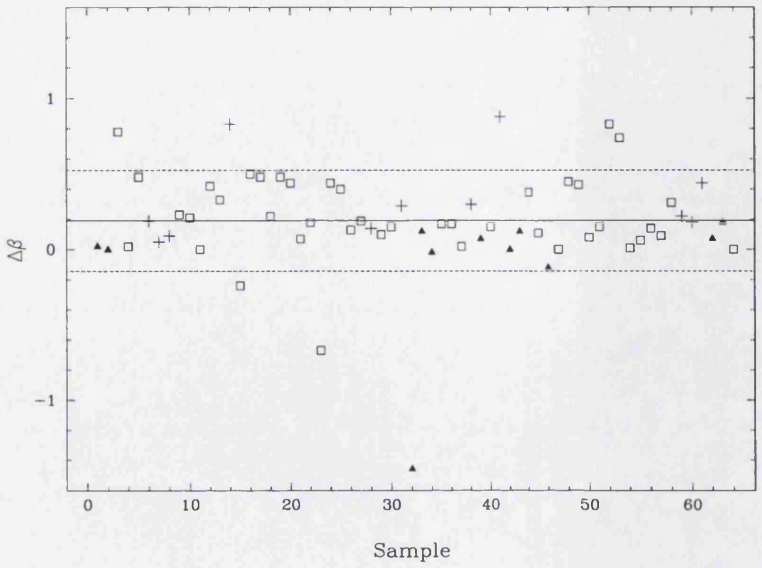

Figure 4.8: The change introduced into β when the b_i are allowed to float. '+' represent early O-type stars, '□' represent late O-type stars, and '▲' represent B-type stars. The solid line indicates the mean value of $\Delta\beta$, and the dashed lines indicate the $\pm$ 1σ levels.

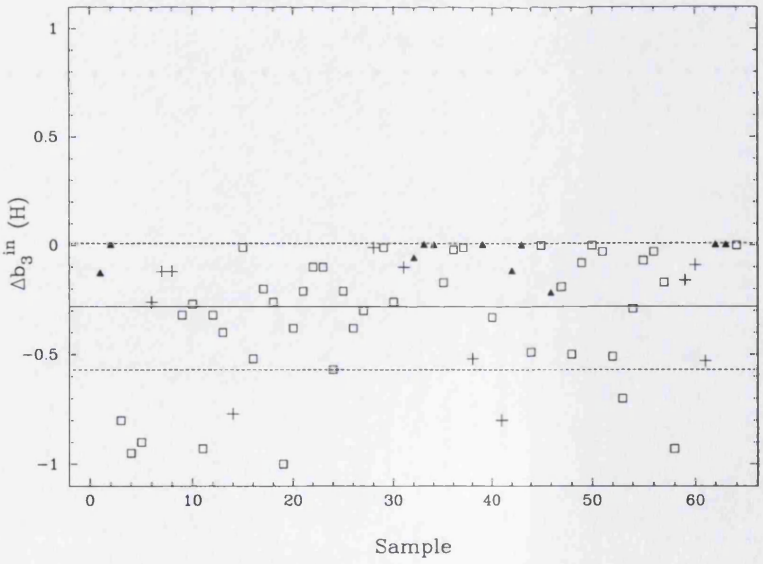

Figure 4.9: The change introduced into $b_3^{\rm in}$ (H) when the b_i are allowed to float. '+' represent early O-type stars, '□' represent late O-type stars, and '▲' represent B-type stars. The solid line indicates the mean value of $\Delta b_3^{\rm in}$ (H), and the dashed lines indicate the $\pm$ 1σ levels.

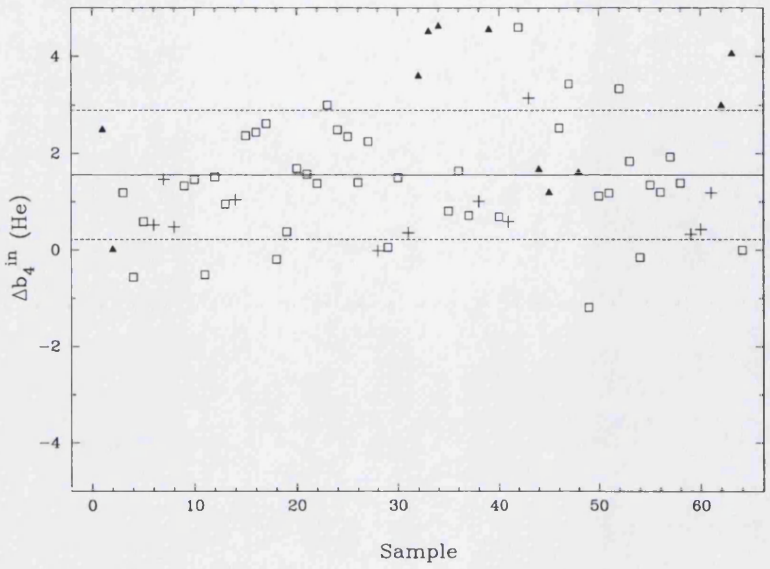

Figure 4.10: The change introduced into $b_4^{\rm in}$ (He) when the b_i are allowed to float. '+' represent early O-type stars, '□' represent late O-type stars, and '▲' represent B-type stars. The solid line indicates the mean value of $\Delta b_4^{\rm in}$ (He), and the dashed lines indicate the $\pm$ 1σ levels.

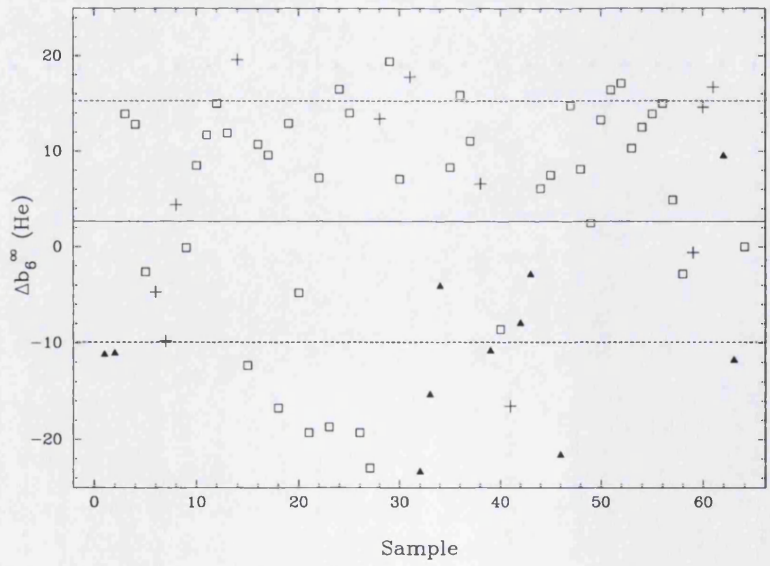

Figure 4.11: The change introduced into b_6^{∞} (He) when the b_i are allowed to float. '+' represent early O-type stars, '□' represent late O-type stars, and '▲' represent B-type stars. The solid line indicates the mean value of Δb_6^{∞} (He), and the dashed lines indicate the $\pm$ 1σ levels.

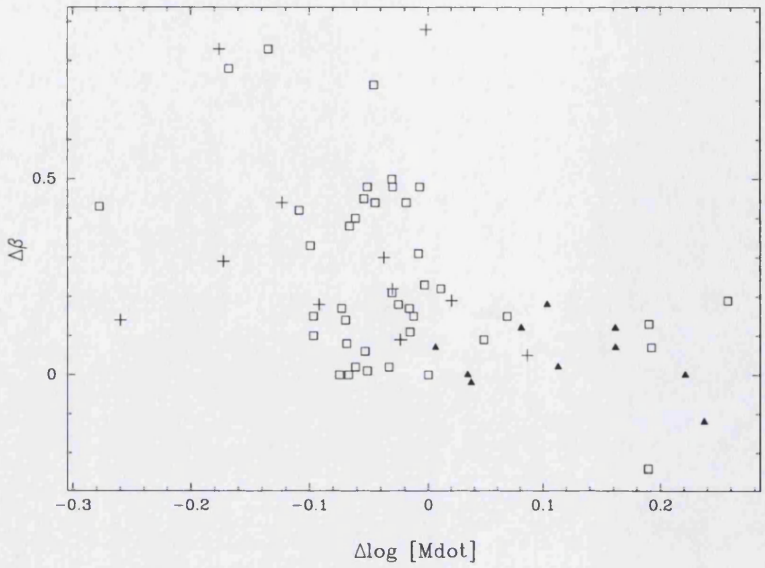

Figure 4.12: The correlation between $\Delta\beta$ and $\Delta \log \dot{M}$. '+' represent early O-type stars, '□' represent late O-type stars, and '▲' represent B-type stars. HD 152405 and HD 168607, with $\Delta \log \dot{M} > 0.6$ lie outside the range of the plot.

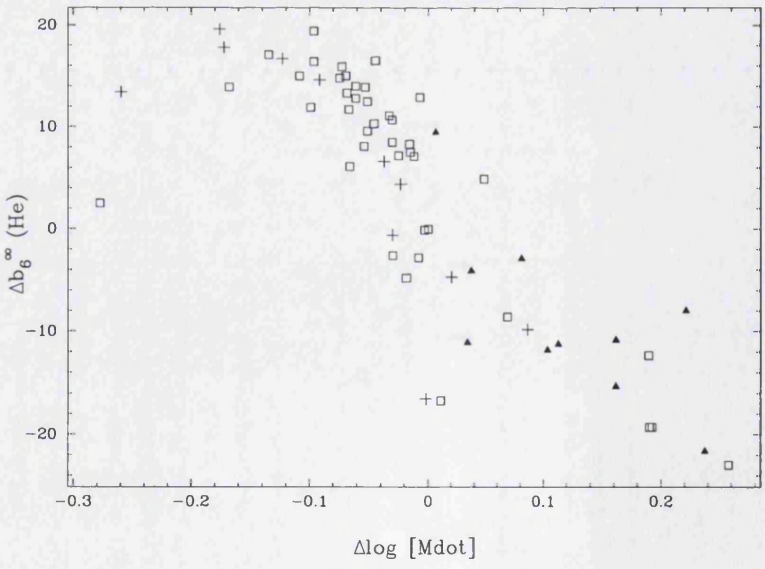

Figure 4.13: The correlation between Δb_6^∞ (He) and $\Delta \log \dot{M}$. '+' represent early O-type stars, '□' represent late O-type stars, and '▲' represent B-type stars. HD 152405 and HD 168607, with $\Delta \log \dot{M} > 0.6$ lie outside the range of the plot.

4.5.1 The correlation between $\dot{M}$ and β

Figure 4.14 shows how the derived value of β correlates with that of $\dot{M}$. The general trend is for β to increase with increasing $\dot{M}$. This result might be expected, as supergiants, which tend to have higher mass-loss rates, also tend to exhibit higher β (see Tables 4.7 and 4.8, respectively). This, however, may or may not be a physical correlation, as the objects to the lower left of the plot have weak Hα emission, and those to the upper right, strong Hα emission (see Figures 4.5 and 4.6 for how W_λ (Hα) correlates with $\dot{M}$ and β, respectively). Because of the sensitivity of the emission peak of the profile to the velocity law, for stars with strong Hα emission, it is possible to determine β in parallel with $\dot{M}$. For stars with weak (or no) Hα emission, however, there is little sensitivity to β, and the additional, complicating factor of sensitivity to the core photospheric spectrum.

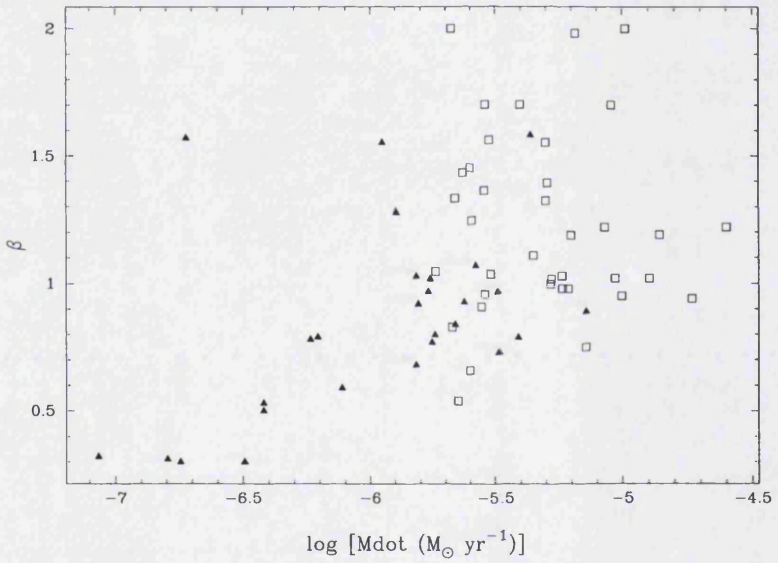

Figure 4.14: β as a function of mass-loss rate for the Hα sample. '□' represent stars with Hα in emission and '▲' represent stars with Hα in absorption.

Let us examine the effects of varying $\dot{M}$ and β for just such an object. Let us consider the star HD 12323 (ON9V). This object has Hα strongly in absorption (i.e., we are essentially seeing the photospheric absorption profile; see Figure 4.16). The line profile is therefore insensitive to changes in the slope of the velocity law: the change in emission with respect to β, $\mathrm{d}I(\lambda)/\mathrm{d}\beta$, is small, meaning that a *large* change in β is required to produce a *small* change in $I(\lambda)$. The Hα profile can therefore provide only limited information on

the value of β. As mentioned in §4.3.2, this can allow the velocity-law exponent to take values that lie outside the 'expected' range of $\beta = 0.7$–1.5 (Kudritzki, 1998). Indeed, when the departure coefficients are allowed to float, the *very* low value of $\beta = 0.32$ is returned for HD 12323. Whilst a low value of β can achieve a 'good' model fit, it is of interest to see how the returned mass-loss rate is affected.

Figure 4.15 shows, for the star HD 12323, the effect on the estimated value of $\dot{M}$, as (fixed) β is increased, in increments of 0.1, from 0.3 to 2.0, with all other parameters held constant. As β is increased, the mass-loss rate required to fit the Hα profile decreases. The reason for this is straightforward: larger β means a more slowly accelerating wind, and hence, for a given mass-loss rate, more emitting material at a given radius from the star. Thus, a smaller value of $\dot{M}$ is required to produce the same observable Hα emission. The values of $\dot{M}$ and β would appear to be correlated. In this particular case, the mass-loss rate is most sensitive to changes in the velocity law exponent (i.e., $\mathrm{d}\dot{M}/\mathrm{d}\beta$ is a maximum) at around $\beta \simeq 0.7$; increasing β from 0.6 to 0.8 results in a change in $\dot{M}$ of roughly 0.5 dex. Therefore, it is possible to fit the observed Hα profile with theoretical models spanning the widest range of mass-loss rates when β is close to this value. The optimum value of β (in terms of the fit to the observed Hα profile), however, is 0.32.

Figure 4.16 shows the observed Hα spectrum of HD 12323, plotted with the optimum TGFORSOL fits, as determined by PHALTEE, as β is increased, in increments of 0.1, from 0.3 to 2.0, with all other parameters, except $\dot{M}$, held constant. All the fits are 'good' (it is possible to 'fit' the profile with $\beta = 2.0$, if $\dot{M}$ is sufficiently reduced), but the 'best' fit is obtained with $\beta = 0.32$. With so little emission in the profile, there is very little sensitivity to β, and hence $\dot{M}$. The profile is also more sensitive to the underlying photospheric core spectrum. If, for example, a slightly different temperature was adopted for the star (thereby changing the core spectrum), a different set of output parameters would be obtained. Other stars with minimal Hα emission are affected in the same way.

This result might go some way towards explaining the much shallower $\dot{M}$–L relationship derived in this work, compared to that found by Howarth and Prinja (1989). If, as a result of significantly decreasing β to fit the profile, PHALTEE systematically overestimates $\dot{M}$ for stars with Hα in absorption (which also tend to be the lower luminosity objects), this would certainly contribute to the shallower $\dot{M}$–L correlation. When PHALTEE searches were conducted with the departure coefficients *and* β fixed at their default (Puls *et al.*, 1996) values (i.e., $\dot{M}$ *alone* was allowed to float), the following $\dot{M}$–L relationship was

obtained for the Hα sample:-

$$\log \dot{M} = (1.69 \pm 0.16) \log L - (15.4 \pm 0.9) \tag{4.8}$$

This is precisely Howarth and Prinja's 1989 result. However, the profile fits thus obtained are considerably poorer than those from searches conducted with additional parameters floating. Better results are obtained when both $\dot{M}$ and β are allowed to float, but the best profile fits are those from searches conducted with *all* parameters floating (as might be expected). Because of the (generally) very good quality of these fits, and the relatively small changes in $\dot{M}$ and β introduced by floating the departure coefficients (see Table 4.14), these results will be adopted henceforth, including the derived $\dot{M}$–L relationship (Equation 4.4), which will be used in §6.4.2 when discriminating between free–free and nonthermal sources.

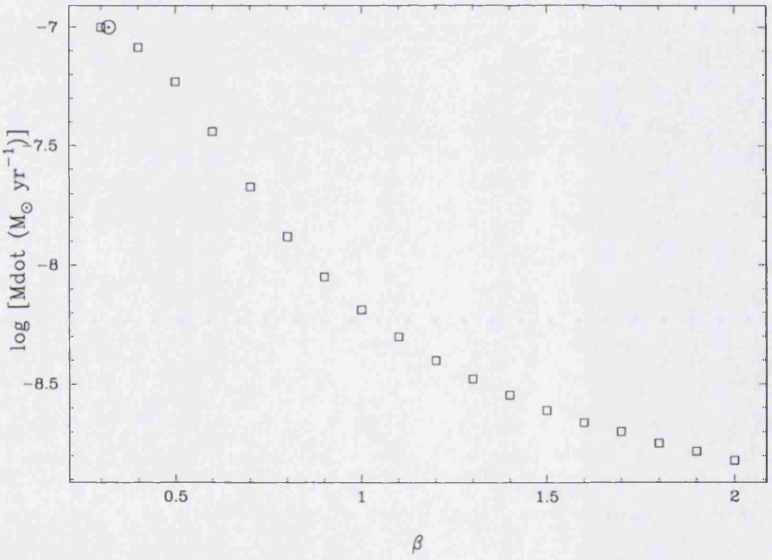

Figure 4.15: The effect on $\dot{M}$ of varying β (with all other parameters held constant), for the star HD 12323. The pairs of $\dot{M}$, β values are represented by '□'; the values corresponding to the 'best' fit to the Hα profile are represented by '⊙'.

4.5.2 Comments

The quality of the 'best' model fit to the observed Hα profile is not equally good for all stars (see Appendix A), making it difficult to assess the likely scale of the errors. The

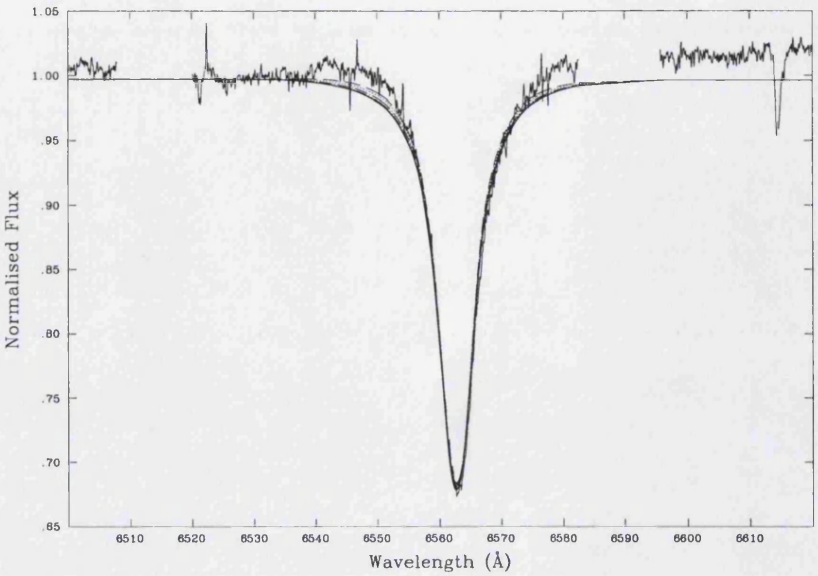

Figure 4.16: Hα line-profile fits to HD 12323, for $\beta = 0.3$–2.0. The solid line represents the observed Hα profile; the dashed and dotted lines represent the optimum TGFORSOL fits to the profile, for the pairs of $\dot{M}$, β values in Figure 4.15.

uncertainties discussed thus far are *internal* uncertainties, resulting from the methodology of the modelling process; there are also *external* uncertainties introduced by adopting parameters from the literature, in particular the assumed distances to objects. This will affect stars with strong Hα emission differently to those with Hα in absorption, as the model photospheric profile is more important for stars with little Hα emission.

Within the framework of the adopted model, and distance, the mass-loss rate for an O supergiant with Hα in emission is probably accurate to within $\sim \pm 50\%$, degrading to a factor $\sim \pm 2$ for stars with weak emission. Uncertainty in the distance is reasonably unimportant from the point of view of the $\dot{M}$–L relationship, and also when comparing, for example, Hα and radio mass-loss rates, as the sensitivity to distance is the same.

CHAPTER 5

Mm: Observations and Mass-Loss Rates

New mm-wave observations of nineteen early-type stars, including a subset of the Hα sample, have been obtained using the Sub-millimetre Common User Bolometer Array (SCUBA). These data serve as a probe of conditions further out in the stellar wind than the Hα observations, generally at $\gtrsim 10\ R_*$ (see Table 5.4), where the outflow has reached its terminal velocity. For the sixteen objects detected, the mm fluxes have been used to calculate mass-loss rates (or upper limits thereto; see Table 5.3). Some of these mm fluxes will be used, in conjunction with the radio data presented in §6, to calculate mass-loss rates for a larger sample, of 53 early-type stars.

5.1 The sample

Mm-wave observations of nineteen Galactic early-type stars were obtained using SCUBA at the 15-m James Clerk Maxwell Telescope (JCMT) on Mauna Kea, Hawaii. The data were acquired in service mode over the period May–July, 1998. The target stars (listed in Table 5.1) comprise nine WR stars, four B supergiants, five O supergiants and one A supergiant (α Cyg). Of these, the following nine stars are also present in the Hα sample:-

- HD 15570
- HD 169454
- HD 193237 (P Cyg)
- HD 197345 (α Cyg/Deneb)
- HD 210839 (λ Cep)
- Cyg OB2 No.5
- Cyg OB2 No.8A
- Cyg OB2 No.9
- Cyg OB2 No.12

5.2 The Sub-millimetere Common User Bolometer Array (SCUBA)

SCUBA is a sub-millimetre continuum array receiver mounted on the left-hand (facing out) Nasmyth platform of the JCMT. It is both a sub-millimetre camera and a photometer, with two arrays of bolometric detectors (pixels) arranged in a close-packed hexagonal configuration. Each array covers a field of view of diameter approximately 2.3′. The short-wavelength (SW) array has 91 pixels for observations at 0.35 mm and 0.45 mm, and the long-wavelength (LW) array has 37 pixels operating at 0.75 mm and 0.85 mm. The two arrays can be used simultaneously by employing a beam-splitter. Additionally, there are three single pixels available for photometry at 1.1, 1.35 and 2.0 mm. These photometric pixels are located around the outside of the LW array, and have beamwidths of 16″, 18″ and 28″, respectively. SCUBA is designed so that the thermal loading on the bolometers is reduced to a minimum. This is because any change in temperature of the responsive element of a bolometer causes gross changes in the electrical conductivity of the element. Background-limited performance is achieved by cooling the bolometric detectors to ~ 100 mK, and by limiting background power through the use of narrow-band filters and single-moded optics. Thus, the intention is that SCUBA has a sensitivity limited only by photon noise from the sky, the telescope and the instrument itself (at all wavelengths). See Holland *et al.* (1999) for an overview of the SCUBA instrument and its observing modes.

The data presented in this thesis were made in SCUBA's photometry mode (the standard mode employed for point-like sources), and the discussion which follows pertains to this particular method of observing. In photometry mode, any of the pixels in either array can be used, although this is usually the centre pixel (apart from observations at 1.1, 1.35 and 2.0 mm). The following nomenclature is used when describing a SCUBA photometry observation:-

(i) **Jiggling.** Photometry mode uses a single bolometer to make small nine-point maps centred on the source. The secondary mirror is moved once per second in order to move the array on the sky. This process is known as a 'jiggle', and, in photometry mode, is used to correct for seeing effects. Data are written to disk once per second.

(ii) **Chopping.** In addition to jiggling, the secondary mirror of the telescope is contin-

uously moved on and off source at a frequency of ~ 7 Hz. This process is known as 'chopping' and is performed in order to remove the sky signal to zeroth order. Typically, more than 99% of the received signal is sky, with less than 0.1% coming from the source. Other off-source pixels are not used for chopping, as there are large fluctuations from bolometer to bolometer. Chopping usually occurs over 60″ (known as the chop throw) and is referred to as either 'left-handed' (right beam on source, left beam on sky) or 'right-handed' (left beam on source, right beam on sky). It is performed in azimuth, not altitude, so that the airmass is the same in both positions. Transputers remove ('demodulate') the chop signal to give sky-subtracted data.

(iii) **Nodding.** The telescope is 'nodded' off source after each nine-point jiggle to measure the sky gradient between the two chopping positions (and also, to a lesser extent, to correct for any electronics imbalance). Nodding reverses the direction of the chop.

(iv) **Switch** In photometry mode, each set of nine jiggle positions measured with the object in the telescope beam is referred to as a 'switch'. Thus, the data from each nod position is a switch lasting nine seconds.

(v) **Integration.** An integration is the average of a nine-point (i.e., nine-second) jiggle.

(vi) **Exposure.** An exposure is the result from a complete set of switches (i.e., it comes from subtracting the off-source position from the on-source position)

(vii) **Sky dip.** As with Hα observations, mm observations are affected by water vapour absorption in the Earth's atmosphere. Indeed, the mm opacity is dominated by H_2O, and this needs to be corrected for. The zenith mm-band optical depth, τ, is a measure of the amount of water vapour present in the atmosphere. To obtain τ, 'sky dip' observations are taken with the central pixels in each array, as well as with the photometric pixels, when the τ-meter (which updates every 15–20 mins) is pointing in the direction of the source. These data can then be used to correct for atmospheric extinction. Throughout the course of a long, coadded set of integrations, the transparency of the sky will most likely change. Thus, skydips are taken before, after (and sometimes between) the integrations to be coadded.

The target stars in this study were observed at one or more of the following wavelengths: a) 0.85 mm; b) 1.35 mm; c) 2.0 mm. Each observation consists of between 60 and 250

integrations, with total integration times ranging from 1080–4500 s. The signal to noise achieved varied significantly from source to source, but was as high as 57 in the case of WR 147 (see Table 5.1).

5.3 Data reduction

Data reduction was performed by the author with the SCUBA User Reduction Facility (SURF; Stevens *et al.*, 1997). The steps listed below are required to generate the final (but still uncalibrated) result. Additionally, data taken with the arrays (in this case observations at 850 μm) can be corrected for sky noise variations by subtracting the signal from surrounding bolometers. The 'raw' fluxes obtained from SCUBA are already background-subtracted: transputers demodulate the 7 Hz chop signal, giving data once per second. SURF uses the demodulated data as input, and the data reduction proceeds with the following series of commands:-

(i) **Reduce switch.** This compensates for the nodding of the telescope. The raw beam-switched data are reduced by subtracting the off-source position from the on-source position ('nods'). Each position in the jiggle map consists of 128 measurements, which together correspond to one second of integration time. If the number of bad data points ('spikes') in a given one-second integration exceeds five (out of the 128 measurements), then that second of integration is removed.

(ii) **Extinction.** This applies an extinction correction for the data. Two values of the sky opacity, τ, are required, together with the sidereal times of their determination. These data are obtained from the skydip observations. If the second opacity differs from the first, then the extinction is linearly interpolated between the two times.

(iii) **Scuphot.** The extinction-corrected data are used to produce a signal (integration) for each switch by averaging the nine points of the jiggle pattern.

(iv) **Scucat.** The individual integrations produced with scuphot are concatenated to generate a final, coadded result.

(v) **Qdraw.** Qdraw uses the KAPPA package (Currie and Berry, 2001) to display the final photometric result. The mean level and the $\pm 3\sigma$ levels are indicated (see Figure 5.1). Numerical values of the mean signal, the standard deviation and the error on

the mean are given for both the full data set and after clipping at the 3σ level. The values used in this work are the 3σ-clipped results.

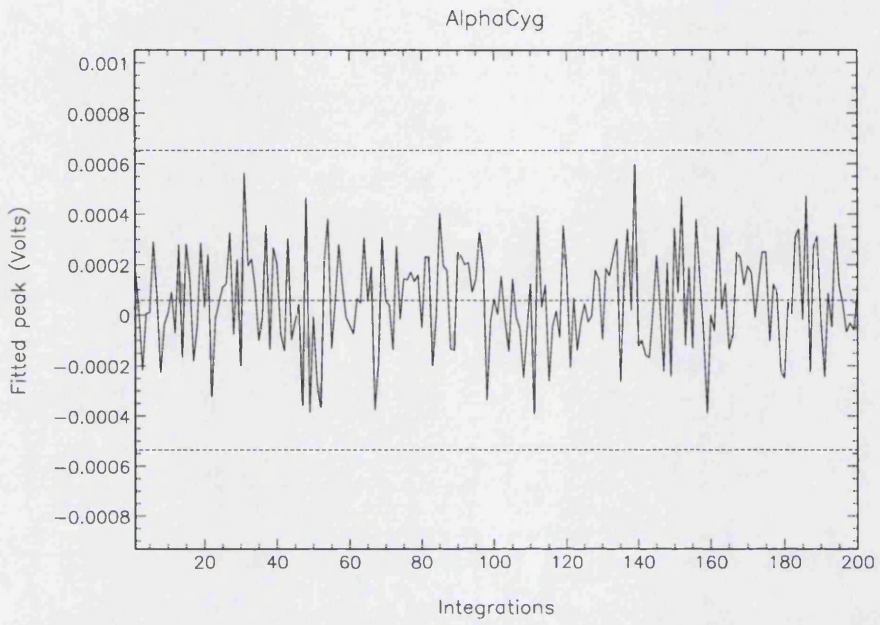

Figure 5.1: Final, mm photometric SCUBA result for α Cyg, generated using qdraw. The mean level and the $\pm 3\sigma$ levels are indicated by the dashed lines.

5.3.1 Calibration

As the stronger sources in mm photometry tend to be extended (and/or variable), planets are often used to calibrate the observed fluxes. The planet Uranus is frequently used (and was in this work), as it is (very nearly) a pointlike source. It is important to ensure that the bolometer used for the calibration observation of Uranus is the same as that used for observing the source. The signal obtained for Uranus is used in conjunction with tabulated values of the planetary flux (at the relevant wavelength and corrected for the SCUBA beamsize) to obtain the flux calibration factor (gain). The gain is then used to calculate the flux received from the source. There can be considered to be an inherent flux calibration error of around 10%; however, the signal to noise will generally be the dominant source of error.

5.4 Flux detections

Mm continuum emission was detected in sixteen out of the nineteen sources. The results are given in the final column of Table 5.1. For three of the objects, the SCUBA bolometers recorded *negative* (i.e., less than zero) results, which is physically unacceptable. In the case of Cyg OB2 No.8A, the small negative flux detection at 1.35 mm of only -2.50 ± 5.95 mJy can be taken to be a simple non-detection (this can arise as a result of random variations). The negative detections for the WC9 stars, WR 95 and WR 104, however, are somewhat larger, and with smaller errors (these are ~ 3–5σ 'anti-detections'). On statistical grounds, these are unlikely to arise purely by chance and warrant further consideration.

One obvious explanation is that the formally significant negative fluxes are due simply to additional errors on all the detections. This would imply that there are large (unaccounted for) errors on the other (positive) fluxes. To investigate this, the 0.85 mm data could be used to produce photometry measurements for some of the other SCUBA bolometers (e.g. the entire second or third ring, or both). It would then be possible to plot a histogram of mean values to determine whether the noise value (deduced from the FWHM of the histogram) is consistent with the measurements obtained from the central bolometer.

Disregarding the possibility of additional errors, the negative fluxes might be due to problems with the SCUBA chopping: there is always the possibility that another source (perhaps a galaxy?) lies within the chop field. This could lead to a negative detection when subtracting the 'off-source' position (which should be sky) from the 'on-source' position. In the case of WR 104, this would seem to be unlikely, as during the course of the two observations on May 6th, two different chop throws were employed. A chop throw of $45''$ was used during the 0.85 mm observation, and during the first 900 s of the 1.35 mm observation. However, because of concerns at the time that there may indeed be something in the chop field, the chop throw was changed to $60''$ for the second 900 s. In spite of this, negative flux detections were still obtained for all these integrations. WR 104 is known to be a persistent dust-former and possesses a huge, circumstellar dust shell (e.g. Allen *et al.*, 1972). A binary nature has been proposed for the star (Cohen *et al.*, 1975; Cohen and Kuhi, 1977) on the basis of the dilution of emission lines by excess continuum flux. Tuthill *et al.* (1999) used the 10-m Keck telescope to obtain infrared images of a spiral of circumstellar dust around WR 104. The dust is thought to be associated with the collision

Table 5.1: SCUBA target stars

HD	Name	Spectral type	Date	Wavelength (mm)	No. Int	Int (s)	Flux (mJy)
4004	WR 1	WN4	5/5/98	1.35	250	4500	13.0 ± 2.8
			1/6/98	1.35	140	2520	5.08 ± 3.95
15570	···	O4If+[a]	3/7/98	1.35	120	2160	4.76 ± 2.43
152236	ζ^1 Sco	B1.5Ia+[d]	5/5/98	0.85	100	1800	52.7 ± 10.0
			5/5/98	1.35	150	2700	38.4 ± 3.9
152408	WR 79A	WN9ha	10/5/98	1.35	200	3600	23.3 ± 4.4
165688	WR 110	WN5–6	12/6/98	1.35	60	1080	31.2 ± 5.1
165763	WR 111	WC5	6/5/98	1.35	200	3600	9.54 ± 2.49
169454	···	B1Ia+[d]	12/6/98	1.35	60	1080	11.4 ± 4.9
193237	P Cyg	B1Ia+[e]	5/5/98	1.35	100	1800	126 ± 3
			5/5/98	2.0	100	1800	82.7 ± 4.2
			3/7/98	0.85	60	1080	177 ± 10
193793	WR 140	WC7pd + O4–5	7/5/98	1.35	200	3600	23.1 ± 2.5
197345	α Cyg/Deneb	A2Ia[b]	4/5/98	1.35	200	3600	7.81 ± 1.87
210839	λ Cep	O6I(n)fp[c]	4/5/98	1.35	250	4500	4.25 ± 1.92
			1/6/98	1.35	130	2340	8.87 ± 3.58
···	WR 95	WC9d	7/5/98	1.35	100	1800	$-18.6 \pm 3.8^{\dagger}$
···	WR 104	WC9d + B0.5V	6/5/98	0.85	100	1800	$-20.0 \pm 8.6^{\dagger}$
			6/5/98	1.35	100	1800	$-12.3 \pm 3.1^{\dagger}$
			7/6/98	0.85	75	1350	$-35.8 \pm 12.7^{\dagger}$
···	WR 105	WN9h	7/5/98	1.35	150	2700	22.0 ± 3.1
···	WR 147	WN8(h) + B0.5V	6/5/98	1.35	100	1800	269 ± 4
···	Cyg OB2 No.5	2× O7Ianfp[c]	6/5/98	1.35	100	1800	42.0 ± 3.4
			3/7/98	0.85	60	1080	22.8 ± 6.6
···	Cyg OB2 No.8A	O5.5I(f)[f]	7/5/98	1.35	200	3600	$-2.50 \pm 5.95^{\dagger}$
···	Cyg OB2 No.9	O5If[f]	7/5/98	1.35	150	2700	20.0 ± 4.4
···	Cyg OB2 No.12	B5Ie[f]	6/5/98	1.35	100	1800	42.6 ± 3.0
			3/7/98	0.85	100	1800	40.9 ± 5.6

NOTES: WR spectral types are from van der Hucht (2001) and references therein. Other spectral types are from: a) Walborn (1971); b) Morgan and Keenan (1973); c) Walborn (1973); d) Walborn (1976); e) Humphreys (1978); f) Massey and Thompson (1991). The fourth column gives the date of the observation. The fifth column gives the wavelength of the observation. The sixth and seventh columns give the number of integrations and the total integration time in seconds, respectively. The integration times listed include both on-source and off-source time; the on-source time is half the value. † — See the text for comments on the (numerically) negative detections.

front between the winds of the WR primary and an OB-type secondary. The dust spiral, however, extends out to a radius of only $\sim$65 mas ($\sim$150 AU), ruling out the possibility that when chopping 'off source', it is the dust spiral (as opposed to sky) that is being observed.

A negative detection at 1.35 mm was made for WR 95 during a single observation on May 7th, 1998. WR 95, like WR 104 and the majority of WC9 stars that have been studied, is also known to be a persistent dust-former (Williams *et al.*, 1987). A search by Williams and van der Hucht (2000) for a binary companion to the star proved inconclusive. It is interesting to note that the two instances of (inexplicable) anomalous flux detection coincide with the two known persistent dust-forming WR stars in the sample.

5.5 Free–free continuum emission

The determination of accurate mass-loss rates for early-type stars is far from trivial, with each available diagnostic having inherent uncertainties. Mass-loss rates derived from UV resonance lines require knowledge of the relative abundances of minority ions in the wind. These abundances are not accurately known and have to be (somewhat uncertainly) modelled (e.g. Groenewegen and Lamers, 1991). Using the Hα recombination line to determine mass-loss rates, whilst being the most straightforward method observationally, often requires that assumptions be made regarding the form of the velocity field of the wind (e.g. Lamers and Leitherer, 1993). This is because the line originates in the inner part of the wind, where the outflow is still undergoing acceleration.

Hydrogen in the winds of early-type stars is virtually fully ionised and emits free–free radiation. This emission is most easily visible from IR to radio wavelengths, and can be used as a mass-loss diagnostic. The use of IR continuum emission (e.g. Barlow and Cohen, 1977) is complicated by the fact that it is again sensitive to the velocity structure of the inner part of the wind, where it is formed. Additionally, at these shorter wavelengths, it becomes difficult to distinguish the free–free radiation from the photospheric emission (the free–free flux varies as λ^{-2}, whereas the photospheric flux varies as λ^{-4}). Longer-wavelength observations, however, provide the most accurate and reliable method for determining the mass-loss rates of early-type stars (e.g. Leitherer and Robert, 1991; Lamers and Leitherer, 1993; Leitherer *et al.*, 1995; Scuderi *et al.*, 1998).

Thermal millimetre and centimetre radiation originates in the outer part of the wind,

where the expanding envelope has reached its terminal velocity. Here, a simple r^{-2} density distribution can be used to describe the outflow. Because of the wavelength dependence of the free–free opacity, the free–free spectrum from $\sim$1 mm–20 cm samples the wind between, typically, $\sim$10–100 R_*. Terminal velocities obtained from UV resonance lines, which sample the wind at $\sim$10 R_*, provide a good representation of the flow velocity in the mm-emitting region (and can be extrapolated to the cm-emitting region, assuming a constant outflow velocity).

In order to model the mm/cm emission, it is assumed that the stellar wind is stationary, spherically symmetric, isothermal, optically thick, and moving at constant (i.e., terminal) velocity. Provided that these conditions are met, and that the observed emission is indeed thermal in origin (i.e., arises from free–free radiation produced in the outer part of the wind), then the measured flux is related to the wind density by a simple analytical formula (Wright & Barlow 1975; Panagia & Felli 1975):-

$$S_\nu = 2.32 \times 10^4 \left(\frac{\dot{M}Z}{v_\infty \mu}\right)^{4/3} \left(\frac{\gamma g_\nu \nu}{d^3}\right)^{2/3} \tag{5.1}$$

Or in terms of the mass-loss rate:-

$$\dot{M} = \frac{(5.32 \times 10^{-4})\mu}{Z(\gamma g_\nu \nu)^{0.5}} S_\nu^{0.75} v_\infty d^{1.5} \tag{5.2}$$

where $\dot{M}$ is the mass-loss rate in $M_\odot$ yr^{-1}; S_ν is the free–free flux in mJy, measured at frequency ν in Hz; d is the distance to the source in kpc; v_∞ is the terminal velocity of the wind in km s^{-1}; μ is the mean molecular weight; Z is the rms ionic charge; and γ is the mean number of free electrons per ion. If A_i, M_i and Z_i are the fractional abundance, molecular weight and ionic charge of the ith species, then μ, Z and γ are defined as:-

$$\mu = \frac{\sum A_i M_i}{\sum A_i} \tag{5.3}$$

$$Z = \frac{(\sum A_i Z_i^2)^{0.5}}{\sum A_i} \tag{5.4}$$

$$\gamma = \frac{\sum A_i Z_i}{\sum A_i} \tag{5.5}$$

The free–free Gaunt factor, g_ν, can be approximated at mm and cm wavelengths by:-

$$g_\nu = 9.77 + 1.27 \log \frac{T_e^{1.5}}{Z\nu} \tag{5.6}$$

(Abbott *et al.*, 1986), where T_e is the electron (wind) temperature in K. This is the local temperature at the mm/cm 'photosphere'. Thus, mass-loss rates can be derived

from observed fluxes if the distance to the source and v_∞ are known, together with the chemical composition and ionisation structure of the wind.

At millimetre and centimetre wavelengths, $g_\nu \propto \nu^{-0.1}$, so that Equation 5.1 predicts a characteristic thermal spectrum with a frequency dependence of $S_\nu \propto \nu^{0.6}$. If one of the assumptions employed in the derivation of Equation 5.1 is incorrect, then the spectrum may deviate slightly from this (Leitherer *et al.*, 1995). Larger deviations can occur if nonthermal processes are contributing to the observed flux; these situations are discussed in §6.4.

5.6 Calculating mm mass-loss rates

Equation 5.2 is used, where possible, to calculate mass-loss rates for the stars in the SCUBA sample, using the detected mm fluxes (Table 5.1) and the adopted parameters listed in Table 5.2. Table 5.3 lists the mass-loss rates thus derived, at specific wavelengths and on specific dates, together with a weighted mean value for $\dot{M}$ for each star, averaged over wavelength and date. As these calculations depend quite crucially upon the parameters adopted and their associated uncertainties, it is worthwhile taking some time to consider them.

5.6.1 Distance, *d*

The distances adopted for the WR stars are photometric distances taken from van der Hucht (2001) and references therein (with the exception of HD 152408, where, for consistency, the distance to the parent cluster, Sco OB1, is taken from Humphreys, 1978). An uncertainty of 20% is assumed if a star is supposedly an established member of a cluster, and 40% for a field star. The distances for the remaining objects in the sample are taken from Humphreys (1978). These OBA stars are all cluster members, and the distances given are derived from the adopted (mean) distance modulus listed for the parent cluster, using:-

$$\log d = \frac{(m - M) + 5}{5} \tag{5.7}$$

where d is the distance in parsecs, m is the apparent magnitude, M is the absolute magnitude and the quantity $(m - M)$ is the distance modulus. As the OBA stars are all cluster members, an uncertainty on the distance of 20% is assumed.

5.6.2 Terminal wind velocity, v_∞

v_∞ for the WR stars are taken from van der Hucht (2001) and references therein. The terminal velocities for the remaining stars in the sample are taken from various sources; these are given in the sections pertaining to the individual stars. An uncertainty of 10% is assumed on the values of v_∞.

5.6.3 Wind electron temperature, T_e

A knowledge of T_e is required for calculation of the Gaunt factor. Previous works by Leitherer and Robert (1991) and Leitherer *et al.* (1995) have adopted an electron temperature of $T_e = 10\,000$ K for WR stars. This is in agreement with the results of the wind models of Hillier (1988, 1989), which suggested wind electron temperatures of the order of $T_e \simeq 10\,000$ K in the regions where mm continuum radiation is emitted. This is attributed to strong cooling in collisionally-excited nitrogen and carbon lines. In reality, however, because of differences in metal abundance, the electron temperature in the winds of WN stars is likely to be somewhat higher than 10 000 K, and in WC stars somewhat lower than 10 000 K. Analyses of nine Galactic WN7 and WN8 stars by Crowther *et al.* (1995*a*) found wind electron temperatures of $T_e \sim 13\,000$ K in all cases. This value has been adopted for the five WN stars in the sample. Hillier (1989) investigated the temperature structure of early-type WC stars and found wind electron temperatures of $T_e \sim 9000$ K. This has been adopted for the WCE star present in the sample. Crowther (1997) found an electron temperature in the wind of WR 104 (WC9) of $T_e \sim 7500$ K, which has been adopted for the WCL stars.

Drew (1989) found that for O-star winds there is a significant temperature decrease from the optical to the radio photosphere, with models suggesting an electron temperature of $T_e \approx 0.4\ T_{\rm eff}$ at a radial distance from the star of 10 R_*. This is in comparison with the electron temperature of $T_e = 0.75\ T_{\rm eff}$ adopted in §3.4.2 for the Hα line-forming region ($\sim$1.0–1.5 R_*). The decrease is a result of radiative losses in metallic lines and the hydrogen and helium continuum, as well as adiabatic cooling. Drew's (1989) relationship has been adopted for the OB stars in the sample (and for α Cyg). The electron temperature in the radio photosphere of the extreme B supergiant, Cyg OB2 No.12 ($T_{\rm eff} = 11\,200$ K), has been measured by White and Becker (1983) to be 5000 K, which is in good agreement with this result. It is worthwhile noting that the value of T_e is not critical to the determination

of $\dot{M}$, entering into the calculation only as a result of the weak temperature dependence of the Gaunt factor (ultimately, $\dot{M} \sim {T_e}^{-0.1}$). Varying T_e from 10 000 K to 20 000 K, for example, decreases the mass-loss rate by only 9%.

5.6.4 Mean molecular weight, μ

For O, B and A stars, as well as for WR stars of types WN6 and later, plausible abundance variations in elements heavier than helium are not likely to affect the mean molecular weight, or the number of free electrons, significantly (Willis, 1991). Thus, for these objects, the value of μ (along with Z and γ) is solely determined by the relative abundances of H and He, and is considered to have an uncertainty of 10%. For WN stars earlier than type WN6, and for WC stars, elements heavier than helium *can* have important contributions to μ, Z and γ. Therefore, for these objects, carbon, nitrogen and oxygen *are* considered in the calculations, and an uncertainty of 20% is assumed.

5.6.5 Mean ionic charge, Z, and number of free electrons per ion, γ

Hydrogen is assumed to be ionised in the winds of all the stars in the sample (with the exception of α Cyg; see the notes to Table 5.2, starting on page 143). The ionisation structure of helium and heavier elements, however, needs further consideration. In the case of WR and O stars, even though temperatures close to the stellar surface are hot enough so that helium is doubly ionised, by the time the flow reaches the radio photosphere, it can recombine to become singly ionised (Hillier, 1988). It is therefore assumed that, for these stars, helium is singly ionised in the wind region sampled by the mm fluxes. That is to say, the recombination radius of He^{2+} into He^{+} should be within the mm/radio photosphere. This might be too simplistic a view to take, however, and small fractions of He^{2+} may still be present in the mm-emitting region. This is taken into account when considering the appropriate uncertainties. For the early-B stars in the sample, the wind electron temperature is also such that helium is expected to be singly ionised. Cyg OB2 No.12 and α Cyg, however, have lower electron temperatures ($T_e \lesssim 5000$ K), and so it is assumed that helium is predominantly neutral at the mm photosphere.

For WN stars earlier than type WN6, and for WC stars, the ionisation structure of the metals also needs to be considered. In the case of WNE stars, metals are generally triply ionised (e.g. Schmutz, 1997); for WC stars, they are generally doubly ionised (e.g. Hillier and Miller, 1999). An uncertainty of 20% is assumed on the values of Z and γ for

the WNE and WC stars, to account for the potentially large errors on the abundances and ionisation fractions. For the remainder of the sample, a 10% uncertainty on each of Z and γ is assumed to account for the presence of some doubly-ionised helium in the mm-emitting region.

5.6.6 Errors

The uncertainties associated with $\dot{M}$ were calculated by propagating errors:-

$$\begin{aligned}\sigma(\log \dot{M}) &= \{[0.75\sigma(\log S_\nu)]^2 + [\sigma(\log v_\infty)]^2 + [1.5\sigma(\log d)]^2 \\ &\quad +[\sigma(\log \mu)]^2 + [\sigma(\log Z)]^2 + [0.5\sigma(\log \gamma)]^2\}^{0.5} \end{aligned} \tag{5.8}$$

The errors on S_ν are taken from Table 5.1; these do not take into account possible additional flux calibration errors of order 10%. Note that any error on T_e is neglected, due to the extremely weak temperature dependence of the mass-loss rate (through the Gaunt factor). The dominant error in the derived mass-loss rates is most often due to the uncertainty in the distance to the source. Even for stars that are members of clusters or associations, distances are uncertain by 10%–20%, and for field stars this can be as much as 40%. Distance uncertainty currently sets the limit for the accuracy of $\dot{M}$ derived from radio and mm data.

It should be mentioned that the mm mass-loss rates have been calculated assuming that the observed flux is thermal in origin. Early-type stars are known also to be emitters of nonthermal (i.e., non-free–free) flux. This can contaminate the thermal emission, invalidating the use of Equation 5.2 to calculate mass-loss rates. Fortunately, nonthermal processes have a negligible contribution at mm wavelengths (Leitherer and Robert, 1991; Altenhoff *et al.*, 1994; Contreras *et al.*, 1996), meaning that the $\dot{M}$ derived here should not be affected by contamination. Longer-wavelength continuum flux can, however, be affected by nonthermal emission, and this will be taken into consideration when calculating mass-loss rates from the cm data presented in §6.

Table 5.2: Adopted parameters for the SCUBA sample

HD	Name	Spectral type	d (kpc)	Cluster	v_∞ (km s^{-1})	μ	Z	γ	T_e (K)
4004	WR 1	WN4	1.82	Cas OB7	2100	4.0	1.0	1.0	13 000
15570	···	O4If+	2.19	Cas OB6	2600[H00]	1.5	1.0	1.0	16 800
152236	ζ^1 Sco	B1.5Ia+	1.91	Sco OB1	390[H97]	1.6	1.0	1.0	8 200
152408	WR 79A	WN9ha	1.91	Sco OB1	935	2.1	1.0	1.0	13 000
165688	WR 110	WN5–6	1.28	···	2100	4.0	1.0	1.0	13 000
165763	WR 111	WC5	1.58	Sgr OB1	2300	6.9	1.4	1.3	9 000
169454	···	B1Ia+	1.66	Sct OB3	850[B89]	1.5	1.0	1.0	8 200
193237	P Cyg	B1Ia+	1.82	Cyg OB1	200[PP90]	1.5	1.0	1.0	7 700
193793	WR 140	WC7pd + O4–5	1.10	···	2870	5.8	1.3	1.2	7 500
197345	α Cyg/Deneb	A2Ia	0.79	Cyg OB7	225[A02]	1.2	0.5	0.5	3 400
210839	λ Cep	O6I(n)fp	0.83	Cep OB2	2250[H00]	1.8	1.0	1.0	14 800
···	WR 95	WC9d	2.09	Tr 27	1100	7.3	1.4	1.4	7 500
···	WR 104	WC9d + B0.5V	2.3	···	1220	7.3	1.4	1.4	7 500
···	WR 105	WN9h	1.58	Sgr OB1	700	2.7	1.0	1.0	13 000
···	WR 147	WN8(h) + B0.5V	0.65	···	950	3.1	1.0	1.0	13 000
···	Cyg OB2 No.5	2× O7Ianfp	1.82	Cyg OB2	2200[B89]	1.3	1.0	1.0	15 900
···	Cyg OB2 No.8A	O5.5I(f)	1.82	Cyg OB2	2650[H01]	1.3	1.0	1.0	17 600
···	Cyg OB2 No.9	O5If	1.82	Cyg OB2	2200[B89]	1.3	1.0	1.0	17 800
···	Cyg OB2 No.12	B5Ie	1.82	Cyg OB2	1400[S80]	1.3	1.0	0.9	4 500

NOTES: References for spectral types are provided with Table 5.1; sources for other data are given in the discussion of the parameters (§5.6.1–5.6.5), and/or are provided starting on page 143.

SOURCES FOR TABLE 5.2:-

- ***d***. WR-star distances are from van der Hucht (2001) (with the exception of HD 152408, which is from Humphreys, 1978); OBA-star distances are from Humphreys (1978).
- v_∞. WR-star values are from van der Hucht (2001). Sources for the OBA stars are:-
  S80 — Souza and Lutz (1980); B89 — Bieging *et al.* (1989); PP90 — Pauldrach and Puls (1990); H97 — Howarth *et al.* (1997*b*); H00 — Herrero *et al.* (2000); H01 — Herrero *et al.* (2001); A02 — Aufdenberg *et al.* (2002).
- μ. Values are calculated using Equation 5.3, together with the assumptions discussed in §5.6.4. See also the notes below concerning elemental abundances and ionisation structures.
- Z. Values are calculated using Equation 5.4, together with the assumptions discussed in §5.6.5. See also the notes below concerning elemental abundances and ionisation structures.
- γ. Values are calculated using Equation 5.5, together with the assumptions discussed in §5.6.5. See also the notes below concerning elemental abundances and ionisation structures.
- T_e. WR-star values are assumed on the basis of the discussion in §5.6.3. OBA-star values are calculated using Drew's (1989) relationship, $T_e \approx 0.4\ T_{\rm eff}$; $T_{\rm eff}$ are given in Tables 4.3 and 6.2.

Notes to individual stars, concerning elemental abundances and ionisation structures:-

HD 4004 (WR 1). Because of the similarity in spectral type between this star (WN 4) and WR 6 (WN5), the same elemental abundances and ionisation structures as derived by Hillier (1988) for WR 6 are assumed. The analysis by Schmutz (1997) of the same star suggested that at a radial distance of $\sim 100\ R_*$, helium is singly ionised, carbon and nitrogen are triply ionised, and oxygen is doubly ionised (there is no hydrogen present in this WNE star). This is in good agreement with Hillier (1988).

HD 15570. A helium abundance of Y(He) = 0.15 is adopted, taken from Herrero *et al.* (2000).

HD 152236 (ζ^1 Sco). In accordance with Leitherer and Robert (1991), to reflect the star's advanced evolutionary status, a significant helium overabundance is assumed, such that Y(He) = 0.20.

HD 152408 (WR 79A). A H/He ratio of 1.6 is adopted, taken from the results of near-IR spectroscopy in Bohannan and Crowther (1999).

HD 165688 (WR 110). As for WR 1, because of the similarity in spectral type between this star (WN5–6) and WR 6 (WN5), the same elemental abundances and ionisation structures as derived by Hillier (1988) for WR 6 are assumed.

HD 165763 (WR 111). The adopted elemental abundances and ionisation structures are from Hillier and Miller (1999): N(C)/N(He) = 0.4, X(C) = 0.462, N(O)/N(He) = 0.1 and X(O) = 0.154.

HD 169454. As for HD 152236, to reflect the advanced evolutionary status of these stars, a helium overabundance relative to solar of a factor of two is assumed, such that Y(He) = 0.18.

HD 193237 (P Cyg). As for HD 152236, to reflect the advanced evolutionary status of these stars, a helium overabundance relative to solar of a factor of two is assumed, such that Y(He) = 0.18.

HD 193793 (WR 140). The same elemental abundances and ionisation structures as derived by Dessart *et al.* (2000) for the similar star WR 90 (WC7) are assumed.

HD 197345 (α Cyg). A helium abundance of Y(He) = 0.07 is adopted, taken from Albayrak (2000). Aufdenberg *et al.* (2002) argued that the observed spectrum of α Cyg between 1.35 mm and 3.6 cm is

inconsistent with hydrogen being fully ionised; the spectral slope exhibited suggests $S_\nu = \nu^{1.26\pm0.01}$. Spherical expanding atmosphere models with a velocity law parameter $\beta = 2.0$ have the majority of hydrogen ionised out to a radius of $R = 1640\ R_\odot$ ($\sim 9\ R_*$), while models with $\beta = 4.0$ have the majority of hydrogen ionised out to only $R = 610\ R_\odot$ ($\sim 3\ R_*$). In both cases, this lies within the mm photosphere ($\sim 10\ R_*$). Thus, hydrogen has been assumed to be $\sim 50\%$ ionised at the mm photosphere of α Cyg.

HD 210839 (λ Cep). A helium abundance of $Y(\mathrm{He}) = 0.25$ is adopted, taken from Herrero *et al.* (2000).

WR 95. Because of the similarity in spectral type between this star and WR 104 (both WC9), the same C/He and O/He ratios are assumed (see next).

WR 104. A C/He ratio of 0.5 and an O/He ratio of 0.1 are adopted, taken from Crowther (1997).

WR 105. A H/He ratio of 0.8 is adopted, taken from the results of near-IR spectroscopy in Bohannan and Crowther (1999).

WR 147. A H/He ratio of 0.4 is adopted, taken from the results of 0.4–20 μm spectroscopy in Morris *et al.* (2000).

Cyg OB2 No.5. $Y(\mathrm{He})$ is assumed to be solar.

Cyg OB2 No.8A. A helium abundance of $Y(\mathrm{He}) = 0.09$ is adopted, taken from Herrero *et al.* (2001).

Cyg OB2 No.9. A helium abundance of $Y(\mathrm{He}) = 0.09$ is adopted, taken from Herrero *et al.* (1999).

Cyg OB2 No.12. $Y(\mathrm{He})$ is assumed to be solar.

5.7 Characteristic radius of emission

The characteristic radius of emission, R_ν, is where free–free radiation from the wind typically originates, and is given by:-

$$R_\nu = 2.8 \times 10^{28} T_\mathrm{e}^{-0.5} (\gamma g_\nu)^{1/3} \left(\frac{\dot{M} Z}{v_\infty \mu \nu} \right)^{2/3} \tag{5.9}$$

(Wright and Barlow, 1975; Panagia and Felli, 1975); where R_ν is in cm, and all other units are as in Equations 5.1 and 5.6. The characteristic radius of emission scales approximately like $R_\nu \propto \nu^{-2/3}$ (neglecting the small frequency dependence of the Gaunt factor). Thus, shorter-wavelength observations sample closer to the stellar surface: the mm photosphere, for example, lies nearer to the star than the cm photosphere. The size of the mm photosphere is of interest here, as if this were to be $< 10\ R_*$ from the star, the assumption of constant wind velocity made in the derivation of $\dot{M}$ might be incorrect: the flow could very well still be undergoing acceleration.

The expression for R_ν is dependent upon the wind electron temperature. It has been assumed that T_e is the same at all R_ν (this assumption would seem to be reasonable,

Table 5.3: Mass-loss rates derived from SCUBA mm fluxes

HD	Name	Date	$\dot{M}$ ($10^{-6} M_{\odot}$ yr^{-1})			
			0.85 mm	1.35 mm	2 mm	Mean
4004	WR 1	5/5/98	...	89.2 ± 41.4	...	61.0 ± 25.4
		1/6/98	...	44.1 ± 32.1	...	
15570	...	3/7/98	...	24.9 ± 12.9	...	24.9 ± 12.9
152236	ζ^1 Sco	5/5/98	18.0 ± 6.8	17.1 ± 6.1	...	17.5 ± 4.5
152408	WR 79A	10/5/98	...	34.7 ± 13.1	...	34.7 ± 13.1
165688	WR 110	12/6/98	...	101 ± 70	...	101 ± 70
165763	WR 111	6/5/98	...	74.6 ± 35.6	...	73.6 ± 35.1
169454	...	12/6/98	...	11.4 ± 5.4	...	11.4 ± 5.4
193237	P Cyg	5/5/98	...	18.8 ± 6.6	16.1 ± 5.7	18.0 ± 3.7
		3/7/98	20.2 ± 7.1	...	...	
193793	WR 140	7/5/98	...	99.5 ± 68.0	...	99.5 ± 68.0
197345	α Cyg/Deneb	4/5/98	...	1.80 ± 0.71	...	1.80 ± 0.71
210839	λ Cep	4/5/98	...	5.63 ± 2.74	...	6.75 ± 2.34
		1/6/98	...	9.78 ± 4.52	...	
...	WR 95	7/5/98	...	†	...	†
...	WR 104	6/5/98	†	†	...	†
		7/6/98	†	...	...	
...	WR 105	7/5/98	...	24.1 ± 8.8	...	24.1 ± 8.8
...	WR 147	6/5/98	...	64.7 ± 40.6	...	64.7 ± 40.6
...	Cyg OB2 No.5	6/5/98	...	71.3 ± 25.3	...	46.3 ± 13.1
		3/7/98	37.2 ± 15.3	...	...	
...	Cyg OB2 No.8A	7/5/98	...	< 13.0‡	...	< 13.0‡
...	Cyg OB2 No.9	7/5/98	...	40.3 ± 15.6	...	40.3 ± 15.6
...	Cyg OB2 No.12	6/5/98	...	58.2 ± 20.6	...	51.9 ± 13.2
		3/7/98	47.5 ± 17.3	...	...	

NOTES: The seventh column gives the weighted mean of $\dot{M}$ (averaged over wavelength and date). † — It was not possible to derive $\dot{M}$ in a number of instances; see §5.4 for explanatory notes. ‡ — Because the mean flux detection for Cyg OB2 No.8A was (numerically) negative, the upper boundary of the error on the flux was used to derive an upper limit to the mass-loss rate.

given that the wavelength range, and hence range in R_ν, being considered here is rather small: 0.85–2 mm). However, at longer wavelengths, this approximation may result in an underestimate of R_ν, as T_e might reasonably be expected to be lower further out in the wind. In addition, it has been assumed that Z and γ are the same at all R_ν.

Table 5.4 gives values of R_ν for the program stars, calculated using Equation 5.9, at the relevant SCUBA wavelengths. Transformation from absolute to relative radius units was performed using the stellar radii provided in column 3. The characteristic radii of emission for WR 1 and HD 210839 were calculated using the weighted mean of $\dot{M}$ (averaged over date). The value of R_* adopted for the WR stars is the 'core radius' (see Schmutz *et al.*, 1989), defined as the inner boundary of the wind, where the expansion velocity of the outflow is negligible (this corresponds to a Rosseland optical depth of 20). This radius is typically smaller than the radius at which the optical continuum of WR stars is formed. The characteristic radius of emission for the WR stars is much greater than 10 R_*. Indeed, there are only two objects in the sample for which $R_\nu < 10\ R_*$: α Cyg and Cyg OB2 No.12. These stars have extremely large stellar radii (180 and 338 $R_\odot$, respectively), thus giving small R_ν upon transformation from absolute to relative units. For these objects, R_ν most probably lies in the region in which the wind is still accelerating. Adopting a flow velocity of v_∞ when using Equation 5.2 would therefore be inappropriate, resulting in too high an estimate of $\dot{M}$. The mass-loss rates listed in Table 5.3 for α Cyg and Cyg OB2 No.12 should therefore be treated with extreme caution. Certainly, they are ~ 4.7 and ~ 3.7 times higher, respectively, than the mass-loss rates derived from Hα in §4.

Table 5.4: Characteristic radii of emission for the SCUBA sample

HD	Name	R_*	Ref.	$R_\nu^{0.85\ \mathrm{mm}}$	$R_\nu^{1.35\ \mathrm{mm}}$	$R_\nu^{2\ \mathrm{mm}}$
		($R_\odot$)		(R_*)	(R_*)	(R_*)
4004	WR 1	2	S89	...	262	...
15570	...	22	H00	...	20	...
152236	ζ^1 Sco	103	B89	11	15	...
152408	WR 79A	35	B99	...	27	...
165688	WR 110	3	S89	...	244	...
165763	WR 111	1.8	HM99	...	338	...
169454	...	74	B89	...	10	...
193237	P Cyg	76	PP90	27	36	43
193793	WR 140	11	S89	...	65	...
197345	α Cyg/Deneb	180	A02	...	2.5	...
210839	λ Cep	19	H00	...	10	...
...	WR 95	...		...	†	...
...	WR 104	...		†	†	...
...	WR 105	23	B99	...	33	...
...	WR 147	21	M00	...	52	...
...	Cyg OB2 No.5	34	B89	15	32	...
...	Cyg OB2 No.8A	28	H01	...	$< 11^\ddagger$	...
...	Cyg OB2 No.9	22	H99	...	33	...
...	Cyg OB2 No.12	338	B89	3.8	6.2	...

NOTES: Sources for the stellar radii, R_*, are:- B89 — Bieging *et al.* (1989); S89 — Schmutz *et al.* (1989); PP90 — Pauldrach and Puls (1990); B99 — Bohannan and Crowther (1999); H99 — Herrero *et al.* (1999); HM99 — Hillier and Miller (1999); H00 — Herrero *et al.* (2000); M00 — Morris *et al.* (2000); H01 — Herrero *et al.* (2001); A02 — Aufdenberg *et al.* (2002).

The value of R_* adopted for WR 110 is the average radius of the WCL stars presented in Schmutz *et al.* (1989). † — In a number of instances, it was not possible to derive R_ν, because of the absence of a value of $\dot{M}$. ‡ — An outer limit to the radius of emission was calculated, using the derived upper limit to the mass-loss rate.

CHAPTER 6

Radio: Mass-Loss Rates

The new Hα and mm measurements presented in §4 and §5 sample the inner regions of the stellar wind (see Table 5.4). With a view to making comparisons with the mass-loss rates derived from these data, the results of a literature survey of published mm and cm fluxes are presented. These comprise observations of 53 Galactic early-type stars, sampling the wind at $\sim$10–100 R_*. Where a star has been detected at two or more wavelengths, the spectral index of the radio continuum has been calculated. For those sources with multiwavelength, multi-epoch detections, time-averaged spectral indices have been derived. Weighted mean fluxes (averaged over date) have been calculated for objects with multi-epoch observations at the same wavelength. These fluxes have been used, together with the relevant stellar parameters and Equation 5.2 (Wright and Barlow, 1975; Panagia and Felli, 1975), to derive time-averaged mass-loss rates (see Table 6.3). The incidence of nonthermal emission amongst the sample has also been examined, and the occurrence of binarity and excess X-ray flux amongst the nonthermal emitters been investigated, looking for evidence that might suggest a causal relationship between these phenomena.

6.1 Published observations

Published radio and mm data for 53 Galactic early-type stars are presented in Table 6.1. Also included are a number of new, unpublished observations (Howarth, personal communication), as well as the new mm detections presented in §5 (with some exclusions: see below). A subset of 36 stars is common with the Hα sample. The observations selected for inclusion have been restricted to definite flux detections; cases where only an upper

flux limit could be obtained have been excluded. Also, with two exceptions, only OB stars have been considered (i.e., WR stars are not included in this part of the study). The exceptions are HD 197345 (α Cyg) and HD 152408 (WR 79A). α Cyg has been included because of its presence in both the Hα sample and the new mm detections, thus permitting a multifrequency comparison of its mass-loss rate. HD 152408 was originally classified as O8:Iafpe by Walborn (1972), and its spectral type has been subject to some discussion (e.g. Crowther and Bohannan, 1997), with the star eventually being re-classified as WN9ha by Bohannan and Crowther (1999). For this reason, and because of the new mm detection of the star (see §5), it has been included here. Because of the very different nature of their wind emission, Be and B[e] stars (see §1.3.2) have also been excluded from the study, with the exception of HD 5394 (γ Cas), which is also present in the Hα sample.

The observations listed in Table 6.1 were acquired over the years 1976–2001, providing a good opportunity for multi-epoch analysis. Column 3 gives the date of the observation. The source of the data is indicated in column 4; references are provided on page 159. The detected fluxes and uncertainties thereon are given in columns 5–12. These data have been grouped into (narrow) wavelength bins to facilitate their display; however, when calculating spectral indices and mass-loss rates, exact wavelengths have been used. For stars that have been detected at *two* or more wavelengths, at *one* epoch, the spectral index (largely determined by weighted least-squares fits) is given in the final column. For objects with multi-epoch observations at the same wavelength, the weighted mean flux (averaged over date) at the relevant wavelength(s) is given immediately after the observations, in the row designated 'Mean'. The use of fluxes, weighted in proportion to the reciprocal of the square of the uncertainty, favours lower flux detections, as higher values with larger uncertainties are reduced in importance, and lower values with smaller uncertainties become dominant. This effect should be borne in mind throughout the analysis. For those sources with multiwavelength, multi-epoch detections, the time-averaged spectral index is given in the final column of the 'Mean' row. Where possible, the mean spectral index is the weighted average of indices determined from separate sets of contemporaneous observations. Where observations are sporadic, the mean spectral index is determined from a weighted least-squares fit to all available data. See §6.2.1 for futher comments regarding the calculation of spectral indices.

Table 6.1: Published radio and mm detections of Galactic early-type stars

HD	Name	Date	Ref.	Flux (mJy)								Spectral
		of obs.		0.8–0.85 mm	1.1–1.35 mm	7 mm	2 cm	3–3.6 cm	6–6.3 cm	13 cm	20–21 cm	index (α)
2905	κ Cas	13/10/94	S98					0.40 ± 0.03				...
5394	γ Cas	27/9/85	D90						0.23 ± 0.06			...
14947	...	13/10/94	S98					0.11 ± 0.03				...
15558	...	5/12/80	B89						0.5 ± 0.1			...
		89/90	†					0.50 ± 0.02				...
		Mean										0.00 ± 0.40
15570	...	5/12/80	B89						0.2 ± 0.1			...
		13–14/5/89	†					0.125 ± 0.025				...
		3/7/98	‡		4.76 ± 2.43							...
		Mean										-0.79 ± 0.28
17505	...	17–18/2/90	†					0.41 ± 0.02				...
26676	...	13/2/76	S77								11 ± 2	...
		28/12/76	S77						4.3 ± 1.1			...
		22/1/77	S77						3.3 ± 1.1			...
		6/2/77	S77						5.8 ± 1.2			...
		21/6/85	B89						0.48 ± 0.13			...
		26/9/86	D90						1.3 ± 0.2			...
		Mean							0.82 ± 0.11			-2.23 ± 1.56
30614	α Cam	21/6/85	B89						0.37 ± 0.07			...
		18/9/85	B89						0.32 ± 0.07			...
		13/10/94	S98				0.65 ± 0.13	0.44 ± 0.04	0.23 ± 0.05			1.11 ± 0.23
		Mean							0.29 ± 0.04			1.11 ± 0.23
34085	β Ori/Rigel	30/1/90	†					0.42 ± 0.03	0.29 ± 0.06			0.73 ± 0.43
36486	δ Ori A	5/12/80	B89						0.37 ± 0.12			...
		14/5/89	†					0.22 ± 0.02				...
		Mean										-1.02 ± 0.66

Continued overleaf

HD	Name	Date of obs.	Ref.	Flux (mJy) 0.8–0.85 mm	1.1–1.35 mm	7 mm	2 cm	3–3.6 cm	6–6.3 cm	13 cm	20–21 cm	Spectral index (α)
37128[a]	ϵ Ori	4/4/84	B02						0.67 ± 0.10			...
		21–22/3/86	B02						0.52 ± 0.06			...
		86–88	A94		12 ± 4							...
		29/1/90	B02					0.92 ± 0.05	0.71 ± 0.06			0.51 ± 0.20
		12/9/90	L91		13.1 ± 2.2							...
		12/10/94	B02				1.65 ± 0.20	1.00 ± 0.06	0.69 ± 0.06			0.79 ± 0.90
		19/5/95	B02						0.47 ± 0.05			...
		28/1–9/3/99	B02						0.51 ± 0.11			...
		5/2/99	B02					0.95 ± 0.07	0.94 ± 0.09			0.02 ± 0.24
		6/2/99	B02					0.95 ± 0.08	0.77 ± 0.10			0.41 ± 0.30
		7/2/99	B02					1.01 ± 0.09	0.81 ± 0.10			0.43 ± 0.30
		8/2/99	B02					0.95 ± 0.08	0.78 ± 0.09			0.39 ± 0.28
		9/2/99	B02					0.95 ± 0.06	0.77 ± 0.07			0.41 ± 0.22
		12/10/00	B02	17.3 ± 2.1								...
		21/12/00	B02						0.70 ± 0.06			...
		Mean			12.8 ± 1.9			0.96 ± 0.03	0.66 ± 0.02			0.37 ± 0.10
37468	σ Ori AB	5/3/84	D90						1.51 ± 0.05			...
		4/4/84	D90				1.20 ± 0.07		1.50 ± 0.06			-0.20 ± 0.06
		2/7/84	D90				2.50 ± 0.25		1.95 ± 0.13			0.23 ± 0.11
		11/3/85	D90				1.40 ± 0.28		2.15 ± 0.20			-0.39 ± 0.20
		16/3/85	D90				1.65 ± 0.16		1.80 ± 0.18		1.05 ± 0.18	-0.07 ± 0.91
		Mean					1.35 ± 0.06		1.57 ± 0.04			-0.12 ± 0.05
37742	ζ Ori	13/7/79	A80						0.7 ± 0.2			...
		87–89	A94		14 ± 2							...
		13/5/89	†					0.81 ± 0.04				...
		Mean										0.81 ± 0.51
41117	χ^2 Ori	29/1/90	†					0.42 ± 0.03				...
		12/9/94	S98					0.44 ± 0.08	0.27 ± 0.06			0.86 ± 0.50
		13/10/94	S98				0.63 ± 0.13	0.38 ± 0.04				0.90 ± 0.41
		Mean						0.41 ± 0.02				0.88 ± 0.32
47839	15/S Mon	24/1/87	D90						0.40 ± 0.13			...
57060	UW CMa	89/90	†					0.32 ± 0.03				...
57061	τ CMa	13/5/89	†					0.29 ± 0.02				...

Continued overleaf

HD	Name	Date of obs.	Ref.	Flux (mJy) 0.8–0.85 mm	1.1–1.35 mm	7 mm	2 cm	3–3.6 cm	6–6.3 cm	13 cm	20–21 cm	Spectral index (α)
66811[b]	ζ Pup	12/7/79	A80						1.4 ± 0.3			...
		6/3/84	B89				3.0 ± 0.2		1.3 ± 0.1			0.76 ± 0.09
		13/5/89	†					1.44 ± 0.06				...
		12/9/90	L91		20.2 ± 1.8							...
		Mean							1.31 ± 0.09			0.76 ± 0.09
80077	PV Vel	7/9/94	L95					0.50 ± 0.11	0.37 ± 0.10			0.53 ± 0.61
93250	...	7/9/94	L95					1.36 ± 0.17				...
149404	V918 Sco	31/5/89	†					0.55 ± 0.03				...
149757	ζ Oph	31/5/89	†					0.13 ± 0.02				...
151804	...	8/5/81	B89						0.4 ± 0.1			...
		18/8/85	B89				0.4 ± 0.1					...
		18–20/3/00	S02					0.64 ± 0.08	0.62 ± 0.07			0.05 ± 0.24
		23/10/00	S02					0.75 ± 0.14	0.84 ± 0.10	1.02 ± 0.17		-0.16 ± 2.47
		Mean						0.67 ± 0.07	0.62 ± 0.05			0.05 ± 0.24
152236	ζ^1 Sco	7/5/81	B89						1.2 ± 0.3			...
		9/3/84	B89						2.0 ± 0.3			...
		3/4/84	B89				4.3 ± 0.1		1.9 ± 0.2			0.74 ± 0.10
		12/9/90	L91		23.0 ± 2.4							...
		5/5/98	‡	52.7 ± 10.0	38.4 ± 3.9							0.68 ± 0.46
		18–20/3/00	S02					2.90 ± 0.31	1.56 ± 0.08			0.90 ± 0.17
		24/10/00	S02					2.88 ± 0.33	1.38 ± 0.28			1.06 ± 0.34
		Mean			27.2 ± 2.0			2.89 ± 0.23	1.59 ± 0.07			0.79 ± 0.08
152408	WR 79A	4/3/84	B89						1.0 ± 0.1			...
		3/4/84	B89				2.4 ± 0.1		1.1 ± 0.1			0.71 ± 0.09
		12/9/90	L91		14.7 ± 3.1							...
		10/5/98	‡		23.3 ± 4.4							...
		6/11/00	S02					0.93 ± 0.12	0.76 ± 0.06	0.96 ± 0.09		0.05 ± 4.21
		Mean			17.6 ± 2.5				0.88 ± 0.05			0.71 ± 0.09
152424	...	31/5/89	†					0.16 ± 0.03				...
		9/11/00	S02						0.24 ± 0.05			...
		Mean										-0.79 ± 0.55
152623		7/11/00	S02					0.24 ± 0.06	0.44 ± 0.07	0.75 ± 0.09	0.76 ± 0.11	-0.79 ± 0.24
153919	...	31/5/89	†					0.43 ± 0.03				...

Continued overleaf

HD	Name	Date of obs.	Ref.	Flux (mJy) 0.8–0.85 mm	1.1–1.35 mm	7 mm	2 cm	3–3.6 cm	6–6.3 cm	13 cm	20–21 cm	Spectral index (α)
160529	...	7/9/94	L95					5.08 ± 0.11	3.82 ± 0.10			0.50 ± 0.06
164794	9 Sgr	13/7/79	A80						1.0 ± 0.4			...
		22/5/80	A81						1.8 ± 0.3			...
		9/2/82	A84						2.5 ± 0.3			...
		26/5/82	A84						2.4 ± 0.3		3.6 ± 0.3	−0.34 ± 0.13
		22/8/83	A84						1.5 ± 0.2		3.9 ± 0.4	−0.79 ± 0.14
		25/8/83	F85						1.3 ± 0.5			...
		27/11/84	B89						2.0 ± 0.2			...
		28/1/85	B89						1.5 ± 0.1			...
		16/2/85	B89				0.7 ± 0.1		1.9 ± 0.1			−0.91 ± 0.14
		8/3/01	R02					1.6 ± 0.4	2.8 ± 0.4		4.5 ± 1.2	−0.52 ± 1.46
		Mean							1.8 ± 0.1		3.7 ± 0.2	−0.66 ± 0.08
166734	...	9/3/84	B89						0.5 ± 0.1			...
		21/6/85	B89						0.3 ± 0.1			...
		18/8/85	B89				0.4 ± 0.1					...
		Mean							0.4 ± 0.1			0.15 ± 0.27
167971[c]	MY Ser	4/3/84	B89						15.4 ± 0.2			...
		4/4/84	B89				7.0 ± 0.2		13.8 ± 0.1			−0.62 ± 0.03
		27/11/84	B89				8.0 ± 1.0		17.0 ± 1.0		25.0 ± 2.0	−0.52 ± 0.78
		21/12/84	B89				4.7 ± 0.1		15.7 ± 0.1		26.3 ± 0.3	−0.82 ± 0.11
		16/2/85	B89				6.6 ± 0.1		14.1 ± 0.1		23.2 ± 0.2	−0.56 ± 0.08
		10/11/89	P90								6.9 ± 2.0	...
		27/4/95	C96				5.8 ± 0.1	7.42 ± 0.04	7.75 ± 0.11			−0.26 ± 0.16
		Mean					5.8 ± 0.1		13.2 ± 0.1		24.2 ± 0.2	−0.61 ± 0.03
168112	...	9/3/84	B89						1.3 ± 0.1			...
		4/4/84	B89				1.2 ± 0.2		1.9 ± 0.1			−0.42 ± 0.16
		21/12/84	B89				1.3 ± 0.1		5.4 ± 0.1		8.2 ± 0.3	−0.47 ± 0.27
		Mean					1.28 ± 0.09		2.87 ± 0.06			−0.43 ± 0.14
168607	...	7/9/94	L95					0.85 ± 0.12				...
169454	...	9/3/84	B89						1.1 ± 0.1			...
		3/4/84	B89				1.9 ± 0.1		1.0 ± 0.1			0.58 ± 0.10
		7–12/3/89	A94		17 ± 3							...
		12/6/98	‡		11.4 ± 4.9							...
		Mean			15.5 ± 2.6				1.05 ± 0.07			0.58 ± 0.10

Continued overleaf

HD	Name	Date of obs.	Ref.	Flux (mJy) 0.8–0.85 mm	1.1–1.35 mm	7 mm	2 cm	3–3.6 cm	6–6.3 cm	13 cm	20–21 cm	Spectral index (α)
169515	RY Sct	86–88	A94		147 ± 15							...
169582	...	17/2/90	†					0.070 ± 0.023				...
190429A	...	13/10/94	S98					0.28 ± 0.03				...
190603	...	13/7/79	A80						0.5 ± 0.2			...
		12/9/94	S98				0.70 ± 0.20	0.70 ± 0.10	0.58 ± 0.06			0.24 ± 0.87
		Mean							0.57 ± 0.06			0.24 ± 0.87
192281	...	17/2/90	†					0.094 ± 0.024				...

Continued overleaf

HD	Name	Date of obs.	Ref.	Flux (mJy) 0.8–0.85 mm	1.1–1.35 mm	7 mm	2 cm	3–3.6 cm	6–6.3 cm	13 cm	20–21 cm	Spectral index (α)
193237[d]	P Cyg	4/11/78	A80						10.8 ± 1.0			...
		22/5/80	A81						5.7 ± 0.5			...
		17/4/81	W82						9.5 ± 0.2			...
		16/10/81	B89						5.1 ± 0.2			...
		26/8/82	B89						1.6 ± 0.4			...
		9/5/83	B89				16.6 ± 0.5		6.7 ± 0.2		3.0 ± 1.5	0.82 ± 0.42
		86 - 88	A94		146 ± 15							...
		9/86–1/93	Sk98				17 ± 1		10 ± 1			0.48 ± 0.11
		12/90–2/91	Sk98						8.6 ± 0.5			...
		3/92	†	235 ± 10	144 ± 8							1.13 ± 14.8
					171 ± 12							...
		1/7/92	E02						8.4 ± 0.5			...
		4/8/92	E02						11.3 ± 1.3			...
		1/93	†	210 ± 20	140 ± 10							1.76 ± 25.5
					98 ± 12							...
		17/4/94	C96			27.4 ± 1.2		9.41 ± 0.04	5.65 ± 0.05			0.92 ± 0.14
		13/10/94	S98				17.3 ± 0.30	10.7 ± 0.07	6.50 ± 0.20			0.89 ± 0.31
		27/4/95	C96			33.8 ± 0.5	16.6 ± 0.2	12.18 ± 0.04	9.13 ± 0.07			0.57 ± 0.11
		15/1/97	E02						8.9 ± 0.5			...
		16/1/97	E02						10.4 ± 2.4			...
		19/1/97	E02						9.4 ± 0.6			...
		30/1/97	E02						5.8 ± 0.3			...
		27/2/97	E02						6.4 ± 0.4			...
		5/5/98	‡		126 ± 3							1.07 ± 0.14
					82.7 ± 4.2							...
		3/7/98	‡	177 ± 10								...
		8/5/01	E02						4.8 ± 0.4			...
		Mean		206 ± 7	130 ± 3	32.9 ± 0.5	16.8 ± 0.2	10.78 ± 0.03	6.81 ± 0.04			0.71 ± 0.06
194279	...	12/9/94	S98					0.44 ± 0.10	0.28 ± 0.08			0.79 ± 0.64
195592	...	12/9/94	S98					0.42 ± 0.10	0.27 ± 0.07			0.77 ± 0.62
		13/10/94	S98				0.90 ± 0.13	0.53 ± 0.04	0.30 ± 0.07			1.00 ± 0.34
		Mean						0.51 ± 0.04	0.29 ± 0.05			0.95 ± 0.30

Continued overleaf

HD	Name	Date of obs.	Ref.	Flux (mJy) 0.8–0.85 mm	1.1–1.35 mm	7 mm	2 cm	3–3.6 cm	6–6.3 cm	13 cm	20–21 cm	Spectral index (α)
197345	α Cyg/Deneb	29/1/90	A02					0.23 ± 0.05				...
		4/5/98	‡		7.81 ± 1.87							...
		Mean										1.07 ± 0.10
206267A	...	27/9/85	D90						0.27 ± 0.06			...
210839	λ Cep	12/7/79	A80						0.80 ± 0.25			...
		31/5/89	†					0.35 ± 0.03				...
		4/5/98	‡		4.25 ± 1.92							...
		1/6/98	‡		8.87 ± 3.58							...
		Mean			5.28 ± 1.69							0.81 ± 0.72
...	Cyg OB2 No.5	22/5/80	A81						1.8 ± 0.3			...
		31/7/83	P85						5.8 ± 0.7			...
		25/8/83	F85						5.5 ± 0.3			...
		6/1/84	P85				7.4 ± 0.8		6.3 ± 0.3		4.4 ± 0.4	0.25 ± 0.45
		86–88	A94		55 ± 5							...
		5/91	†		42 ± 9							...
		4/7/91	W98						5.69 ± 0.16			...
		3/92	†		42 ± 5							...
		24/6/92	W98					7.24 ± 0.06				...
		1/5/93	W98					3.27 ± 0.07	2.48 ± 0.08			0.54 ± 0.08
		17/4/94	C96			9.4 ± 1.1		3.33 ± 0.04	2.02 ± 0.05			0.87 ± 0.30
		27/4/95	C96			14.3 ± 0.6	8.8 ± 0.1	7.48 ± 0.04	5.15 ± 0.10			0.44 ± 0.14
		27/12/96	C97					7.89 ± 0.02				...
		4/1/97	C97						6.73 ± 0.03			...
		6/5/98	‡		42.0 ± 3.4							...
		3/7/98	‡	22.8 ± 6.6								...
		Mean			44.9 ± 2.4	13.2 ± 0.5	8.78 ± 0.10	6.89 ± 0.02	5.20 ± 0.02			0.53 ± 0.07
...	Cyg OB2 No.7	22/5/80	A81						0.4 ± 0.2			...

Continued overleaf

HD	Name	Date of obs.	Ref.	Flux (mJy) 0.8–0.85 mm	1.1–1.35 mm	7 mm	2 cm	3–3.6 cm	6–6.3 cm	13 cm	20–21 cm	Spectral index (α)
...	Cyg OB2 No.8A	22/5/80	A81						1.0 ± 0.2			...
		4/3/84	B89						0.8 ± 0.1			...
		4/4/84	B89				0.5 ± 0.2		0.7 ± 0.1			-0.31 ± 0.39
		21/12/84	B89						0.4 ± 0.1		1.0 ± 0.1	-0.76 ± 0.22
		4/7/91	W98						*0.66 ± 0.10*			...
		24/6/92	W98					0.94 ± 0.06				...
		1/5/93	W98					0.94 ± 0.05	1.04 ± 0.08			-0.20 ± 0.18
		Mean						0.94 ± 0.04	0.76 ± 0.04			-0.41 ± 0.13
...	Cyg OB2 No.9[e]	22/5/80	A81						7.1 ± 0.4			...
		16/10/81	A84						4.3 ± 0.4			...
		9/2/82	B89						2.5 ± 0.3			...
		27/3/82	W83						7.87 ± 0.03			...
		1/7/82	W83				8 ± 2		7.5 ± 0.2		4.8 ± 0.5	0.34 ± 0.60
		26/8/82	A84						4.6 ± 0.2		4.5 ± 0.2	0.02 ± 0.05
		9/5/83	A84				1.2 ± 0.3		0.65 ± 0.20			0.56 ± 0.36
		22/8/83	A84						1.6 ± 0.2			...
		4/3/84	B89						5.6 ± 0.1			...
		4/4/84	B89				4.2 ± 0.2		6.0 ± 0.4			-0.33 ± 0.07
		27/11/84	B89				6.2 ± 0.6		8.1 ± 0.1		6.3 ± 0.2	0.16 ± 0.21
		21/12/84	B89				5.7 ± 0.1		7.4 ± 0.1		4.9 ± 0.1	0.06 ± 0.09
		13/1/85	B89				4.5 ± 1.1					...
		16/2/85	B89				5.1 ± 0.1					...
		12/6/85	B89				4.4 ± 0.3		5.3 ± 0.2			-0.17 ± 0.07
		86–88	A94		24 ± 3							...
		10/11/89	P90								10.4 ± 0.9	...
		4/7/91	W98						5.97 ± 0.17			...
		3/92	†		5 ± 6							...
		24/6/92	W98					7.30 ± 0.07				...
		1/5/93	W98					4.02 ± 0.05	2.98 ± 0.08			0.59 ± 0.06
		17/4/94	C96			3.9 ± 1.0		7.67 ± 0.04	7.93 ± 0.05			-0.07 ± 0.13
		27/4/95	C96				1.8 ± 0.2					...
		7/5/98	‡		20.0 ± 4.4							...
		Mean			20.1 ± 2.3		4.8 ± 0.1	6.42 ± 0.03	7.11 ± 0.02		5.1 ± 0.1	0.06 ± 0.03

Continued overleaf

HD	Name	Date of obs.	Ref.	Flux (mJy) 0.8–0.85 mm	1.1–1.35 mm	7 mm	2 cm	3–3.6 cm	6–6.3 cm	13 cm	20–21 cm	Spectral index (α)
...	Cyg OB2 No.12[f]	22/5/80	A81						3.2 ± 0.3			...
		16/10/81	B89				6.0 ± 2.0		3.4 ± 0.2			0.52 ± 0.31
		27/3/82	W83						4.5 ± 0.3			...
		26/8/82	B89						2.2 ± 0.2		2.0 ± 0.2	0.08 ± 0.11
		86–89	A94		41 ± 4							...
		5/91	†	84 ± 18	41 ± 6							2.26 ± 0.82
		3/92	†		40 ± 10							...
		1/5/93	W98					6.06 ± 0.07	3.94 ± 0.07			0.80 ± 0.04
		12/9/94	S98				7.70 ± 0.30	4.74 ± 0.14	4.00 ± 0.20			0.60 ± 0.43
		13/10/94	S98				12.0 ± 0.20	7.40 ± 0.08	5.03 ± 0.10			0.78 ± 0.21
		27/4/95	C96			22.9 ± 0.6	11.3 ± 0.1	7.18 ± 0.04	3.64 ± 0.12			0.86 ± 0.14
		6/5/98	‡		42.6 ± 3.0							...
		3/7/98	‡	40.9 ± 5.6								...
		Mean		44.7 ± 5.3	41.8 ± 2.2		11.1 ± 0.1	6.87 ± 0.03	4.01 ± 0.05			0.73 ± 0.04
...	V433 Sct	12/9/94	S98					0.72 ± 0.08	0.63 ± 0.05			0.23 ± 0.24
		13/10/94	S98				1.10 ± 0.20	0.97 ± 0.05	0.53 ± 0.07			0.77 ± 3.61
		Mean						0.90 ± 0.04	0.60 ± 0.04			0.23 ± 0.24
...	MWC 349	86–89	A94		1630 ± 163							...

NOTES: Sources for the observations and notes pertaining to individual stars are provided on page 159.

NOTES TO TABLE 6.1: Data are from: S77 — Strom and Harris (1977); A80 — Abbott *et al.* (1980); A81 — Abbott *et al.* (1981); W82 — White and Becker (1982); W83 — White and Becker (1983); A84 — Abbott *et al.* (1984*a*); F85 — Florkowski *et al.* (1985); P85 — Persi *et al.* (1985); B89 — Bieging *et al.* (1989); D90 — Drake (1990); P90 — Phillips and Titus (1990); L91 — Leitherer and Robert (1991); A94 — Altenhoff *et al.* (1994); L95 — Leitherer *et al.* (1995); C96 — Contreras *et al.* (1996); C97 — Contreras *et al.* (1997); S98 — Scuderi *et al.* (1998); Sk98 — Skinner *et al.* (1998); W98 — Waldron *et al.* (1998); A02 — Aufdenberg *et al.* (2002); B02 — Blomme *et al.* (2002); E02 — Exter *et al.* (2002); S02 — Setia Gunawan *et al.* (2002); R02 — Rauw *et al.* (2002*a*); † — Howarth (personal communication — some of the observations from 1989 and 1990 were first published in Lamers and Leitherer (1993); the values listed here are from a re-reduction of the original Very Large Array [VLA] data, performed by I. D. Howarth); ‡ — this thesis.

Notes to individual stars:-

(a) HD 37128 (ϵ Ori) — The data from Blomme *et al.* (2002, B02) comprise, in addition to new observations, re-reductions of published (Scuderi *et al.*, 1998) and unpublished, archival VLA observations. On the basis of their observed fluxes and their failure to detect ϵ Ori upon re-reduction of the archival VLA data, Blomme *et al.* (2002) found the 6-cm, 1.6 ± 0.5 mJy detection of November 5th, 1978, reported by Abbott *et al.* (1980), to be in error. Thus, it has not been included here.

(b) HD 66811 (ζ Pup) — An extensive set of new radio and sub-millimetre observations, supplemented by re-reductions of published and unpublished archival VLA observations will be presented by Blomme *et al.* (2003).

(c) HD 167971 (MY Ser) — The 6.9 ± 2.0 mJy detection of Phillips and Titus (1990, P90) is at 18 cm; it is binned with the 20–21 cm data simply for display purposes.

(d) HD 193237 (P Cyg) — The 1986–83 and 1990–91 data from Skinner *et al.* (1998, Sk98) are mean fluxes obtained from long-term monitoring with the VLA and the Broad Band Interferometer (BBI) at Jodrell Bank, respectively. The July 1st and August 4th, 1992 data from Exter *et al.* (2002, E02) are re-reductions of the Multi-Element Radio Linked Interferometer Network (MERLIN) datasets first presented in Skinner *et al.* (1997), and misidentified as having being observed on August 4th and June 24th, 1992, respectively. The new 82.7 ± 4.2 mJy detection from May 5th, 1998 is at 2 mm; it is binned with the 1.1–1.35 mm data simply for display purposes. Further observations are given by van den Oord *et al.* (1985).

(e) Cyg OB2 No.9 — The 10.4 ± 0.9 mJy detection of Phillips and Titus (1990, P90) is at 18 cm; it is binned with the 20–21 cm data simply for display purposes.

(f) Cyg OB2 No.12 — Further observations are given by Becker and White (1985).

See §6.2.1 for comments regarding the calculation of spectral indices for the sample.

Figure 6.1 shows the location of the radio sample in the H-R diagram. The ZAMS line for solar metallicity is included for reference (taken from Meynet *et al.*, 1994). The $\log L$ and $T_{\rm eff}$ values were largely taken from the literature and are given, along with the relevant references, in Table 6.2. Figure 6.2 is a histogram showing the distribution over spectral type of the stellar sample (see Table 6.2 for spectral classifications), which comprises 34 O stars, seventeen B stars, one A supergiant (α Cyg), and one WR star (HD 152408). As with the Hα sample, there is a bias towards supergiants (higher luminosity stars are more easily detected at radio wavelengths), with 38 stars of luminosity class I–II, three of luminosity class III, and twelve of luminosity class IV–V. The radio sample is more evenly spread over the O-star subtypes than the Hα sample; the sharp peak in sampling at spectral types O9–O9.7 is absent. B stars are also better represented here (especially the early subtypes).

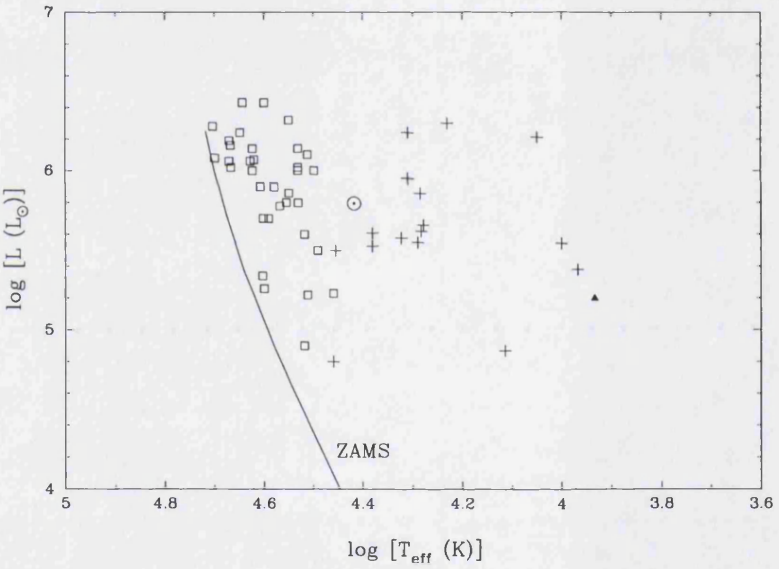

Figure 6.1: Temperature-luminosity H-R diagram showing the location of the radio sample stars. '□' represent O stars, '+' represent B stars, '▲' represents the A2Ia star, α Cyg, and '⊙' represents the WR star, HD 152408. The ZAMS line for solar metallicity is also given (Meynet *et al.*, 1994). HD 26676, with a luminosity of $\log L\ (L_{\odot}) = 2.26$, lies outside the range of the plot.

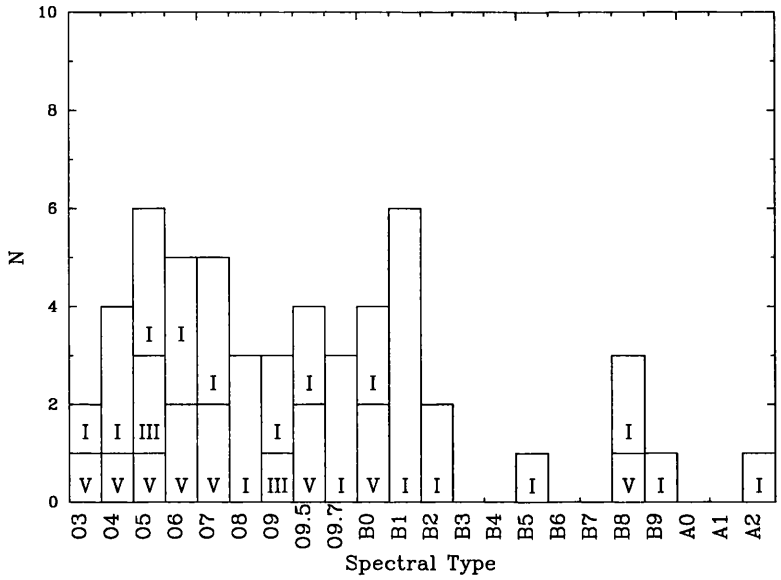

Figure 6.2: Histogram showing the distribution over spectral type of the radio sample. 'I' denotes luminosity class I–II, 'III' denotes luminosity class III, and 'V' denotes luminosity class IV–V. For the purposes of this figure, the WR star, HD 152408, has been ascribed its original O8:Iafpe spectral classification (Walborn, 1972).

6.2 Spectral index

The spectral index, α, of a source describes how the observed flux varies with frequency. Mathematically, the spectral index can be defined as:-

$$\alpha(\nu_1, \nu_2) = \frac{\log(S_{\nu_1}/S_{\nu_2})}{\log(\nu_1/\nu_2)} \tag{6.1}$$

or more simply:-

$$\alpha = \frac{d\log S_\nu}{d\log \nu} \tag{6.2}$$

where S_ν is the observed flux at frequency ν. Thus, in general:-

$$S_\nu \propto \nu^\alpha \tag{6.3}$$

Using Wright and Barlow's (1975) result for an isothermal, spherically symmetric, stationary outflow at constant velocity (Equation 5.1), it can be seen that:-

$$S_\nu \propto (g_\nu \nu)^{2/3} \tag{6.4}$$

The Gaunt factor (Equation 5.6) at mm and cm wavelengths is such that:-

$$g_\nu \propto \nu^{-0.1} \tag{6.5}$$

meaning that within this wavelength regime, the characteristic thermal (i.e., free–free) spectrum of a hot star undergoing mass loss has the following frequency dependence:-

$$S_\nu \propto \nu^{0.6} \tag{6.6}$$

i.e., $\alpha = 0.6$. A *nonthermal* source invariably has a much flatter (i.e., $\alpha < 0.6$) spectral index than the $\nu^{0.6}$ power law expected from a thermally-emitting region (e.g. Abbott *et al.*, 1984*a*; Contreras *et al.*, 1996). Indeed, many stars are observed to have spectral indices $\alpha \leq 0$ (e.g. Bieging *et al.*, 1989), making them readily distinguishable from sources exhibiting a thermal spectrum.

6.2.1 Observed spectral indices

Equation 6.2 implies that a plot of $\log S_\nu$ against $\log \nu$ will yield the spectral index, α, over a given frequency range. For each star in Table 6.1 for which there are contemporaneous multiwavelength observations available (34 of the 53 objects listed), the spectral index has been derived. These are given in the final column of Table 6.1. The spectral indices for stars observed at *three* or more frequencies were obtained from weighted least-squares fits to the data; those indices based on only *two* flux measurements were calculated using Equation 6.2. Because of the longer wavelength baseline, the spectral indices derived from a combination of both mm and cm data are (in general) less uncertain than those obtained from cm data alone.

For sources with multiwavelength, multi-epoch detections, a mean, time-averaged value for the slope, α, of the radio spectrum has been derived. These are provided in the final column of the 'Mean' row in Table 6.1, and are summarised in Table 6.4. Where possible, the mean spectral index is the weighted average of indices determined from separate sets of contemporaneous observations. Where observations are sporadic, the mean spectral index is determined from a weighted least-squares fit to *all* available data (the associated errors include only the formal errors resulting from the fit). Caution must be exercised when interpreting an index derived using the latter method. Consider a source which has a constant spectral index, but varies in intensity (at all wavelengths). If observations are made at different frequencies, at different times, a spectral index will be derived which is not representative of the true value at *any* time.

The λ^{-4}-dependence of the photospheric flux (compared to the λ^{-2}-dependence of the free–free flux) might suggest that detection of free–free radiation at radio wavelengths

is easier than at shorter wavelengths, because the photospheric contamination is less. However, the actual level of free–free 'excess' (in mJy) is less at longer wavelengths, making detection more difficult (in practice, only the most luminous OB stars with strong stellar winds, opaque to free–free radiation out to hundreds of stellar radii are detected; e.g. Bieging *et al.*, 1989). Within the radio regime, the spectral index should be constant with wavelength (and time) for thermal emission; the spectral index for *nonthermal* emitters has been observed to steepen for wavelengths shorter than ~ 6 cm (and also show temporal variability).

The *time-averaged* radio spectrum of Cyg OB2 No.9 displays a very flat spectral index, of $\alpha = 0.06 \pm 0.03$. At *specific epochs*, however, the star has exhibited negative, positive, or even complex spectral indices. This might be explicable in terms of (variable) nonthermal emission, with an underlying thermal contribution from the stellar wind (Cyg OB2 No.9 is an extremely luminous star, so an observable thermal contribution would be expected). At two epochs, May 9th, 1983, and May 1st, 1993, Cyg OB2 No.9 exhibited a positive spectral index, of $\alpha = 0.56 \pm 0.36$ and $\alpha = 0.59 \pm 0.06$, respectively. These distributions are indicative of free–free emission, perhaps suggesting that the nonthermal component was absent at these times. Coincident with these events were significant decreases in absolute flux levels (see Table 6.1), again suggestive of an 'absent' nonthermal contribution. Interestingly, the level of intensity of the 6 cm flux was a factor ~ 4 greater in May 1993, which, assuming that the observed emission at these epochs was thermal, implies an increase in mass-loss rate of a factor of ~ 3, as compared to May 1983. If $\dot{M}$ is calculated using the lower, May 1983 flux (this is the lowest 6-cm flux recorded for Cyg OB2 No.9), the result is still a factor ~ 2 higher than the Hα mass-loss rate derived in §4 (see the notes to Table 6.3, on page 176, for a comparison of the values). It would be desirable to obtain multiwavelength observations (including Hα) of Cyg OB2 No.9 at other epochs of decreased flux (February 9th, 1982, and August 22nd, 1983, also saw reduced emission), to investigate whether or not the nonthermal contribution ever disappears entirely.

The seemingly anomalously high spectral index of $\alpha = 2.26 \pm 0.82$, displayed by Cyg OB2 No.12 in May 1991, could well be attributable to the very short wavelength baseline used in the calculation (the result, however, is only $\sim 2\sigma$ away from $\alpha = 0.6$).

6.3 Calculating radio mass-loss rates

Hot-star winds are opaque at radio wavelengths, which enables measurements of the free–free continuum from ~ 1 mm–20 cm to be used to determine mass-loss rates (e.g. Abbott *et al.*, 1980, 1981; Leitherer and Robert, 1991; Leitherer *et al.*, 1995; Scuderi *et al.*, 1998, and see also §5.5 of this thesis). The radio fluxes listed in Table 6.1 are used with Equation 5.2 (Wright and Barlow, 1975; Panagia and Felli, 1975) to calculate mass-loss rates for the stellar sample. Where possible, weighted mean fluxes (averaged over date) are used. The mass-loss rates thus derived are done so assuming that the observed radio fluxes are due to *free–free* emission. For some of the objects considered, this may not be the case; the implications of this will be considered in §6.4.2.

Table 6.2 lists the adopted stellar and wind parameters used in the caculation of $\dot{M}$ (a homogeneous set of parameters has been used throughout this thesis). For multiple objects, the parameters refer to the primary. Where possible, data have been taken from the literature, but in certain instances reasonable assumptions were made on the basis of spectral type and luminosity class. Additionally, in some cases, atmospheric parameters were calculated using Equation 4.1. A discussion of the parameters used to calculate mass-loss rates from *mm* continuum emission is presented in §5.6. The wavelength regime now being considered, however, extends from 0.8 mm to 21 cm. This implies that any assumptions made regarding the parameters must be robust over distances in the wind from ~ 10–$100\ R_*$ (see Equation 5.1). These assumptions and their associated uncertainties are now considered.

6.3.1 Stellar and wind parameters

- **Distance, *d*.** An uncertainty of 20% is assumed if a star is supposedly an established member of a cluster, and 40% for a field star.

- **Terminal wind velocity, v_∞.** Terminal velocities, typically obtained from UV resonance lines, which sample the wind at $\sim 10\ R_*$, are extrapolated to the region of the radio (cm) 'photosphere', assuming that v_∞ is constant over this distance. An uncertainty of 10% is assumed on the value of v_∞.

- **Wind electron temperature, T_e.** With the exception of the WR star in the sample (HD 152408; see §5.6.3), Drew's (1989) result that $T_e \approx 0.4\ T_{\rm eff}$ has been

adopted. For simplicity, it has been assumed that the electron temperature is the same at all radii in the wind (although T_e probably decreases further away from the star). Any error on T_e has been neglected, due to the extremely weak temperature dependence (through the Gaunt factor) of the mass-loss rate.

- **Mean molecular weight, μ.** For the stars under consideration, reasonable abundance variations in elements heavier than helium are not likely to affect the mean molecular weight, or the number of free electrons, significantly (Willis, 1991). Hence, the values of μ (along with Z and γ) can be determined solely by the relative H and He abundances. An uncertainty of 10% is assumed on the value of μ.

- **Mean ionic charge, Z, and number of free electrons per ion, γ.** Hydrogen is assumed to be ionised in the winds of all the stars under consideration (with the exception of α Cyg; see §5.6.6). For the O and early-B stars in the sample (and for HD 152408), it has been assumed that helium is singly ionised at the mm and cm photospheres. HD 26676, β Ori, HD 160529, HD 168607, α Cyg and Cyg OB2 No.12, however, have lower wind electron temperatures ($T_e \lesssim 5000$ K); for these stars it is assumed that helium is predominantly neutral. See §5.6.5 for further comment. For simplicity, it has been assumed that Z and γ are the same at all radii in the wind. An uncertainty of 10% is assumed on the values of Z and γ.

- **Errors.** As for the mm mass-loss rates derived in §5, the uncertainties associated with $\dot{M}$ were calculated by propagating errors (see Equation 5.8). The errors on S_ν are taken from Table 6.1; these do not take into account possible additional flux calibration errors of order 10%.

Table 6.2: Adopted parameters for the radio sample

HD	Name	Spectral type	d (kpc)	Cluster	$\log L$ ($L_\odot$)	$T_{\rm eff}$ (K)	v_∞ (km s^{-1})	μ	Z	γ	$T_{\rm e}$ (K)
2905	κ Cas	BC0.7Ia	1.10	Cas OB14	5.61$^{\rm M99}$	24 000$^{\rm M99}$	1105	1.3	1.0	1.0	9 600
5394	γ Cas	B0.5IVe$^{\rm R68}$	0.23$^{\rm R68}$	...	4.80	28 800	1600$^{\rm B89}$	1.3	1.0	1.0	11 500
14947	...	O5If+$^{\rm W73}$	2.29	Per OB1	5.70$^{\rm H00}$	40 000$^{\rm H00}$	2400$^{\rm H00}$	1.6	1.0	1.0	16 000
15558	...	O5III(f)$^{\rm W71}$	2.19	Cas OB6	6.16$^{\rm H00}$	46 500$^{\rm H00}$	2800$^{\rm H00}$	1.2	1.0	1.0	18 600
15570	...	O4If+$^{\rm W71}$	2.19	Cas OB6	6.14$^{\rm H00}$	42 000$^{\rm H00}$	2600$^{\rm H00}$	1.5	1.0	1.0	16 800
17505	...	O6.5V((f))	2.19	Cas OB6	5.9$^{\rm H89}$	40 500$^{\rm H89}$	2310	1.3	1.0	1.0	16 200
26676	...	B8Vn$^{\rm C72}$	0.14$^{\rm R68}$	Tau R2	2.26	12 000	200†	1.3	1.0	0.9	4 800
30614	α Cam	O9.5Ia$^{\rm W71}$	0.87$^{\rm M99}$	...	5.6$^{\rm S99}$	33 000$^{\rm S99}$	1590	1.4	1.0	1.0	13 200
34085	β Ori/Rigel	B8Ia$^{\rm M55}$	0.50	Ori OB1	4.87$^{\rm M99}$	13 000$^{\rm M99}$	500$^{\rm L88}$	1.3	1.0	0.9	5 200
36486	δ Ori A	O9.5II	0.50	Ori OB1	5.8$^{\rm S99}$	34 000$^{\rm S99}$	2060	1.3	1.0	1.0	13 600
37128	ϵ Ori	B0Ia$^{\rm W71}$	0.50	Ori OB1	5.50$^{\rm M99}$	28 500$^{\rm M99}$	1910	1.6	1.0	1.0	11 400
37468	σ Ori AB	O9.5V$^{\rm M55}$	0.50	Ori OB1	4.9$^{\rm H89}$	33 000$^{\rm H89}$	2150$^{\rm L88}$	1.3	1.0	1.0	13 200
37742	ζ Ori	O9.7Ib$^{\rm W71}$	0.50	Ori OB1	6.0$^{\rm S99}$	34 000$^{\rm S99}$	1860	1.3	1.0	1.0	13 600
41117	χ^2 Ori	B2Ia$^{\rm W71}$	1.51	*Gem* OB1	5.55$^{\rm M99}$	19 500$^{\rm M99}$	510	1.5	1.0	1.0	7 800
47839	15/S Mon	O7V((f))$^{\rm W71}$	0.71	Mon OB1	5.34$^{\rm L93}$	40 100$^{\rm L93}$	2110	1.2	1.0	1.0	16 000
57060	UW CMa	O7Ia:fp var$^{\rm W73}$	1.51	NGC 2362	5.8$^{\rm H89}$	35 900$^{\rm H89}$	1425	1.3	1.0	1.0	14 400
57061	τ CMa	O9II	1.51	NGC 2362	6.02$^{\rm L93}$	34 000$^{\rm L93}$	1960	1.5	1.0	1.0	13 600
66811	ζ Pup	O4I(n)f	0.45$^{\rm B71}$	Gum Neb	6.0$^{\rm P96}$	42 000$^{\rm P96}$	2485	1.4	1.0	1.0	16 800
80077	PV Vel	B2Ia+$^{\rm M77}$	3.2$^{\rm M77}$	Pismis 11	6.3$^{\rm C89}$	17 000$^{\rm C89}$	140$^{\rm C89}$	1.6	0.9	0.8	6 800
93250	...	O3V((f))	2.63	Tr 16	6.28$^{\rm P96}$	50 500$^{\rm P96}$	3230	1.3	1.0	1.0	20 200
149404	V918 Sco	O9Ia	1.38	Ara OB1a	6.1†	32 500$^{\rm S98}$	2450	1.4	1.0	1.0	13 000
149757	ζ Oph	O9.5V$^{\rm M55}$	0.15$^{\rm B89}$	...	5.22$^{\rm P96}$	32 500$^{\rm P96}$	1505	1.6	1.0	1.0	13 000
151804	...	O8Iaf$^{\rm W71}$	1.91	Sco OB1	6.14$^{\rm L93}$	34 000$^{\rm L93}$	1600$^{\rm L93}$	1.5	1.0	1.0	13 600

Continued overleaf

HD	Name	Spectral type	d (kpc)	Cluster	$\log L$ ($L_\odot$)	$T_{\rm eff}$ (K)	v_∞ (km s^{-1})	μ	Z	γ	$T_{\rm e}$ (K)
152236	ζ^1 Sco	B1.5Ia+[W76]	1.91	Sco OB1	6.24	20 400	390	1.6	1.0	1.0	8 200
152408	WR 79A	WN9ha[V01]	1.91	Sco OB1	5.79[B99]	26 200[B99]	935[V01]	2.1	1.0	1.0	13 000
152424	···	OC9.7Ia	1.91	Sco OB1	6.0†	31 500[S98]	1760	1.3	1.0	1.0	12 600
152623	···	O7V(n)((f))	1.91	Sco OB1	5.7[H89]	39 000[H89]	3095	1.3	1.0	1.0	15 600
153919	···	O6.5Iaf+[W73]	1.72	···	5.90	38 000	1820	1.3	1.0	1.0	15 200
160529	···	B8Ia+[S91]	2.5[S91]	···	5.55†	10 000[S91]	180[S91]	1.6	0.9	0.8	4 000
164794	9 Sgr	O4:V((f))	1.58	Sgr OB1	6.02[L93]	46 400[L93]	2750	1.3	1.0	1.0	18 600
166734	···	O7Ib(f) + O8-9I[W73]	2.30[B89]	···	6.32	35 500	2600[B89]	1.3	1.0	1.0	14 200
167971	MY Ser	O8Ib(f)p	2.00	Ser OB2	5.86	35 500	2185	1.3	1.0	1.0	14 200
168112	···	O5III(f)[W73]	2.00	Ser OB2	6.06	46 800	2700[B89]	1.3	1.0	1.0	18 700
168607	···	B9Ia+[H78]	2.19	Ser OB1	5.38[V92]	9 300[V92]	140[C80]	1.5	0.9	0.8	3 700
169454	···	B1Ia+[W76]	1.66	Sct OB3	5.95	20 400	850[B89]	1.5	1.0	1.0	8 200
169515	RY Sct	B0V + O5.5V[K79]	2.19[D01]	Ser OB1	5.53†	24 000[D01]	1500[P90]	1.3	1.0	1.0	9 600
169582	···	O6If[W73]	2.12[K85]	···	6.07[V96]	41 700[V96]	2300[P90]	1.3	1.0	1.0	16 700
190429A	···	O4If+	2.7[L93]	···	6.06[L93]	42 400[L93]	1880	1.5	1.0	1.0	17 000
190603	···	B1.5Ia+[W71]	1.51[M99]	···	5.58[M99]	21 000[M99]	485	1.5	1.0	1.0	8 400
192281	···	O5Vn((f))p	2.29	Cyg OB8	6.19	46 800	2700[B89]	1.3	1.0	1.0	18 700
193237	P Cyg	B1Ia+[H78]	1.82	Cyg OB1	5.86[PP90]	19 300[PP90]	200[PP90]	1.5	1.0	1.0	7 700
194279	···	B1.5Ia[H78]	1.20	Cyg OB9	5.66[M99]	19 000[M99]	750[P90]	1.5	1.0	1.0	7 600
195592	···	O9.7Ia[W71]	1.15[B89]	···	5.5[S99]	31 000[S99]	1735[P90]	1.4	1.0	1.0	12 400
197345	α Cyg/Deneb	A2Ia[M73]	0.79	Cyg OB7	5.20[A02]	8 600[A02]	225[A02]	1.2	1.0	0.9	3 400
206267A	...	O6.5V((f))[W73]	0.83	Cep OB2	5.26	39 800	2745	1.3	1.0	1.0	15 900
210839	λ Cep	O6I(n)fp[W73]	0.83	Cep OB2	5.78[H00]	37 000[H00]	2250[H00]	1.8	1.0	1.0	14 800
···	Cyg OB2 No.5	2× O7Ianfp[W73]	1.82	Cyg OB2	6.43	39 800	2200[B89]	1.3	1.0	1.0	15 900
···	Cyg OB2 No.7	O3If[M91]	1.82	Cyg OB2	6.08†	50 000[H01]	3080[H01]	1.5	1.0	1.0	20 000

Continued overleaf

HD	Name	Spectral type	d (kpc)	Cluster	$\log L$ ($L_\odot$)	$T_{\rm eff}$ (K)	v_∞ (km s^{-1})	μ	Z	γ	$T_{\rm e}$ (K)
...	Cyg OB2 No.8A[M91]	O5.5I(f)	1.82	Cyg OB2	6.43†	44 000[H01]	2650[H01]	1.3	1.0	1.0	17 600
...	Cyg OB2 No.9	O5If[M91]	1.82	Cyg OB2	6.24[H99]	44 500[H99]	2200[B89]	1.3	1.0	1.0	17 800
...	Cyg OB2 No.12	B5Ie[M91]	1.82	Cyg OB2	6.21	11 200	1400[S80]	1.3	1.0	0.9	4 500
...	V433 Sct	B1.5Ia[H78]	1.66	Sct OB3	5.62[L88]	19 200†	1100[L88]	1.5	1.0	1.0	7 700
...	MWC 349	O9:III:[L98] + B0III[C85]	1.2[C85]	...	5.23[L98]	28 800[L98]	50[A81]	1.3	1.0	1.0	11 500

NOTES: References for spectral types and other data are provided starting on page 169.

SOURCES FOR TABLE 6.2:-

- **Spectral type.** Otherwise unreferenced spectral types are from Walborn (1972).
- ***d*.** Otherwise unreferenced values are from Humphreys (1978), and are derived from the adopted (mean) distance modulus listed for the parent cluster, together with Equation 5.7.
- **log *L*.** Otherwise unreferenced values are from Bieging *et al.* (1989). † — Calculated using Equation 4.1 and the listed values of $T_{\rm eff}$ and R_* (R_* are given in the notes to individual stars; see below).
- **$T_{\rm eff}$.** Otherwise unreferenced values are from Bieging *et al.* (1989). † — Calculated using Equation 4.1 and the listed values of $\log L$ and R_* (R_* are given in the notes to individual stars; see below).
- **v_∞.** Otherwise unreferenced values are from Howarth *et al.* (1997*b*). † — Assumed value.
- **μ.** Values are calculated using Equation 5.3, together with the assumptions discussed in §5.6.4. See also the notes below concerning elemental abundances and ionisation structures.
- ***Z*.** Values are calculated using Equation 5.4, together with the assumptions discussed in §5.6.5. See also the notes below concerning elemental abundances and ionisation structures.
- **γ.** Values are calculated using Equation 5.5, together with the assumptions discussed in §5.6.5. See also the notes below concerning elemental abundances and ionisation structures.
- **$T_{\rm e}$.** Values are calculated using Drew's (1989) relationship, $T_{\rm e} \approx 0.4\,T_{\rm eff}$; $T_{\rm eff}$ are given in column 7 of Table 6.2.

The parameters were obtained as detailed above unless indicated otherwise in Table 6.2. In these instances the sources are:-

M55 — Morgan *et al.* (1955); R68 — Racine (1968); B71 — Brandt *et al.* (1971); W71 — Walborn (1971); C72 — Cowley (1972); W72 — Walborn (1972); M73 — Morgan and Keenan (1973); W73 — Walborn (1973); W76 — Walborn (1976); M77 — Moffat and Pim FitzGerald (1977); K79 — King and Jameson (1979); C80 — Chentsov (1980); S80 — Souza and Lutz (1980); A81 — Altenhoff *et al.* (1981); C85 — Cohen *et al.* (1985); K85 — Kozok (1985); L88 — Leitherer (1988*a*); B89 — Bieging *et al.* (1989); C89 — Carpay *et al.* (1989); H89 — Howarth and Prinja (1989); P90 — Prinja *et al.* (1990); PP90 — Pauldrach and Puls (1990); L91 — Leitherer and Robert (1991); M91 — Massey and Thompson (1991); S91 — Sterken *et al.* (1991); V92 — van Genderen *et al.* (1992); L93 — Lamers and Leitherer (1993); P96 — Puls *et al.* (1996); V96 — Vacca *et al.* (1996); H97 — Howarth *et al.* (1997*b*); L98 — Lamers *et al.* (1998); S98 — Smith *et al.* (1998); B99 — Bohannan and Crowther (1999); H99 — Herrero *et al.* (1999); M99 — McErlean *et al.* (1999); S99 — Siebert (1999); A00 — Albayrak (2000); H00 — Herrero *et al.* (2000); H01 — Herrero *et al.* (2001); D01 — Djurašević *et al.* (2001); V01 — van der Hucht (2001); A02 — Aufdenberg *et al.* (2002).

Notes to individual stars:-

HD 2905 (κ Cas). A value of Y(He) = 0.09 is assumed on the basis that McErlean *et al.* (1999) noted the star's CN status was normal-to-moderate.

HD 5394 (γ Cas). The distance was derived from the star's distance modulus, together with Equation 5.7. Y(He) is assumed to be solar.

HD 14947. A helium abundance of $Y(\mathrm{He}) = 0.20$ is adopted, taken from Herrero *et al.* (2000).

HD 15558. A helium abundance of $Y(\mathrm{He}) = 0.07$ is adopted, taken from Herrero *et al.* (2000).

HD 15570. A helium abundance of $Y(\mathrm{He}) = 0.15$ is adopted, taken from Herrero *et al.* (2000).

HD 17505. $Y(\mathrm{He})$ is assumed to be solar.

HD 26676. The distance was derived from the adopted (mean) distance modulus listed for the parent association, together with Equation 5.7. No published value for v_∞ could be found, so a value of 200 km s^{-1} is assumed, based on published values for stars of a similar spectral type. $Y(\mathrm{He})$ is assumed to be solar.

HD 30614 (α Cam). The distance was derived from the star's distance modulus, together with Equation 5.7. A helium abundance of $Y(\mathrm{He}) = 0.13$ is adopted, taken from Siebert (1999).

HD 34085 (β Ori/Rigel). A value of $Y(\mathrm{He}) = 0.09$ is assumed on the basis that McErlean *et al.* (1999) noted the star's CN status was normal-to-moderate.

HD 36486 (δ Ori A). A helium abundance of $Y(\mathrm{He}) = 0.10$ is adopted, taken from Siebert (1999).

HD 37128 (ϵ Ori). In accordance with Leitherer and Robert (1991), a significant helium overabundance is adopted, such that $Y(\mathrm{He}) = 0.20$.

HD 37468 (σ Ori AB). $Y(\mathrm{He})$ is assumed to be solar.

HD 37742 (ζ Ori). A helium abundance of $Y(\mathrm{He}) = 0.10$ is adopted, taken from Siebert (1999).

HD 41117 (χ^2 Ori). A value of $Y(\mathrm{He}) = 0.18$ is assumed on the basis that McErlean *et al.* (1999) noted the star's CN status was highly processed.

HD 47839 (15/S Mon). A helium abundance of $Y(\mathrm{He}) = 0.07$ is adopted, taken from Lamers and Leitherer (1993).

HD 57060 (UW CMa). $Y(\mathrm{He})$ is assumed to be solar.

HD 57061 (τ CMa). A helium abundance of $Y(\mathrm{He}) = 0.15$ is adopted, taken from Lamers and Leitherer (1993).

HD 66811 (ζ Pup). A helium abundance of $Y(\mathrm{He}) = 0.12$ is adopted, taken from Puls *et al.* (1996).

HD 80077 (PV Vel). Carpay *et al.* (1991) presented arguments for and against cluster membership for this star, and concluded that HD 80077 is most probably a member of Pismis 11. This has been adopted. In accordance with Leitherer *et al.* (1995), a significant helium overabundance is adopted, such that $\mu = 1.6$ (this star is a highly-evolved B hypergiant; De Jager, 1984).

HD 93250. A solar helium abundance is adopted, in accordance with Kudritzki *et al.* (1991); this is an unevolved star, still close to the main sequence.

HD 149404 (V918 Sco). A value of $R_* = 34\ R_\odot$ taken from Lamers and Leitherer (1993) was used to calculate $\log L$. A helium abundance of $Y(\mathrm{He}) = 0.12$ is adopted, taken from Smith *et al.* (1998).

HD 149757 (ζ Oph). A helium abundance of $Y(\mathrm{He}) = 0.19$ is adopted, taken from Puls *et al.* (1996).

HD 151804. A helium abundance of $Y(\mathrm{He}) = 0.15$ is adopted, taken from Lamers and Leitherer (1993).

HD 152236 (ζ^1 Sco). In accordance with Leitherer and Robert (1991), to reflect the star's advanced evolutionary status, a significant helium overabundance is assumed, such that $Y(\mathrm{He}) = 0.20$.

HD 152408 (WR 79A). A H/He ratio of 1.6 is adopted, taken from the results of near-IR spec-

troscopy in Bohannan and Crowther (1999). In this instance, the effective temperature is determined at the radius, $R_{2/3}$, at which the Rosseland optical depth equals 2/3.

HD 152424. A value of $R_* = 33\ R_\odot$ taken from Lamers and Leitherer (1993) was used to calculate $\log L$. A helium abundance of $Y(\mathrm{He}) = 0.09$ is adopted, taken from Smith *et al.* (1998).

HD 152623. $Y(\mathrm{He})$ is assumed to be solar.

HD 153919. $Y(\mathrm{He})$ is assumed to be solar.

HD 160529. A value of $R_* = 200\ R_\odot$ taken from Sterken *et al.* (1991) was used to calculate $\log L$. In accordance with Leitherer *et al.* (1995), a significant helium overabundance is adopted, such that $\mu = 1.5$. Sterken *et al.* (1991) found this object to be a new case of a Galactic LBV, and that its spectral type had changed from A9Ia (Houk, 1982) to B8Ia+ over two decades, coinciding with a decrease in visual brightness (typical of LBVs). As the observations of HD 160529 are from 1994, when the star was of spectral type B8Ia+, the adopted stellar parameters characterise the B8 (minimum brightness) state.

HD 164794 (9 Sgr). A helium abundance of $Y(\mathrm{He}) = 0.10$ is adopted, taken from Lamers and Leitherer (1993).

HD 166734. $Y(\mathrm{He})$ is assumed to be solar.

HD 167971 (MY Ser). $Y(\mathrm{He})$ is assumed to be solar.

HD 168112. $Y(\mathrm{He})$ is assumed to be solar.

HD 168607. In accordance with Leitherer *et al.* (1995), a significant helium overabundance is adopted, such that $\mu = 1.5$.

HD 169454. To reflect the evolved nature of this star, a significant helium overabundance is adopted, such that $\mu = 1.5$.

HD 169515 (RY Sct). Djurašević *et al.* (2001) found that HD 169515 is probably a member of the Ser OB1 association; thus, the adopted value of d is derived from the adopted (mean) distance modulus for this cluster given in Humphreys (1978). A value of $R_* = 34\ R_\odot$ taken from Djurašević *et al.* (2001) was used to calculate $\log L$. v_∞ is the mean value for the star's approximate spectral type and luminosity class, as given in Prinja *et al.* (1990); however, because no value was available for spectral type B0V, the value used is that for an O9V star. In accordance with Djurašević *et al.* (2001), $Y(\mathrm{He})$ is assumed to be solar.

HD 169582. v_∞ is the mean value for the star's spectral type and luminosity class, as given in Prinja *et al.* (1990). $Y(\mathrm{He})$ is assumed to be solar.

HD 190429A. A helium abundance of $Y(\mathrm{He}) = 0.15$ is adopted, taken from Lamers and Leitherer (1993).

HD 190603. The distance was derived from the star's distance modulus, together with Equation 5.7. A value of $Y(\mathrm{He}) = 0.18$ is assumed on the basis that McErlean *et al.* (1999) noted the star's CN status was highly processed.

HD 192281. $Y(\mathrm{He})$ is assumed to be solar.

HD 193237 (P Cyg). $Y(\mathrm{He})$ is assumed to be the same as for HD 168607 (reflecting the evolved nature of this object).

HD 194279. v_∞ is the mean value for the star's spectral type and luminosity class, as given in Prinja *et al.* (1990). A value of $Y(\mathrm{He}) = 0.18$ is assumed on the basis that McErlean *et al.* (1999) noted the star's

CN status was highly processed.

HD 195592. v_∞ is the mean value for the star's spectral type and luminosity class, as given in Prinja *et al.* (1990). A helium abundance of Y(He) = 0.12 is adopted, taken from Siebert (1999).

HD 197345 (α Cyg/Deneb). A helium abundance of Y(He) = 0.07 is adopted, taken from Albayrak (2000).

HD 206267A. Y(He) is assumed to be solar.

HD 210839 (λ Cep). A helium abundance of Y(He) = 0.25 is adopted, taken from Herrero *et al.* (2000).

Cyg OB2 No.5. Y(He) is assumed to be solar.

Cyg OB2 No.7. A value of $R_* = 15\ R_\odot$ taken from Herrero *et al.* (2001) was used to calculate $\log L$. A helium abundance of Y(He) = 0.18 was adopted, taken from Herrero *et al.* (2001).

Cyg OB2 No.8A. A value of $R_* = 28\ R_\odot$ taken from Herrero *et al.* (2001) was used to calculate $\log L$. A helium abundance of Y(He) = 0.09 was adopted, taken from Herrero *et al.* (2001).

Cyg OB2 No.9. A helium abundance of Y(He) = 0.09 was adopted, taken from Herrero *et al.* (1999).

Cyg OB2 No.12. Y(He) is assumed to be solar.

V433 Sct. A value of $R_* = 59\ R_\odot$ taken from Leitherer (1988*a*) was used to calculate $T_{\rm eff}$. Y(He) is assumed to be the same as for HD 168607 (reflecting the evolved nature of this object).

MWC 349. Y(He) is assumed to be solar.

6.3.2 Results

Table 6.3 shows the inferred radio mass-loss rates, at each wavelength detected, for each star in the sample. The final column gives the weighted mean mass-loss rate, averaged over all wavelengths. (For the 36 stars common to both the Hα and radio samples, a comparison is made in §7.1, between the mean radio mass-loss rates and the Hα mass-loss rates derived in §4).

A number of objects exhibit inferred $\dot{M}$ values that decrease with increasing wavelength (i.e., increasing distance from the star). This is most evident in the cooler, B-type stars, such as HD 37128 (B0Ia), HD 41117 (B2Ia) and HD 152236 (B1.5Ia+). Lower temperatures could mean that recombination of the wind material is occurring *within* the radio photosphere. This material would not contribute to the observed free–free flux; only the contribution from the ionised fraction would be seen. The inferred radio mass-loss rates seem to imply that the ionised fraction decreases as a function of distance from the star, making the simple assumption of a single value for the wind temperature, $T_{\rm e}$, mean ionic charge, Z, and number of free electrons per ion, γ, for all radio wavelengths, invalid.

Several objects show a marked and consistent increase in inferred mass-loss rate with increasing wavelength, notably, HD 37468, HD 151804, HD 152623, HD 164794, HD 167971, HD 168112, and Cyg OB2 No.8A. This is most likely due to the presence of nonthermal emission. Nonthermal processes have greater contributions at longer wavelengths; the increase in nonthermal contribution with wavelength increases the error introduced into $\dot{M}$ through the inappropriate use of Equation 5.2. At mm wavelengths, any nonthermal contribution is negligible, and, mass-loss rates derived from mm free–free emission can, in general, be considered to be more accurate than those derived from longer-wavelength data (Leitherer and Robert, 1991; Altenhoff *et al.*, 1994; Contreras *et al.*, 1996). With the exception of HD 152623 and HD 151804, the stars listed above have indeed previously been identified as nonthermal emitters (Abbott *et al.*, 1984*b*; Bieging *et al.*, 1989; Drake, 1990). An attempt will be made in §6.4.2 to classify (as far as possible) each of the stars in the radio sample, as being either thermal or nonthermal sources.

Table 6.3: Radio mass-loss rates

HD	Name	Spectral	$\dot{M}$ ($10^{-6} M_\odot$ yr^{-1})							
		type	0.8–0.85 mm	1.1–1.35 mm	7 mm	2 cm	3–3.6 cm	6–6.3 cm	13 cm	20–21 cm	Mean
2905	κ Cas	BC0.7Ia					2.20 ± 0.78				2.20 ± 0.78
5394	γ Cas	B0.5IVe						0.25 ± 0.17			0.25 ± 0.17
14947	···	O5If+					6.43 ± 2.61				6.43 ± 2.61
15558	···	O5III(f)					16.4 ± 5.8	20.6 ± 7.9			17.9 ± 4.7
15570	···	O4If+		24.9 ± 12.9			6.78 ± 2.58	12.1 ± 6.2			8.14 ± 2.34
17505	···	O6.5V						12.8 ± 5.0			12.8 ± 5.0
26676	···	B8Vn						0.04 ± 0.02		0.54 ± 0.20	0.04 ± 0.02
30614	α Cam	O9.5Ia				2.62 ± 1.69	2.51 ± 1.58	2.37 ± 1.50			2.49 ± 0.91
34085	β Ori/Rigel	B8Ia					0.36 ± 0.13	0.34 ± 0.13			0.35 ± 0.09
36486	δ Ori A	O9.5II					0.79 ± 0.28	1.46 ± 0.62			0.90 ± 0.26
37128	ϵ Ori	B0Ia	4.88 ± 1.76	4.62 ± 1.70		3.19 ± 1.16	2.76 ± 0.97	2.62 ± 0.92			3.17 ± 0.52
37468	σ Ori AB	O9.5V				2.48 ± 0.87		4.53 ± 1.59		5.76 ± 2.15	3.27 ± 0.72
37742	ζ Ori	O9.7Ib		3.70 ± 1.35			1.89 ± 0.67	2.13 ± 0.88			2.21 ± 0.50
41117	χ^2 Ori	B2Ia				2.11 ± 0.81	1.96 ± 0.69	1.84 ± 0.71			1.96 ± 0.42
47839	15/S Mon	O7V((f))						2.45 ± 1.05			2.45 ± 1.05
57060	UW CMa	O7Ia:fp var					3.78 ± 1.35				3.78 ± 1.35
57061	τ CMa	O9II					5.59 ± 1.98				5.59 ± 1.98
66811	ζ Pup	O4I(n)f		6.02 ± 2.14		4.70 ± 1.67	3.52 ± 1.24	4.12 ± 1.46			4.26 ± 0.77
80077	PV Vel	B2Ia+					2.56 ± 0.99	2.63 ± 1.06			2.59 ± 0.72
93250	···	O3V((f))					56.0 ± 20.3				56.0 ± 20.3
149404	V918 Sco	O9Ia					9.25 ± 3.26				9.25 ± 3.26
149757	ζ Oph	O9.5V					0.08 ± 0.05				0.08 ± 0.05
151804	···	O8Iaf				6.37 ± 2.53	11.2 ± 4.0	14.4 ± 5.1	29.7 ± 11.0		9.40 ± 1.94

Continued overleaf

HD	Name	Spectral	$\dot{M}$ ($10^{-6} M_\odot$ yr^{-1})								
		type	0.8–0.85 mm	1.1–1.35 mm	7 mm	2 cm	3–3.6 cm	6–6.3 cm	13 cm	20–21 cm	Mean
152236	ζ^1 Sco	B1.5Ia+	18.0 ± 6.8	13.2 ± 4.7		10.3 ± 3.6	9.13 ± 3.24	7.92 ± 2.78			9.97 ± 1.65
152408	WR 79A	WN9ha		27.7 ± 10.1		20.1 ± 7.1	11.8 ± 4.3	15.4 ± 5.4	23.3 ± 8.3		16.4 ± 2.7
152424	···	OC9.7Ia					3.99 ± 1.51	6.79 ± 2.60			4.70 ± 1.31
152623	···	O7V(n)((f))					8.62 ± 3.42	18.5 ± 6.8	39.1 ± 14.1	48.1 ± 17.6	12.9 ± 2.9
153919	···	O6.5Iaf+					7.29 ± 4.58				7.29 ± 4.58
160529	···	B8Ia+					12.8 ± 8.0	13.2 ± 8.3			13.0 ± 5.8
164794	9 Sgr	O4:V((f))				10.6 ± 3.9	25.6 ± 10.2	35.1 ± 12.4		104 ± 37	15.1 ± 3.5
166734	···	O7Ib(f) + O8–9I				11.8 ± 7.7		19.3 ± 12.6			13.8 ± 6.6
167971†	MY Ser	O8Ib(f)p				59.8 ± 20.9	92.2 ± 32.3	181 ± 63		490 ± 172	86.2 ± 16.4
168112	···	O5III(f)				23.2 ± 8.2		69.7 ± 24.4		264 ± 93	29.6 ± 7.7
168607	···	B9Ia+					2.15 ± 0.79				2.15 ± 0.79
169454	···	B1Ia+		14.3 ± 5.3		9.24 ± 3.26		9.61 ± 3.40			10.2 ± 2.2
169515	RY Sct	B0V + O5.5V		167 ± 60							167 ± 60
169582	···	O6If					3.21 ± 2.16				3.21 ± 2.16
190429A	···	O4If+					12.1 ± 7.7				12.1 ± 7.7
190603	···	B1.5Ia+				2.16 ± 1.43	2.76 ± 1.75	3.04 ± 1.92			2.56 ± 0.96
192281	···	O5Vn((f))p					5.22 ± 2.08				5.22 ± 2.08
193237†	P Cyg	B1Ia+	22.1 ± 7.8	18.4 ± 6.4	13.6 ± 4.8	12.9 ± 4.5	11.8 ± 4.1	10.6 ± 3.7		9.82 ± 5.04	13.1 ± 1.7
194279	···	B1.5Ia					2.15 ± 0.84	1.97 ± 0.81			2.06 ± 0.58
195592	···	O9.7Ia				5.58 ± 3.55	4.67 ± 2.94	3.94 ± 2.52			4.55 ± 1.68
197345	α Cyg/Deneb	A2Ia		0.73 ± 0.29			0.20 ± 0.08				0.24 ± 0.08
206267A	···	O6.5V((f))						3.26 ± 1.26			3.26 ± 1.26
210839	λ Cep	O6I(n)fp		6.63 ± 2.81			3.59 ± 1.28	8.39 ± 3.53			4.53 ± 1.11
...	Cyg OB2 No.5	2× O7Ianfp	37.2 ± 15.3	71.4 ± 25.1	60.5 ± 21.2	70.6 ± 24.7	75.6 ± 26.4	77.9 ± 27.3		118 ± 42	61.4 ± 8.7
···	Cyg OB2 No.7	O3If						18.2 ± 9.3			18.2 ± 9.3

Continued overleaf

HD	Name	Spectral	$\dot{M}$ ($10^{-6} M_\odot$ yr^{-1})								
		type	0.8–0.85 mm	1.1–1.35 mm	7 mm	2 cm	3–3.6 cm	6–6.3 cm	13 cm	20–21 cm	Mean
···	Cyg OB2 No.8A	O5.5I(f)				9.84 ± 4.53	20.5 ± 7.2	22.0 ± 7.8		46.6 ± 16.7	15.9 ± 3.4
···	Cyg OB2 No.9†	O5If		38.5 ± 13.9	24.0 ± 9.6	44.5 ± 15.6	71.9 ± 25.2	97.7 ± 34.2		131 ± 46	40.4 ± 6.6
···	Cyg OB2 No.12	B5Ie	50.8 ± 18.3	54.9 ± 19.3	70.6 ± 24.7	63.8 ± 22.3	56.6 ± 19.8	47.8 ± 16.7		48.3 ± 17.3	54.3 ± 7.3
···	V433 Sct	B1.5Ia				7.99 ± 3.00	8.78 ± 3.09	8.33 ± 2.95			8.36 ± 1.74
···	MWC 349	O9:III: + B0III		13.4 ± 8.5							13.4 ± 8.5

NOTES: † — For these stars, additional mass-loss rates were calculated at the following wavelengths (these results have been incorporated when calculating the mean mass-loss rates, averaged over all wavelengths):-

HD 167971 — $(182 \pm 75) \times 10^{-6}$ $M_\odot$ yr^{-1} at 18 cm.

HD 193237 — $(16.1 \pm 5.7) \times 10^{-6}$ $M_\odot$ yr^{-1} at 2 mm.

Cyg OB2 No.9 — $(213 \pm 76) \times 10^{-6}$ $M_\odot$ yr^{-1} at 18 cm.

The mass-loss rate of Cyg OB2 No.9 on May 9th, 1983 has been calculated separately. At this time, the spectral index of the star was indicative of a thermal source, and the observed flux at 2 and 6 cm was appreciably lower than at other epochs, perhaps suggesting that any nonthermal contribution had disappeared. Mass-loss rates of (15.7 ± 6.3) and $(16.2 \pm 6.8) \times 10^{-6}$ $M_\odot$ yr^{-1} were derived at 2 and 6 cm, respectively. These values are in good agreement with each other, but are still a factor ~ 2 higher than the Hα mass-loss rate of 8.51×10^{-6} $M_\odot$ yr^{-1}, derived in §4.

6.4 Nonthermal emission

The mass-loss rates presented in Table 6.3 have been derived assuming a free–free interpretation of the observed radio emission. However, some early-type stars are also known to be strong sources of *nonthermal* emission (e.g Abbott *et al.*, 1984*a*; Bieging *et al.*, 1989). This greatly complicates the interpretation of the radio flux, as the presence of nonthermal emission invalidates the use of Equation 5.2 to determine $\dot{M}$ from radio continuum observations. It is therefore important to establish which of the stars in the radio sample are nonthermal emitters.

6.4.1 Observable characteristics of nonthermal emission

In the early 1980s, the inferred radio mass-loss rates of the stars HD 164794 (9 Sgr) and Cyg OB2 No.9 were discovered to be too high (by an order of magnitude), compared to mass-loss rates derived from UV, optical and IR diagnostics (e.g. Abbott *et al.*, 1980; Garmany *et al.*, 1981; Leitherer *et al.*, 1982). Further to this, White and Becker (1983), using the VLA, found that Cyg OB2 No.9 was spatially unresolved at 6 cm. Combining this result with the observed radio spectrum of the star, they derived a wind electron temperature in excess of 300 000 K. This would imply that the wind gets hotter as it recedes from the star, requiring some (unknown) source of heating. Subsequent multiwavelength observations (e.g. Abbott *et al.*, 1984*a*; Contreras *et al.*, 1996; Waldron *et al.*, 1998) have shown that the flux distributions of 9 Sgr and Cyg OB2 No.9 are such that their spectral indices differ from the value of $\alpha = 0.6$ predicted for a thermal source: there is too much radio emission. Abbott *et al.* (1984*b*) recognised that the excess radio flux from these two stars is characteristic of nonthermal emission, which contaminates the free–free flux and results in an overestimate of the mass-loss rate.

Since the first studies, many more early-type stars have been found to be nonthermal emitters. Bieging *et al.* (1989) undertook a distance-limited survey of early-type stars in the northern hemisphere, and, using the radio spectral index as their primary criterion, concluded that 24% of the detected radio sources have a nonthermal contribution to their emission. They also found that nonthermal sources display short-term variability (i.e., on timescales not longer than months) in both monochromatic flux levels and spectral index. It is evident from inspection of the data in Table 6.1 that many of the sources listed *are* variable in their emission, with changes over time in both spectral intensity and

spectral index. Nonthermal sources are observed to have relatively high radio fluxes (as compared to their thermal counterparts), because of the additional nonthermal contribution. They are also systematically the most bolometrically luminous stars (Bieging *et al.*, 1989), enabling them to be seen to greater distances than free–free emitters. It should be expected, therefore, that the radio sample assembled here will contain a significant number of nonthermal sources.

6.4.2 Criteria for establishing nonthermal emission

The indicators used to discriminate between free–free and nonthermal emission are as follows:-

(a) **Spectral index.** Probably the most useful criterion for establishing whether or not a source exhibits nonthermal emission, is its spectral index in the radio. Where there are multiwavelength observations available, this will serve as the primary indicator. If the spectral index differs appreciably from 0.6, the star will be classified as nonthermal. In instances where limited observations mean that there is no spectral index available, or where other indicators contradict the classification that would be made on the basis of the spectral index, the classification is suffixed '?'. This is to be interpreted as 'probable'.

(b) **$\log(\dot{M}_{\rm radio}/\dot{M}_{\rm H\alpha})$.** If the mass-loss rate implied by a free–free interpretation of the observed radio flux disagrees strongly with the mass-loss rate from other observational diagnostics, a nonthermal contribution may be present. A comparison will therefore be made between the mean radio mass-loss rate, $\dot{M}_{\rm radio}$ (which has been derived assuming free–free emission), and the mass-loss rate derived from Hα, $\dot{M}_{\rm H\alpha}$. A large value of $\log(\dot{M}_{\rm radio}/\dot{M}_{\rm H\alpha})$ would be expected from a nonthermal source. For stars common to both the radio and Hα samples, the $\dot{M}_{\rm H\alpha}$ results derived in §4 using PHALTEE (see Table 4.6) are used. For those objects in the radio sample only, the empirical dependence of mass-loss rate on luminosity, derived in §4.3.1, is used to calculate '$\dot{M}_{\rm H\alpha}$'. In the absence of any supporting spectral index information, or other evidence, a value of $\log(\dot{M}_{\rm radio}/\dot{M}_{\rm H\alpha}) \gtrsim 0.3$ (i.e., $\dot{M}_{\rm radio}/\dot{M}_{\rm H\alpha} \gtrsim 2$) will be used to classify a source as being (probably) nonthermal.

(c) **Variability.** If a source exhibits significant variability in its monochromatic flux levels and/or spectral index, this will be taken as being evidence of nonthermal emission.

These criteria have been used to classify the radio sample as shown in Table 6.4. Column 4 gives, where possible, the time-averaged spectral index of the source. The value of $\log(\dot{M}_{\rm radio}/\dot{M}_{\rm H\alpha})$ is given in column 5. Column 6 provides an indication, where observations permit, as to whether or not the source is variable in the radio. If, in either column 4 or 6, there is no entry (represented by '$\cdots$'), there were insufficient observations to be able to use this indicator. Finally, column 7 gives an indication as to the probable nature of the source. Of the 53 stars in the sample, there are seventeen definite and fifteen probable thermal emitters, and twelve definite and nine probable nonthermal emitters. The fraction of nonthermal sources in the sample could therefore be as low as 23%, or as high as 40%, depending on the true nature of the 'probable' nonthermal candidates. In Bieging *et al.*'s (1989) distance-limited sample of all 25 OB stars within 2.5 kpc of the sun, 24% (six out of 25) were found to be clear nonthermal emitters. *This* sample is not distance-limited, however, and, given that Bieging *et al.* (1989) found that nonthermal sources tend to be bolometrically more luminous than their nonthermal counterparts (and thus visible out to greater distances), it is biased in favour of nonthermal sources.

Unless non-detections are taken into account, this will result in an *overestimate* of the fraction of nonthermal emitters. To do this, it would first be necessary to make an estimate of the radio-flux detection threshold. The *expected* thermal emission could then be computed (using, for example, $\dot{M}$ predicted from L) for as complete a catalogue of O stars as is available (e.g. Garmany's unpublished catalogue of O stars). It would then be possible to identify which of these stars *should* be detectable as thermal emitters. The fraction of these stars which *are* thermal is a fair (unbiased) estimate of the fraction of thermal emitters.

The criteria have produced results that are generally internally consistent, in the sense that stars with larger $\log(\dot{M}_{\rm radio}/\dot{M}_{\rm H\alpha})$ tend to have spectral indices, $\alpha < 0.6$. Radio variability would appear to be less reliable an indicator of nonthermal emission, however. Both P Cyg and Cyg OB2 No.12 are observed to be variable in spectral intensity *and* index, although their time-averaged spectral indices ($\alpha = 0.71 \pm 0.06$, and 0.73 ± 0.04, respectively) strongly suggest that they are thermal sources. White and Becker (1982), using the VLA (and more recently, Skinner *et al.*, 1997, using MERLIN) were able to spatially resolve the 6 cm emission from the wind of P Cyg, showing that the outflow is consistent with spherical symmetry, and that the radial brightness function is in good agreement with a thermal wind model. The same result was obtained for Cyg OB2 No.12

by White and Becker (1983), although the wind temperature was found to be rather low, and there were suggestions of deviations from spherical symmetry in the data. The free–free interpretation for these stars is thus well founded (unfortunately, only a few early-type stars are sufficiently strong radio emitters to be spatially resolved, meaning that, generally, alternative diagnostics must be found to discriminate between thermal and nonthermal sources). Some other mechanism must therefore be responsible for the variability seen in these stars. Skinner *et al.* (1998), for example, suggested that the (rather rapid) variability exhibited by P Cyg might be explicable in terms of changes in the ionisation structure in the inner part of the circumstellar envelope. Variability can also be interpreted as being due to large-scale structure in the wind (e.g. Blomme *et al.*, 2002).

Low values of $\log(\dot{M}_{\rm radio}/\dot{M}_{\rm H\alpha})$ were found for a number of the B stars (and α Cyg). This arises probably from incorrect assumptions being made with regard to the ionisation state of the wind (see §6.3.2). For the WR star in the sample (HD 152408), the empirical $\dot{M}$–L relationship used to calculate $\dot{M}_{\rm H\alpha}$ most likely does not apply. WR stars are observed to have significantly higher mass-loss rates than OB stars of similar luminosity (by as much as an order of magnitude; e.g. Crowther *et al.*, 1995*b*). Therefore, the very high mass-loss rate implied by the free–free interpretation of the radio emission for HD 152408 has been considered to be correct and, despite a high $\log(\dot{M}_{\rm radio}/\dot{M}_{\rm H\alpha})$ value, the star has been classified as thermal.

Table 6.4: Criteria for establishing nonthermal emission

HD	Name	Spectral type	Spectral index	log $(\dot{M}_{\rm radio}/\dot{M}_{\rm H\alpha})$	Radio variability	Nature of source
2905	κ Cas	BC0.7Ia	···	−0.12	···	Thermal?
5394	γ Cas	B0.5IVe	···	−0.92	···	Thermal?
14947	···	O5If+	···	0.11	···	Thermal?
15558	···	O5III(f)	0.00 ± 0.40	0.40	···	Nonthermal
15570	···	O4If+	-0.79 ± 0.28	−0.19	···	Nonthermal
17505	···	O6.5V	···	0.49†	···	Nonthermal?
26676	···	B8Vn	-2.23 ± 1.56	1.88†	Yes	Nonthermal
30614	α Cam	O9.5Ia	1.11 ± 0.23	−0.09	No	Thermal
34085	β Ori/Rigel	B8Ia	0.73 ± 0.43	0.03†	···	Thermal
36486	δ Ori A	O9.5II	-1.02 ± 0.66	−0.47	···	Nonthermal?
37128	ϵ Ori	B0Ia	0.37 ± 0.10	0.32†	No	Thermal
37468	σ Ori AB	O9.5V	-0.12 ± 0.05	0.97†	Yes	Nonthermal
37742	ζ Ori	O9.7Ib	0.81 ± 0.51	−0.42	···	Thermal
41117	χ^2 Ori	B2Ia	0.88 ± 0.32	0.05†	No	Thermal
47839	15/S Mon	O7V((f))	···	0.38†	···	Nonthermal?
57060	UW CMa	O7Ia:fp var	···	0.07†	···	Thermal?
57061	τ CMa	O9II	···	0.01†	···	Thermal?
66811	ζ Pup	O4I(n)f	0.76 ± 0.09	−0.07	No	Thermal
80077	PV Vel	B2Ia+	0.53 ± 0.61	−0.63†	···	Thermal
93250	···	O3V((f))	···	0.73†	···	Nonthermal?
149404	V918 Sco	O9Ia	···	0.01	···	Thermal?
149757	ζ Oph	O9.5V	···	−0.86	···	Thermal?
151804	···	O8Iaf	0.05 ± 0.24	0.10†	No	Nonthermal
152236	ζ^1 Sco	B1.5Ia+	0.79 ± 0.08	0.02†	No	Thermal
152408	WR 79A	WN9ha	0.71 ± 0.09	0.72†	Yes	Thermal
152424	···	OC9.7Ia	-0.79 ± 0.55	−0.03	···	Nonthermal?
152623	···	O7V(n)((f))	-0.79 ± 0.24	0.71†	···	Nonthermal
153919	···	O6.5Iaf+	···	0.25†	···	Thermal?
160529	···	B8Ia+	0.50 ± 0.06	0.88†	···	Thermal?
164794	9 Sgr	O4:V((f))	-0.66 ± 0.08	0.93	Yes	Nonthermal
166734	···	O7Ib(f) + O8–9I	0.15 ± 0.27	−0.13	No	Thermal?
167971	MY Ser	O8Ib(f)p	-0.61 ± 0.03	1.15	Yes	Nonthermal
168112	···	O5III(f)	-0.43 ± 0.14	0.96	Yes	Nonthermal
168607	···	B9Ia+	···	−0.02	···	Thermal?
169454	···	B1Ia+	0.58 ± 0.10	0.04	No	Thermal
169515	RY Sct	B0V + O5.5V	···	1.41	···	Nonthermal?
169582	···	O6If	···	−0.22	···	Thermal?
190429A	···	O4If+	···	0.32	···	Nonthermal?
190603	···	B1.5Ia+	0.24 ± 0.87	0.01	No	Thermal
192281	···	O5Vn((f))p	···	0.08	···	Thermal?

Continued overleaf

HD	Name	Spectral type	Spectral index	log $(\dot{M}_{\rm radio}/\dot{M}_{\rm H\alpha})$	Radio variability	Nature of source
193237	P Cyg	B1Ia+	0.71 ± 0.06	0.10	Yes	Thermal
194279	···	B1.5Ia	0.79 ± 0.64	0.05	···	Thermal
195592	···	O9.7Ia	0.95 ± 0.30	0.18	No	Thermal
197345	α Cyg/Deneb	A2Ia	1.07 ± 0.10	−0.20	···	Thermal
206267A	···	O6.5V((f))	···	1.23	···	Nonthermal?
210839	λ Cep	O6I(n)fp	0.81 ± 0.72	0.06	Yes	Thermal?
···	Cyg OB2 No.5	2× O7Ianfp	0.53 ± 0.07	0.39	Yes	Nonthermal
···	Cyg OB2 No.7	O3If	···	0.46	···	Nonthermal?
···	Cyg OB2 No.8A	O5.5I(f)	-0.41 ± 0.13	0.20	Yes	Nonthermal
···	Cyg OB2 No.9	O5If	0.06 ± 0.03	0.68	Yes	Nonthermal
···	Cyg OB2 No.12	B5Ie	0.73 ± 0.04	0.59	Yes	Thermal
···	V433 Sct	B1.5Ia	0.23 ± 0.24	0.20	No	Thermal
···	MWC 349	O9:III: + BOIII	···	0.27	···	Thermal?

NOTES: † — '$\dot{M}_{\rm H\alpha}$' for these objects was calculated using the empirical dependence of mass-loss rate on luminosity, derived in §4.3.1.

As mentioned in §4.3.1, stellar luminosity is the dominant factor in determining $\dot{M}$ for radiatively-driven winds (e.g. Castor *et al.*, 1975; Kudritzki, 1998). Figure 6.3 plots the radio mass-loss rates (reiterating here that these values were obtained assuming a free–free interpretation of the observed flux) as a function of stellar luminosity. The thermal/nonthermal classification of the stars is indicated, and the solid line represents the empirical relationship between mass-loss rate and luminosity, derived from Hα data in §4.3.1:-

$$\log \dot{M} = (1.07 \pm 0.09) \log L - (11.7 \pm 0.5) \tag{6.7}$$

where $\dot{M}$ is in $M_\odot$ yr^{-1} and L is in $L_\odot$. For comparison, and represented by the dashed line, also included is the empirical $\dot{M}$–L relationship of Howarth and Prinja (1989), who, using UV and radio data, found:-

$$\log \dot{M} = 1.69 \log L - 15.4 \tag{6.8}$$

for O-type stars, irrespective of luminosity class.

If Equation 5.2 is applied to sources with an appreciable nonthermal contribution to their radio flux, this will result in an overestimate of the mass-loss rate. Such objects will have a higher-than-expected (inferred) $\dot{M}$ for their luminosity, and ought to be located in

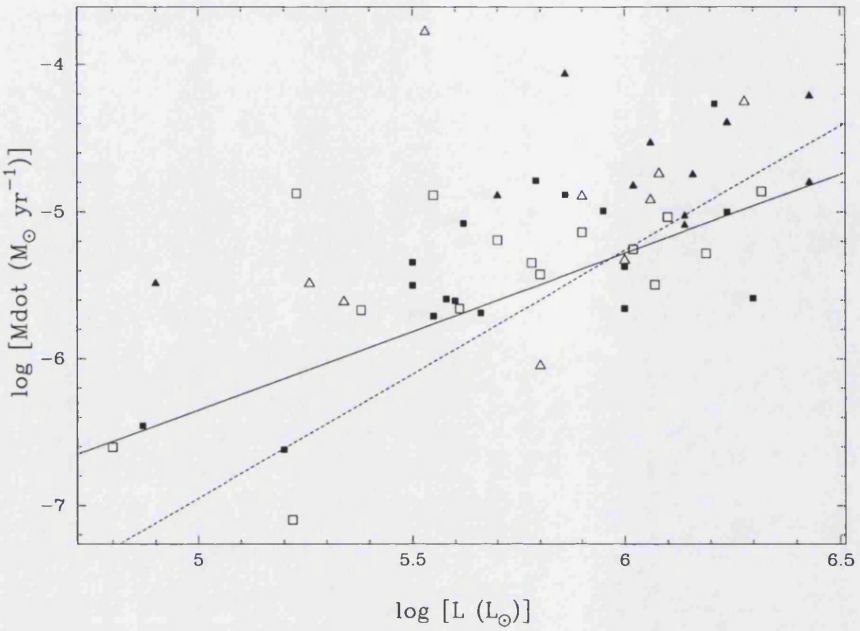

Figure 6.3: Mass-loss rate (calculated assuming a free–free interpretation of the observed flux) as a function of stellar luminosity for the entire radio sample. '■' represent definite thermal emitters, '□' represent probable thermal emitters, '▲' represent definite nonthermal emitters, and '△' represent stars that show some evidence of being (i.e., are probable) nonthermal emitters. The solid line represents the empirical $\dot{M}$–L relationship derived from Hα data in §4.3.1; for comparison, the dashed line represents the empirical $\dot{M}$–L relationship found for O stars by Howarth and Prinja (1989). HD 26676, with a luminosity of $\log L\ (L_\odot) = 2.26$, lies outside the range of the plot.

the upper part of Figure 6.3. Indeed, all the definite nonthermal emitters, and all but two of the probable nonthermal emitters, lie above the line of the empirical $\dot{M}$–L relationship from §4.3.1. The nonthermal sources are also systematically the most luminous stars in the sample (as found by Bieging *et al.*, 1989): only four of the twelve definite nonthermal emitters have $\log L\ (L_\odot) < 6.0$.

Figure 6.4 plots the radio mass-loss rates (calculated assuming a free–free interpretation of the observed flux) as a function of stellar luminosity, but this time for the 32 thermal, or probably thermal sources, only. The spectral types of the stars are indicated, and the solid line represents a least-squares fit to the data, with:-

$$\log \dot{M} = (1.00 \pm 0.21) \log L - (11.2 \pm 1.2) \tag{6.9}$$

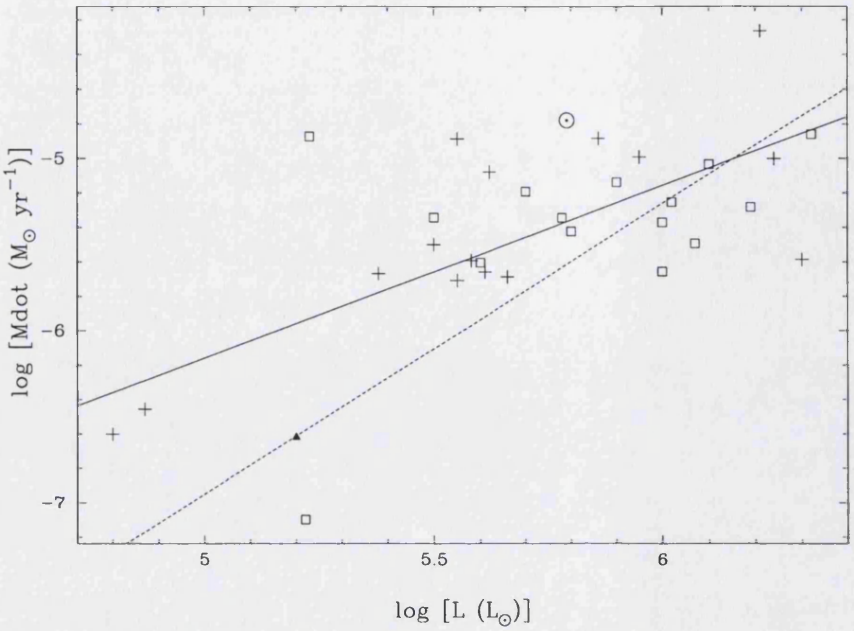

Figure 6.4: Mass-loss rate as a function of stellar luminosity for the thermal, or probably thermal sources, in the radio sample. '□' represent O stars, '+' represent B stars, '▲' represents the A2Ia star, α Cyg, and '⊙' represents the WR star, HD 152408. The solid line represents a least-squares fit to the data; for comparison, the dashed line represents the empirical $\dot{M}$–L relationship found for O stars by Howarth and Prinja (1989). HD 26676, with a luminosity of $\log L\ (L_\odot) = 2.26$, lies outside the range of the plot.

Again, for comparison, the empirical $\dot{M}$–L relationship of Howarth and Prinja (1989) is included (the dashed line). Equation 6.9 is, within the error margins, in good agreement with the $\dot{M}$–L relationship derived from the Hα data (Equation 6.7). The errors on the radio-derived correlation are larger, but the thermal radio sample of 32 stars is half the size of the 64 objects considered in the Hα analysis.

6.4.3 Possible origins of nonthermal emission

A significant fraction (40%) of the stellar sample display one or more of: a) a spectral index, $\alpha \ll 0.6$; b) a high value of $\log(\dot{M}_{\rm radio}/\dot{M}_{\rm H\alpha})$; or c) significant radio variability. Why is this? One possibility already discussed is that the sources are nonthermal. In other words, the assumption that the observed flux is thermal, free–free emission is wrong. An alternative explanation for the high incidence of $\alpha \ll 0.6$ is that one (or more) of the other basic assumptions made when interpreting the radio observations is incorrect; i.e., the

wind is not: a) stationary; b) spherically symmetric; c) isothermal; d) optically thick; or e) flowing at constant velocity. Schmid-Burgk (1982) modelled non-spherical stellar envelopes and winds, and found that departures from spherical symmetry do not significantly affect the reliability of spectral index and mass-loss estimates (major exceptions, however, are winds composed of numerous, narrow, radial streamers). Leitherer and Robert (1991) studied the influence of various departures from the model used to derive Equation 5.1 (i.e., deviations from assumptions [a]–[e], above) and found that, in general, these effects do not modify α by more than ~ 0.1.

Let us then assume that the incidences of discrepant spectral index and high inferred radio mass-loss rate are indeed consequences of nonthermal emission; i.e., that the 21 stars classified as 'nonthermal' or 'probable nonthermal' are really so. Although synchrotron radiation from relativistic electrons is most probably responsible for the observed nonthermal flux, the nature of the accelerating agent is still unknown. Various scenarios have been discussed in the literature: wind accretion onto a compact companion in a wide orbit (Abbott *et al.*, 1984*a*); electrons spiralling to mildly relativistic energies by interactions with shocks in a weak stellar magnetic field (White, 1985, however, the origin of such a field is still uncertain at the present time); first-order Fermi acceleration in shocked stellar winds (Chen and White, 1994); and wind–wind interactions in binary systems (Stevens, 1995). This final possibility will now be given further consideration.

6.5 Wind–wind interactions

The colliding winds of binary systems consisting of hot, luminous stars present a range of complex astrophysical phenomena (see Vol. 260 of the ASP Conference Series on 'Interacting Winds from Massive Stars'; Moffat and St-Louis, 2002). The observational signatures of wind–wind interactions have been found over a broad wavelength range, from the radio to X-rays. Analysis of phase-locked variations of appropriate emission-line profiles can yield information about the geometry (and hence physics) of the outflows and interaction regions (e.g. Nazé *et al.*, 2002; Rauw *et al.*, 2002*b*; Sana *et al.*, 2002). Perhaps the most noticeable indication of wind–wind interactions, however, is the excess X-ray emission observed in massive binaries (e.g. Chlebowski and Garmany, 1991), thought to be produced by shock-heated material in the wind interaction regions (e.g. Stevens *et al.*, 1992).

6.5.1 Binarity

Most massive stars are, or were, members of multiple systems (e.g. Zinnecker, 2003, and references therein). Mason *et al.* (1998), in a magnitude-limited ($V < 8$) survey of 227 O-type systems, found that after combining their speckle interferometric results with those already published, $> 59\%$ of O stars in clusters and associations have a visual or spectroscopic companion. The multiplicity of massive stars is crucial to our understanding of stellar evolution, as the properties (and hence evolutionary history) of a single star are very different to those of an (unresolved) multiple object. In the case of massive close binaries, mass transfer is expected between the components, with the change in stellar masses leading to complex evolutionary tracks and altering the ultimate fate of the stars (e.g. Wellstein and Langer, 1999). The multiple nature of a stellar system is not, however, always straightforwardly apparent, and many ostensibly single stars are found not to be so upon closer inspection. For example, the combined light of the binary star Cyg OB2 No.22AB was classified as O4III(f) by Massey and Thompson (1991). The star was later spatially resolved into its two constituent components by Walborn *et al.* (2002): component A being of spectral type O3If*, and component B, spectral type O6V((f)). Cyg OB2 No.22A thus became only the second O3 star of any kind known in the northern hemisphere, with properties (and an evolutionary history) very different to the O4III(f)-type object it was previously thought to be.

6.5.2 X-ray emission

O stars were first discovered to be X-ray emitters with the *Einstein X-ray Observatory* (Harnden *et al.*, 1979; Seward *et al.*, 1979). It was soon found that the observed soft X-ray luminosity is correlated with the stellar bolometric luminosity such that:-

$$\log\left(L_{\rm x}/L_{\rm bol}\right) \approx 10^{-7} \tag{6.10}$$

(Seward *et al.*, 1979; Pallavicini *et al.*, 1981); this simple linear proportionality is valid only for ISM-corrected X-ray luminosities, and shows a scatter of around two orders of magnitude. The correlation was later confirmed by Chlebowski *et al.* (1989), in an analysis of a relatively large sample of O stars. Berghöfer *et al.* (1997) demonstrated that the relationship is valid for single, isolated stars down to spectral type B1–B1.5.

Soft X-ray emission from early-type stars is believed to be produced by shock-heated gas propagating in the radiation-driven winds of these stars (Lucy and White, 1980; Lucy,

1982; Feldmeier, 1995). The shocks are thought to be formed as a consequence of hydrodynamical instability (e.g., Owocki *et al.*, 1988; Puls *et al.*, 1994). Some stars, however, are observed to emit 'excess' flux in X-rays. Chlebowski (1989) found that massive binaries are almost two times brighter in X-rays than single stars, and suggested that this could be due to the collision of stellar winds. Chlebowski (1989) also found evidence for a positive correlation between the ratio of X-ray luminosity to bolometric luminosity, and the observed radio luminosity: in general, the most energetic X-ray sources appear to be the strongest radio emitters. He suggested that since the strongest nonthermal radio sources are also observed to be the strongest X-ray emitters, the emission processes responsible for these two phenomena may be related to a common mechanism: 'excess' radio flux and 'excess' X-ray flux might indeed be related. This idea will now be explored.

6.5.3 Possible correlations

Given that both nonthermal radio emission and excess X-ray luminosity have been associated with binarity (e.g. Stevens, 1995; Chlebowski and Garmany, 1991, respectively), it is of interest to see whether the nonthermal emitters in the radio sample are also overluminous in X-rays, and whether this correlates with the incidence of binarity.

Table 6.5 summarises the status, with regard to binarity, nonthermal radio emission, and excess X-ray flux, of the radio sample stars. Column 4 gives the binary status of the star. Where a star has been classified as single, this is based on the best information available at the time of writing: it is very difficult to establish with certainty that a star is *not* a binary, but much easier to establish that it *is* a binary. The nature of the radio emission (nonthermal or otherwise, as determined in §6.4.2), is given in column 5. The 'nonthermal' label from the final column of Table 6.4 is represented here as 'yes', 'probable nonthermal' as 'probable', 'thermal' as 'no' and 'probable thermal' as 'unknown'. Published values of $\log(L_{\rm x}/L_{\rm bol})$ are given in column 6. Most of these data were obtained with the *Einstein* and *ROSAT* satellites; sources are provided on page 189, after Table 6.5. Due to the independence of $\log(L_{\rm x}/L_{\rm bol})$ on distance, it is unimportant whether the distances assumed in the references differ from those used to calculate $\log(\dot{M}_{\rm radio}/\dot{M}_{\rm H\alpha})$, which is also distance-independent. Finally, using the value of $\log(L_{\rm x}/L_{\rm bol})$, column 8 provides an indication as to whether or not the star is overluminous in X-rays: excess X-ray emission is defined here as $\log(L_{\rm x}/L_{\rm bol}) > 10^{-7}$ (from Relationship 6.10). If, in columns 6, 7 and 8, there are no entries (represented by '$\cdots$'), there were no available X-ray data.

Table 6.5: Binarity and X-ray emission

HD	Name	Spectral type	Binary?	Nonthermal radio?	$\log(L_x/L_{bol})$	Ref.	Excess X-ray?
2905	κ Cas	BC0.7Ia	No	Unknown	< -7.77	B96	No
5394	γ Cas	B0.5IVe	Yes	Unknown	-6.44	B96	Yes
14947	...	O5If+	No	Unknown	...	...	...
15558	...	O5III(f)	Yes	Yes	-6.13	C89	Yes
15570	...	O4If+	No	Yes	< -6.04	C89	Possible
17505	...	O6.5V	Possible	Probable	...	...	...
26676	...	B8Vn	Possible	Yes	< -6.34	B96	Possible
30614	α Cam	O9.5Ia	No	No	-7.37	B96	No
34085	β Ori/Rigel	B8Ia	No	No	-8.25	B96	No
36486	δ Ori A	O9.5II	Yes	Probable	-6.69	B96	Yes
37128	ϵ Ori	B0Ia	Possible	No	-6.78	B96	Yes
37468	σ Ori AB	O9.5V	Yes	Yes	-6.67	B96	Yes
37742	ζ Ori	O9.7Ib	No	No	-6.74	B96	Yes
41117	χ^2 Ori	B2Ia	No	No	< -7.78	B96	No
47839	15/S Mon	O7V((f))	Yes	Probable	-6.63	B96	Yes
57060	UW CMa	O7Ia:fp var	Yes	Unknown	-7.49	B96	No
57061	τ CMa	O9II	Yes	Unknown	-6.98	B96	No
66811	ζ Pup	O4I(n)f	No	No	-7.24	B96	No
80077	PV Vel	B2Ia+	No	No	...	...	...
93250	...	O3V((f))	No	Probable	-6.40	C89	Yes
149404	V918 Sco	O9Ia	Yes	Unknown	-7.39	B96	No
149757	ζ Oph	O9.5V	No	Unknown	-7.68	B96	No
151804	...	O8Iaf	No	Yes	< -7.96	B96	No
152236	ζ^1 Sco	B1.5Ia+	No	No	< -8.09	B96	No
152408	WR 79A	WN9ha	No	No	< -7.85	B96	No
152424	...	OC9.7Ia	Possible	Probable	< -6.25	C89	Possible
152623	...	O7V(n)((f))	Yes	Yes	-6.33	C89	Yes
153919	...	O6.5Iaf+	Yes	Unknown	...	...	...
160529	...	B8Ia+	No	Unknown	...	...	...
164794	9 Sgr	O4:V((f))	Possible	Yes	-6.46	B96	Yes
166734	...	O7Ib(f) + O8–9I	Yes	Unknown	...	...	...
167971	MY Ser	O8Ib(f)p	Yes	Yes	-5.91	C89	Yes
168112	...	O5III(f)	No	Yes	-6.13	C89	Yes
168607	...	B9Ia+	No	Unknown	-5.70	G92	Yes
169454	...	B1Ia+	No	No	...	...	...
169515	RY Sct	B0V + O5.5V	Yes	Probable	< -6.32	C89	Possible
169582	...	O6If	No	Unknown	< -6.12	C89	Possible
190429A	...	O4If+	No	Probable	$-6.36^{\dagger}$	C89	Yes
190603	...	B1.5Ia+	Yes	No	< -7.82	B96	No
192281	...	O5Vn((f))p	No	Unknown	...	...	...

Continued overleaf

HD	Name	Spectral type	Binary?	Nonthermal radio?	$\log(L_x/L_{bol})$	Ref.	Excess X-ray?
193237	P Cyg	B1Ia+	No	No	< -8.36	B96	No
194279	···	B1.5Ia	No	No	···	···	···
195592	···	O9.7Ia	Possible	No	···	···	···
197345	α Cyg/Deneb	A2Ia	Yes	No	$< -8.06^{\ddagger}$	C81	No
206267A	···	O6.5V((f))	Yes	Probable	-7.36	B96	No
210839	λ Cep	O6I(n)fp	No	Unknown	-7.68	B96	No
···	Cyg OB2 No.5	2× O7Ianfp	Yes	Yes	-5.63	W98	Yes
···	Cyg OB2 No.7	O3If	No	Probable	< -6.19	C89	Possible
···	Cyg OB2 No.8A	O5.5I(f)	No	Yes	-5.02	W98	Yes
···	Cyg OB2 No.9	O5If	No	Yes	-5.61	W98	Yes
···	Cyg OB2 No.12	B5Ie	No	No	-5.56	W98	Yes
···	V433 Sct	B1.5Ia	No	No	···	···	···
···	MWC 349	O9:III: + BOIII	Possible	Unknown	···	···	···

NOTES: Sources for $\log(L_x/L_{bol})$: C81 — Cassinelli *et al.* (1981); C89 — Chlebowski *et al.* (1989); G92 — Grillo *et al.* (1992); B96 — Berghöfer *et al.* (1996); W98 — Waldron *et al.* (1998).

The Waldron *et al.* (1998) data are wind + ISM-corrected luminosities, based on the average of two detections, approximately two years apart.

† — The detection of HD 190429A was rejected by Chlebowski *et al.* (1989), because the star was partially obscured by the Imaging Proportional Counter (IPC) of the *Einstein Observatory* entrance window support structure (Harnden *et al.*, 1984). However, the star was detected by the on-line software (Harnden *et al.*, 1984), and so the result is listed here.

‡ — A bolometric luminosity of 10^{39} erg s^{-1}, as given in Cassinelli *et al.* (1981), was used to calculate $\log(L_x/L_{bol})$ for α Cyg.

References for individual stars regarding binarity:-

HD 2905 — Jarad *et al.* (1989); HD 5394 — Harmanec *et al.* (2000) and Miroshnichenko *et al.* (2002); HD 14947 — Underhill and Gilroy (1990); HD 15558 — Garmany and Massey (1981); HD 15570 — Underhill and Gilroy (1990); HD 17505 — Howarth *et al.* (1997*b*); HD 26676 — Bieging *et al.* (1989); HD 30614 — Gies and Bolton (1986); HD 34085 — Jarad *et al.* (1989); HD 36486 — Harvey *et al.* (1987); HD 37128 — Levato *et al.* (1988) and Morrell and Levato (1991); HD 37468 — Bolton (1974); HD 37742 — Jarad *et al.* (1989); HD 41117 — Mason *et al.* (2003); HD 47839 — Gies *et al.* (1993); HD 57060 — Stickland (1989); HD 57061 — van Leeuwen and van Genderen (1997) and Stickland *et al.* (1997); HD 66811 — Reid and Howarth (1996) and Howarth (personal communication); HD 80077 — Mason *et al.* (2003); HD 93250 — Levato *et al.* (1991); HD 149404 — Stickland and Koch (1996); HD 149757 — McAlister *et al.* (1993); HD 151804 — Fullerton *et al.* (1996); HD 152236 — Mason *et al.* (2003); HD 152408 — Fullerton *et al.* (1996); HD 152424 — Fullerton *et al.* (1996); HD 152623 — Fullerton (1990) and Mason *et al.* (1998); HD 153919 — Stickland and Lloyd (1993); HD 160529 — Mason *et al.* (2003); HD 164794 — Fullerton (1990); HD 166734 — Conti *et al.* (1980); HD 167971 — Leitherer *et al.* (1987); HD 168112 — Mason *et al.* (2003); HD 168607 — Mason *et al.* (2003); HD 169454 — Mason *et al.* (2003); HD 169515 — Cowley and Hutchings (1976); HD 169582 — Mason *et al.* (2003); HD 190429A — Fullerton *et al.* (1996);

HD 190603 — Mason *et al.* (2003); HD 192281 — Gies and Bolton (1986); HD 193237 — Mason *et al.* (2003); HD 194279 — Mason *et al.* (2003); HD 195592 — Plaskett and Pearce (1931); HD 197345 — Mason *et al.* (2003); HD 206267A — Stickland (1995); HD 210839 — Fullerton *et al.* (1996); Cyg OB2 No.5 — Hall (1974); Cyg OB2 No.7 — Mason *et al.* (2003); Cyg OB2 No.8A — Mason *et al.* (2003); Cyg OB2 No.9 — Mason *et al.* (2003); Cyg OB2 No.12 — Mason *et al.* (2003); V433 Sct — Mason *et al.* (2003); MWC 349 — Hofmann *et al.* (2002).

It is possible to use the Hα mass-loss rates, $\dot{M}_{\mathrm{H}\alpha}$, derived in §4 (or, for those stars not in the Hα sample, the empirical dependence of mass-loss rate on luminosity) to predict the expected thermal component of the radio mass-loss rate (which is a measure of the thermal component of the wind emission). For the 41 stars with available X-ray data, Figure 6.5 plots the values of $\log(\dot{M}_{\mathrm{radio}}/\dot{M}_{\mathrm{H}\alpha})$ from Table 6.4 against $\log(L_{\mathrm{x}}/L_{\mathrm{bol}})$: it essentially plots the excess (i.e., nonthermal) radio emission against the excess X-ray emission. A correlation between these two quantities might be suggestive of a causal relationship. If excess radio emission does correlate with excess X-ray emission, this will manifest itself as a significantly non-zero correlation coefficient for Figure 6.5.

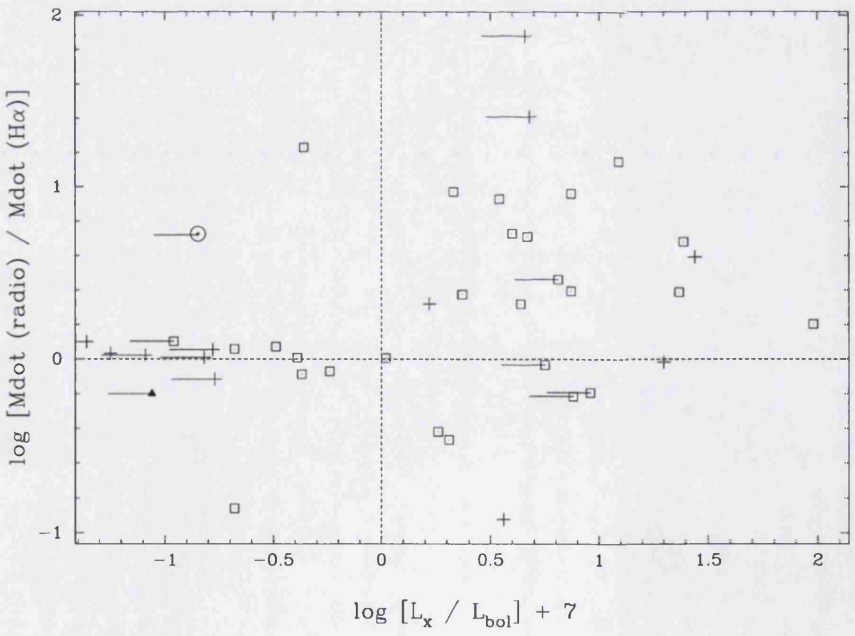

Figure 6.5: Correlation between excess (i.e., nonthermal) radio emission and excess X-ray emission. '□' represent O stars, '+' represent B stars, '▲' represents the A2Ia star, α Cyg, and '⊙' represents the WR star, HD 152408. '——' denote upper limits to $\log(L_{\mathrm{x}}/L_{\mathrm{bol}})$.

Relationship 6.10 was first demonstrated to be valid for O stars (e.g. Chlebowski, 1989), and then down to spectral type B1–B1.5 by Berghöfer *et al.* (1997). To gauge the effect of including B stars in Figure 6.5, correlation coefficients have been computed for the fit to: a) *all* 41 stars with X-ray data; b) the 35 O and early-B stars, only; and c) the 27 O stars only. These are given in Table 6.6. In each case, for the sample size concerned, the correlation coefficient is such that the probability of the correlation arising by chance is less than 10%. Thus, there is indeed a statistically significant correlation between excess radio emission and excess X-ray emission, suggestive of a causal relationship between the two phenomena.

Table 6.6: Correlation between excess (i.e., nonthermal) radio emission and excess X-ray emission for different spectral types

Spectral type	Sample size	Correlation coefficient	Probability of arising by chance
All	41	0.305	$< 10\%$
O/Early-B	35	0.327	$< 10\%$
O	27	0.328	$< 10\%$

Is this relationship also associated with binarity? Figure 6.5 is divided into four quadrants. The seventeen objects in the upper right-hand quadrant are the 'excess' group: those that exhibit excess radio *and* excess X-ray emission. These stars are listed in Table 6.7, together with their binary status and bolometric luminosity. Of these stars, ten are binaries or possible binaries. The fraction of binaries in the excess group is therefore potentially as high as 59%, compared to 45% (24 out of 53) in the radio sample as a whole. These data are displayed in Table 6.8. Applying Fisher's exact test for 2x2 contingency tables, the probability of there being this many, or more, binaries in the excess group is about 14%. The formal probability of there being a real physical difference between the two groups is suggestive, but not statistically significant, at the conventional 5% level. Of the seven objects in Table 6.7 that are believed to be *single*, all have extremely high bolometric luminosities, of $\log L\ (L_{\odot}) > 6.0$. Excess radio and X-ray emission appear to be intrinsic to the highest-luminosity, single objects, also.

Table 6.7: Stars exhibiting excess (i.e., nonthermal) radio emission and excess X-ray emission

HD	Name	Spectral type	Binary?	log $(L/L_{\odot})$
15558	···	O5III(f)	Yes	6.16
26676	···	B8Vn	Possible	2.26
37128	ϵ Ori	B0Ia	Possible	5.50
37468	σ Ori AB	O9.5V	Yes	4.9
47839	15/S Mon	O7V((f))	Yes	5.34
93250	···	O3V((f))	No	6.28
152623	···	O7V(n)((f))	Yes	5.7
164794	9 Sgr	O4:V((f))	Possible	6.02
167971	MY Ser	O8Ib(f)p	Yes	5.86
168112	···	O5III(f)	No	6.06
169515	RY Sct	B0V + O5.5V	Yes	5.53
190429A	···	O4If+	No	6.06
···	Cyg OB2 No.5	2× O7Ianfp	Yes	6.43
···	Cyg OB2 No.7	O3If	No	6.08
···	Cyg OB2 No.8A	O5.5I(f)	No	6.43
···	Cyg OB2 No.9	O5If	No	6.24
···	Cyg OB2 No.12	B5Ie	No	6.21

NOTE: Bolometric luminosities were taken from Table 4.3.

Table 6.8: Fisher's exact test for binarity and nonthermal/excess X-ray emission

	'Normal' group	'Excess' group	Total
Binary	14	10	24
Non-binary	22	7	29
Total	36	17	53

CHAPTER 7

Discussion and Future Work

A general enquiry into the physics of mass loss from hot, luminous stars has been presented.

The observational considerations and data reduction of the Hα spectroscopy of 64 Galactic early-type stars were described in §2. In §3, the physics of stellar atmospheres, and in particular the formation of the Hα line in the winds of early-type stars, was discussed. This was in anticipation of using the FORSOL code of Puls *et al.* (1996) to model Hα line profiles and determine stellar mass-loss rates. After introducing the FORSOL code, sensitivity tests were performed to investigate the effect of different stellar and wind parameters on a model Hα profile; particular attention was given to the effect of the hydrogen and helium departure coefficients. In §4, a new program, PHALTEE, was introduced, which uses a genetic algorithm to search within a specified parameter space for the 'best' (quasi-least-squares) FORSOL fit to an observed Hα profile. This renders Hα modelling both more objective and automated, while minimising the necessity for manual intervention. PHALTEE was used to model quantitatively the data presented in §2, thereby deriving mass-loss rates and velocity law β-exponents.

New mm-wave observations of nineteen early-type stars (including a subset of the Hα sample) were presented in §5. These data were obtained using the Sub-millimetre Common User Bolometer Array (SCUBA). For the objects detected, the mm fluxes were used to calculate mass-loss rates (or upper limits thereto). In §6, the results of a literature survey of published mm and cm fluxes were presented. These data were combined with the mm fluxes from §5 to create a larger sample, of 53 Galactic early-type stars (a subset of 36 stars being common with the Hα sample). Again, where possible, mean fluxes were

calculated and used to determine mass-loss rates. For those sources with multiwavelength, multi-epoch detections, time-averaged spectral indices were calculated. The incidence of nonthermal emission was examined, with 23% of the sample being found to exhibit strong evidence for nonthermal flux. The occurrence of binarity and excess X-ray emission amongst the nonthermal emitters was also investigated, looking for evidence of a causal relationship between these phenomena.

7.1 Comparison of Hα and radio mass-loss rates

An important test of using PHALTEE to derive mass-loss rates from observed Hα profiles, is to compare the PHALTEE results with those derived from radio fluxes. Hα- and radio-derived mass-loss rates should be (approximately) equivalent if the radio emission is free–free and the procedure for deriving the Hα mass-loss rates is correct (the latter being highly dependent upon the assumed/derived velocity law of the wind; see, e.g. Leitherer, 1988*a*, and §4 of this thesis).

Table 7.1 lists, for the 36 stars common to both samples, the mass-loss rates derived from the Hα data, and those from the radio data. The derived mass-loss rates, in general, confirm trends apparent from earlier works (e.g. Abbott *et al.*, 1980, 1981; Lamers and Leitherer, 1993; Puls *et al.*, 1996; Scuderi *et al.*, 1998; Herrero *et al.*, 2000, 2002): OB stars have mass-loss rates of order $10^{-6}\ M_{\odot}\ \mathrm{yr}^{-1}$, with the most luminous objects losing mass at a rate of $\sim 10^{-5}\ M_{\odot}\ \mathrm{yr}^{-1}$. In order to make a meaningful comparison between the Hα and radio mass-loss rates, it is necessary to eliminate those stars which are known to be nonthermal emitters (the fourteen nonthermal sources are flagged with a '†' in the final column of Table 7.1). This leaves a total of 22 stars.

Figure 7.1 compares the Hα mass-loss rates derived using PHALTEE, with the radio-derived mass-loss rates. Distance uncertainty currently sets the limit for the accuracy of $\dot{M}$ derived from radio and mm data. However, mass-loss rates derived from Hα and free–free radio/mm observations have the same distance dependence, so that a comparison of the two is distance-independent. Thus, to a reasonable approximation, the uncertainty in most cases is dominated simply by the uncertainty in the observed radio flux. Two further stars, HD 5394 (γ Cas) and HD 149757 (ζ Oph), have also been removed from the comparison, as their radio mass-loss rates seem anomalously low (12% and 14% of the Hα rate, respectively); these discrepancies are not accommodated by the errors (the

radio result for ζ Oph, however, seems more in line with the Hα-derived mass-loss rate of $\leq 0.03 \times 10^{-6}\ M_{\odot}\ \mathrm{yr}^{-1}$, obtained by Puls *et al.*, 1996). Also, in each of these two cases, the radio mass-loss rate was calculated from just a *single* observation.

In general, the agreement between the radio and Hα rates is good. It should be borne in mind, however, that one of the selection criteria employed in §6.4.2 to discriminate between free–free and nonthermal emission, is the ratio of the radio mass-loss rate, $\dot{M}_{\mathrm{radio}}$ (derived assuming free–free emission), to that of the mass-loss rate derived from Hα, $\dot{M}_{\mathrm{H}\alpha}$. If $\dot{M}_{\mathrm{radio}}/\dot{M}_{\mathrm{H}\alpha} \gtrsim 2$, an object is classified as nonthermal and will therefore have been eliminated from this comparison, thereby removing the potentially most 'troublesome' cases, and ensuring a certain degree of agreement in Figure 7.1.

The solid line represents a least-squares fit to the data of slope 1.08 ± 0.11; the dashed line represents a 1:1 relationship. The mean value of $\log(\dot{M}_{\mathrm{radio}}/\dot{M}_{\mathrm{H}\alpha})$ is 0.02 ± 0.05, compared with a value of -0.07 ± 0.21 obtained by Puls *et al.* (1996). This might suggest that the Hα mass-loss rates derived from PHALTEE are systematically lower than those derived by Puls *et al.* (1996), and indeed, the PHALTEE-derived mass-loss rates *are* smaller for seven out of the nine stars common to both samples (see §4.4). The large discrepancy between the radio and Hα mass-loss rates of ζ Pup (this points to structure in the wind), noted by other authors (e.g. Petrenz and Puls, 1996), is not seen here: the two rates are in good agreement with each other, to within the errors.

Table 7.1: Comparison of Hα and radio mass-loss rates

HD	Name	Spectral type	$\dot{M}$ (10^{-6} $M_\odot$ yr^{-1})		Nonthermal
			Hα	Radio	source (†)
2905	κ Cas	BC0.7Ia	2.88	2.20 ± 0.78	
5394‡	γ Cas	B0.5IVe	2.10	0.25 ± 0.17	
14947	···	O5If+	5.01	6.43 ± 2.61	
15558	···	O5III(f)	7.21	17.9 ± 4.7	†
15570	···	O4If+	12.7	8.14 ± 2.34	†
30614	α Cam	O9.5Ia	3.04	2.49 ± 0.91	
36486	δ Ori	O9.5II	2.64	0.90 ± 0.26	†
37742	ζ Ori	O9.7Ib	5.81	2.21 ± 0.50	
66811	ζ Pup	O4I(n)f	5.00	4.26 ± 0.77	
149404	V918 Sco	O9Ia	9.07	9.25 ± 3.26	
149757‡	ζ Oph	O9.5V	0.58	0.08 ± 0.05	
152424	···	OC9.7Ia	5.08	4.70 ± 1.31	†
164794	9 Sgr	O4:V((f))	1.76	15.1 ± 3.5	†
166734	···	O7Ib(f) + O8-9I	18.5	13.8 ± 6.6	
167971	MY Ser	O8Ib(f)p	6.13	86.2 ± 16.4	†
168112	···	O5III(f)	3.24	29.6 ± 7.7	†
168607	···	B9Ia+	2.24	2.15 ± 0.79	
169454	···	B1Ia+	9.37	10.2 ± 2.2	
169515	RY Sct	B0V + O5.5V	6.54	167 ± 60	†
169582	···	O6If	5.27	3.21 ± 2.16	
190429A	···	O4If+	5.79	12.1 ± 7.7	†
190603	···	B1.5Ia+	2.51	2.56 ± 0.96	
192281	···	O5Vn((f))p	4.36	5.22 ± 2.08	
193237	P Cyg	B1Ia+	10.3	13.1 ± 1.7	
194279	···	B1.5Ia	1.82	2.06 ± 0.58	
195592	···	O9.7Ia	3.00	4.55 ± 1.68	
197345	α Cyg	A2Ia	0.38	0.24 ± 0.08	
206267A	···	O6.5V	0.19	3.26 ± 1.26	†
210839	λ Cep	O6I(n)fp	3.96	4.53 ± 1.11	
···	Cyg OB2 No.5	2× O7Ianfp	25.1	61.4 ± 8.7	†
···	Cyg OB2 No.7	O3If	6.28	18.2 ± 9.3	†

Continued overleaf

HD	Name	Spectral type	$\dot{M}$ (10^{-6} $M_\odot$ yr^{-1})		Nonthermal
			Hα	Radio	source (†)
···	Cyg OB2 No.8A	O5.5I(f)	9.96	15.9 ± 3.4	†
···	Cyg OB2 No.9	O5If	8.51	40.4 ± 6.6	†
···	Cyg OB2 No.12	B5Ie	13.9	54.3 ± 7.3	
···	V433 Sct	B1.5Ia	5.23	8.36 ± 1.74	
···	MWC 349	O9:III: + B0III	7.2	13.4 ± 8.5	

NOTES: † — The fourteen sources flagged as being nonthermal (or probably nonthermal) were eliminated from the comparison of Hα and radio mass-loss rates in Figure 7.1. ‡ — HD 5394 (γ Cas) and HD 149757 (ζ Oph) were also excluded from the comparison, because of their seemingly anomalously low $\dot{M}_{\rm radio}$.

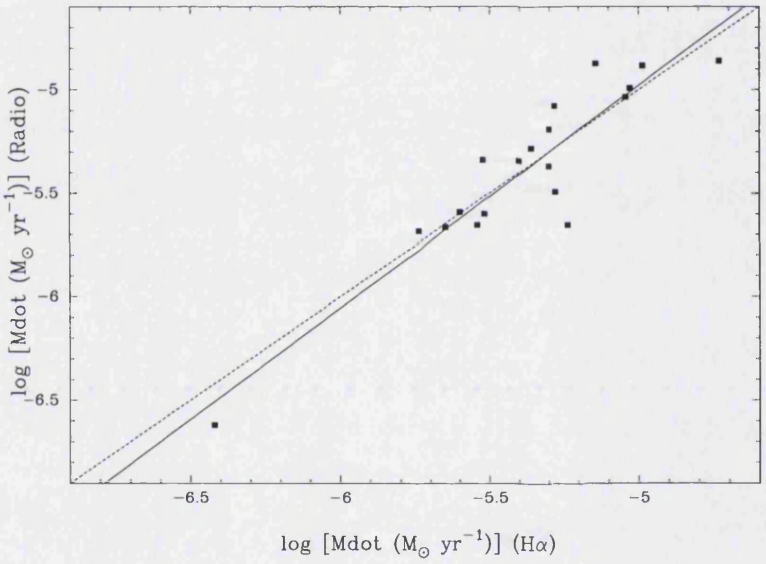

Figure 7.1: Comparison of Hα and radio mass-loss rates for 20 Galactic early-type stars. The solid line represents a least-squares fit to the data. The dashed line represents a 1:1 relationship.

Hα emission samples the wind at $\sim$1.0–1.5 R_*, whilst the free–free continuum regime extends from, typically, $\sim$5 R_* at 1 mm to $\sim$100 R_* at 20 cm. Thermal, free–free radio emission has two characteristics which make it particularly useful as a diagnostic of stellar winds. First, the bremsstrahlung opacity varies as wavelength squared, λ^2. Thus, the characteristic radius of emission increases with increasing wavelength: anything inside this radius does not influence observations. By obtaining measurements of a star at different wavelengths, it is possible to effectively 'scan' the wind. The free–free emission

also depends on the density squared, ρ^2 (as is also the case for Hα recombination radiation; Abbott *et al.*, 1981; Lamers and Waters, 1984). It is therefore sensitive to structure. The dependency on λ^2 and ρ^2 means that it is possible to trace structure out through the wind using thermal radio emission (with Hα observations serving as a probe of conditions even closer to the star).

When using Equation 5.2 to derive mass-loss rates from mm and radio continuum data, it was assumed that the wind outflow has a density structure that is homogeneous and stationary. Because the properties of thermal radio emission are such that a structured wind *enhances* emission, if the wind were to have large density contrasts, or 'clumps', this would lead to an overestimate of $\dot{M}$. Clumping has been demonstrated to be particularly important for WR stars (e.g. Moffat *et al.*, 1988; Hillier, 1991). Nugis *et al.* (1998) found that for WR stars, clumping-corrected mass-loss rates are indeed generally lower than those obtained using smooth wind models. Runacres and Blomme (1996), and Blomme and Runacres (1997), investigated the effect of clumping on the IR and radio continuum of O- and early B-type stars, and found that applying a smooth wind model to the radio observations of these objects could lead to an overestimate of the mass-loss rate. The degree of overestimation depends upon the nature of the density contrasts, and in particular the volume filling factor, f, which, in the simplifying assumption that all material is in the form of clumps, with no inter-clump matter, varies as:-

$$\dot{M}^{4/3} \propto f^{-2/3} \Rightarrow \dot{M} \propto f^{-0.5} \tag{7.1}$$

(Abbott *et al.*, 1981). In this simplifying assumption, the clumping factor:-

$$f_{\rm cl} = \frac{<\rho^2>}{<\rho>^2} \tag{7.2}$$

(Runacres and Owocki, 2002, where '<>' stands for 'time-averaged') is the inverse of the volume filling factor; it equals the density contrast of the clumps with respect to the mean density. The clumping factor becomes larger as mass is concentrated in a smaller volume.

As both free–free radio and Hα emission have emissivities proportional to ρ^2, clumping, if present, should affect $\dot{M}$ derived from both diagnostics in the same way. The earlier result, $\log(\dot{M}_{\rm radio}/\dot{M}_{\rm H\alpha}) = 0.02 \pm 0.05$, suggests that, if clumping is present in both the Hα- and radio-emitting regions, the radio and Hα clumping factors are such that $\log[f_{\rm cl}\,({\rm radio})/f_{\rm cl}\,({\rm H}\alpha)] = 0.04 \pm 0.10$. The fact that the clumping factors differ by only $\sim 10\%$ suggests that any structure forming in the inner wind persists to the radio regime,

over a distance $\sim$1.0–100 R_*. Is this plausible? Various authors have modelled the effects of clumping. Abbott *et al.* (1981) assumed a clumping law that is constant throughout the wind, whilst more recently, Runacres and Owocki (2002) adopted a distance-dependent clumping law. All models, however, show clumping ending at $\sim$40 R_*. The fact that the radio and Hα mass-loss rates agree so well does not seem to be consistent with this result. The Hα variability seen in many O-type stars does not necessarily provide evidence for clumping either. Ebbets (1982) saw no significant Hα variability on timescales comparable to the flow timescales ($\sim$ hours), which, if present, might be suggestive of inhomogeneities in the outflow.

Variability at a given radio wavelength can be used as an indication that any structure present in that region of the wind is large scale. In the winds of early-type stars, large-scale structure is believed to take the form of co-rotating interaction regions (CIRs; Mullan, 1986), formed by the interaction of fast and slow streams of gas. Variability over a large wavelength range would suggest that structure persists out to great distances from the star. Many of the stars in the radio sample do show variability at mm and cm wavelengths (see Table 6.1), suggestive of large-scale structure out to great distances in the wind. These objects, however, also tend to be nonthermal sources, for which variability is most likely due to changes in the synchrotron, not thermal, emission. The thermal sources show relatively little variability in flux at a given wavelength (with some notable exceptions, such as P Cyg and Cyg OB2 No.12; see §6.4.2). In order to investigate the formation and run of large-scale structure in the wind, extensive, multiwavelength monitoring of individual objects is required, such as that undertaken for 9 Sgr (Rauw *et al.*, 2002*a*) and ϵ Ori (Blomme *et al.*, 2002).

7.2 Wind-momentum–luminosity relationship (WLR)

A useful way of considering the strength of a stellar wind is in terms of the wind-momentum–luminosity relationship (WLR). By looking at the observed WLR, the extent to which the derived wind quantities are consistent with the predictions of radiation-driven wind theory can be examined.

7.2.1 Theoretical WLR

The WLR is a consequence of radiation-driven stellar wind theory. Put simply, given that the wind of an early-type star is driven by radiation pressure, the mechanical momentum of the outflow should be a function of photon momentum. Kudritzki (1998) used a simplified theoretical description of radiation-driven wind theory to derive an elementary relationship between the wind momentum and the luminosity of a star (i.e., the WLR).

For radiation-driven stellar winds, the mechanical momentum flow of the wind, $\dot{M}v_\infty$, ought to be a function of the photon momentum rate, L/c, provided by the stellar photosphere and interior:-

$$\dot{M}v_\infty = f(L/c) \tag{7.3}$$

If the function, f, could be found, then simply inverting the above relationship would enable the determination of the stellar luminosity directly from the stellar wind:-

$$L = f^{-1}(\dot{M}v_\infty) \tag{7.4}$$

Thus, with knowledge of the mass-loss rate and the terminal velocity, it would be possible to determine the luminosity of the star. From radiation-driven wind theory (Castor *et al.*, 1975; Pauldrach *et al.*, 1986; Kudritzki *et al.*, 1989), the following relation is expected to hold:-

$$\dot{M}v_\infty \propto \frac{1}{R_*^{0.5}} L^{1/\alpha} (M[1-\Gamma])^{\frac{3}{2}-\frac{1}{\alpha}} \tag{7.5}$$

where α is the line-strength distribution, a dimensionless number incorporated to account for the contributions from wind-driving lines of different optical thicknesses. The line-strength distribution is primarily determined by atomic physics, and reflects the distribution function of the oscillator strengths of the transitions concerned. It takes values in the range $\alpha = 0.6 \ldots 0.7$ at OB-star temperatures. The Eddington factor:-

$$\Gamma = g_{\rm rad}^{\rm Thom}/g \propto L/M \tag{7.6}$$

is the ratio of the (outward) radiative acceleration caused by Thomson electron scattering to the (inward) acceleration caused by gravity. The 'Eddington limit' provides an upper limit to the luminosity–mass ratio for a *stable* star in which the outward force is dominated by electron scattering. It is defined by the condition that the outward-directed force induced by radiation balances the inward-directed gravity.

The term $[1 - \Gamma]$ in Relation 7.5 describes the distance from the Eddington limit. It is a correction factor applied to the local gravitational acceleration to account for the photon momentum transfer by Thomson scattering. The quantity $M[1 - \Gamma]$ is known as the 'effective mass', and can vary widely for early-type stars, contributing to the large scatter seen in the correlation of mass-loss rate with luminosity (see §4.3.1). However, the atomic physics of oscillator strengths yields a line-strength distribution of $\alpha \approx 2/3$ (Kudritzki, 1998), meaning that the exponent, $\frac{3}{2} - \frac{1}{\alpha}$, in Relation 7.5 is very close to zero. Thus, to first order, the wind momentum is given by:-

$$\dot{M}v_{\infty} \propto \frac{1}{R_*^{0.5}} L^{1/\alpha} \tag{7.7}$$

This is the 'wind-momentum–luminosity relationship' (WLR). It predicts a strong dependence of the wind momentum on the stellar luminosity (the exponent, $1/\alpha$, is determined by the statistics of the multitude of lines driving the wind). The weak dependence on stellar radius arises because the wind must work against the gravitational potential of the star whilst being outwardly accelerated by photospheric photons. Rearranging Relation 7.7, we obtain:-

$$L^{1/\alpha} \propto \dot{M}v_{\infty}R_*^{0.5} \tag{7.8}$$

The quantity $\dot{M}v_{\infty}R_*^{0.5}$ is known as the 'modified wind momentum' (although it is often simply referred to as the 'wind momentum'; this convention will be adopted henceforth).

If reliably calibrated, Relation 7.8 implies that the wind momentum (calculated using a mass-loss rate and terminal velocity determined directly from the stellar spectrum) can be used to determine the luminosity of a star. This in turn can be used to derive a distance. For this reason, the WLR has become of great interest in extragalactic astronomy, where it has potential as an independent distance indicator (e.g. McCarthy *et al.*, 1997, 2001).

7.2.2 Observed WLR

Works by Kudritzki *et al.* (1995), Puls *et al.* (1996), Kudritzki *et al.* (1999), and Herrero *et al.* (2000, 2002) show a tight relationship between stellar wind momentum and luminosity. The WLR is observed to vary as a function of spectral type, with wind momenta being strongest for O supergiants, decreasing from early- to mid-B spectral types, then becoming stronger for A supergiants (Kudritzki *et al.*, 1999). The slope of the WLR is observed to be steeper for A and mid-B supergiants than for their O-type counterparts.

The dependence on spectral type is thought to be due to ionisation changing the effective number, and also the line-strength distribution, of spectral lines scattering photon flux around the stellar flux maximum (Kudritzki *et al.*, 1999). The WLR for O giants and dwarfs is shifted downwards with respect to the relationship for supergiants, towards lower wind momenta (Puls *et al.*, 1996). The relationship is also less tight, and for luminosities $\log L/L_{\odot} \lesssim 5.3$, the situation is unclear, with some objects falling well below the line of the WLR.

Table 7.2 lists, for each star in the Hα sample, the stellar luminosity and the logarithm of the observed wind momentum:-

$$D_{\rm mom} = \dot{M} v_{\infty} R_{*}^{0.5} \tag{7.9}$$

where $\dot{M}$ (the Hα mass-loss rate) and v_{∞} are in cgs units, and R_{*} is in units of $R_{\odot}$.

Table 7.2: Observed wind momenta for the Hα sample

HD	Name	Spectral type	$\log(L/L_\odot)$	$\log D_{\rm mom}$
2905	κ Cas	BC0.7Ia	5.61	29.09
5394	γ Cas	B0.5IVe	4.80	28.83
10125	···	O9.7II	5.5	28.76
12323	···	ON9V	4.7	27.15
13745	V354 Per	O9.7II((n))	5.3	28.83
14947	···	O5If+	5.70	29.47
15558	···	O5III(f)	6.16	29.74
15570	···	O4If+	6.14	29.99
16429	···	O9.5II((n))	5.9	29.34
30614	α Cam	O9.5Ia	5.6	29.13
34078	AE Aur	O9.5V	4.9	27.66
36486	δ Ori	O9.5II	5.8	29.23
37742	ζ Ori	O9.7Ib	6.0	29.57
66811	ζ Pup	O4I(n)f	6.0	29.53
105056	GS Mus	ON9.7Iae	5.5	28.64
123008	···	ON9.7Iab	5.8	28.96
149038	μ Nor	O9.7Iab	5.7	28.83
149404	V918 Sco	O9Ia	6.1	29.91
149757	ζ Oph	O9.5V	5.22	28.30
152003	···	O9.7Iab	5.7	29.20
152147	···	O9.7Ib	5.7	29.08
152249	···	OC9.5Iab	5.8	29.20
152405	···	O9.7Ib–II	5.2	28.45
152424	···	OC9.7Ia	6.0	29.51
154368	···	O9.5Iab	5.7	29.10
154811	···	OC9.7Iab	5.7	29.24
156212	···	O9.7Iab	5.6	28.92
164794	9 Sgr	O4:V((f))	6.02	29.09
166734	···	O7Ib(f) + O8–9I	6.32	30.27
167971	MY Ser	O8Ib(f)p	5.86	29.60
168112	···	O5III(f)	6.06	29.34
168607	···	B9Ia+	5.38	28.44

Continued overleaf

HD	Name	Spectral type	$\log(L/L_\odot)$	$\log D_{\rm mom}$
169454	···	B1Ia+	5.95	29.64
169515	RY Sct	B0V + O5.5V	5.53	29.56
169582	···	O6If	6.07	29.54
188209	···	O9.5Iab	5.6	28.89
189957	···	O9.5III	5.2	28.10
190429A	···	O4If+	6.06	29.49
190603	···	B1.5Ia+	5.58	28.72
191781	···	ON9.7Iab	5.5	29.14
192281	···	O5Vn((f))p	6.19	29.51
193237	P Cyg	B1Ia+	5.86	29.05
194279	···	B1.5Ia	5.66	28.83
194280	···	OC9.7Iab	5.6	29.07
195592	···	O9.7Ia	5.5	29.17
197345	α Cyg	A2Ia	5.20	27.86
201345	···	ON9V	4.9	27.91
202124	···	O9.5Iab	5.6	29.16
206267A	···	O6.5V((f))	5.26	27.99
207198	···	O9Ib–II	5.5	28.87
209975	19 Cep	O9.5Ib	5.5	28.96
210809	···	O9Iab	5.8	29.24
210839	λ Cep	O6I(n)fp	5.78	29.39
214680	10 Lac	O9V	5.1	27.51
218195	···	O9III	5.3	28.51
218915	···	O9.5Iab	5.6	28.94
225160	···	O8Ib(f)	6.0	29.31
···	Cyg OB2 No.5	2× O7Ianfp	6.43	30.31
···	Cyg OB2 No.7	O3If	6.08	29.67
···	Cyg OB2 No.8A	O5.5I(f)	6.43	29.94
···	Cyg OB2 No.9	O5If	6.24	29.74
···	Cyg OB2 No.12	B5Ie	6.21	30.35
···	V433 Sct	B1.5Ia	5.62	29.45
···	MWC 349	O9:III: + B0III	5.23	27.97

NOTES: $\log D_{\rm mom}$ was calculated with $\dot{M}$ and v_∞ in cgs units, and R_* in units of $R_\odot$. L, v_∞ and R_* were taken from Table 4.3. Hα mass-loss rates, $\dot{M}$, were taken from Table 4.6.

Figures 7.2 and 7.3 plot (for the O and B stars, respectively) $\log D_{\rm mom}$ as a function of luminosity; i.e., they show the observed WLR. Adopting a WLR of the form:-

$$\log D_{\rm mom} = \log D_0 + x \log (L/L_\odot) \tag{7.10}$$

it is possible to determine the coefficients D_0 and x from Figures 7.2 and 7.3. The reciprocal value of the slope, x, is the exponent, α, that describes the line-strength distribution. Values for $\log D_0$, x and α are given in Table 7.3.

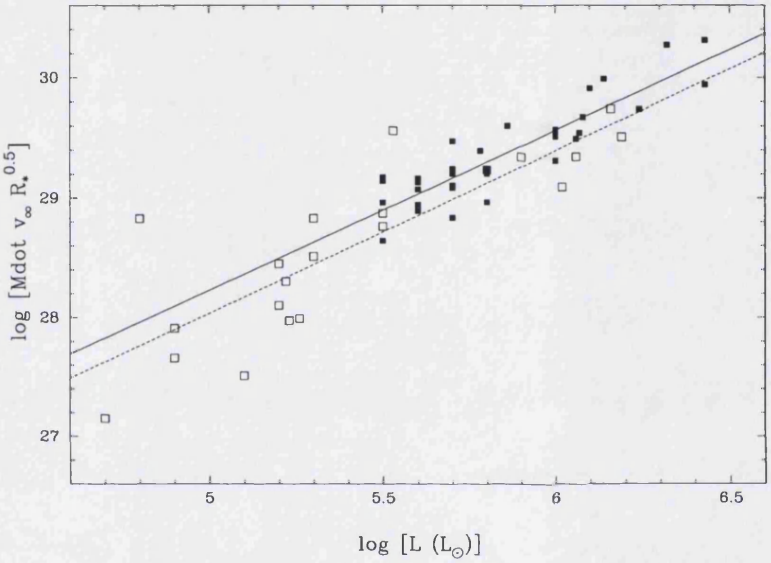

Figure 7.2: The observed WLR for the O stars in the Hα sample. $\dot{M}$ and v_∞ are in cgs units; R_* is in units of $R_\odot$. '■' represent O supergiants and '□' represent O stars of luminosity class II–V (here including the two non-supergiant B stars in the sample, HD 5394 and HD 169515). The solid line represents a least-squares fit to the O supergiant data, and the dashed line represents a least-squares fit to the non-supergiant data.

As found by Puls *et al.* (1996), the O supergiants (Figure 7.2) follow a tight relation, with a slope corresponding to a value of $\alpha = 0.75$. O stars of luminosity class II–V follow a less tight relation, with ~ 0.2 dex smaller momentum, but with an almost parallel slope of $\alpha = 0.74$. Again, in agreement with Puls *et al.* (1996), for luminosities $\log (L/L_\odot) \lesssim 5.3$, the relationship appears to change, becoming rather steeper.

The situation for the B supergiants is less well constrained, as there are far fewer data points than for the O stars (nine, compared with 55 for the O stars). The early-B stars (defined as B0–B1.5) exhibit a slope of $\alpha = 0.76$, almost parallel to that for the O stars (the

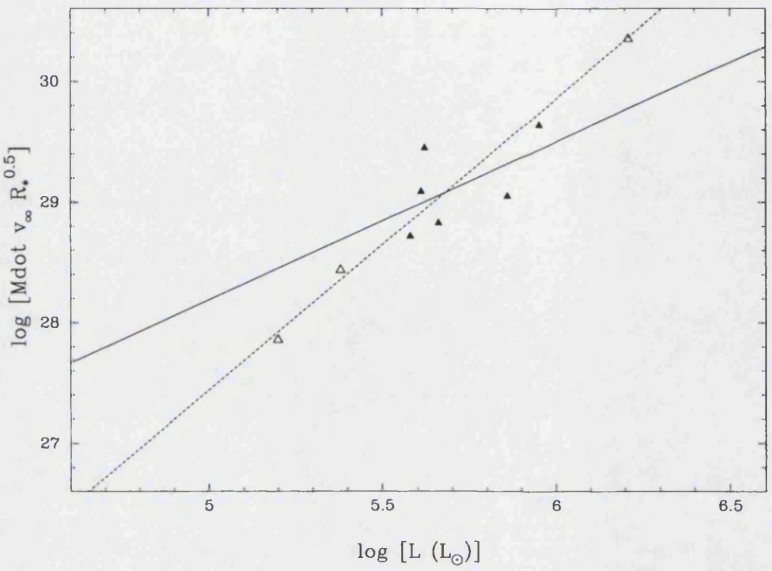

Figure 7.3: The observed WLR for the B stars in the Hα sample. $\dot{M}$ and v_∞ are in cgs units; R_* is in units of $R_\odot$. '▲' represent early-B stars (defined as B0–B1.5), and '△' represent late-B stars (defined as later than type B1.5, and here including the A2Ia star, α Cyg). The solid line represents a least-squares fit to the early-B data, and the dashed line represents a least-squares fit to the late-B data.

Table 7.3: Coefficients of the WLR for different spectral types and luminosity classes

Spectral type	Luminosity class	$\log D_0$	x	α
O	I	21.54 ± 0.68	1.34 ± 0.12	0.75 ± 0.07
O	II–V	21.24 ± 1.11	1.36 ± 0.20	0.74 ± 0.11
Early B	All	21.64 ± 5.45	1.31 ± 0.95	0.76 ± 0.56
Late B	All	15.37 ± 0.77	2.41 ± 0.14	0.41 ± 0.02

NOTES: 'Early B' is defined as B0–B1.5, and 'late B' as later than type B1.5. The two non-supergiant B stars in the sample, HD 5394 (B0.5IVe) and HD 169515 (B0V + O5.5V) have been included with the non-supergiant O stars. The A2Ia star, α Cyg, has been included with the late B-type stars.

error on this value, however, is much larger than for the O stars). The wind momentum is marginally smaller ($\lesssim 0.1$ dex) than for the O supergiants, but the scatter is large. There are only three data points for the late-B stars (α Cyg has been included here, as it is the only A star in the sample; Kudritzki *et al.*, 1999, derived the WLR for A supergiants, using observations of four objects), but they appear to follow quite a tight relationship, which is appreciably steeper ($\alpha = 0.41$) than that obtained for earlier spectral types.

With regard to the potential use of the WLR as an independent distance indicator, it is worthwhile noting that it has been necessary to know a star's distance, *a priori*, in order to determine both $R_*^{0.5}$ and $\dot{M}$ (through R_*). Thus, it is questionable whether Hα mass-loss rates can really be used to derive stellar distances via the WLR.

7.3 Future work

The Hα line-profile fits presented in §4 were for the most part performed using input parameters derived from theoretical models that neglect the effects of line blanketing (exceptions being, for example, those stars with parameters taken from the analyses of Herrero *et al.*, 2000, 2001). Results from line-blanketed models show that effective temperatures are rather lower than those derived from unblanketed studies. Martins *et al.* (2002) constructed model atmospheres for O-type dwarfs, using the CMFGEN code of Hillier and Miller (1998). CMFGEN is a spherically expanding, non-LTE, line-blanketed atmosphere code that includes the effects of stellar winds. Martins *et al.* (2002) found that the inclusion of line blanketing leads to lower $T_{\rm eff}$ by $\sim$4000–1500 K for spectral types O3–O9.5V, respectively (when compared with the calibration of Vacca *et al.*, 1996). Crowther *et al.* (2002*b*) used CMFGEN to analyse the wind and photospheric spectra of four LMC and SMC, O4–O9.7, extreme supergiants. The He I and He II photospheric lines showed that the stars could be modelled with effective temperatures that are systematically (5000–7500 K) and considerably (15%–20%) lower than previously derived from unblanketed, plane-parallel, non-LTE photospheric studies. The reason for this is twofold: a) the use of line blanketing; and b) in-filling of the photospheric lines because of the presence of the stellar wind (which is incorporated by CMFGEN).

The star HD 225160 (spectral type O8Ib(f); see Table 4.3 for stellar parameters) has, in this work, hitherto been modelled using an effective temperature of 38 000 K. This value was taken from Siebert (1999), having been derived from unblanketed models. The

star has been modelled again with PHALTEE, but this time using an effective temperature of 33 000 K, a value 13% lower than the unblanketed $T_{\rm eff}$. A lower effective temperature implies a lower luminosity and should result in a lower mass-loss rate. Figure 7.4 shows the observed Hα profile of HD 225160 (solid line), together with the optimum TGFORSOL fits obtained using: a) $T_{\rm eff}$ suggested by blanketed models (dashed line); and b) $T_{\rm eff}$ derived from unblanketed models (dotted line). Table 7.4 compares the numerical results returned by PHALTEE for the two cases. The mass-loss rate derived using the lower ('blanketed') effective temperature is 35% lower than that obtained using the higher ('unblanketed') $T_{\rm eff}$.

Figure 7.4: Comparison of the optimum TGFORSOL fits to the observed Hα profile of HD 225160 (solid line), obtained using: a) $T_{\rm eff}$ suggested by line-blanketed models (dashed line); and b) $T_{\rm eff}$ derived from unblanketed models (dotted line). The gaps in the observed spectrum are echelle inter-order gaps.

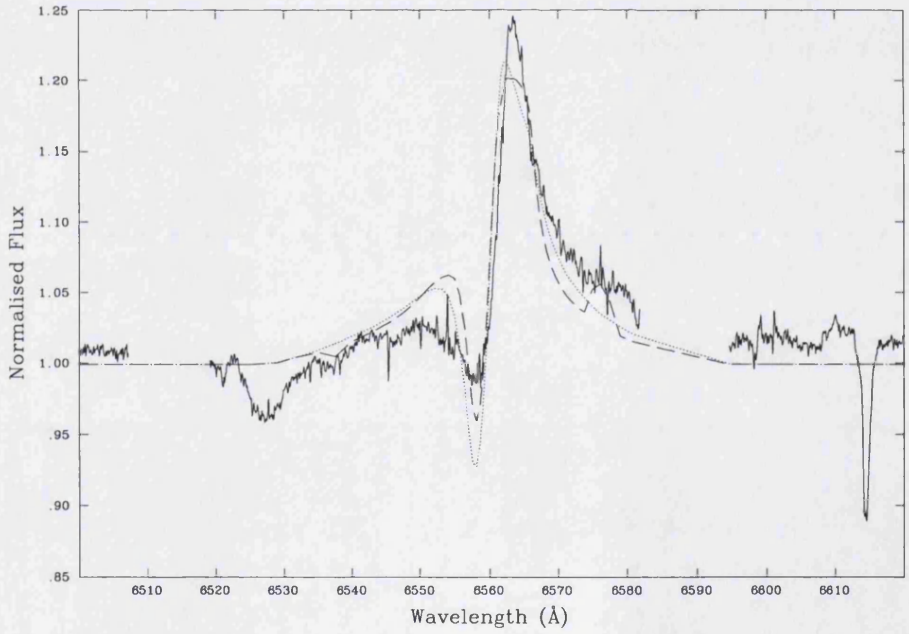

It would therefore be of interest, in order to examine the effect on the derived $\dot{M}$ (and WLR), to re-model (as far as is possible) the Hα sample, using the lower effective temperatures predicted by Crowther *et al.* (2002*b*), Martins *et al.* (2002), and Bianchi and Garcia (2002). Puls *et al.* (2003) re-analysed the O-star spectra first described in Herrero

Table 7.4: Comparison of the numerical PHALTEE results (i.e., the set of optimised parameter values) for HD 225160, obtained using: a) $T_{\rm eff}$ suggested by line-blanketed models; and b) $T_{\rm eff}$ derived from unblanketed models.

Parameter	Unblanketed ($T_{\rm eff} = 38\,000$ K)	Blanketed ($T_{\rm eff} = 33\,000$ K)
$\dot{M}$ (10^{-6} $M_{\odot}$ yr^{-1})	4.46	2.88
β	1.11	1.43
$b_3^{\rm in}$ (H)	1.03	0.67
$b_4^{\rm in}$ (He)	3.28	4.21
b_6^{∞} (He)	20.8	33.4

et al. (1992) and Puls *et al.* (1996), using a version of the FASTWIND code (Santolaya-Rey *et al.*, 1997), updated to incorporate line blanketing. They found that the derived $T_{\rm eff}$ were significantly lower, but also that the wind momentum, $\dot{M}v_{\infty}R_{*}^{0.5}$, remained essentially unchanged, resulting in a new WLR.

It is intended that CMFGEN be used to model a subset of the Hα sample, in order to verify that the results returned by PHALTEE are consistent with the more thorough treatment provided by a spherically expanding, line-blanketed atmosphere code. CMFGEN also allows for the effects of clumping in the wind; this is neglected in the PHALTEE analysis. As discussed in §7.1, if the Hα-forming region were to be significantly clumped, a larger mass-loss rate than is actually present would be mimicked.

Kudritzki *et al.* (1987) showed that the winds of stars in lower-metallicity environments, such as the Magellanic Clouds, are significantly weaker, with smaller mass-loss rates and terminal velocities. New Hα multi-fibre spectroscopy of ~ 2000 early-type stars in the SMC was obtained by I. D. Howarth, C. J. Evans and the author on the nights of September 28th and 29th, 1999, using the 2dF instrument on the AAT. Evans (2001), using intermediate-resolution blue spectra of the hot-star population of the SMC (also obtained using 2dF), classified 4054 stars in the MK system, many of which are common with the 2dF Hα sample. Of these stars, those with observable Hα emission should provide an opportunity to model mass loss in a low-metallicity ($Z = 0.002$ in the SMC, compared to $Z = 0.02$ in the solar neighbourhood), extragalactic environment. The computationally efficient, objective and automated method of Hα modelling afforded by PHALTEE is particularly

suited to analysing such a large sample of objects.

At the current time, the usefulness of mm and cm continuum measurements of the winds of early-type stars is limited by the spatial resolution and instrumental sensitivity required to detect the intrinsically weak flux (usually less than a few mJy) from these (typically) distant objects. On February 25th, 2003, the European Southern Observatory (ESO) and the US National Science Foundation (NSF) agreed to construct and operate the Atacama Large Millimetre Array (ALMA). When (hopefully) complete in 2011, ALMA will be the world's largest and most sensitive millimetre- and sub-millimetre-wavelength telescope. The facility will encompass 64 inter-connected, 12-m radio antennae at a high-altitude site in northern Chile. The sensitivity of ALMA is expected to be 20 times better than that of the VLA, enabling the detection of much fainter sources, and hopefully expanding the number of stars for which it is possible to derive reliable, mm-continuum mass-loss rates.

APPENDIX A

Optimised Hα Line-Profile Fits

For the 64 stars modelled in §4 using PHALTEE, the following pages contain the observed Hα profile (solid line), together with the optimum TGFORSOL fit to the profile (dashed line). Also provided is a list of the stellar and wind parameters adopted for the PHALTEE searches, and the numerical results (i.e., the set of 'best' parameters) from the search conducted with *all* parameters ($\dot{M}$, β *and* the departure coefficients) floating (see §4.2). The parenthesised values for the departure coefficients are the precomputed Puls values, calculated using the adopted and derived stellar parameters (see Tables 3.3 and 3.4). References for spectral types are provided with Tables 2.1, 2.2, 2.3 and 2.4; sources for other data are provided starting on page 97. The observing run during which each observation was obtained is also given; the four runs are denoted by the following acronyms: INT00 ≡ INT run in July 2000; WHT95 ≡ WHT run in August 1995; AAT92 ≡ AAT run in June 1992; AAT00 ≡ AAT run in December 2000. See §2 for further details regarding the observations.

The quality of 'fit' is (evidently) not equally good in all cases. The B stars are, in general, more poorly fitted by PHALTEE, with the strengths of the emission peaks not being well-reproduced. Particularly 'bad' fits were obtained for the following stars: HD 5394 (B0.5IVe), HD 105056 (ON9.7Iae), HD 154368 (O9.5Iab), HD 168607 (B9Ia+), HD 169454 (B1Ia+), HD 169515 (B0V + O5.5V), HD 190603 (B1.5Ia+), HD 193237 (B1Ia+), HD 197345 (A2Ia), Cyg OB2 No.12 (B5Ie), and V433 Sct (B1.5Ia). Numerical problems meant that it was not possible to fit MWC 349 (O9:III: + B0III) using PHALTEE: the model profile shown is the result of an interactive fit (see §4.2.4).

The absorption feature at 6527 Å is a He II line; the feature at 6612 Å is a diffuse interstellar band (DIB). See the atlas of yellow-red OB-star spectra by Walborn (1980)

for a discussion of the spectral region 5400–6600 Å for a sample of O3–B8 stars. Note the echelle inter-order gaps in the observed spectra for the WHT95 sample.

A.1 HD 2905 (κ Cas)

Spectral type:	BC0.7Ia	Y(He):	0.09	(Observing run: INT00)
$T_{\rm eff}$:	24 000 K	$b_3^{\rm in}$ (H):	1.07 (1.20)	
$\log g$:	2.70	$b_4^{\rm in}$ (He):	4.28 (1.61)	
R_*:	37 $R_\odot$	b_6^{∞} (He):	9.57 (19.2)	
v_∞:	1105 km s^{-1}	β:	0.96	
$v \sin i$:	91 km s^{-1}	$\dot{M}$:	2.88×10^{-6} $M_\odot$ yr^{-1}	

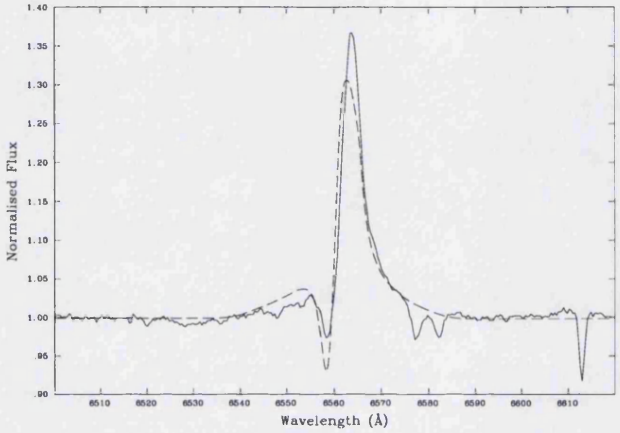

A.2 HD 5394 (γ Cas)

Spectral type:	B0.5IVe	Y(He):	0.09	(Observing run: INT00)
$T_{\rm eff}$:	28 800 K	$b_3^{\rm in}$ (H):	1.20 (1.20)	
$\log g$:	3.69	$b_4^{\rm in}$ (He):	1.36 (1.35)	
R_*:	10 $R_\odot$	b_6^{∞} (He):	2.01 (12.6)	
v_∞:	1600 km s^{-1}	β:	2.00	
$v \sin i$:	260 km s^{-1}	$\dot{M}$:	2.10×10^{-6} $M_\odot$ yr^{-1}	

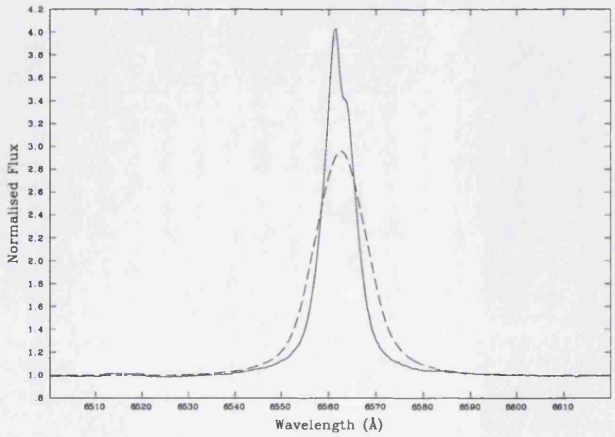

A.3 HD 10125

Spectral type:	O9.7II	Y(He):	0.15	(Observing run: WHT95)
$T_{\rm eff}$:	32 500 K	$b_3^{\rm in}$ (H):	0.40 (1.20)	
$\log g$:	3.3	$b_4^{\rm in}$ (He):	2.76 (1.84)	
R_*:	17 $R_\odot$	b_6^{∞} (He):	32.8 (21.2)	
v_∞:	1735 km s^{-1}	β:	1.28	
$v \sin i$:	132 km s^{-1}	$\dot{M}$:	1.27×10^{-6} $M_\odot$ yr^{-1}	

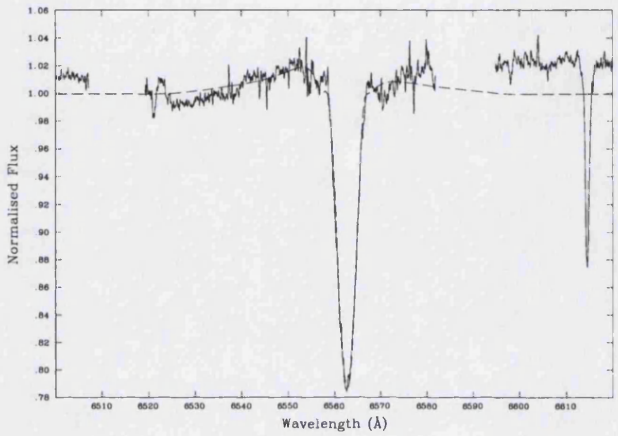

A.4 HD 12323

Spectral type:	ON9V	Y(He):	0.17	(Observing run: WHT95)
$T_{\rm eff}$:	36 000 K	$b_3^{\rm in}$ (H):	0.25 (1.20)	
$\log g$:	4.1	$b_4^{\rm in}$ (He):	1.37 (2.03)	
R_*:	5 $R_\odot$	b_6^{∞} (He):	34.8 (22.9)	
v_∞:	1175 km s^{-1}	β:	0.32	
$v \sin i$:	131 km s^{-1}	$\dot{M}$:	8.63×10^{-8} $M_\odot$ yr^{-1}	

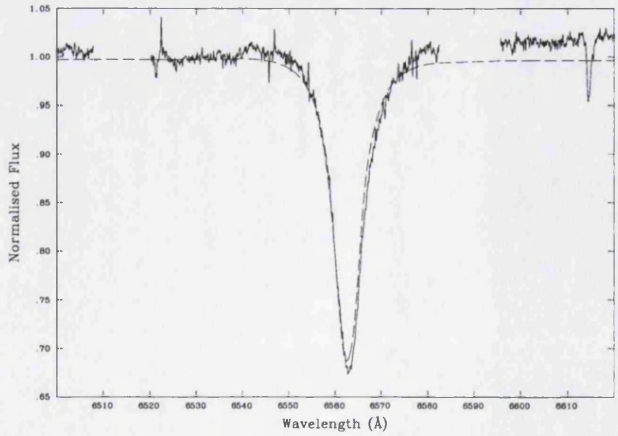

A.5 HD 13745 (V354 Per)

Spectral type:	O9.7II((n))	Y(He):	0.20	(Observing run: WHT95)
$T_{\rm eff}$:	33 000 K	$b_3^{\rm in}$ (H):	0.30 (1.20)	
$\log g$:	3.3	$b_4^{\rm in}$ (He):	2.05 (1.51)	
R_*:	13 $R_\odot$	b_6^{∞} (He):	15.4 (18.4)	
v_∞:	1905 km s^{-1}	β:	0.92	
$v \sin i$:	176 km s^{-1}	$\dot{M}$:	1.55×10^{-6} $M_\odot$ yr^{-1}	

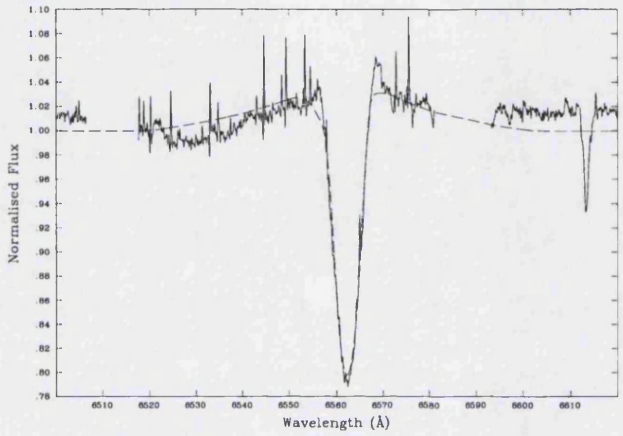

A.6 HD 14947

Spectral type:	O5If+	Y(He):	0.20	(Observing run: INT00)
$T_{\rm eff}$:	40 000 K	$b_3^{\rm in}$ (H):	0.94 (1.20)	
$\log g$:	3.67	$b_4^{\rm in}$ (He):	1.87 (1.35)	
R_*:	15 $R_\odot$	b_6^{∞} (He):	10.2 (14.6)	
v_∞:	2400 km s^{-1}	β:	1.32	
$v \sin i$:	140 km s^{-1}	$\dot{M}$:	5.01×10^{-6} $M_\odot$ yr^{-1}	

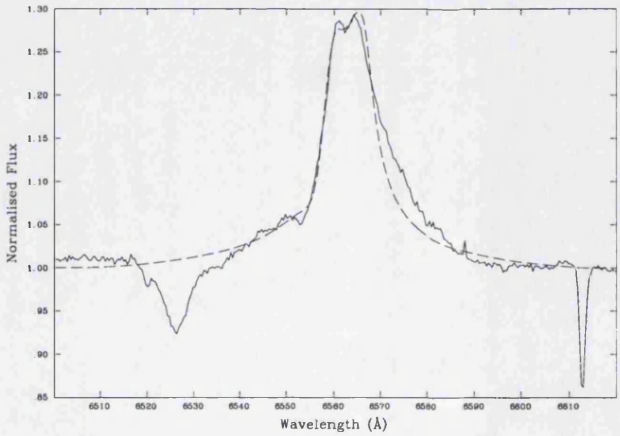

A.7 HD 15558

Spectral type:	O5III(f)	Y(He):	0.07	(Observing run: INT00)
$T_{\rm eff}$:	46 500 K	$b_3^{\rm in}$ (H):	1.08 (1.20)	
$\log g$:	3.86	$b_4^{\rm in}$ (He):	2.81 (1.35)	
R_*:	19 $R_\odot$	b_6^{∞} (He):	7.17 (15.8)	
v_∞:	2800 km s^{-1}	β:	0.89	
$v \sin i$:	120 km s^{-1}	$\dot{M}$:	7.21×10^{-6} $M_\odot$ yr^{-1}	

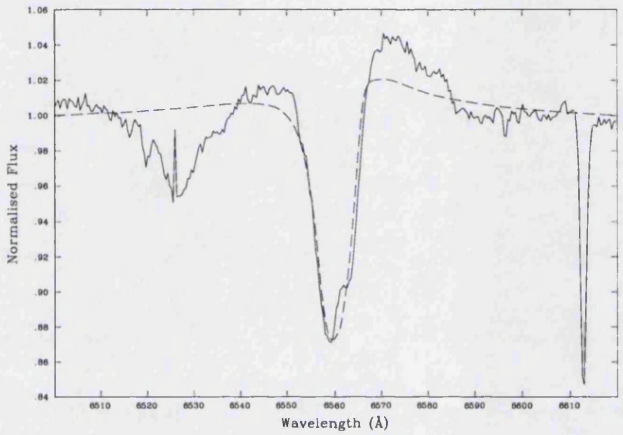

A.8 HD 15570

Spectral type:	O4If+	Y(He):	0.15	(Observing run: INT00)
$T_{\rm eff}$:	42 000 K	$b_3^{\rm in}$ (H):	1.08 (1.20)	
$\log g$:	3.80	$b_4^{\rm in}$ (He):	1.83 (1.35)	
R_*:	22 $R_\odot$	b_6^{∞} (He):	17.3 (13.3)	
v_∞:	2600 km s^{-1}	β:	1.02	
$v \sin i$:	105 km s^{-1}	$\dot{M}$:	1.27×10^{-5} $M_\odot$ yr^{-1}	

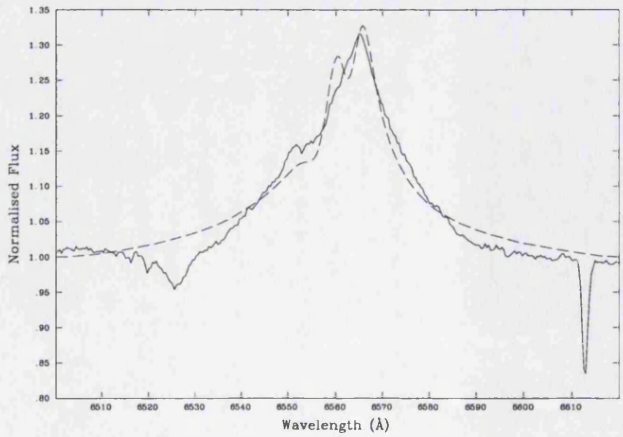

A.9 HD 16429

Spectral type:	O9.5II((n))	Y(He):	0.12	(Observing run: WHT95)
$T_{\rm eff}$:	35 000 K	$b_3^{\rm in}$ (H):	0.88 (1.20)	
$\log g$:	3.4	$b_4^{\rm in}$ (He):	2.80 (1.47)	
R_*:	25 $R_\odot$	b_6^{∞} (He):	17.9 (18.1)	
v_∞:	1765 km s^{-1}	β:	0.79	
$v \sin i$:	216 km s^{-1}	$\dot{M}$:	3.89×10^{-6} $M_\odot$ yr^{-1}	

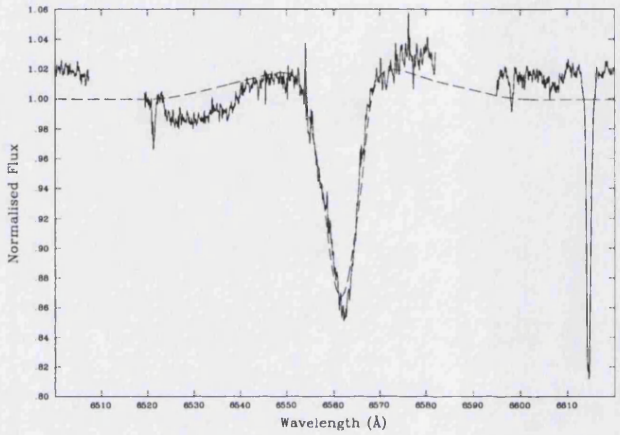

A.10 HD 30614 (α Cam)

Spectral type:	O9.5Ia	Y(He):	0.13	(Observing run: WHT95)
$T_{\rm eff}$:	33 000 K	$b_3^{\rm in}$ (H):	0.93 (1.20)	
$\log g$:	3.1	$b_4^{\rm in}$ (He):	2.81 (1.35)	
R_*:	20 $R_\odot$	b_6^{∞} (He):	24.7 (16.6)	
v_∞:	1590 km s^{-1}	β:	1.04	
$v \sin i$:	90 km s^{-1}	$\dot{M}$:	3.04×10^{-6} $M_\odot$ yr^{-1}	

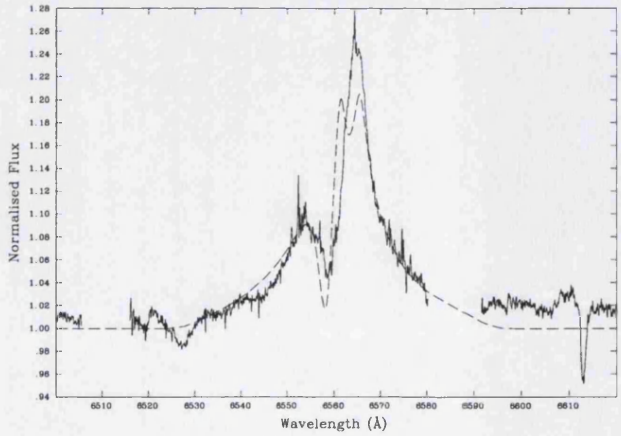

A.11 HD 34078 (AE Aur)

Spectral type:	O9.5V	Y(He):	0.09	(Observing run: WHT95)
$T_{\rm eff}$:	37 000 K	$b_3^{\rm in}$ (H):	0.27 (1.20)	
$\log g$:	4.2	$b_4^{\rm in}$ (He):	1.51 (2.12)	
R_*:	7 $R_\odot$	b_6^{∞} (He):	34.4 (23.6)	
v_∞:	1505 km s^{-1}	β:	0.30	
$v \sin i$:	30 km s^{-1}	$\dot{M}$:	1.83×10^{-7} $M_\odot$ yr^{-1}	

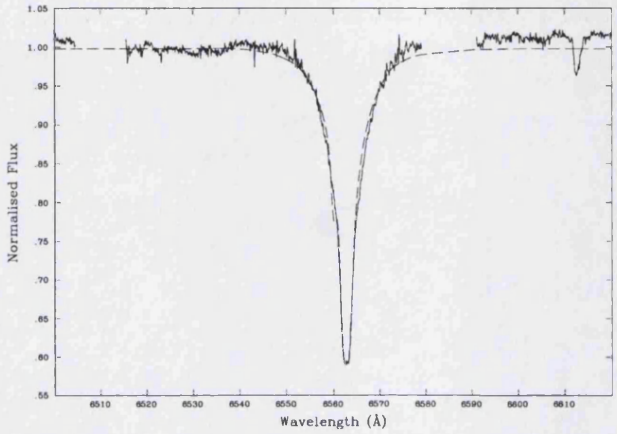

A.12 HD 36486 (δ Ori A)

Spectral type:	O9.5II	Y(He):	0.10	(Observing run: WHT95)
$T_{\rm eff}$:	34 000 K	$b_3^{\rm in}$ (H):	0.88 (1.20)	
$\log g$:	3.4	$b_4^{\rm in}$ (He):	3.20 (1.87)	
R_*:	24 $R_\odot$	b_6^{∞} (He):	35.0 (21.5)	
v_∞:	2060 km s^{-1}	β:	1.07	
$v \sin i$:	126 km s^{-1}	$\dot{M}$:	2.64×10^{-6} $M_\odot$ yr^{-1}	

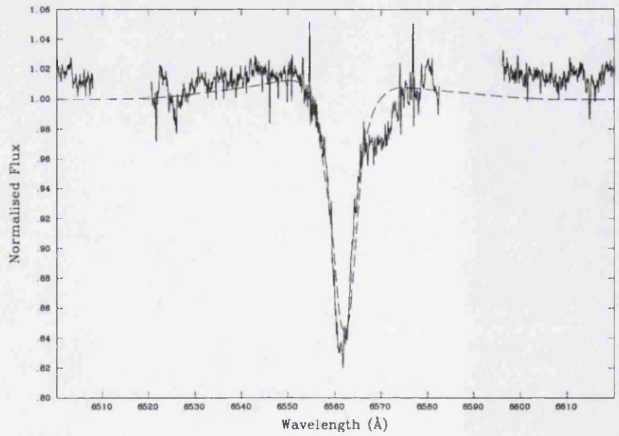

A.13 HD 37742 (ζ Ori)

Spectral type:	O9.7Ib	Y(He):	0.10	(Observing run: WHT95)
$T_{\rm eff}$:	34 000 K	$b_3^{\rm in}$ (H):	0.80 (1.20)	
$\log g$:	3.3	$b_4^{\rm in}$ (He):	2.30 (1.44)	
R_*:	30 $R_\odot$	b_6^{∞} (He):	28.3 (17.8)	
v_∞:	1860 km s^{-1}	β:	0.98	
$v \sin i$:	109 km s^{-1}	$\dot{M}$:	5.81×10^{-6} $M_\odot$ yr^{-1}	

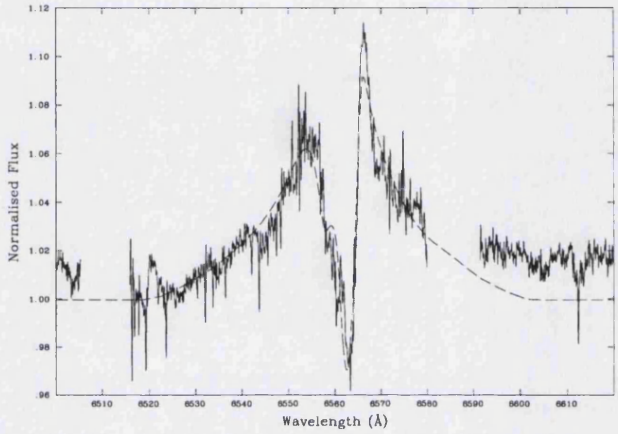

A.14 HD 66811 (ζ Pup)

Spectral type:	O4I(n)f	Y(He):	0.12	(Observing run: AAT00)
$T_{\rm eff}$:	42 000 K	$b_3^{\rm in}$ (H):	0.43 (1.20)	
$\log g$:	3.60	$b_4^{\rm in}$ (He):	2.39 (1.37)	
R_*:	19 $R_\odot$	b_6^{∞} (He):	34.3 (17.2)	
v_∞:	2485 km s^{-1}	β:	1.55	
$v \sin i$:	219 km s^{-1}	$\dot{M}$:	5.00×10^{-6} $M_\odot$ yr^{-1}	

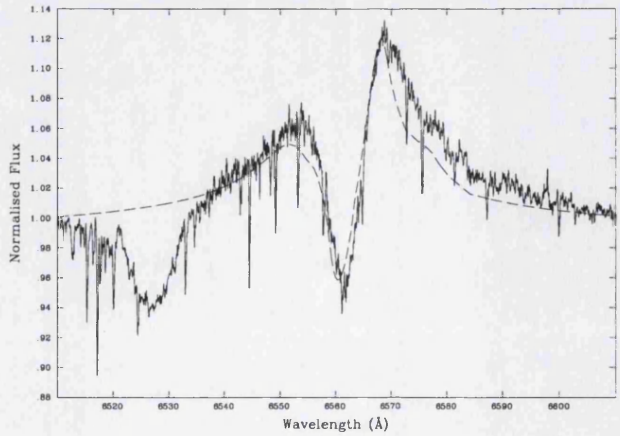

A.15 HD 105056 (GS Mus)

Spectral type:	ON9.7Iae	Y(He):	0.09	(Observing run: AAT92)
$T_{\rm eff}$:	28 900 K	$b_3^{\rm in}$ (H):	1.19 (1.20)	
$\log g$:	3.25	$b_4^{\rm in}$ (He):	3.72 (1.35)	
R_*:	23 $R_\odot$	b_6^{∞} (He):	2.64 (12.3)	
v_∞:	680 km s^{-1}	β:	0.83	
$v \sin i$:	68 km s^{-1}	$\dot{M}$:	2.12×10^{-6} $M_\odot$ yr^{-1}	

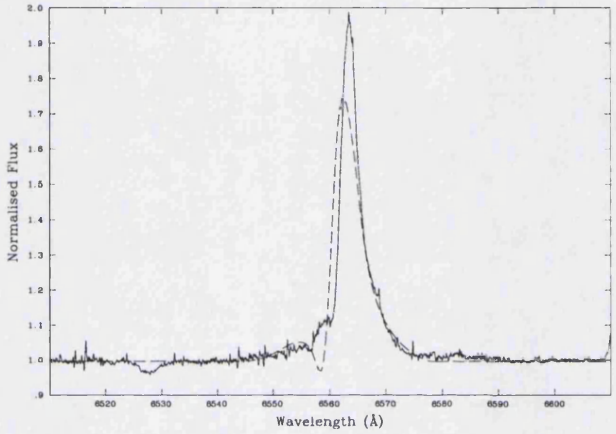

A.16 HD 123008

Spectral type:	ON9.7Iab	Y(He):	0.15	(Observing run: AAT92)
$T_{\rm eff}$:	33 000 K	$b_3^{\rm in}$ (H):	0.68 (1.20)	
$\log g$:	3.05	$b_4^{\rm in}$ (He):	3.81 (1.42)	
R_*:	24 $R_\odot$	b_6^{∞} (He):	27.9 (17.7)	
v_∞:	1250 km s^{-1}	β:	1.43	
$v \sin i$:	98 km s^{-1}	$\dot{M}$:	2.34×10^{-6} $M_\odot$ yr^{-1}	

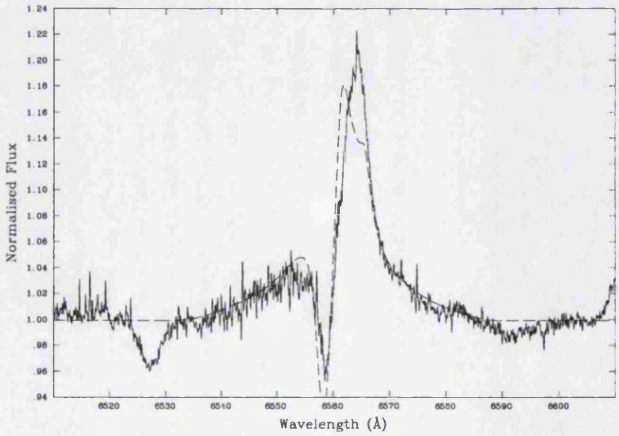

A.17 HD 149038 (μ Nor)

Spectral type:	O9.7Iab	Y(He):	0.09	(Observing run: AAT92)
$T_{\rm eff}$:	30 000 K	$b_3^{\rm in}$ (H):	1.00 (1.20)	
$\log g$:	3.05	$b_4^{\rm in}$ (He):	5.02 (2.48)	
R_*:	27 $R_\odot$	b_6^{∞} (He):	35.0 (25.4)	
v_∞:	1830 km s^{-1}	β:	1.55	
$v \sin i$:	86 km s^{-1}	$\dot{M}$:	1.12×10^{-6} $M_\odot$ yr^{-1}	

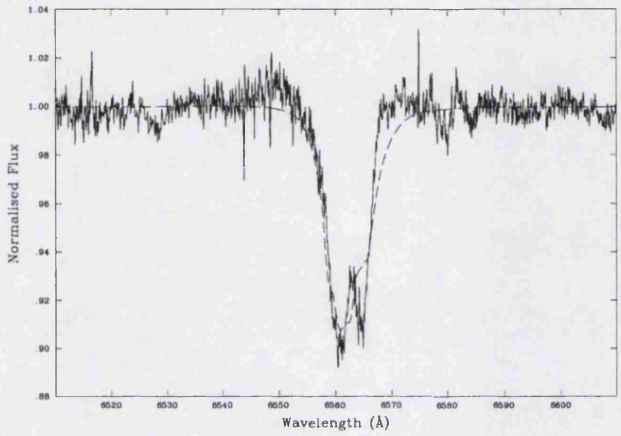

A.18 HD 149404 (V918 Sco)

Spectral type:	O9Ia	Y(He):	0.12	(Observing run: AAT92)
$T_{\rm eff}$:	32 500 K	$b_3^{\rm in}$ (H):	0.94 (1.20)	
$\log g$:	2.95	$b_4^{\rm in}$ (He):	1.38 (1.55)	
R_*:	34 $R_\odot$	b_6^{∞} (He):	2.17 (18.7)	
v_∞:	2450 km s^{-1}	β:	1.70	
$v \sin i$:	100 km s^{-1}	$\dot{M}$:	9.07×10^{-6} $M_\odot$ yr^{-1}	

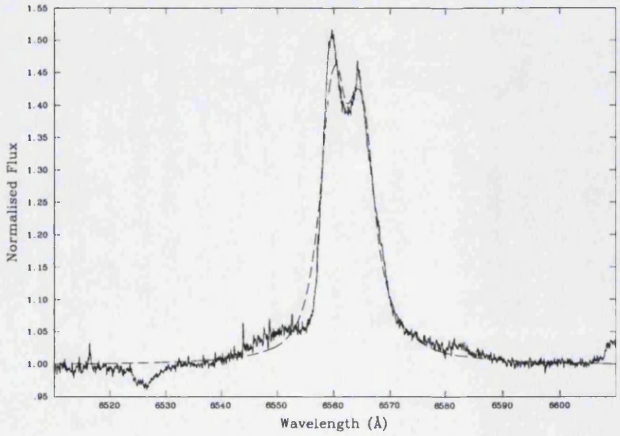

A.19 HD 149757 (ζ Oph)

Spectral type:	O9.5V	Y(He):	0.19	(Observing run: INT00)
$T_{\rm eff}$:	32 500 K	$b_3^{\rm in}$ (H):	0.20 (1.20)	
$\log g$:	3.85	$b_4^{\rm in}$ (He):	2.33 (1.96)	
R_*:	13 $R_\odot$	b_6^{∞} (He):	35.0 (22.2)	
v_∞:	1505 km s^{-1}	β:	0.78	
$v \sin i$:	372 km s^{-1}	$\dot{M}$:	5.75×10^{-7} $M_\odot$ yr^{-1}	

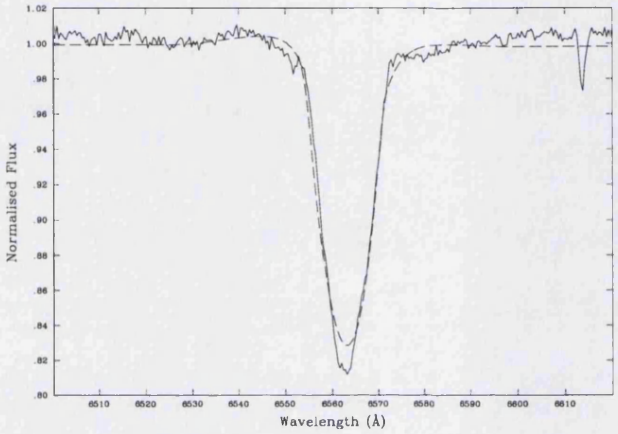

A.20 HD 152003

Spectral type:	O9.7Iab	Y(He):	0.09	(Observing run: AAT92)
$T_{\rm eff}$:	30 500 K	$b_3^{\rm in}$ (H):	0.82 (1.20)	
$\log g$:	3.00	$b_4^{\rm in}$ (He):	3.59 (1.93)	
R_*:	25 $R_\odot$	b_6^{∞} (He):	16.9 (21.9)	
v_∞:	2010 km s^{-1}	β:	1.45	
$v \sin i$:	110 km s^{-1}	$\dot{M}$:	2.51×10^{-6} $M_\odot$ yr^{-1}	

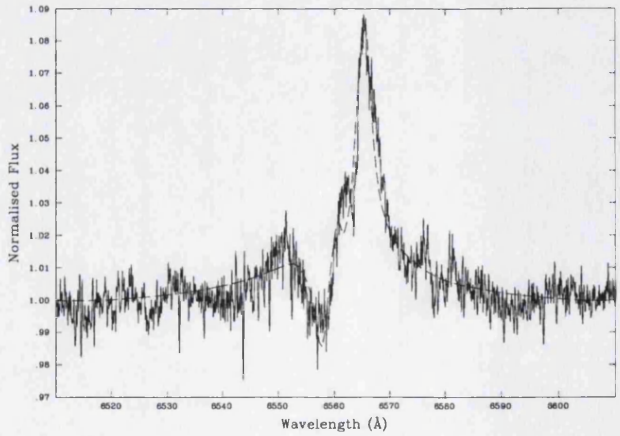

A.21 HD 152147

Spectral type:	O9.7Ib	Y(He):	0.09	(Observing run: AAT92)
$T_{\rm eff}$:	30 000 K	$b_3^{\rm in}$ (H):	0.99 (1.20)	
$\log g$:	3.15	$b_4^{\rm in}$ (He):	3.75 (1.87)	
R_*:	25 $R_\odot$	b_6^{∞} (He):	4.80 (21.4)	
v_∞:	1735 km s^{-1}	β:	0.84	
$v \sin i$:	88 km s^{-1}	$\dot{M}$:	2.18×10^{-6} $M_\odot$ yr^{-1}	

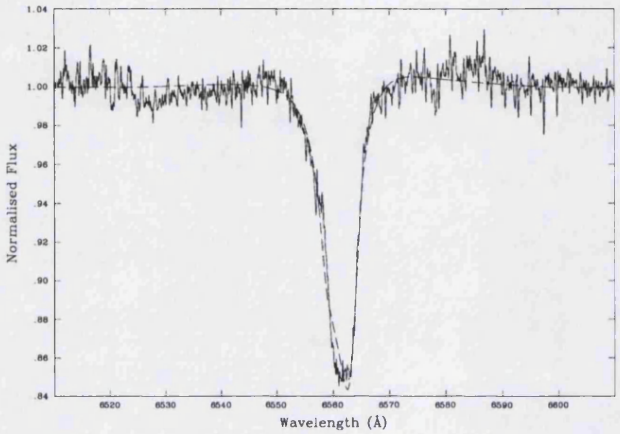

A.22 HD 152249

Spectral type:	OC9.5Iab	Y(He):	0.08	(Observing run: AAT92)
$T_{\rm eff}$:	32 500 K	$b_3^{\rm in}$ (H):	1.10 (1.20)	
$\log g$:	3.15	$b_4^{\rm in}$ (He):	3.21 (1.87)	
R_*:	24 $R_\odot$	b_6^{∞} (He):	28.3 (21.5)	
v_∞:	2010 km s^{-1}	β:	1.25	
$v \sin i$:	99 km s^{-1}	$\dot{M}$:	2.54×10^{-6} $M_\odot$ yr^{-1}	

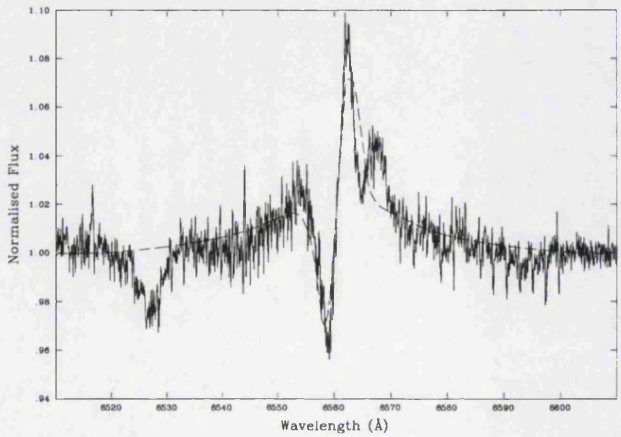

A.23 HD 152405

Spectral type:	O9.7Ib–II	Y(He):	0.09	(Observing run: AAT92)
$T_{\rm eff}$:	30 500 K	$b_3^{\rm in}$ (H):	1.10 (1.20)	
$\log g$:	3.20	$b_4^{\rm in}$ (He):	6.00 (2.30)	
R_*:	15 $R_\odot$	b_6^{∞} (He):	6.70 (25.1)	
v_∞:	1860 km s^{-1}	β:	0.79	
$v \sin i$:	77 km s^{-1}	$\dot{M}$:	6.16×10^{-7} $M_\odot$ yr^{-1}	

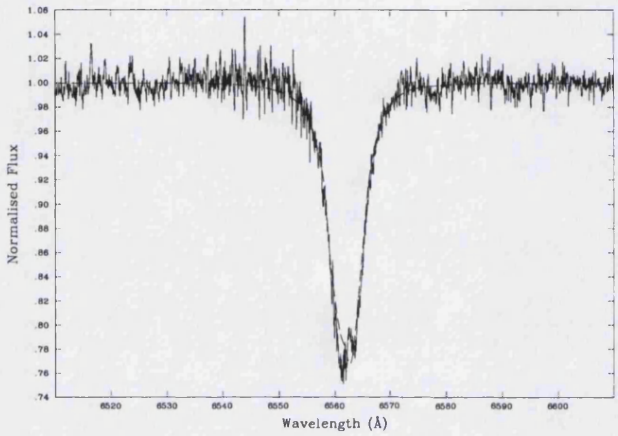

A.24 HD 152424

Spectral type:	OC9.7Ia	Y(He):	0.09	(Observing run: AAT92)
$T_{\rm eff}$:	31 500 K	$b_3^{\rm in}$ (H):	0.63 (1.20)	
$\log g$:	2.95	$b_4^{\rm in}$ (He):	3.99 (1.58)	
R_*:	33 $R_\odot$	b_6^{∞} (He):	34.8 (19.0)	
v_∞:	1760 km s^{-1}	β:	1.39	
$v \sin i$:	86 km s^{-1}	$\dot{M}$:	5.08×10^{-6} $M_\odot$ yr^{-1}	

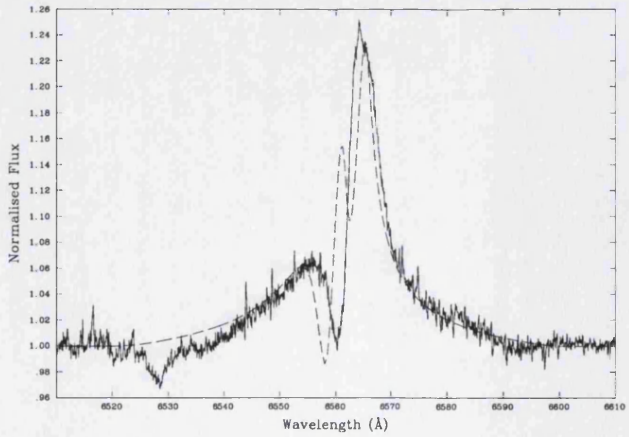

A.25 HD 154368

Spectral type:	O9.5Iab	Y(He):	0.13	(Observing run: AAT92)
$T_{\rm eff}$:	32 000 K	$b_3^{\rm in}$ (H):	0.99 (1.20)	
$\log g$:	3.00	$b_4^{\rm in}$ (He):	4.14 (1.89)	
R_*:	24 $R_\odot$	b_6^{∞} (He):	34.8 (21.7)	
v_∞:	1850 km s^{-1}	β:	1.33	
$v \sin i$:	102 km s^{-1}	$\dot{M}$:	2.18×10^{-6} $M_\odot$ yr^{-1}	

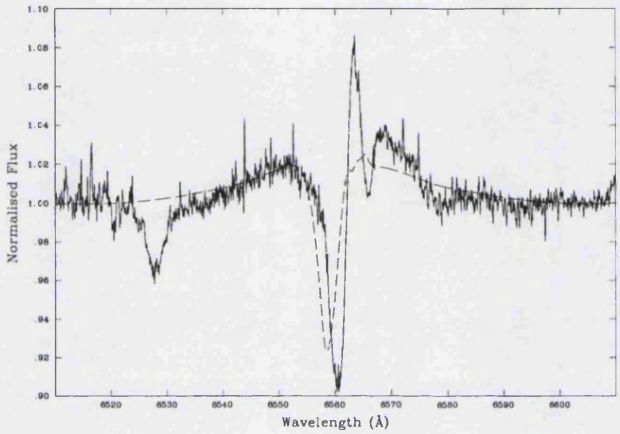

A.26 HD 154811

Spectral type:	OC9.7Iab	Y(He):	0.09	(Observing run: AAT92)
$T_{\rm eff}$:	31 000 K	$b_3^{\rm in}$ (H):	0.82 (1.20)	
$\log g$:	3.10	$b_4^{\rm in}$ (He):	3.25 (1.53)	
R_*:	24 $R_\odot$	b_6^{∞} (He):	2.00 (18.6)	
v_∞:	1735 km s^{-1}	β:	0.73	
$v \sin i$:	125 km s^{-1}	$\dot{M}$:	3.27×10^{-6} $M_\odot$ yr^{-1}	

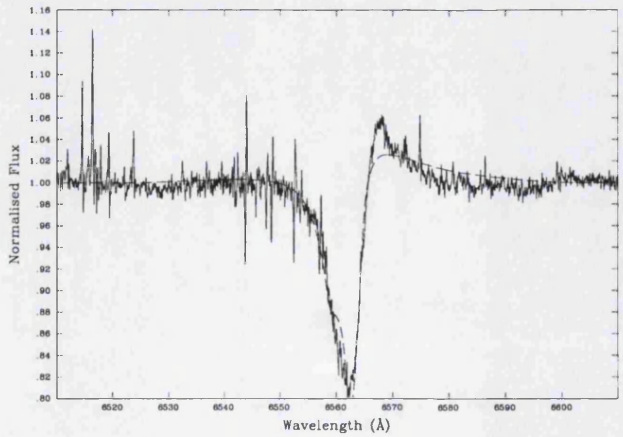

A.27 HD 156212

Spectral type:	O9.7Iab	Y(He):	0.08	(Observing run: AAT92)
$T_{\rm eff}$:	29 500 K	$b_3^{\rm in}$ (H):	0.90 (1.20)	
$\log g$:	3.15	$b_4^{\rm in}$ (He):	4.80 (2.13)	
R_*:	25 $R_\odot$	b_6^{∞} (He):	2.42 (23.6)	
v_∞:	1735 km s^{-1}	β:	1.03	
$v \sin i$:	88 km s^{-1}	$\dot{M}$:	1.52×10^{-6} $M_\odot$ yr^{-1}	

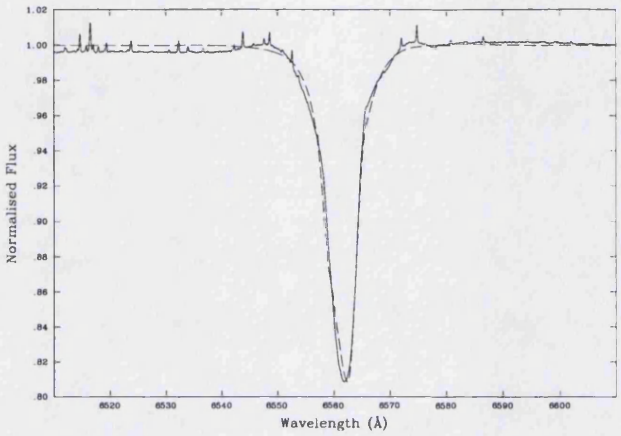

A.28 HD 164794 (9 Sgr)

Spectral type:	O4:V((f))	Y(He):	0.10	(Observing run: INT00)
$T_{\rm eff}$:	46 400 K	$b_3^{\rm in}$ (H):	1.19 (1.20)	
$\log g$:	3.68	$b_4^{\rm in}$ (He):	1.60 (2.04)	
R_*:	16 $R_\odot$	b_6^{∞} (He):	32.7 (22.9)	
v_∞:	2750 km s^{-1}	β:	0.77	
$v \sin i$:	70 km s^{-1}	$\dot{M}$:	1.76×10^{-6} $M_\odot$ yr^{-1}	

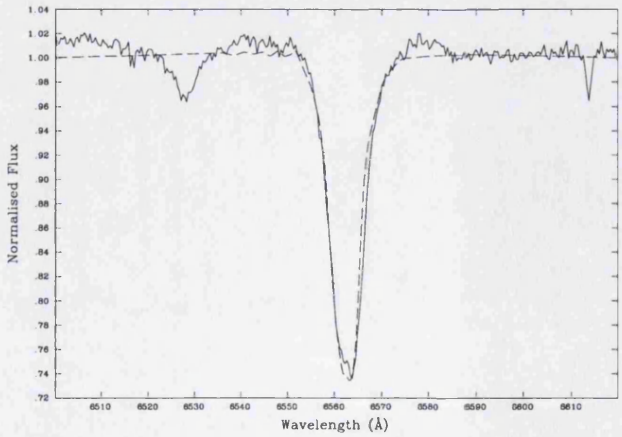

A.29 HD 166734

Spectral type:	O7Ib(f) + O8–9I	Y(He):	0.09	(Observing run: INT00)
$T_{\rm eff}$:	35 500 K	$b_3^{\rm in}$ (H):	1.19 (1.20)	
$\log g$:	3.20	$b_4^{\rm in}$ (He):	1.41 (1.35)	
R_*:	38 $R_\odot$	b_6^{∞} (He):	34.0 (15.9)	
v_∞:	2600 km s^{-1}	β:	0.94	
$v \sin i$:	150 km s^{-1}	$\dot{M}$:	1.85×10^{-5} $M_\odot$ yr^{-1}	

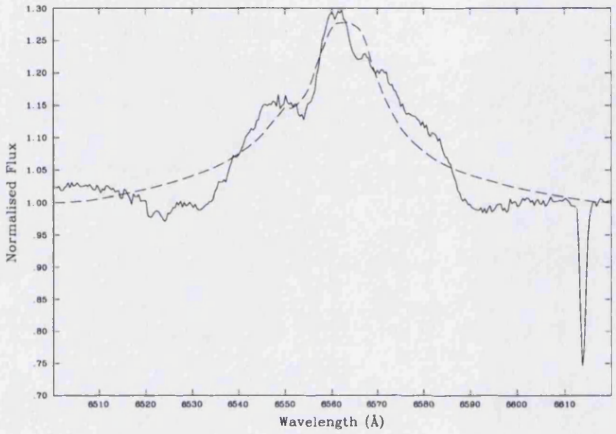

A.30 HD 167971 (MY Ser)

Spectral type:	O8Ib(f)p	Y(He):	0.09	(Observing run: INT00)
$T_{\rm eff}$:	35 500 K	$b_3^{\rm in}$ (H):	0.94 (1.20)	
$\log g$:	3.45	$b_4^{\rm in}$ (He):	2.85 (1.35)	
R_*:	22 $R_\odot$	b_6^{∞} (He):	23.0 (16.1)	
v_∞:	2185 km s^{-1}	β:	0.98	
$v \sin i$:	97 km s^{-1}	$\dot{M}$:	6.13×10^{-6} $M_\odot$ yr^{-1}	

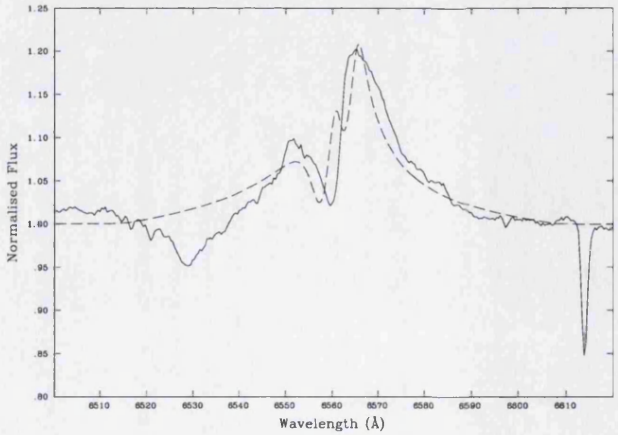

A.31 HD 168112

Spectral type:	O5III(f)	Y(He):	0.09	(Observing run: INT00)
$T_{\rm eff}$:	46 800 K	$b_3^{\rm in}$ (H):	1.10 (1.20)	
$\log g$:	3.92	$b_4^{\rm in}$ (He):	1.71 (1.58)	
R_*:	16 $R_\odot$	b_6^{∞} (He):	34.4 (19.0)	
v_∞:	2700 km s^{-1}	β:	0.97	
$v \sin i$:	90 km s^{-1}	$\dot{M}$:	3.24×10^{-6} $M_\odot$ yr^{-1}	

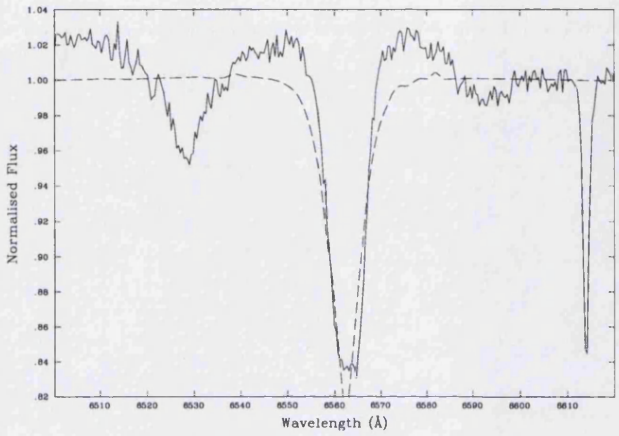

A.32 HD 168607

Spectral type:	B9Ia+	Y(He):	0.18	(Observing run: INT00)
$T_{\rm eff}$:	9 300 K	$b_3^{\rm in}$ (H):	1.14 (1.20)	
$\log g$:	1.0	$b_4^{\rm in}$ (He):	5.98 (1.35)	
R_*:	190 $R_\odot$	b_6^{∞} (He):	2.01 (16.8)	
v_∞:	140 km s^{-1}	β:	0.54	
$v \sin i$:	25 km s^{-1}	$\dot{M}$:	2.24×10^{-6} $M_\odot$ yr^{-1}	

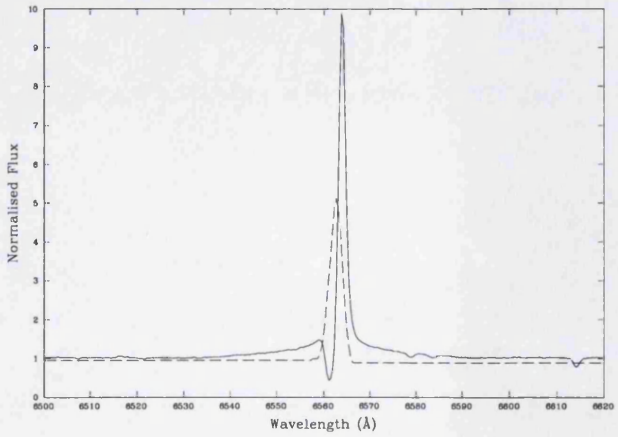

A.33 HD 169454

Spectral type:	B1Ia+	Y(He):	0.18	(Observing run: INT00)
$T_{\rm eff}$:	20 400 K	$b_3^{\rm in}$ (H):	1.20 (1.20)	
$\log g$:	2.35	$b_4^{\rm in}$ (He):	6.00 (1.35)	
R_*:	74 $R_\odot$	b_6^{∞} (He):	2.84 (16.0)	
v_∞:	850 km s^{-1}	β:	1.02	
$v \sin i$:	60 km s^{-1}	$\dot{M}$:	9.37×10^{-6} $M_\odot$ yr^{-1}	

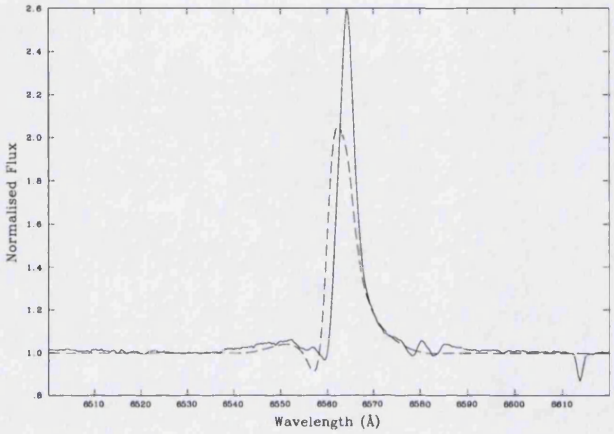

A.34 HD 169515 (RY Sct)

Spectral type:	B0V + O5.5V	Y(He):	0.09	(Observing run: INT00)
$T_{\rm eff}$:	24 000 K	$b_3^{\rm in}$ (H):	1.20 (1.20)	
$\log g$:	2.78	$b_4^{\rm in}$ (He):	5.97 (1.35)	
R_*:	34 $R_\odot$	b_6^{∞} (He):	12.7 (16.2)	
v_∞:	1500 km s^{-1}	β:	1.98	
$v \sin i$:	89 km s^{-1}	$\dot{M}$:	6.54×10^{-6} $M_\odot$ yr^{-1}	

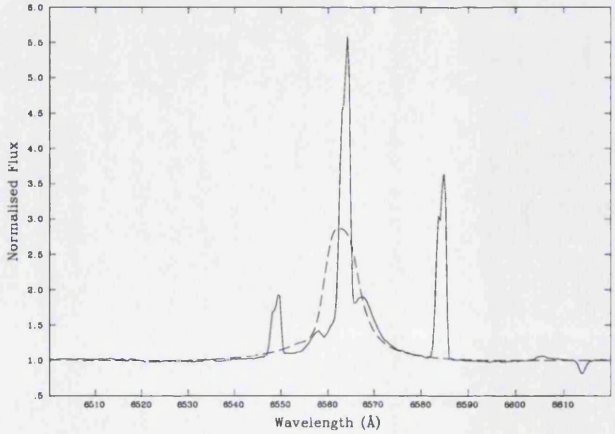

A.35 HD 169582

Spectral type:	O6If	Y(He):	0.09	(Observing run: INT00)
$T_{\rm eff}$:	41 700 K	$b_3^{\rm in}$ (H):	1.03 (1.20)	
$\log g$:	3.44	$b_4^{\rm in}$ (He):	2.16 (1.35)	
R_*:	21 $R_\odot$	b_6^{∞} (He):	25.1 (17.1)	
v_∞:	2300 km s^{-1}	β:	1.02	
$v \sin i$:	127 km s^{-1}	$\dot{M}$:	5.27×10^{-6} $M_\odot$ yr^{-1}	

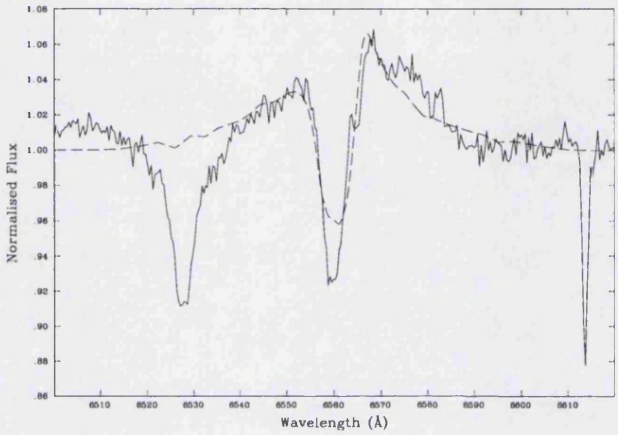

A.36 HD 188209

Spectral type:	O9.5Iab	Y(He):	0.14	(Observing run: WHT95)
$T_{\rm eff}$:	33 000 K	$b_3^{\rm in}$ (H):	1.18 (1.20)	
$\log g$:	3.1	$b_4^{\rm in}$ (He):	3.22 (1.70)	
R_*:	19 $R_\odot$	b_6^{∞} (He):	34.9 (20.0)	
v_∞:	1650 km s^{-1}	β:	0.97	
$v \sin i$:	65 km s^{-1}	$\dot{M}$:	1.70×10^{-6} $M_\odot$ yr^{-1}	

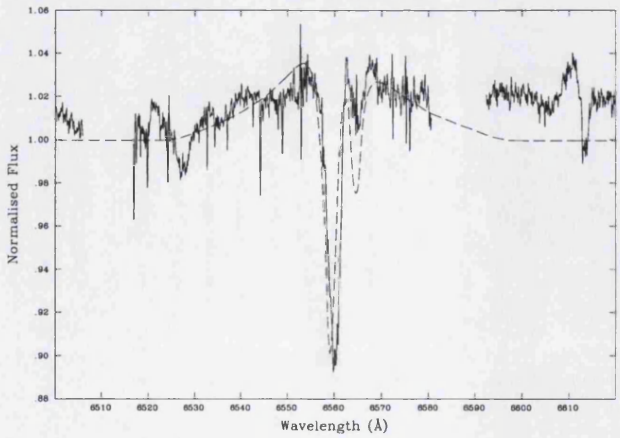

A.37 HD 189957

Spectral type:	O9.5III	Y(He):	0.11	(Observing run: WHT95)
$T_{\rm eff}$:	33 000 K	$b_3^{\rm in}$ (H):	1.19 (1.20)	
$\log g$:	3.5	$b_4^{\rm in}$ (He):	2.85 (2.18)	
R_*:	12 $R_\odot$	b_6^{∞} (He):	34.7 (24.1)	
v_∞:	1505 km s^{-1}	β:	0.53	
$v \sin i$:	85 km s^{-1}	$\dot{M}$:	3.78×10^{-7} $M_\odot$ yr^{-1}	

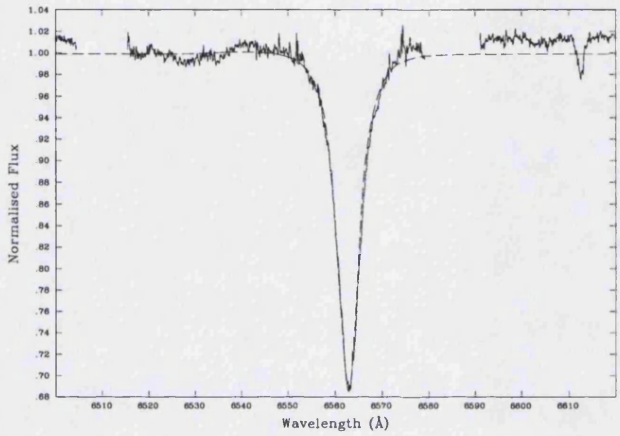

A.38 HD 190429A

Spectral type:	O4If+	Y(He):	0.15	(Observing run: INT00)
$T_{\rm eff}$:	42 400 K	$b_3^{\rm in}$ (H):	0.68 (1.20)	
$\log g$:	3.48	$b_4^{\rm in}$ (He):	2.36 (1.35)	
R_*:	20 $R_\odot$	b_6^{∞} (He):	20.3 (14.2)	
v_∞:	1880 km s^{-1}	β:	1.03	
$v \sin i$:	105 km s^{-1}	$\dot{M}$:	5.79×10^{-6} $M_\odot$ yr^{-1}	

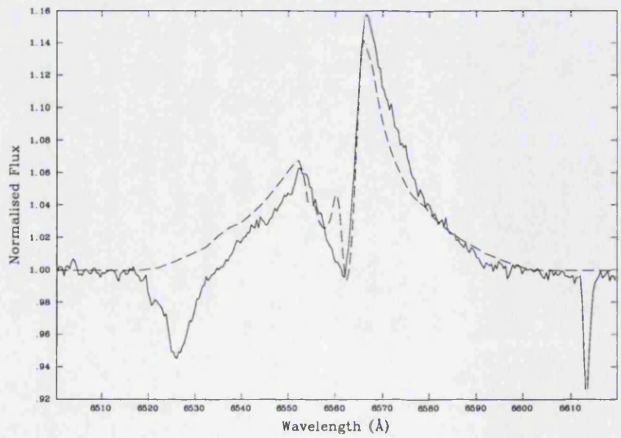

A.39 HD 190603

Spectral type:	B1.5Ia+	Y(He):	0.18	(Observing run: INT00)
$T_{\rm eff}$:	21 000 K	$b_3^{\rm in}$ (H):	1.20 (1.20)	
$\log g$:	2.35	$b_4^{\rm in}$ (He):	5.90 (1.35)	
R_*:	47 $R_\odot$	b_6^{∞} (He):	6.14 (14.7)	
v_∞:	485 km s^{-1}	β:	0.66	
$v \sin i$:	79 km s^{-1}	$\dot{M}$:	2.51×10^{-6} $M_\odot$ yr^{-1}	

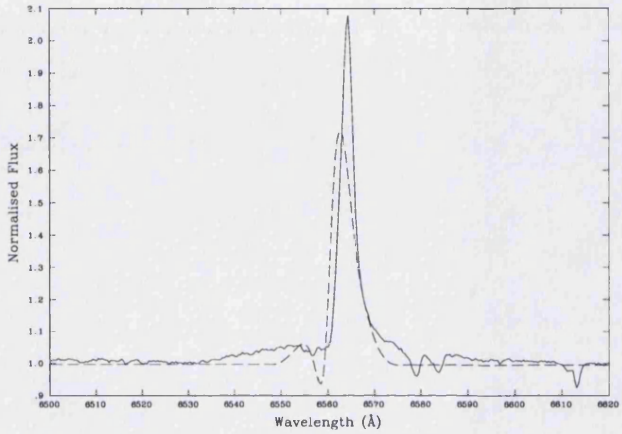

A.40 HD 191781

Spectral type:	ON9.7Iab	Y(He):	0.16	(Observing run: WHT95)
$T_{\rm eff}$:	31 000 K	$b_3^{\rm in}$ (H):	0.87 (1.20)	
$\log g$:	3.1	$b_4^{\rm in}$ (He):	2.25 (1.45)	
R_*:	20 $R_\odot$	b_6^{∞} (He):	10.3 (17.9)	
v_∞:	1735 km s^{-1}	β:	0.91	
$v \sin i$:	89 km s^{-1}	$\dot{M}$:	2.79×10^{-6} $M_\odot$ yr^{-1}	

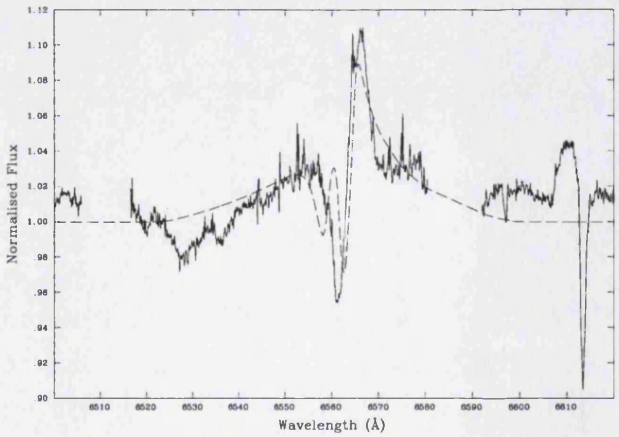

A.41 HD 192281

Spectral type:	O5Vn((f))p	Y(He):	0.09	(Observing run: INT00)
$T_{\rm eff}$:	46 800 K	$b_3^{\rm in}$ (H):	0.40 (1.20)	
$\log g$:	3.85	$b_4^{\rm in}$ (He):	2.14 (1.55)	
R_*:	19 $R_\odot$	b_6^{∞} (He):	2.17 (18.8)	
v_∞:	2700 km s^{-1}	β:	1.58	
$v \sin i$:	270 km s^{-1}	$\dot{M}$:	4.36×10^{-6} $M_\odot$ yr^{-1}	

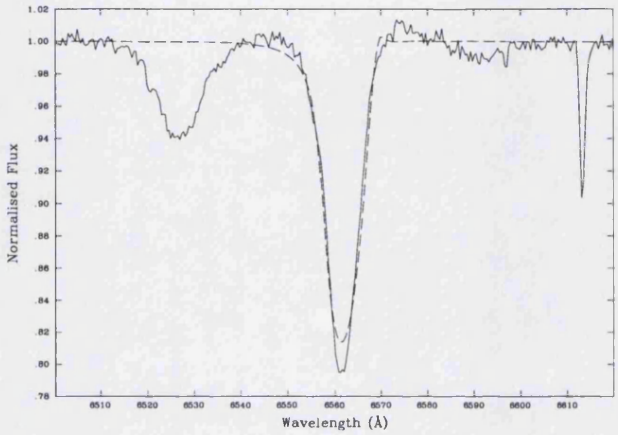

A.42 HD 193237 (P Cyg)

Spectral type:	B1Ia+	Y(He):	0.18	(Observing run: INT00)
$T_{\rm eff}$:	19 300 K	$b_3^{\rm in}$ (H):	1.08 (1.20)	
$\log g$:	2.04	$b_4^{\rm in}$ (He):	5.95 (1.35)	
R_*:	76 $R_\odot$	b_6^{∞} (He):	2.00 (10.00)	
v_∞:	200 km s^{-1}	β:	2.00	
$v \sin i$:	65 km s^{-1}	$\dot{M}$:	1.03×10^{-5} $M_\odot$ yr^{-1}	

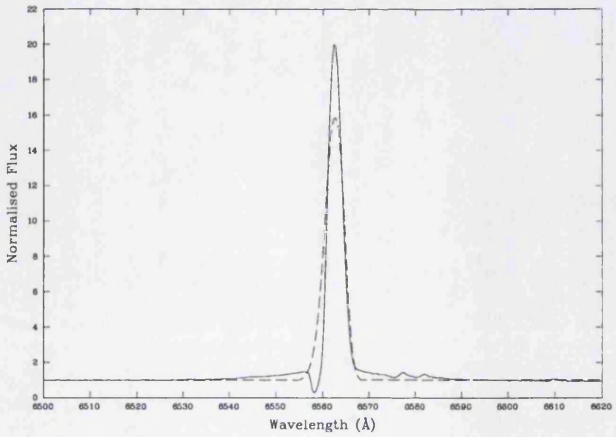

A.43 HD 194279

Spectral type:	B1.5Ia	Y(He):	0.18	(Observing run: INT00)
$T_{\rm eff}$:	19 000 K	$b_3^{\rm in}$ (H):	1.20 (1.20)	
$\log g$:	2.15	$b_4^{\rm in}$ (He):	5.37 (2.09)	
R_*:	63 $R_\odot$	b_6^{∞} (He):	21.6 (23.3)	
v_∞:	750 km s^{-1}	β:	1.05	
$v \sin i$:	70 km s^{-1}	$\dot{M}$:	1.82×10^{-6} $M_\odot$ yr^{-1}	

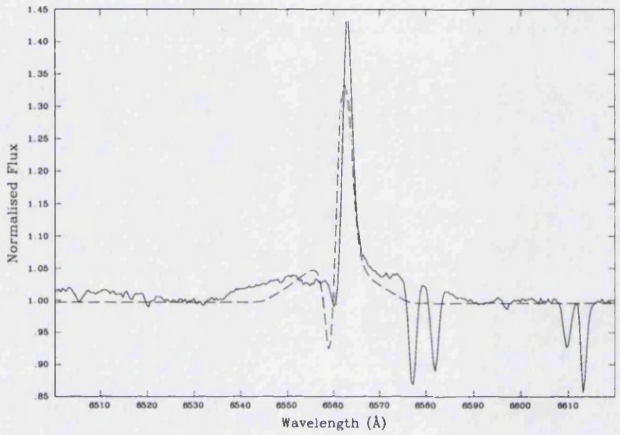

A.44 HD 194280

Spectral type:	OC9.7Iab	Y(He):	0.09	(Observing run: WHT95)
$T_{\rm eff}$:	32 000 K	$b_3^{\rm in}$ (H):	0.71 (1.20)	
$\log g$:	3.2	$b_4^{\rm in}$ (He):	3.18 (1.62)	
R_*:	21 $R_\odot$	b_6^{∞} (He):	24.5 (19.4)	
v_∞:	1735 km s^{-1}	β:	0.93	
$v \sin i$:	101 km s^{-1}	$\dot{M}$:	2.37×10^{-6} $M_\odot$ yr^{-1}	

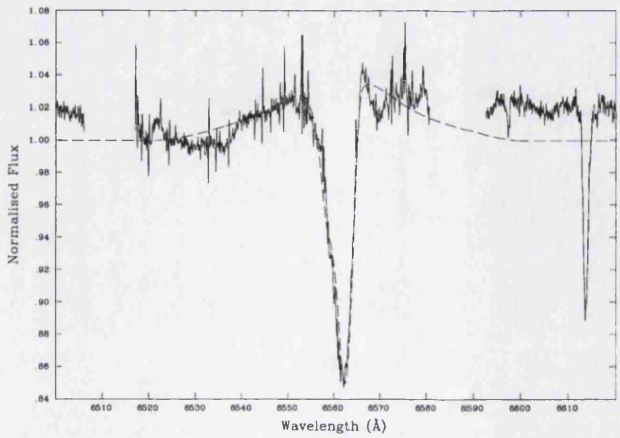

A.45 HD 195592

Spectral type:	O9.7Ia	Y(He):	0.12	(Observing run: INT00)
$T_{\rm eff}$:	31 000 K	$b_3^{\rm in}$ (H):	1.20 (1.20)	
$\log g$:	3.0	$b_4^{\rm in}$ (He):	2.56 (1.40)	
R_*:	20 $R_\odot$	b_6^{∞} (He):	24.8 (17.5)	
v_∞:	1735 km s^{-1}	β:	1.56	
$v \sin i$:	54 km s^{-1}	$\dot{M}$:	3.00×10^{-6} $M_\odot$ yr^{-1}	

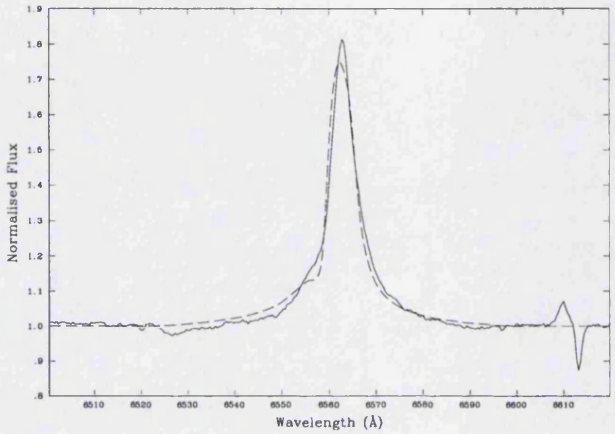

A.46 HD 197345 (α Cyg)

Spectral type:	A2Ia	Y(He):	0.07	(Observing run: INT00)
$T_{\rm eff}$:	8 600 K	$b_3^{\rm in}$ (H):	0.98 (1.20)	
$\log g$:	1.3	$b_4^{\rm in}$ (He):	5.53 (3.00)	
R_*:	180 $R_\odot$	b_6^{∞} (He):	3.76 (25.4)	
v_∞:	225 km s^{-1}	β:	0.50	
$v \sin i$:	25 km s^{-1}	$\dot{M}$:	3.80×10^{-7} $M_\odot$ yr^{-1}	

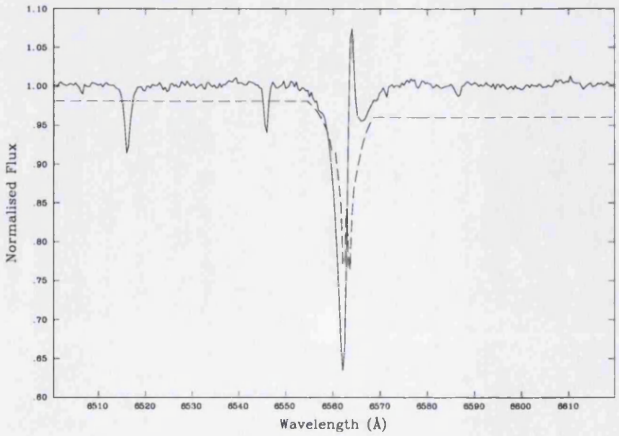

A.47 HD 201345

Spectral type:	ON9V	Y(He):	0.14	(Observing run: WHT95)
$T_{\rm eff}$:	36 000 K	$b_3^{\rm in}$ (H):	1.01 (1.20)	
$\log g$:	3.9	$b_4^{\rm in}$ (He):	5.12 (1.80)	
R_*:	8 $R_\odot$	b_6^{∞} (He):	34.7 (20.9)	
v_∞:	1425 km s^{-1}	β:	0.30	
$v \sin i$:	109 km s^{-1}	$\dot{M}$:	3.21×10^{-7} $M_\odot$ yr^{-1}	

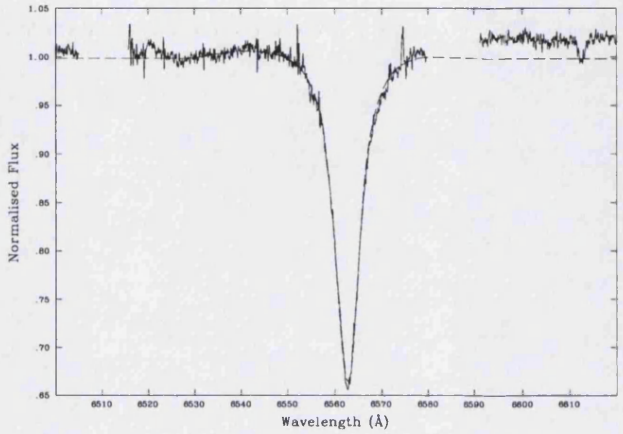

A.48 HD 202124

Spectral type:	O9.5Iab	Y(He):	0.13	(Observing run: WHT95)
$T_{\rm eff}$:	34 000 K	$b_3^{\rm in}$ (H):	0.70 (1.20)	
$\log g$:	3.2	$b_4^{\rm in}$ (He):	2.95 (1.43)	
R_*:	19 $R_\odot$	b_6^{∞} (He):	25.1 (17.7)	
v_∞:	1820 km s^{-1}	β:	1.36	
$v \sin i$:	93 km s^{-1}	$\dot{M}$:	2.87×10^{-6} $M_\odot$ yr^{-1}	

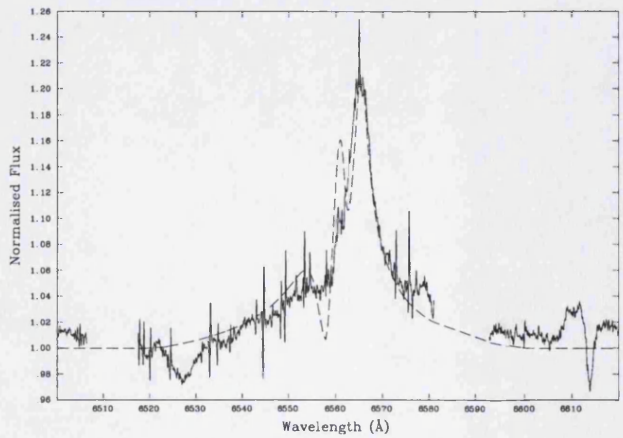

A.49 HD 206267A

Spectral type:	O6.5V((f))	Y(He):	0.09	(Observing run: INT00)
$T_{\rm eff}$:	39 800 K	$b_3^{\rm in}$ (H):	1.12 (1.20)	
$\log g$:	4.03	$b_4^{\rm in}$ (He):	1.37 (3.00)	
R_*:	9 $R_\odot$	b_6^{∞} (He):	27.9 (25.4)	
v_∞:	2745 km s^{-1}	β:	1.57	
$v \sin i$:	108 km s^{-1}	$\dot{M}$:	1.87×10^{-7} $M_\odot$ yr^{-1}	

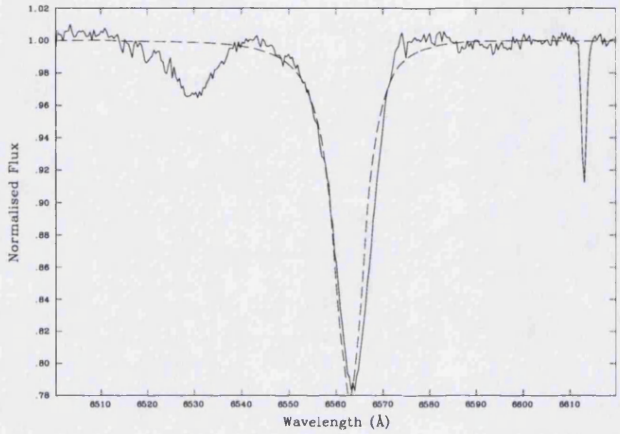

A.50 HD 207198

Spectral type:	O9Ib–II	Y(He):	0.12	(Observing run: WHT95)
$T_{\rm eff}$:	36 000 K	$b_3^{\rm in}$ (H):	1.20 (1.20)	
$\log g$:	3.4	$b_4^{\rm in}$ (He):	2.71 (1.70)	
R_*:	14 $R_\odot$	b_6^{∞} (He):	32.4 (20.0)	
v_∞:	2090 km s^{-1}	β:	0.68	
$v \sin i$:	67 km s^{-1}	$\dot{M}$:	1.52×10^{-6} $M_\odot$ yr^{-1}	

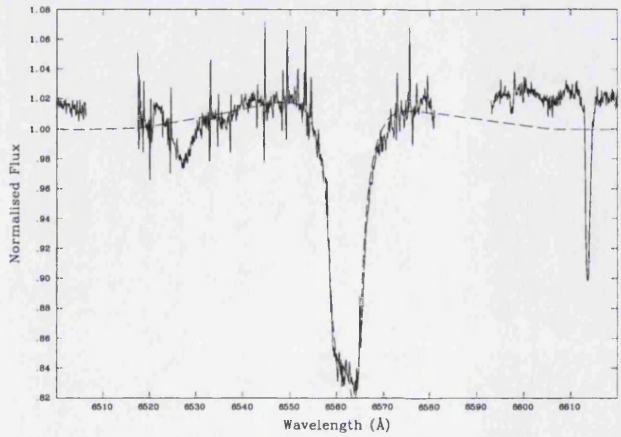

A.51 HD 209975 (19 Cep)

Spectral type:	O9.5Ib	Y(He):	0.09	(Observing run: WHT95)
$T_{\rm eff}$:	35 000 K	$b_3^{\rm in}$ (H):	1.17 (1.20)	
$\log g$:	3.4	$b_4^{\rm in}$ (He):	2.70 (1.68)	
R_*:	16 $R_\odot$	b_6^{∞} (He):	34.9 (19.8)	
v_∞:	2010 km s^{-1}	β:	0.80	
$v \sin i$:	69 km s^{-1}	$\dot{M}$:	1.81×10^{-6} $M_\odot$ yr^{-1}	

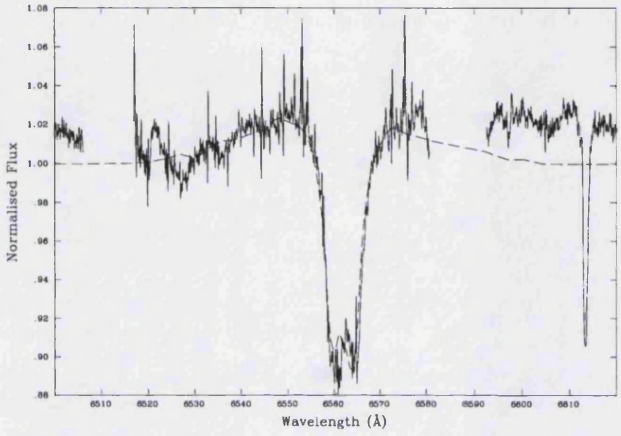

A.52 HD 210809

Spectral type:	O9Iab	Y(He):	0.13	(Observing run: WHT95)
$T_{\rm eff}$:	36 000 K	$b_3^{\rm in}$ (H):	0.69 (1.20)	
$\log g$:	3.3	$b_4^{\rm in}$ (He):	4.77 (1.65)	
R_*:	20 $R_\odot$	b_6^{∞} (He):	34.8 (19.6)	
v_∞:	2135 km s^{-1}	β:	1.70	
$v \sin i$:	89 km s^{-1}	$\dot{M}$:	2.89×10^{-6} $M_\odot$ yr^{-1}	

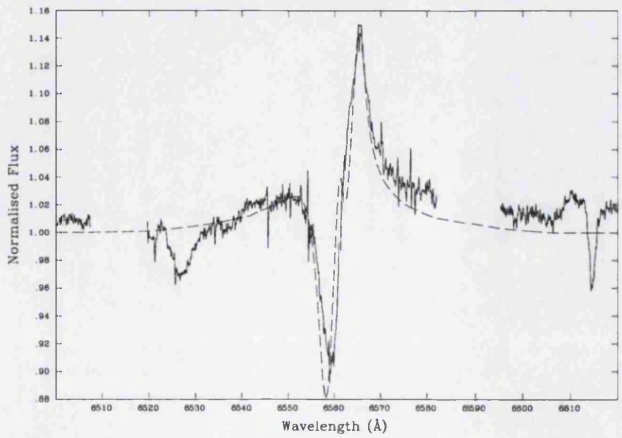

A.53 HD 210839 (λ Cep)

Spectral type:	O6I(n)fp	Y(He):	0.25	(Observing run: INT00)
$T_{\rm eff}$:	37 000 K	$b_3^{\rm in}$ (H):	0.50 (1.20)	
$\log g$:	3.55	$b_4^{\rm in}$ (He):	3.19 (1.42)	
R_*:	19 $R_\odot$	b_6^{∞} (He):	27.3 (17.6)	
v_∞:	2250 km s^{-1}	β:	1.70	
$v \sin i$:	250 km s^{-1}	$\dot{M}$:	3.96×10^{-6} $M_\odot$ yr^{-1}	

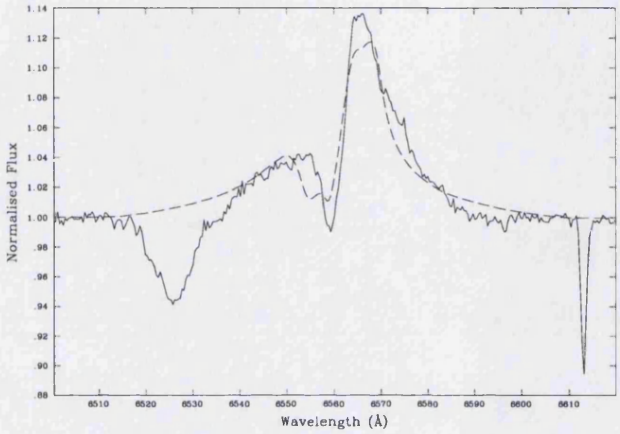

A.54 HD 214680 (10 Lac)

Spectral type:	O9V	Y(He):	0.09	(Observing run: WHT95)
$T_{\rm eff}$:	38 000 K	$b_3^{\rm in}$ (H):	0.91 (1.20)	
$\log g$:	4.2	$b_4^{\rm in}$ (He):	1.84 (2.06)	
R_*:	8 $R_\odot$	b_6^{∞} (He):	35.0 (23.0)	
v_∞:	1140 km s^{-1}	β:	0.31	
$v \sin i$:	30 km s^{-1}	$\dot{M}$:	1.62×10^{-7} $M_\odot$ yr^{-1}	

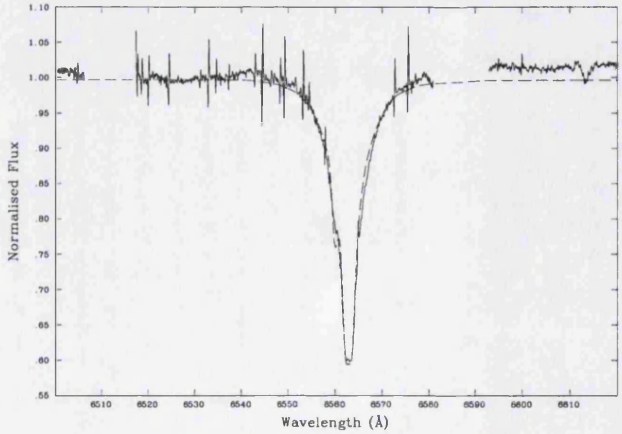

A.55 HD 218195

Spectral type:	O9III	Y(He):	0.12	(Observing run: WHT95)
$T_{\rm eff}$:	37 000 K	$b_3^{\rm in}$ (H):	1.13 (1.20)	
$\log g$:	3.6	$b_4^{\rm in}$ (He):	3.16 (1.90)	
R_*:	11 $R_\odot$	b_6^{∞} (He):	34.8 (21.7)	
v_∞:	2025 km s^{-1}	β:	0.59	
$v \sin i$:	59 km s^{-1}	$\dot{M}$:	7.66×10^{-7} $M_\odot$ yr^{-1}	

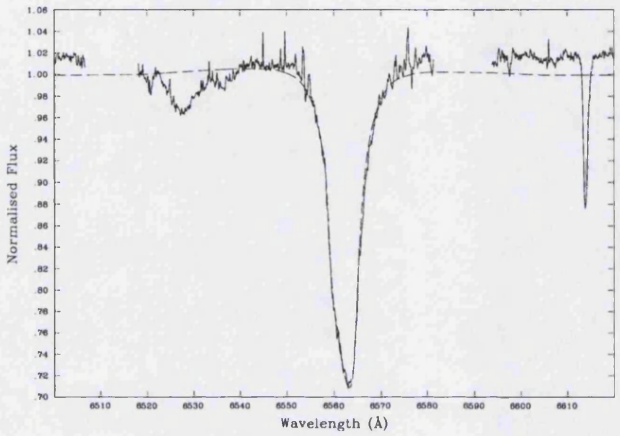

A.56 HD 218915

Spectral type:	O9.5Iab	Y(He):	0.10	(Observing run: WHT95)
$T_{\rm eff}$:	34 000 K	$b_3^{\rm in}$ (H):	1.17 (1.20)	
$\log g$:	3.2	$b_4^{\rm in}$ (He):	2.88 (1.79)	
R_*:	19 $R_\odot$	b_6^{∞} (He):	34.9 (20.8)	
v_∞:	1830 km s^{-1}	β:	1.02	
$v \sin i$:	68 km s^{-1}	$\dot{M}$:	1.73×10^{-6} $M_\odot$ yr^{-1}	

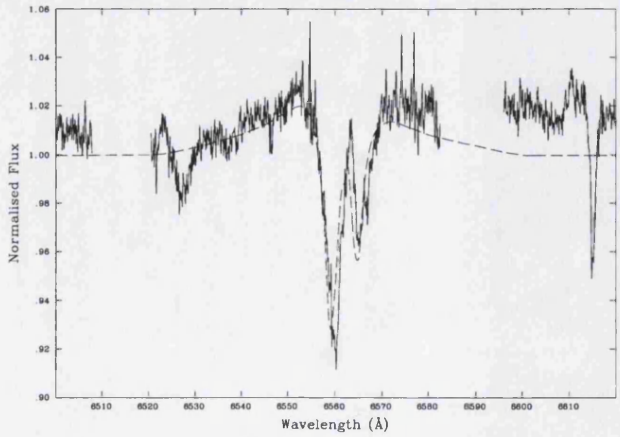

A.57 HD 225160

Spectral type:	O8Ib(f)	Y(He):	0.15	(Observing run: WHT95)
$T_{\rm eff}$:	38 000 K	$b_3^{\rm in}$ (H):	1.03 (1.20)	
$\log g$:	3.4	$b_4^{\rm in}$ (He):	3.28 (1.35)	
R_*:	23 $R_\odot$	b_6^{∞} (He):	20.8 (15.2)	
v_∞:	1530 km s^{-1}	β:	1.11	
$v \sin i$:	109 km s^{-1}	$\dot{M}$:	4.46×10^{-6} $M_\odot$ yr^{-1}	

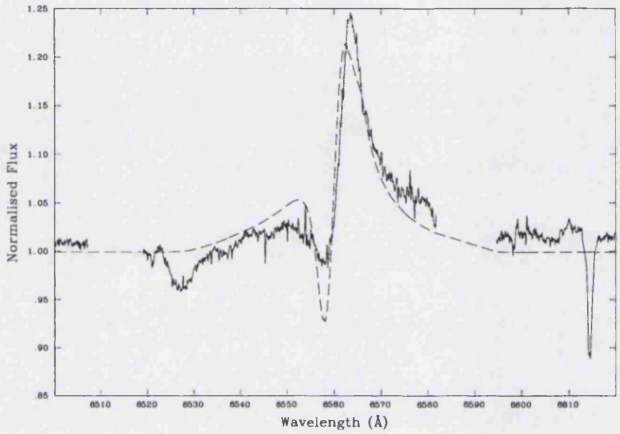

A.58 Cyg OB2 No.5

Spectral type:	2× O7Ianfp	Y(He):	0.09	(Observing run: INT00)
$T_{\rm eff}$:	39 800 K	$b_3^{\rm in}$ (H):	0.27 (1.20)	
$\log g$:	3.45	$b_4^{\rm in}$ (He):	2.74 (1.35)	
R_*:	34 $R_\odot$	b_6^{∞} (He):	8.57 (11.6)	
v_∞:	2200 km s^{-1}	β:	1.22	
$v \sin i$:	180 km s^{-1}	$\dot{M}$:	2.51×10^{-5} $M_\odot$ yr^{-1}	

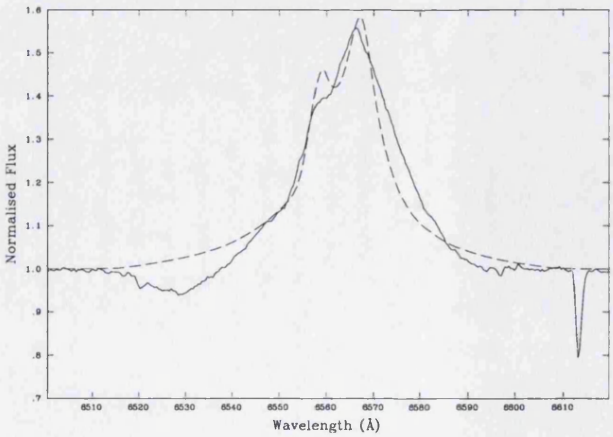

A.59 Cyg OB2 No.7

Spectral type:	O3If	Y(He):	0.18	(Observing run: INT00)
$T_{\rm eff}$:	50 000 K	$b_3^{\rm in}$ (H):	1.04 (1.20)	
$\log g$:	3.72	$b_4^{\rm in}$ (He):	1.68 (1.35)	
R_*:	15 $R_\odot$	b_6^{∞} (He):	14.5 (15.5)	
v_∞:	3080 km s^{-1}	β:	1.19	
$v \sin i$:	105 km s^{-1}	$\dot{M}$:	6.28×10^{-6} $M_\odot$ yr^{-1}	

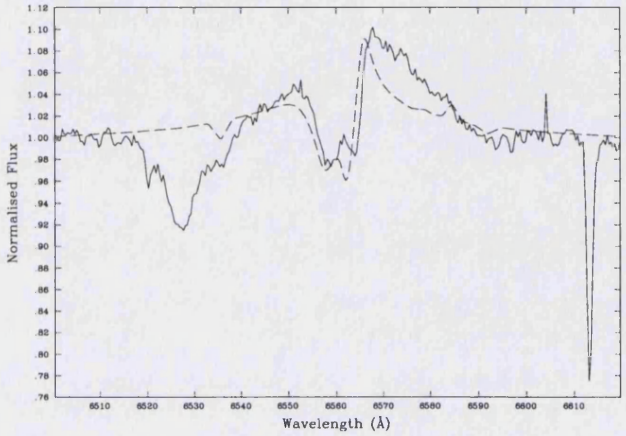

A.60 Cyg OB2 No.8A

Spectral type:	O5.5I(f)	Y(He):	0.09	(Observing run: INT00)
$T_{\rm eff}$:	44 000 K	$b_3^{\rm in}$ (H):	1.11 (1.20)	
$\log g$:	3.51	$b_4^{\rm in}$ (He):	1.78 (1.37)	
R_*:	28 $R_\odot$	b_6^{∞} (He):	30.5 (17.2)	
v_∞:	2650 km s^{-1}	β:	0.95	
$v \sin i$:	95 km s^{-1}	$\dot{M}$:	9.96×10^{-6} $M_\odot$ yr^{-1}	

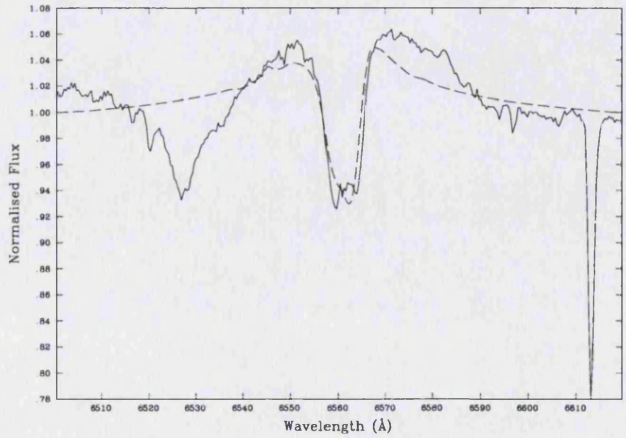

A.61 Cyg OB2 No.9

Spectral type:	O5If	Y(He):	0.09	(Observing run: INT00)
$T_{\rm eff}$:	44 500 K	$b_3^{\rm in}$ (H):	0.67 (1.20)	
$\log g$:	3.52	$b_4^{\rm in}$ (He):	2.54 (1.35)	
R_*:	22 $R_\odot$	b_6^{∞} (He):	29.2 (14.2)	
v_∞:	2200 km s^{-1}	β:	1.22	
$v \sin i$:	135 km s^{-1}	$\dot{M}$:	8.51×10^{-6} $M_\odot$ yr^{-1}	

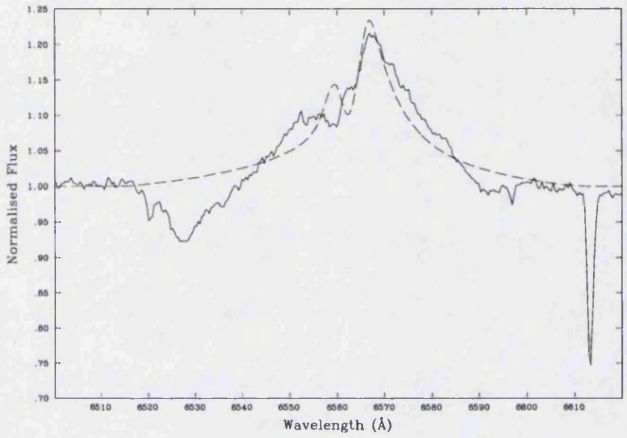

A.62 Cyg OB2 No.12

Spectral type:	B5Ie	Y(He):	0.09	(Observing run: INT00)
$T_{\rm eff}$:	11 200 K	$b_3^{\rm in}$ (H):	1.20 (1.20)	
$\log g$:	1.23	$b_4^{\rm in}$ (He):	5.99 (3.00)	
R_*:	338 $R_\odot$	b_6^{∞} (He):	34.9 (25.4)	
v_∞:	1400 km s^{-1}	β:	1.19	
$v \sin i$:	75 km s^{-1}	$\dot{M}$:	1.39×10^{-5} $M_\odot$ yr^{-1}	

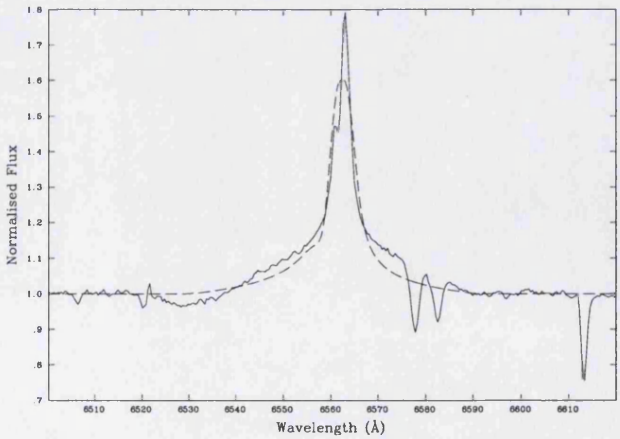

A.63 V433 Sct

Spectral type:	B1.5Ia	Y(He):	0.18	(Observing run: INT00)
$T_{\rm eff}$:	19 200 K	$b_3^{\rm in}$ (H):	1.20 (1.20)	
$\log g$:	2.37	$b_4^{\rm in}$ (He):	5.90 (1.68)	
R_*:	59 $R_\odot$	b_6^{∞} (He):	9.47 (19.8)	
v_∞:	1100 km s^{-1}	β:	1.00	
$v \sin i$:	75 km s^{-1}	$\dot{M}$:	5.23×10^{-6} $M_\odot$ yr^{-1}	

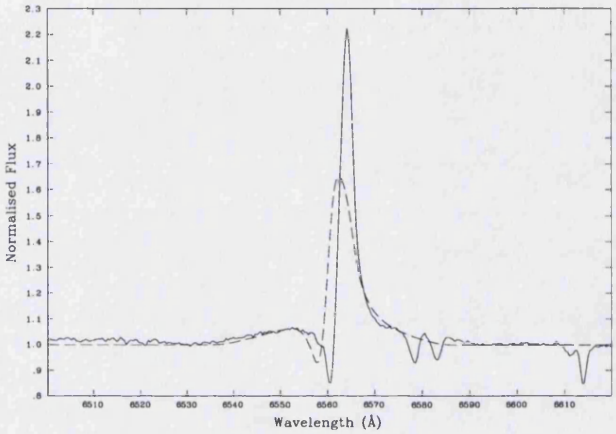

A.64 MWC 349

Spectral type:	O9:III: + B0III	Y(He):	0.09	(Observing run: INT00)
$T_{\rm eff}$:	28 800 K	$b_3^{\rm in}$ (H):	1.20 (1.20)	
$\log g$:	3.52	$b_4^{\rm in}$ (He):	1.35 (1.35)	
R_*:	17 $R_\odot$	b_6^{∞} (He):	10.0 (10.0)	
v_∞:	50 km s^{-1}	β:	0.75	
$v \sin i$:	97 km s^{-1}	$\dot{M}$:	7.2×10^{-6} $M_\odot$ yr^{-1}	

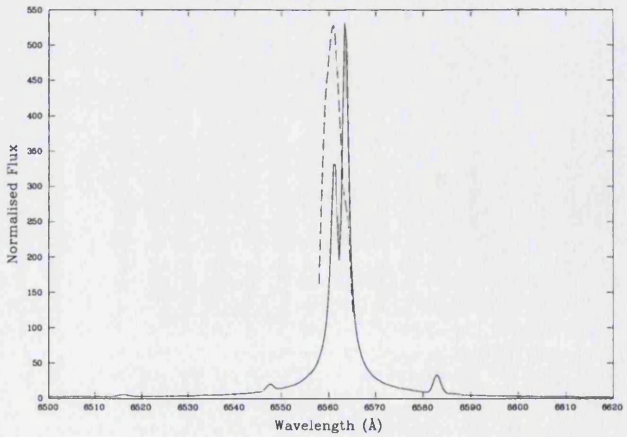

Bibliography

Abbott, D. C., 1982, *ApJ*, **263**, 723

Abbott, D. C., Bieging, J. H. and Churchwell, E., 1981, *ApJ*, **250**, 645

Abbott, D. C., Bieging, J. H. and Churchwell, E., 1984*a*, *ApJ*, **280**, 671

Abbott, D. C., Bieging, J. H., Churchwell, E. and Cassinelli, J. P., 1980, *ApJ*, **238**, 196

Abbott, D. C., Bieging, J. H., Churchwell, E. and Torres, A. V., 1986, *ApJ*, **303**, 239

Abbott, D. C., Telesco, C. M. and Wolff, S. C., 1984*b*, *ApJ*, **279**, 225

Albayrak, B., 2000, *A&A*, **364**, 237

Allen, D. A. and Swings, J. P., 1976, *A&A*, **47**, 293

Allen, D. A., Swings, J. P. and Harvey, P. M., 1972, *A&A*, **20**, 333

Altenhoff, W. J., Strittmatter, P. A. and Wendker, H. J., 1981, *A&A*, **93**, 48

Altenhoff, W. J., Thum, C. and Wendker, H. J., 1994, *A&A*, **281**, 161

Aufdenberg, J. P., Hauschildt, P. H., Baron, E., Nordgren, T. E., Burnley, A. W., Howarth, I. D., Gordon, K. D. and Stansberry, J. A., 2002, *ApJ*, **570**, 344

Baade, D., 1991, in Baade, D. (ed.), *Rapid Variability of OB stars: Nature and Diagnostic Value*, Proceedings of an ESO Workshop, p. 21

Baade, D. and Balona, L. A., 1994, in Balona, L. A., Henrichs, H. F. and Le Contel, J. M. (eds.), *Pulsation, Rotation and Mass Loss in Early-Type Stars*, IAU Symposium No. 162, p. 311

Baldwin, J. E., Stella Harris, C. and Ryle, M., 1973, *Nature*, **241**, 38

Barlow, M. J. and Cohen, M., 1977, *ApJ*, **213**, 737

Becker, R. H. and White, R. L., 1985, in Hjellming, R. M. and Gibson, D. M. (eds.), *Radio Stars*, Dordrecht: Reidel, p. 139

Berghöfer, T. W., Schmitt, J. H. M. M. and Cassinelli, J. P., 1996, *A&AS*, **118**, 481

Berghöfer, T. W., Schmitt, J. H. M. M., Danner, R. and Cassinelli, J. P., 1997, *A&A*, **322**, 167

Bianchi, L. and Garcia, M., 2002, *ApJ*, **581**, 610

Bieging, J. H., Abbott, D. C. and Churchwell, E. B., 1989, *ApJ*, **340**, 518

Bjorkman, J. E. and Cassinelli, J. P., 1993, *ApJ*, **409**, 429

Blomme, R., Prinja, R. K., Runacres, M. C. and Colley, S., 2002, *A&A*, **382**, 921

Blomme, R. and Runacres, M. C., 1997, *A&A*, **323**, 886

Blomme, R., Van de Steene, G. C., Prinja, R. K., Runacres, M. C. and Clark, J. S., 2003, *A&A, in prep.*

Bohannan, B. and Crowther, P. A., 1999, *ApJ*, **511**, 374

Bolton, C. T., 1974, *ApJ*, **192**, L7

Brandt, J. C., Stecher, T. P., Crawford, D. L. and Maran, S. P., 1971, *ApJ*, **163**, L99

Bresolin, F., Kudritzki, R.-P., Lennon, D. J., Smartt, S. J., Herrero, A., Urbaneja, M. A. and Puls, J., 2002, *ApJ*, **580**, 213

Butler, K., 1984, *PhD thesis* (University of London)

Butler, K. and Giddings, J. R., 1985, *CCP7 Newsletter on Analysis of Astronomical Spectra No. 9* (Daresbury Laboratory, UK)

Cannon, A. and Pickering, E., 1918, *Annals Harvard Obs.*, **91**, 1

Carpay, J., de Jager, C. and Nieuwenhuijzen, H., 1991, *A&A*, **248**, 475

Carpay, J., de Jager, C., Nieuwenhuijzen, H. and Moffat, A. F. J., 1989, *A&A*, **216**, 143

Cassinelli, J. P., Waldron, W. L., Sanders, W. T., Harnden, Jr., F. R., Rosner, R. and Vaiana, G. S., 1981, *ApJ*, **250**, 677

Castor, J. I., Abbott, D. C. and Klein, R. I., 1975, *ApJ*, **195**, 157

Charbonneau, P. and Knapp, B., 1996, *A User's Guide to PIKAIA 1.0, NCAR Technical Note 418+IA* (Boulder: National Center for Atmospheric Research)

Chen, W. and White, R. L., 1994, *Ap&SS*, **221**, 259

Chentsov, E. L., 1980, *SvAL*, **6**, 199

Chiosi, C. and Maeder, A., 1986, *ARA&A*, **24**, 329

Chlebowski, T., 1989, *ApJ*, **342**, 1091

Chlebowski, T. and Garmany, C. D., 1991, *ApJ*, **368**, 241

Chlebowski, T., Harnden, F. R. and Sciortino, S., 1989, *ApJ*, **341**, 427

Chu, Y.-H., 2002, in Moffat, A. F. J. and St-Louis, N. (eds.), *Interacting Winds from Massive Stars*, ASP Conference Series Vol. 260, p. 109

Cohen, M., Bieging, J. H., Dreher, J. W. and Welch, W. J., 1985, *ApJ*, **292**, 249

Cohen, M. and Kuhi, L. V., 1977, *MNRAS*, **180**, 37

Cohen, M., Kuhi, L. V. and Barlow, M. J., 1975, *A&A*, **40**, 291

Conti, P. S., 1984, in Maeder, A. and Renzini, A. (eds.), *Observational Tests of the Stellar Evolution Theory*, IAU Symposium No. 105, p. 233

Conti, P. S. and Leep, E. M., 1974, *ApJ*, **193**, 113

Conti, P. S., Massey, P., Ebbets, D. and Niemela, V. S., 1980, *ApJ*, **238**, 184

Contreras, M. E., Rodríguez, L. F., Gómez, Y. and Velázquez, A., 1996, *ApJ*, **469**, 329

Contreras, M. E., Rodríguez, L. F., Tapia, M., Cardini, D., Emanuele, A., Badiali, M. and Persi, P., 1997, *ApJ*, **488**, L153

Cowley, A. P., 1972, *AJ*, **77**, 750

Cowley, A. P. and Hutchings, J. B., 1976, *PASP*, **88**, 456

Crowther, P. A., 1997, *MNRAS*, **290**, L59

Crowther, P. A. and Bohannan, B., 1997, *A&A*, **317**, 532

Crowther, P. A., Dessart, L., Hillier, D. J., Abbott, J. B. and Fullerton, A. W., 2002*a*, *A&A*, **392**, 653

Crowther, P. A., Hillier, D. J., Evans, C. J., Fullerton, A. W., de Marco, O. and Willis, A. J., 2002*b*, *ApJ*, **579**, 774

Crowther, P. A., Hillier, D. J. and Smith, L. J., 1995*a*, *A&A*, **293**, 403

Crowther, P. A., Smith, L. J., Hillier, D. J. and Schmutz, W., 1995*b*, *A&A*, **293**, 427

Currie, M. J. and Berry, D. S., 2001, *Starlink User Note 95.19*

De Jager, C., 1984, *A&A*, **138**, 246

Dessart, L., Crowther, P. A., Hillier, D. J., Willis, A. J., Morris, P. W. and van der Hucht, K. A., 2000, *MNRAS*, **315**, 407

Divan, L. and Prévot-Burnichon, M.-L., 1988, in Conti, P. S. and Underhill, A. B. (eds.), *O stars and Wolf-Rayet stars*, NASA SP-497, p. 1

Djurašević, G., Zakirov, M., Eshankulova, M. and Erkapić, S., 2001, *A&A*, **374**, 638

Donati, J.-F., Babel, J., Harries, T. J., Howarth, I. D., Petit, P. and Semel, M., 2002, *MNRAS*, **333**, 55

Donati, J.-F., Semel, M., Carter, B. D., Rees, D. E. and Cameron, A. C., 1997, *MNRAS*, **291**, 658

Drake, S. A., 1990, *AJ*, **100**, 572

Drew, J. E., 1989, *ApJS*, **71**, 267

Ebbets, D., 1981, *PASP*, **93**, 119

Ebbets, D., 1982, *ApJS*, **48**, 399

Evans, C. J., 2001, *PhD thesis* (University of London)

Exter, K. M., Watson, S. K., Barlow, M. J. and Davis, R. J., 2002, *MNRAS*, **333**, 715

Feldmeier, A., 1995, *A&A*, **299**, 523

Florkowski, D. R., Johnston, K. J., Wade, C. M. and de Vegt, C., 1985, *AJ*, **90**, 2381

Friend, D. B. and Abbott, D. C., 1986, *ApJ*, **311**, 701

Friend, D. B. and Castor, J. I., 1983, *ApJ*, **272**, 259

Fullerton, A. W., 1990, *PhD thesis* (University of Toronto)

Fullerton, A. W., 1997, in De Greve, J. P., Blomme, R. and Hensberge, H. (eds.), *Stellar Atmospheres: Theory and Observations*, New York: Springer, p. 187

Fullerton, A. W., Gies, D. R. and Bolton, C. T., 1996, *ApJS*, **103**, 475

Gabler, R., Gabler, A., Kudritzki, R.-P., Puls, J. and Pauldrach, A., 1989, *A&A*, **226**, 162

Gabler, R., Gabler, A., Kudritzki, R.-P., Puls, J. and Pauldrach, A., 1990, in Garmany, C. D. (ed.), *Properties of Hot, Luminous Stars: Boulder-Munich Workshop*, ASP Conference Series Vol. 7, p. 64

Garmany, C. D. and Conti, P. S., 1984, *ApJ*, **284**, 705

Garmany, C. D. and Massey, P., 1981, *PASP*, **93**, 500

Garmany, C. D., Olson, G. L., Conti, P. S. and Van Steenberg, M., 1981, *ApJ*, **250**, 660

Giddings, J. R., 1981, *PhD thesis* (University of London)

Gies, D. R. and Bolton, C. T., 1986, *ApJS*, **61**, 419

Gies, D. R., Mason, B. D., Hartkopf, W. I., McAlister, H. A., Frazin, R. A., Hahula, M. E., Penny, L. R., Thaller, M. L., Fullerton, A. W. and Shara, M. M., 1993, *AJ*, **106**, 2072

Gilmore, G. and Howell, D. (eds.), 1998, *The Stellar Initial Mass Function, 38th Herstmonceux Conference*, ASP Conference Series Vol. 142

Grillo, F., Sciortino, S., Micela, G., Vaiana, G. S. and Harnden, Jr., F. R., 1992, *ApJS*, **81**, 795

Groenewegen, M. A. T. and Lamers, H. J. G. L. M., 1989, *A&AS*, **79**, 359

Groenewegen, M. A. T. and Lamers, H. J. G. L. M., 1991, *A&A*, **243**, 429

Hall, D. S., 1974, *Acta Astron.*, **24**, 69

Hamann, F. and Simon, M., 1986, *ApJ*, **311**, 909

Hamann, F. and Simon, M., 1988, *ApJ*, **327**, 876

Hamann, W.-R., 1981*a*, *A&A*, **93**, 353

Hamann, W.-R., 1981*b*, *A&A*, **100**, 169

Harmanec, P., 1987, in Slettebak, A. and Snow, T. P. (eds.), *Physics of Be stars*, IAU Colloquium No. 92, p. 339

Harmanec, P., Habuda, P., Štefl, S., Hadrava, P., Korčáková, D., Koubský, P., Krtička, J., Kubát, J., Škoda, P., Šlechta, M. and Wolf, M., 2000, *A&A*, **364**, L85

Harnden, Jr., F. R., Branduardi, G., Elvis, M., Gorenstein, P., Grindlay, J., Pye, J. P., Rosner, R., Topka, K. and Vaiana, G. S., 1979, *ApJ*, **234**, L51

Harnden, Jr., F. R., Fabricant, D. G., Harris, D. E. and Schwarz, J., 1984, *Scientific Specification of the Data Analysis System for the Einstein Observatory (HEAO-2) Imaging Proportional Counter (SAO Spec. Rept. 393)*

Harvey, A. S., Stickland, D. J., Howarth, I. D. and Zuiderwijk, E. J., 1987, *Observatory*, **107**, 205

Haser, S. M., 1995, *PhD thesis* (Universitäts-Sternwarte der Ludwig-Maximillian Universität, München)

Herrero, A., Corral, L. J., Villamariz, M. R. and Martín, E. L., 1999, *A&A*, **348**, 542

Herrero, A., Kudritzki, R.-P., Vilchez, J. M., Kunze, D., Butler, K. and Haser, S., 1992, *A&A*, **261**, 209

Herrero, A., Puls, J., Corral, L. J., Kudritzki, R.-P. and Villamariz, M. R., 2001, *A&A*, **366**, 623

Herrero, A., Puls, J. and Najarro, F., 2002, *A&A*, **396**, 949

Herrero, A., Puls, J. and Villamariz, M. R., 2000, *A&A*, **354**, 193

Hillier, D. J., 1988, *ApJ*, **327**, 822

Hillier, D. J., 1989, *ApJ*, **347**, 392

Hillier, D. J., 1991, *A&A*, **247**, 455

Hillier, D. J., Kudritzki, R.-P., Pauldrach, A. W. A., Baade, D., Cassinelli, J. P., Puls, J. and Schmitt, J. H. M. M., 1993, *A&A*, **276**, 117

Hillier, D. J. and Miller, D. L., 1998, *ApJ*, **496**, 407

Hillier, D. J. and Miller, D. L., 1999, *ApJ*, **519**, 354

Hofmann, K.-H., Balega, Y., Ikhsanov, N. R., Miroshnichenko, A. S. and Weigelt, G., 2002, *A&A*, **395**, 891

Holland, W. S., Robson, E. I., Gear, W. K., Cunningham, C. R., Lightfoot, J. F., Jenness, T., Ivison, R. J., Stevens, J. A., Ade, P. A. R., Griffin, M. J., Duncan, W. D., Murphy, J. A. and Naylor, D. A., 1999, *MNRAS*, **303**, 659

Houk, N., 1982, *Michigan Catalogue of Two-Dimensional Spectral Types for the HD Stars* (University of Michigan)

Howarth, I. D., Murray, J., Mills, D. and Berry, D. S., 1997*a*, *Starlink User Note 50*

Howarth, I. D. and Prinja, R. K., 1989, *ApJ*, **69**, 527

Howarth, I. D., Siebert, K. W., Hussain, G. A. J. and Prinja, R. K., 1997*b*, *MNRAS*, **284**, 265

Hubeny, I., 1988, *Computer Phys. Comm.*, **52**, 103

Hubeny, I., Heap, S. R. and Lanz, T., 1998, in Howarth, I. D. (ed.), *Boulder–Munich II: Properties of Hot, Luminous Stars*, ASP Conference Series Vol. 131, p. 108

Hubeny, I. and Lanz, T., 1995, *ApJ*, **439**, 875

Humphreys, R. M., 1978, *ApJS*, **38**, 309

Humphreys, R. M., 1989, in Davidson, K., Moffat, A. F. J. and Lamers, H. J. G. L. M. (eds.), *Physics of Luminous Blue Variables*, Kluwer: Dordrecht, p. 3

Humphreys, R. M. and Davidson, K., 1979, *ApJ*, **232**, 409

Jarad, M. M., Hilditch, R. W. and Skillen, I., 1989, *MNRAS*, **238**, 1085

King, A. R. and Jameson, R. F., 1979, *A&A*, **71**, 326

Klein, R. I. and Castor, J. I., 1978, *ApJ*, **220**, 902

Kozok, J. R., 1985, *A&AS*, **62**, 7

Kudritzki, R.-P., 1998, in Aparicio, A., Herrero, A. and Sánchez, F. (eds.), *Stellar Astrophysics for the Local Group*, Cambridge Contemporary Astrophysics, p. 149

Kudritzki, R.-P., Gabler, R., Kunze, D., Pauldrach, A. W. A. and Puls, J., 1991, in Leitherer, C., Walborn, N. R., Heckman, T. M. and Norman, C. A. (eds.), *Massive Stars in Starbursts*, Cambridge University Press, p. 59

Kudritzki, R.-P., Lennon, D. J. and Puls, J., 1995, in Walsh, J. R. and Danziger, I. J. (eds.), *Quantitative Spectroscopy of Luminous Blue Stars in Distant Galaxies*, Proceedings of the ESO Workshop, Science with the VLT, p. 246

Kudritzki, R.-P., Pauldrach, A. W. A. and Puls, J., 1987, *A&A*, **173**, 293

Kudritzki, R.-P., Pauldrach, A. W. A. and Puls, J., 1989, *A&A*, **219**, 205

Kudritzki, R.-P., Puls, J., Lennon, D. J., Venn, K. A., Reetz, J., Najarro, F., McCarthy, J. K. and Herrero, A., 1999, *A&A*, **350**, 970

Lamers, H. J. G. L. M., Cerruti-Sola, M. and Perinotto, M., 1987, *ApJ*, **314**, 726

Lamers, H. J. G. L. M. and Leitherer, C., 1993, *ApJ*, **412**, 771

Lamers, H. J. G. L. M. and Waters, L. B. F. M., 1984, *A&A*, **138**, 25

Lamers, H. J. G. L. M., Zickgraf, F.-J., de Winter, D., Houziaux, L. and Zorec, J., 1998, *A&A*, **340**, 117

Langer, N., García-Segura, G. and Mac Low, M.-M., 1999, *ApJ*, **520**, L49

Langer, N., Hamann, W.-R., Lennon, M., Najarro, F., Pauldrach, A. W. A. and Puls, J., 1994, *A&A*, **290**, 819

Leitherer, C., 1988*a*, *ApJ*, **326**, 356

Leitherer, C., 1988*b*, *ApJ*, **334**, 626

Leitherer, C., Chapman, J. M. and Koribalski, B., 1995, *ApJ*, **450**, 289

Leitherer, C., Forbes, D., Gilmore, A. C., Hearnshaw, J., Klare, G., Krautter, J., Mandel, H., Stahl, O., Strupat, W., Wolf, B., Zickgraf, F.-J. and Zirbel, E., 1987, *A&A*, **185**, 121

Leitherer, C., Hefele, H., Stahl, O. and Wolf, B., 1982, *A&A*, **108**, 102

Leitherer, C. and Robert, C., 1991, *ApJ*, **377**, 629

Levato, H., Malaroda, S., Morrell, N., Garcia, B. and Hernández, C., 1991, *ApJS*, **75**, 869

Levato, H., Morrell, N., Garcia, B. and Malaroda, S., 1988, *ApJS*, **68**, 319

Lucy, L. B., 1982, *ApJ*, **255**, 278

Lucy, L. B. and Solomon, P. M., 1970, *ApJ*, **159**, 879

Lucy, L. B. and White, R. L., 1980, *ApJ*, **241**, 300

Martins, F., Schaerer, S. and Hillier, D. J., 2002, *A&A*, **382**, 999

Mason, B. D., Gies, D. R., Hartkopf, W. I., Bagnuolo, Jr., W. G., Brummelaar, T. T. and McAlister, H. A., 1998, *AJ*, **115**, 821

Mason, B. D., Wycoff, G. L. and Hartkopf, W. I., 2003, *The Washington Double Star Catalogue* (Astrometry Department, U.S. Naval Observatory)

Massey, P., 1998, in Gilmore, G. and Howell, D. (eds.), *The Stellar Initial Mass Function, 38th Herstmonceux Conference*, ASP Conference Series Vol. 142, p. 17

Massey, P. and Thompson, A. B., 1991, *AJ*, **101**, 1408

McAlister, H. A., Mason, B. D., Hartkopf, W. I. and Shara, M. M., 1993, *AJ*, **106**, 1639

McCarthy, J. K., Kudritzki, R.-P., Lennon, D. J., Venn, K. A. and Puls, J., 1997, *ApJ*, **482**, 757

McCarthy, J. K., Kudritzki, R.-P., Lennon, D. J., Venn, K. A., Smartt, S. J. and Herrero, A., 2001, *AAS*, **198**, 9504

McErlean, N. D., Lennon, D. J. and Dufton, P. L., 1998, *A&A*, **329**, 613

McErlean, N. D., Lennon, D. J. and Dufton, P. L., 1999, *A&A*, **349**, 553

Meynet, G., Maeder, A., Schaller, G., Schaerer, D. and Charbonnel, C., 1994, *A&AS*, **103**, 97

Mihalas, D., 1978, *Stellar Atmospheres* (The University of California Press)

Mills, D., Webb, J. and Clayton, M., 1997, *Starlink User Note 152*

Miroshnichenko, A. S., Bjorkman, K. S. and Krugov, V. D., 2002, *PASP*, **114**, 1226

Moffat, A. F. J., Drissen, L., Lamontagne, R. and Robert, C., 1988, *ApJ*, **334**, 1038

Moffat, A. F. J. and Pim FitzGerald, M., 1977, *A&A*, **54**, 263

Moffat, A. F. J. and St-Louis, N. (eds.), 2002, *Interacting Winds from Massive Stars*, ASP Conference Series Vol. 260

Morgan, W. W., Code, A. D. and Whitford, A. E., 1955, *ApJS*, **2**, 41

Morgan, W. W. and Keenan, P. C., 1973, *ARA&A*, **11**, 29

Morgan, W. W., Keenan, P. C. and Kellman, E., 1943, *An Atlas of Stellar Spectra* (Chicago University Press)

Morrell, N. and Levato, H., 1991, *ApJS*, **75**, 965

Morris, P. W., van der Hucht, K. A., Crowther, P. A., Hillier, D. J., Dessart, L., Williams, P. M. and Willis, A. J., 2000, *A&A*, **353**, 624

Morton, D. C., 1967*a*, *ApJ*, **150**, 535

Morton, D. C., 1967*b*, *ApJ*, **147**, 1017

Mullan, D. J., 1986, *A&A*, **165**, 157

Nazé, Y., Carrier, F. and Rauw, G., 2002, in Moffat, A. F. J. and St-Louis, N. (eds.), *Interacting Winds from Massive Stars*, ASP Conference Series Vol. 260, p. 457

Nugis, T., Crowther, P. A. and Willis, A. J., 1998, *A&A*, **333**, 956

Owocki, S. P., 1992, in Heber, U. and Jeffery, S. (eds.), *The Atmospheres of Early-Type Stars*, Springer-Verlag: Heidelberg, p. 393

Owocki, S. P., 1994, in Moffat, A. F. J., Owocki, S. P., Fullerton, A. W., and St.-Louis, N. (eds.), *Instability and Variability of Hot-Star Winds*, Kluwer: Dordrecht, p. 3

Owocki, S. P., Castor, J. I. and Rybicki, G. B., 1988, *ApJ*, **335**, 914

Pallavicini, R., Golub, L., Rosner, R., Vaiana, G. S., Ayres, T. and Linsky, J. L., 1981, *ApJ*, **248**, 279

Panagia, N. and Felli, M., 1975, *A&A*, **39**, 1

Pauldrach, A. W. A., Kudritzki, R.-P., Puls, J., Butler, K. and Hunsinger, J., 1994, *A&A*, **283**, 525

Pauldrach, A. W. A. and Puls, J., 1990, *A&A*, **237**, 409

Pauldrach, A. W. A., Puls, J. and Kudritzki, R.-P., 1986, *A&A*, **164**, 86

Persi, P., Ferrari-Toniolo, M., Tapia, M., Roth, M. and Rodriguez, L. F., 1985, *A&A*, **142**, 263

Petrenz, P. and Puls, J., 1996, *A&A*, **312**, 195

Petrenz, P. and Puls, J., 2000, *A&A*, **358**, 956

Phillips, R. B. and Titus, M. A., 1990, *ApJ*, **359**, L15

Plaskett, J. S. and Pearce, J. A., 1931, *PDAO*, **5**, 1

Prinja, R. K., Barlow, M. J. and Howarth, I. D., 1990, *ApJ*, **361**, 607

Prinja, R. K. and Howarth, I. D., 1986, *ApJS*, **61**, 357

Prinja, R. K. and Howarth, I. D., 1988, *MNRAS*, **233**, 123

Prinja, R. K., Howarth, I. D. and Henrichs, H. F., 1987, *ApJ*, **317**, 389

Puls, J., Feldmeier, A., Springmann, U. W. E., Owocki, S. P. and Fullerton, A. W., 1994, in Moffat, A. F. J., Owocki, S. P., Fullerton, A. W. and St-Louis, N. (eds.), *Instability and Variability of Hot-Star Winds*, Kluwer: Dordrecht, p. 409

Puls, J., Kudritzki, R.-P., Herrero, A., Pauldrach, A. W. A., Haser, S. M., Lennon, D. J., Gabler, R., Voels, S. A., Vilchez, J. M., Wachter, S. and Feldmeier, A., 1996, *A&A*, **305**, 171

Puls, J., Owocki, S. P. and Fullerton, A. W., 1993, *A&A*, **279**, 457

Puls, J., Repolust, T., Hoffmann, T. L. and Jokuthy, A., 2003, in van der Hucht, K. A., Herrero, A. and Esteban, C. (eds.), *A Massive Star Odyssey: from Main Sequence to Supernova*, IAU Symposium No. 212, p. 61

Racine, R., 1968, *AJ*, **73**, 233

Rauch, K. and Werner, K., 1988, *A&A*, **202**, 159

Rauw, G., Blomme, R., Waldron, W. L., Corcoran, M. F., Pittard, J. M., Pollock, A. M. T., Runacres, M. C., Sana, H., Stevens, I. R. and Van Loo, S., 2002*a*, *A&A*, **394**, 993

Rauw, G., Sana, H., Vreux, J.-M. and Gosset, E., 2002*b*, in Moffat, A. F. J. and St-Louis, N. (eds.), *Interacting Winds from Massive Stars*, ASP Conference Series Vol. 260, p. 449

Reid, A. H. N. and Howarth, I., 1996, *A&A*, **311**, 616

Runacres, M. C. and Blomme, R., 1996, *A&A*, **309**, 544

Runacres, M. C. and Owocki, S. P., 2002, *A&A*, **381**, 1015

Salpeter, E. E., 1955, *ApJ*, **121**, 161

Sana, H., Rauw, G., Gosset, E. and Vreux, J.-M., 2002, in Moffat, A. F. J. and St-Louis, N. (eds.), *Interacting Winds from Massive Stars*, ASP Conference Series Vol. 260, p. 431

Santolaya-Rey, A. E., Puls, J. and Herrero, A., 1997, *A&A*, **323**, 488

Scalo, J. M., 1986, *Fund. Cosmic Phys.*, **11**, 1

Schaerer, D. and Schmutz, W., 1994, *A&A*, **288**, 231

Schaller, G., Schaerer, D., Meynet, G. and Maeder, A., 1992, *A&AS*, **96**, 269

Schmid-Burgk, J., 1982, *A&A*, **108**, 169

Schmutz, W., 1997, *A&A*, **321**, 268

Schmutz, W., Hamann, W.-R. and Wessolowski, U., 1989, *A&A*, **210**, 236

Schulte, D. H., 1958, *ApJ*, **128**, 41

Scuderi, S., Bonanno, G., di Benedetto, R., Spadara, D. and Panagia, N., 1992, *ApJ*, **392**, 201

Scuderi, S., Panagia, N., Stanghellini, C., Trigilio, C. and Umana, G., 1998, *A&A*, **332**, 251

Setia Gunawan, D. Y. A., Chapman, J. M., Stevens, I. R., Rauw, G. and Leitherer, C., 2002, *in prep.*

Seward, F. D., Forman, W. R., Giacconi, R., Griffiths, R. E., Harnden, Jr., F. R., Jones, C. and Pye, J. P., 1979, *ApJ*, **234**, L55

Shortridge, K., Meyerdierks, H., Currie, M., Clayton, M. and Lockley, J., 1997, *Starlink User Note 86*

Siebert, K. W., 1999, *PhD thesis* (University of London)

Skinner, C. J., Becker, R. H., White, R. L., Exter, K. M., Barlow, M. J. and Davis, R. J., 1998, *MNRAS*, **296**, 669

Skinner, C. J., Exter, K. M., Barlow, M. J., Davis, R. J. and Bode, M. F., 1997, *MNRAS*, **288**, L7

Slettebak, A., 1988, *PASP*, **100**, 770

Smith, K. C. and Howarth, I. D., 1994, *A&A*, **290**, 868

Smith, K. C. and Howarth, I. D., 1998, *MNRAS*, **299**, 1146

Smith, K. C., Howarth, I. D. and Siebert, K. W., 1998, in Howarth, I. D. (ed.), *Boulder–Munich II: Properties of Hot, Luminous Stars*, ASP Conference Series Vol. 131, p. 153

Snow, T. P., 1977, *ApJ*, **217**, 760

Souza, S. P. and Lutz, B. L., 1980, *ApJ*, **235**, L87

Sterken, C., Gosset, E., Jüttner, A., Stahl, O., Wolf, B. and Axer, M., 1991, *A&A*, **247**, 383

Stevens, I. R., 1995, *MNRAS*, **277**, 163

Stevens, I. R., Blondin, J. M. and Pollock, A. M. T., 1992, *ApJ*, **386**, 265

Stevens, J. A., Ivison, R. J. and Jenness, T., 1997, *Starlink Cookbook 10.1*

Stickland, D. J., 1989, *Observatory*, **109**, 74

Stickland, D. J., 1995, *Observatory*, **115**, 180

Stickland, D. J. and Koch, R. H., 1996, *Observatory*, **116**, 145

Stickland, D. J. and Lloyd, C., 1993, *MNRAS*, **264**, 935

Stickland, D. J., Lloyd, C. and Sweet, I., 1997, *Observatory*, **118**, 7

Strom, R. G. and Harris, D. E., 1977, *Nature*, **269**, 581

Thum, C., Martín-Pintado, J. and Bachiller, R., 1992, *A&A*, **256**, 507

Torres-Dodgen, A. V., Tapia, M. and Carroll, M., 1991, *MNRAS*, **249**, 1

Tuthill, P. G., Monnier, J. D. and Danchi, W. C., 1999, *Nature*, **398**, 487

Underhill, A. B. and Gilroy, K. K., 1990, *ApJ*, **364**, 626

Urbaneja, M. A., Herrero, A., Kudritzki, R.-P., Bresolin, F., Corral, L. J. and Puls, J., 2002, *A&A*, **386**, 1019

Vacca, W. D., Garmany, C. D. and Shull, J. M., 1996, *ApJ*, **460**, 914

van den Oord, G. H. J., Waters, L. B. F. M., Lamers, H. J. G. L. M., Abbott, D. C., Bieging, J. H. and Churchwell, E., 1985, in Hjellming, R. M. and Gibson, D. M. (eds.), *Radio Stars*, Dordrecht: Reidel, p. 111

van der Hucht, K. A., 2001, *NewAR*, **45**, 135

van Genderen, A. M., 1989, *A&A*, **208**, 135

van Genderen, A. M., van den Bosch, F. C., Dessing, F., Fehmers, G. C., van Grunsven, J., van der Heiden, R., Janssens, A. M., Kalter, R., van der Meer, R. L. J., van Ojik, R., Smit, J. M. and Zijderveld, M. J., 1992, *A&A*, **264**, 88

van Leeuwen, F. and van Genderen, A. M., 1997, *A&A*, **327**, 1070

Walborn, N. R., 1971, *ApJS*, **23**, 257

Walborn, N. R., 1972, *AJ*, **77**, 312

Walborn, N. R., 1973, *AJ*, **78**, 1067

Walborn, N. R., 1976, *ApJ*, **205**, 419

Walborn, N. R., 1980, *ApJS*, **44**, 535

Walborn, N. R., Howarth, I. D., Lennon, D. J., Massey, P., Oey, M. S., Moffat, A. F. J., Skalkowski, G., Morrell, N. I., Drissen, L. and Parker, J. W., 2002, *AJ*, **123**, 2754

Waldron, W. L., Corcoran, M. F., Drake, S. A. and Smale, A. P., 1998, *ApJS*, **118**, 217

Wellstein, S. and Langer, N., 1999, *A&A*, **350**, 148

White, R. L., 1985, *ApJ*, **289**, 698

White, R. L. and Becker, R. H., 1982, *ApJ*, **262**, 657

White, R. L. and Becker, R. H., 1983, *ApJ*, **272**, L19

Williams, P. M. and van der Hucht, K. A., 2000, *MNRAS*, **314**, 23

Williams, P. M., van der Hucht, K. A. and Thé, P. S., 1987, *A&A*, **182**, 91

Willis, A. J., 1991, in van der Hucht, K. A. and Hidayat, B. (eds.), *Wolf-Rayet Stars and Interrelations with Other Massive Stars in Galaxies*, IAU Symposium No. 143, p. 265

Wright, A. E. and Barlow, M. J., 1975, *MNRAS*, **170**, 41

Zinnecker, H., 2003, in van der Hucht, K. A., Herrero, A. and Esteban, C. (eds.), *A Massive Star Odyssey: from Main Sequence to Supernova*, IAU Symposium No. 212, p. 80